

# *eROSITA*'s View on 1H 0707–495 and the Near-Real-Time Analysis Pipeline

Master's Thesis in Physics

Presented by  
**Philipp Weber**  
November 2, 2021

Dr. Karl Remeis Sternwarte Bamberg  
Friedrich-Alexander-Universität Erlangen-Nürnberg



Supervisor Prof. Dr. Jörn Wilms



## Abstract

Twenty-nine Years after *ROSAT* was launched to perform an all-sky survey in the X-ray regime for six months its predecessor *eROSITA* started its mission onboard the *SRG* spacecraft to greatly improve upon the sensitivity and resolution of *ROSAT*'s survey by scanning the entire sky in six months for a total of eight times. The instrument is the result of multiple decades of advancement in the technology behind X-ray observatories aiming to investigate the most extreme phenomena in the universe. *eROSITA* is expected to discover and catalog the active cores of millions of galaxies and create a map of the large scale structure of the universe based on galaxy clusters. Because compared to other current X-ray observatories such as *XMM-Newton* and *Chandra* *eROSITA* covers a large area in the sky in a short period of time makes it a suitable instrument to discover and study transient X-ray sources.

To harvest some of this potential we created the Near Real-Time Analysis (NRTA) pipeline targeting the detection and fast analysis of the most time-critical events enabling rapid follow-up observations with dedicated pointing observatories and the notification of the scientific community. The pipeline directly processes the data retrieved during the telemetry downlink, identifies bright sources passing through the field of view (FOV) during the survey using a Bayesian Block algorithm developed by Scargle et al. (2013b) and targets externally defined regions for source detection and point sources for monitoring. After calculating additional parameters for each source and matching their positions to a variety of catalogs containing sources from different wavelengths a set of trigger criteria is evaluated and if applicable an alert is generated which consists of the notification of the relevant scientists via e-mail. Easy and fast access to the data is provided by a browser-based user interface to assess the quality of the alert and decide which actions have to be taken.

On New Year's Eve 2019, shortly after the beginning of the survey, the NRTA identified a very bright source with more than 100 cts/s passing through the FOV of *eROSITA*. It was not detected in any previous scan and only a very faint source was found during the following pass. The detection was independently verified by *ART-XC*, the second instrument onboard *SRG* operating in a higher energy band. No counterpart to the source could be identified in any other catalog except three stars which are unlikely to be related to the source. During the  $\sim 40$ s long scan by *eROSITA* the count-rate decreased by a factor of at least two. To determine the flux of the source a combination of simple empirical models was fitted to its spectrum in the 0.5 to 7.0 keV range which resulted in a value of  $(2.1 \pm 0.30) \times 10^{-10}$  erg cm $^{-2}$  s $^{-1}$ . A subsequent radio observation performed by Ho (2020) identified two possible counterparts, one coinciding with a star which is unlikely to be related to the transient X-ray source. Because the source completely vanished over the course of 8 h after the event its true nature will probably remain a mystery.

As part of the Calibration and Performance Verification phase in 2019, before *eROSITA* started its all-sky survey, it observed the known active galactic nucleus 1H 0707–495 together with *XMM-Newton*, another X-ray observatory. The narrow-line Seyfert I type galaxy is known to show a sharp drop in flux at  $\sim 7$  keV in its spectrum which in the past was mostly explained by a model considering either reflections off the ionized accretion disk in the relativistic environment close to the central black hole or partial obscuration by an absorber in the line of sight towards the central emission region. During the observation large amplitude variability in the flux of the source was detected originating mainly from the soft energy band below 0.8 keV. Compared to previous observations by *XMM-Newton* the flux of the source in the 0.5 to 7.0 keV range was found to be historically low. We show that the spectrum taken over the entire observation can be fitted by the relativist reflection model *relxill* (García et al., 2014) in its lamp-post flavor which assumes that the primary source of radiation is located above the black hole and irradiates an ionized accretion disk. The parameters of the source were found to agree with that of previous work, and it is highlighted that almost all of radiation observed from the source originates from the reflection off the accretion disk which is found to have a strongly elevated abundance of iron. Motivated by the alternative explanation for the spectrum taking a partial coverer into account we further performed flux-resolved spectroscopy of three different ranges selected by count-rate from the lightcurve and added a partial absorption component for which the covering fraction  $f_{\text{pc}}$  was free to vary between the three spectra. The resulting fits strongly suggest that the reason for the soft variability is a change in this covering fraction which is with  $f_{\text{pc}} < 0.05$

almost not present for the spectra taken from intervals with high flux, increases to  $f_{\text{pc}} = 0.28^{+0.16}_{-0.22}$  for intermediate flux and further to  $f_{\text{pc}} = 0.75 \pm 0.06$  for the low flux spectrum. To achieve a good fit also the ionization state of the accretion disk had to be allowed to vary between the different spectra but in our interpretation of the observed behavior we consider this effect to be caused by the absorbing material and not the accretion disk. The strong variations in the brightness of the source indicate that the absorbing material is located close to the central emission region thus it can be expected to be ionized and therefore be more transparent to soft X-rays. Because of the low signal-to-noise ration of the data it was not possible to test this hypothesis. The result of our analysis links together the two most common explanations for the peculiar shape of the spectrum observed from 1H 0707–495 and draws a connection to the variability found in the recent observation by *eROSITA* and *XMM-Newton*.

## Zusammenfassung

Neunundzwanzig Jahre nachdem *ROSAT* gestartet wurde um für ein halbes Jahr eine Himmeldurchmusterung im Röntgenbereich durchzuführen hat sein Nachfolger *eROSITA* seine Mission an Bord des Raumfahrzeugs *SRG* aufgenommen um eine deutlich bessere Sensitivität und Auflösung als *ROSAT*'s Durchmusterung zu erreichen, indem es den gesamten Himmel achtmal in einem halben Jahr abtastet. Das Instrument ist das Resultat von mehreren Jahrzehnten Fortschritt in der Technologie hinter Röntgen Observatorien der darauf abzielt die extremsten Phänomene im Universum zu untersuchen. Es wird erwartet, dass *eROSITA* Millionen aktive Kerne von Galaxien katalogisiert und eine Karte der großräumigen Struktur des Universums basierend auf Galaxienhaufen erstellt. Weil es verglichen mit anderen derzeitigen Röntgen Observatorien wie *XMM-Newton* oder *Chandra* eine große Fläche des Himmels in einer kurzen Zeitspanne abdeckt, macht es das ein geeignetes Instrument um transiente Röntgenquellen zu finden und untersuchen.

Um einiges dieses Potenzials aus zu schöpfen haben wir die NRTA (nahezu Echtzeit Analyse) Pipeline geschaffen, welche die Detektion und schnelle Analyse der zeitkritischsten Ereignisse adressiert um rasche Anschlussbeobachtungen mit dedizierten Observatorien und die Bekanntgabe in der wissenschaftlichen Gemeinde zu ermöglichen. Die Pipeline verarbeitet direkt die Daten erhalten während eines Telemetrie Downlinks, identifiziert mit einem Bayesischen Block Algorithmus, welcher von Scargle et al. (2013b) entwickelt wurde, helle Quellen, die während der Durchmusterung durch das Gesichtsfeld wandern und adressiert extern definierte Regionen zur Quelldetektion und Punktquellen zur Überwachung. Nachdem zusätzliche Parameter für jede Quelle berechnet wurden und die Positionen mit einer Reihe von Katalogen, die Quellen aus verschiedenen Bereichen der Wellenlängen beinhalten, verglichen wurden, wird ein Satz Trigger Kriterien evaluiert und falls zutreffend ein Alarm generiert, welcher darin besteht, dass die relevanten Wissenschaftler\*innen via E-Mail benachrichtigt werden. Ein einfacher und schneller Zugriff zu den Daten wird durch eine browserbasierte Benutzerschnittstelle bereitgestellt um die Qualität des Alarms zu beurteilen und darüber zu entscheiden, welche Maßnahmen getroffen werden sollten.

An Silvester 2019, kurz nach dem Beginn der Durchmusterung von *eROSITA*, hat die NRTA eine sehr helle Quelle mit mehr als 100 Photonen pro Sekunde identifiziert, die durch das Gesichtsfeld wanderte. Sie wurde in keinem vorhergehenden Scan detektiert und nur eine sehr schwache Quelle wurde während der nachfolgenden Abtastung gefunden. Die Detektion wurde unabhängig von *ART-XC* verifiziert, dem zweiten Instrument an Bord *SRG*, das in einem höheren Energie Bereiche arbeitet. Kein Gegenstück zur Quelle konnte in einem anderen Katalog identifiziert werden, außer drei Sterne welche wahrscheinlich nicht mit der Quelle in Zusammenhang stehen. Während des ca. 40s langen Scans von *eROSITA* hat die Zählrate um mindestens einen Faktor zwei abgenommen. Um den Fluss der Quelle zu bestimmen wurde eine Kombination empirischer Modelle an deren Spektrum im Bereich von 0.5 bis 7.0 keV gefittet, was in einem Wert von  $(2.1 \pm 0.30) \times 10^{-10} \text{ erg cm}^{-2} \text{ s}^{-1}$  resultierte. Eine nachfolgende Radiobeobachtung von Ho (2020) identifizierte zwei mögliche Gegenstücke wovon eine mit einem Stern übereinstimmt, welcher wahrscheinlich nicht mit der transienten Röntgenquelle in Zusammenhang steht. Weil die Quelle über die acht Stunden nach dem Ereignis komplett verschwunden ist, wird ihr wahres Wesen vermutlich ein Geheimnis bleiben.

Als Teil der Kalibrations und Leistungs Verifikationsphase, bevor *eROSITA* seine Durchmusterung begann, hat es 2019 zusammen mit *XMM-Newton*, einem anderen Röntgenobservatorium, den bekannten aktiven Galaxienkern 1H0707–495 beobachtet. Die dünn-linige Seyfert I Galaxie ist bekannt dafür einen scharfen Abfall im Fluss bei  $\sim 7 \text{ keV}$  in ihrem Spektrum zu zeigen, was in der Vergangenheit meistens mit einem Modell erklärt wurde, das entweder Reflexionen von einer ionisierten Akkretionsscheibe im relativistischen Umfeld nahe des zentralen schwarzen Lochs betrachtet, oder eine teilweise Verdunkelung durch einen Absorber in der Blickrichtung auf den zentralen Bereich der Emission. Während der Beobachtung wurde Variabilität mit hoher Amplitude im Fluss der Quelle detektiert, welche hauptsächlich von dem weichen Energieband unter 0.8 keV stammt. Verglichen mit vorangegangenen Beobachtungen von *XMM-Newton* wurde ein historisch niedriger Fluss der Quelle im Bereich von 0.5 bis 7.0 keV festgestellt. Wir zeigen, dass das Spektrum genommen über die gesamte Beobachtung hinweg mit dem *relxill* Modell für relativistische Reflexionen (García et al., 2014) in seiner Laternenmast Variante gefittet werden kann, welche annimmt,

dass die primäre Quelle der Strahlung sich über dem schwarzen Loch befindet und die ionisierte Akkretionsscheibe beleuchtet. Die Parameter der Quelle wurden festgestellt mit denen vorangegangener Arbeit übereinzustimmen und es wird hervorgehoben, dass die überwiegende Mehrheit der Strahlung, welche von der Quelle beobachtet wurde, von Reflexionen von der Akkretionsscheibe stammt, für welche sich eine stark erhöhte Häufigkeit von Eisen ergab. Motiviert von der alternativen Erklärung für das Spektrum, welche eine teilweise Bedeckung berücksichtigt, haben wir ferner fluss-aufgelöste Spektroskopie in drei anhand der Zählrate aus der Lichtkurve ausgewählten Bereichen durchgeführt und eine teilweise Absorptionskomponente hinzugefügt, für welche der Bedeckungsgrad  $f_{\text{pc}}$  sich frei zwischen den Spektren ändern konnte. Die resultierenden Fits legen stark nahe, dass der Grund für die weiche Variabilität eine Veränderung in diesem Bedeckungsgrad ist, welcher mit  $f_{\text{pc}} < 0.05$  für das Spektrum des Intervalls mit dem höchsten Fluss fast nicht vorhanden ist, zunimmt auf  $f_{\text{pc}} = 0.28^{+0.16}_{-0.22}$  bei intermediären Fluss und weiter steigt auf  $f_{\text{pc}} = 0.75 \pm 0.06$  bei niedrigem Fluss. Um einen guten Fit zu erzielen, musste es auch dem Ionisationsgrad der Akkretionsscheibe erlaubt sein zwischen den verschiedenen Spektren zu variieren, allerdings betrachten wir dieses beobachtete Verhalten in unserer Interpretation als tatsächlich verursacht von dem absorbierenden Material und nicht der Akkretionsscheibe. Die starken Variationen der Helligkeit der Quelle deuten darauf hin, dass das absorbierende Material dem zentral Strahlungsbereich sehr nahe ist, deshalb ist es zu erwarten, dass es ionisiert und damit transparenter für weiche Röntgenstrahlen ist. Aufgrund des niedrigen Signal-Rausch-Verhältnisses der Daten war es nicht möglich diese Hypothese zu testen. Das Resultat unserer Analyse verknüpft die beiden gängigsten Erklärungen für die eigentümliche Form des Spektrums beobachtet von 1H 0707–495 und zeigt eine Verbindung auf zu der Variabilität gefunden in der neuen Beobachtung von *eROSITA* and *XMM-Newton*.

# Contents

<b>1</b>	<b>Studying Temporal Phenomena with <i>eROSITA</i></b>	<b>9</b>
1.1	The Variable X-ray Sky . . . . .	9
1.2	The Nature of 1H 0707–495 . . . . .	9
1.3	The Aim of this Thesis . . . . .	10
<b>2</b>	<b>A Brief History</b>	<b>11</b>
2.1	Astronomy in General . . . . .	11
2.2	Black Holes and Accretion Physics . . . . .	16
<b>3</b>	<b>Active Galactic Nuclei</b>	<b>19</b>
3.1	Black Holes . . . . .	22
3.1.1	Field Equations . . . . .	22
3.1.2	Metrics of Black Holes . . . . .	23
3.2	Accretion Disks . . . . .	30
3.3	Radiation Processes . . . . .	36
3.3.1	Blackbody Emission . . . . .	36
3.3.2	Inverse Compton Scattering . . . . .	38
3.3.3	Fluorescent Line Emission . . . . .	41
3.3.4	X-ray Absorption . . . . .	42
3.4	Ionized Reflection . . . . .	43
3.5	The Lamp-post Model . . . . .	45
3.5.1	Geometry . . . . .	46
3.5.2	Models considering Relativistic Effects . . . . .	47
3.5.3	Manifestation of Relativistic Effects . . . . .	49
<b>4</b>	<b>X-ray Astronomy</b>	<b>53</b>
4.1	Detecting and Measuring X-rays . . . . .	53
4.1.1	The Need to go to Space . . . . .	53
4.1.2	Focusing High-Energy Photons . . . . .	54
4.1.3	Detectors for X-rays . . . . .	61
4.2	Historical X-ray Observations of Astrophysical Sources . . . . .	65
4.2.1	Rocket Experiments . . . . .	65
4.2.2	X-ray Observatories in Space . . . . .	66
4.2.3	<i>ROSAT</i> - The Predecessor of <i>eROSITA</i> . . . . .	70
4.2.4	Between <i>ROSAT</i> and <i>eROSITA</i> . . . . .	72
4.3	Working with X-ray Data . . . . .	76
<b>5</b>	<b>The X-ray Survey Instrument <i>eROSITA</i></b>	<b>79</b>
5.1	The <i>Spectrum-Roentgen-Gamma</i> Mission . . . . .	79
5.2	The <i>eROSITA</i> Instrument . . . . .	80
5.2.1	Optical Tube Assembly . . . . .	81
5.2.2	Camera Modules . . . . .	81
5.3	Launch and Commissioning . . . . .	82
5.4	Orbit and Mission Planing . . . . .	84
5.5	Data Ownership and Release . . . . .	85
5.6	Instrument Performance . . . . .	85
5.6.1	Point Spread Function . . . . .	86

Contents

5.6.2	Effective Area . . . . .	86
5.6.3	Vignetting . . . . .	87
5.6.4	Optical Light Leak . . . . .	88
5.6.5	Impacts of Cosmic Rays on Camera Electronics . . . . .	89
5.6.6	MIP Rejection and Corrupt Frames . . . . .	89
5.7	Science Objectives . . . . .	92
5.7.1	Sensitivity & Expected Detections . . . . .	92
5.7.2	Cosmology with Galaxy Clusters . . . . .	92
5.7.3	Active Galactic Nuclei . . . . .	93
5.7.4	Compact Galactic Sources . . . . .	93
5.7.5	Diffuse Emission . . . . .	93
5.7.6	Variable Sources . . . . .	94
5.8	The <i>eROSITA</i> Near-Real-Time Analysis Pipeline . . . . .	94
5.8.1	Transient Events in the X-ray Sky . . . . .	95
5.8.2	Implementation of the NRTA . . . . .	98
5.8.3	Browser-Based User-Interface . . . . .	108
5.8.4	Statistics from the NRTA . . . . .	108
5.8.5	Example: The New-Years-Eves Transient . . . . .	110
<b>6</b>	<b>The X-ray Observatory <i>XMM-Newton</i></b>	<b>117</b>
6.1	Optical Tube Assembly . . . . .	117
6.2	EPIC-pn . . . . .	118
6.3	EPIC-MOS . . . . .	119
6.4	Reflection Grating Spectrometer . . . . .	120
6.5	Optical Monitor . . . . .	120
<b>7</b>	<b><i>eROSITA</i>'s view of the Active Galactic Nucleus 1H 0707–495</b>	<b>121</b>
7.1	Past Developments around the Source . . . . .	121
7.2	Observational Details . . . . .	123
7.2.1	Time Coverage and Operating Modes . . . . .	123
7.2.2	Data Extraction . . . . .	124
7.3	Timing Analysis . . . . .	125
7.4	Spectral Analysis . . . . .	128
7.4.1	A Simple Empirical Model . . . . .	130
7.4.2	Comparison to Previous <i>XMM-Newton</i> Observations . . . . .	130
7.4.3	Relativistic Modelling . . . . .	131
7.5	Time Selected Spectra: Partial Covering . . . . .	134
7.6	Cross-Calibration . . . . .	136
7.7	Conclusion . . . . .	136
<b>8</b>	<b>Summary and Outlook</b>	<b>143</b>
8.1	Discovering Transient Events with the <i>eROSITA</i> NRTA . . . . .	143
8.2	The Variable Nature of 1H 0707–495 . . . . .	144
	<b>References</b>	<b>146</b>
	<b>Acknowledgments</b>	<b>161</b>
	<b>Eigenständigkeitserklärung</b>	<b>162</b>

# 1 Studying Temporal Phenomena with *eROSITA*

## 1.1 The Variable X-ray Sky

A large variety of astrophysical X-ray sources and events, such as X-ray binaries, gamma-ray bursts (GRBs), tidal disruption events (TDEs), stellar flares, and active galactic nuclei (AGN), can show variability and momentary emission on every timescale, from milliseconds to years (Merloni et al., 2012). Several approaches, implemented in numerous X-ray observatories in the past and present, such as the *RXTE* (Jahoda et al., 1996; Gruber et al., 1996), *Swift* (Gehrels et al., 2004), *MAXI* (Matsuoka et al., 2009), and *NICER* (Arzoumanian et al., 2014) missions, were taken to detect and analyze variable X-ray sources. The *eROSITA* instrument onboard *SRG* performs an all-sky survey in the energy range from 0.1 to 10 keV by scanning the sky with its FOV of  $\sim 1^\circ$  in revolutions of 4 h (Predehl et al., 2021). In this way, the entire sky is covered every six months, which is repeated for a total of eight times. With this sampling pattern *eROSITA* provides a unique opportunity to discover and study transient X-ray phenomena. Because each object only spends a limited amount of time in the FOV follow-up observations with other X-ray observatories have to be performed if an interesting event was detected. These can be accompanied by other observing facilities operating at different wavelengths.

The data obtained by *eROSITA* are transmitted to ground during ground contact sessions taking place roughly every 24 h. Given the time critical nature of transient events, these data have to be processed immediately and in a short period of time, as soon as they are available. This task can be accomplished by a Near Real-Time Analysis pipeline which implements different mechanisms to identify and characterize potential variability of X-ray sources covered by *eROSITA*'s survey. The layout of this pipeline is the first major component of this thesis and is complemented by the presentation of a particular X-ray transient detected shortly after *SRG* started its survey operation.

## 1.2 The Nature of 1H 0707–495

Active galactic nuclei are one of the most extreme types of X-ray sources. They consist of a supermassive black hole at the center of a galaxy which attracts surrounding matter, forming an accretion disk (Netzer, 2015). Due to viscosity, angular momentum can be transported outward in this accretion disk which causes matter to lose energy and move closer towards the central black hole until it passes the innermost stable circular orbit, at which point it inevitably falls towards the central object (Longair, 1994). During this process energy of the particles in the disk is converted to thermal energy, thus the disk is a source of soft blackbody emission (Mitsuda et al., 1984). These photons can interact with a X-ray corona of hot, optically thin plasma and gain energy through inverse Compton scattering (Sunyaev & Titarchuk, 1980). In the past, the X-ray corona was assumed to be located above the surface of the disk (Haardt, 1993; Dove et al., 1997), but also an alternative location for a compact corona above the rotational axis of the black hole, named lamp-post structure, was often suggested, because in this configuration the emissivity profile of the accretion disk is more realistic (Martocchia & Matt, 1996; Dauser et al., 2013). For both cases effects caused by the relativistic environment in the vicinity of the black hole (Dauser, 2014) and the reprocessing of radiation by the potentially ionized accretion disk (García et al., 2013, 2014) have to be considered to explain the spectrum observed from these kind of sources.

Models assuming both types of coronae have been used to explain the observed spectrum of 1H 0707–495, a narrow line Seyfert I type galaxy (see for example Fabian et al., 2002a, 2009; Zoghbi et al., 2010; Dauser et al., 2012). The spectrum of the source shows a distinct drop in flux at  $\sim 7$  keV which was attributed to the 6.4 keV Fe-K $\alpha$  emission line distorted by relativistic effects. The other model most commonly used to explain the shape of the spectrum employs at least one partial covering component obscuring the view

## 1 Studying Temporal Phenomena with *eROSITA*

towards the central emission region of the AGN (see for example Boller et al., 2002; Tanaka et al., 2004; Miller et al., 2010; Mizumoto et al., 2014).

Before *eROSITA* started its all-sky survey it observed 1H 0707–495 in October 2019 for  $\sim 50$  ks, accompanied by *XMM-Newton*. During this observation rapid variability at energies below 0.8 keV could be detected from the source. Explaining this observed behavior in the context of previous studies by performing a timing analysis and spectral modelling of the data is the second major component of this thesis.

### 1.3 The Aim of this Thesis

As explained the two previous sections, this thesis pursues two main goals: a description of the *eROSITA* NRTA pipeline, including the presentation and analysis of a X-ray transient which it discovered, and an analysis of *eROSITA*'s observation of 1H 0707–495. To place the *eROSITA* instrument into a historical context, a brief description of the development of astronomy in general, with a focus on black holes and accretion physics, is given in Chapter 2. The processes generating X-rays observed from AGN, with a particular focus on relativistic and reflection effects in the lamp-post model, are discussed in Chapter 3, followed by Chapter 4, in which the techniques of observational X-ray astronomy are presented, including historical experiments which paved the way towards the *eROSITA* instrument. It is the main subject of Chapter 5, which includes a description of the NRTA pipeline and an analysis of an X-ray transient it detected on New Year's Eve 2019. In Chapter 7 the analysis of the observation of 1H 0707–495 is provided, followed by a summary of the results of this thesis and a brief outlook into the capabilities of future missions in Chapter 8.

## 2 A Brief History

### 2.1 Astronomy in General

Since time immemorial the everyday life of the early modern human has been governed by the external circumstances enforced upon them by the very basic facts predetermined by astronomical conditions. A very basic but dramatic example is the rising and setting of the main source of energy for the entire planet Earth: the Sun. Given by the rotation of the Earth, it enforces an inherent periodicity of 24 h upon almost the entirety of species on the planet, not only animals, but also plants and fungi. Additionally, the seasons caused by the Earth's movement around the Sun in combination with the tilt of its rotational axis (which itself is not stable due to precession and nutation) have massive influence on flora and fauna.

Discoveries such as electricity and inventions of modern technologies such as electronics made during the Anthropocene have drastically diminished the effect of astronomical conditions on the daily routine and activity of humans. Before that the easiest way to keep track of time intervals, from hours to years, or to do sophisticated navigation was to use the information provided by the observation of celestial bodies such as the Sun, the Moon, the planets or stars. The oldest known piece of evidence of this was presented by Rappenglück (2003): An ivory plate which on one side has the silhouette of a human engraved and on the other side a pattern of notches. The age of this plate could be determined by radiocarbon dating to roughly 32,000 years. Because the shape of the human-like being is interpreted to possibly resemble a goddess of the sky and the marks a (possibly lunar) calendar (Hahn, 1982) a connection was drawn to the appearance of the constellation Orion at the vernal equinox about 32,000 years ago, including the different positions caused by the apparent motion of the stars. Especially the narrow waist following Orion's belt and the raised arms of the figure support this idea, thus this piece of ivory might be the oldest known star chart. The number of notches on the other side of the plate is  $87 \pm 1$ , with the uncertainty caused by the degraded material. At the site in Germany where the plate was found Betelgeuse remained invisible for roughly 86 days around the summer solstice which is almost identical with the number of notches on the plate. A human pregnancy on average lasts about 280 days. The date of birth can be estimated by a rule which states that three months, meaning 92 days, shall be subtracted from and one year and seven days added to the first day of the last menstrual period. These 92 days are close to the 86 days of Betelgeuse not being visible and therefore the number of notches on the plate. Thus, this 32,000-year-old artifact might show that already at that era systematic observations of celestial bodies were performed to aid the determination of very basic aspects of the human life, such as the date of birth.

Another more recent example for documented observations of stars can be found in the Lascaux caves in southwestern France. The walls of this complex of caves are covered with paintings which are believed to be roughly 18,000 years old (Genty et al., 2011). A specific segment of these paintings shows an aurochs which has a variety of dots in its face and above its shoulder. The location of the spots would coincide with the Hyades, an open star cluster, where the bright star Aldebaran is directly next to it. The spots above the shoulder then would perfectly resemble another open star cluster, the Pleiades. Together with the horns of the aurochs the star cluster in the face of the animal depict the stellar constellation of Taurus (Rappenglück, 2001, 1997).

During the time of the Pre-Pottery Neolithic (8800–7000 BC) humans started to exploit sedentary agriculture and stock breeding (Kuijt & Goring-Morris, 2002). From this era a tower in Jericho was excavated which is located at the position where the nearby mountain Quruntul casts a shadow on the settlement on summer solstice (Liran, Roy, 2011), indicating that it might have served as a marker or time keeping device. Additionally, the stairway at the center of the tower is oriented towards this point, supporting the idea that systematic observations of astronomical events were performed.

In the Linear Pottery culture (5100–4600 BC) a variety of “Neolithic Roundels” have been created located in the area from Northern Germany to Hungary (Vondrovský et al., 2015). Up to this point over 200 of these

## 2 A Brief History

structures were discovered which mostly consist of two or more circles or ellipses with a diameter of few to multiple ten meters marked by wooden palisades interleaved with aligned openings at distinct positions aligned with the center of the structure. Remarkably, the openings of some of these compounds were found to mark certain astronomical events, mainly related to the solar cycle. The oldest known roundel from roughly 4800 BC is located in Goseck, Saxony-Anhalt, Germany. It had two openings which marked the sunrise and sunset at winter solstice and one opening which was most likely aligned with the north celestial pole at that time. The purpose of these constructions is not entirely clear but very likely related to the importance of the Sun for the emerging agricultural activity in this era (Ridderstad, 2009).

From the Tarxien temple phase of the Maltese historical era around 3000–2500 BC a slab of globigerina limestone was found in the temple of Tal-Qadi which appears to show a star map or Moon calendar which can be used to measure the ecliptic latitude of the Moon or planets. Additionally, the temple appears to have been aligned with main solar and lunar events of that era (Micallef, 2001). The famous monument of Stonehenge was erected in the same period (Nash et al., 2020) and even though the exact purpose of the construction is still unclear it is widely accepted that it was used in some context of celestial events (Steel, 1998; Kirk, 2000).

On 22nd of October in the year 2137 BC a solar eclipse occurred which is probably the oldest solar eclipse recorded. It was visible from China as a partial eclipse. The “Book of Historical Documents” describes how two officers have been executed for failing to predict the event (Birt, 1863; Butler, 1924; Tsu, 1934; Wang & Siscoe, 1980; Steele, 2012b).

Most probably at the time of the Bronze Age the Nebra sky disk was constructed. Radiocarbon dating suggests it was buried around 1600 BC, but it is believed to have been created in the epoch from 2100 BC up to this time in three distinct steps (Gebhard & Krause, 2010; Pernicka et al., 2020). In the first stage the roughly 30 cm in diameter large bronze plate showed a full circle (depicting the full Moon or the Sun) and a crescent Moon side by side. A variety of dots are distributed among the surface depicting stars. While most of them appear to be randomly distributed a particular group of seven stars most probably resemble the Pleiades. In the second stage, two arches on opposite sides were added which mark the rising and setting position of the Sun on winter and summer solstice at the finding spot in Saxony-Anhalt, Germany. In a last modification an additional arch was added which is interpreted to be a “Sun boat” which probably only serves a decorative purpose. Because of its appearance and age it is considered the oldest concrete representation of the sky (Herten & Waldmann, 2018).

Starting from the time around 2100 BC also the oldest star tables of the Ancient Egypt society are known which have been engraved onto coffin lids and have been found in pyramids (Imhausen, 2010). They have been used by the Egyptians to identify the time with the positions of certain small constellation of stars recorded in these tables, called the Decans, which were used to divide the night into 12 h of equal length (Cotterell et al., 1986). The knowledge accumulated about the movement of these celestial objects in combination with their mythological interpretations for the Egyptian culture was written down in the “Book of Nut” starting around 1800 BC (Lincke, 2011).

The first recorded observation of a planet was performed around 1700–1500 BC. A series of clay tablets with cuneiform imprints was recovered from the library of Nineveh and offer a 21-year-long record of the 584 days long synodic cycle of the planet Venus. While only copies from the 7th century BC are available the actual observation dates are from the time of 1700–1500 BC (Weir, 1982; Gurzadyan, 2000, 2003; Steele, 2012a; Gertoux, 2013).

A number of “Golden Hats” from the period starting around 1400 BC have been found in Germany and France which might show indications of the first lunisolar calendars (Menghin, 2000). They were cones up to a meter high made of thin gold and most likely worn on the heads of calendar priests.

Around 1000 BC the Babylonians created their first star catalog with the rising, setting and culmination dates of 66 stars recorded on clay tablets (de Jong, 2007; Brack-Bernsen, 2005).

The first solar eclipse which has been clearly recorded occurred on June 15th 763 BC. It has been noted on the “Eponym Canon” that “the Sun was eclipsed” (Lynn, 1891). In the Bible Amos 8:9 might also refer to this event as Amos is from the same era and states that “the Sun [will] go down at noon and I will darken the Earth in the clear day” (Ben-Menahem, 1992).

Around 400 BC the Greek philosopher Philolaus was the first to describe a model of the solar system where the Earth is not the central body (Huffman, 2020). Roughly at the same time the Babylonians introduced

the “Zodiac”, an area around the ecliptic which was divided into 12 segments of  $30^\circ$  each, centered in a particular constellation (Britton, 2010). The constellations of the Zodiac are still used for astrological purposes today (the horoscope). Shortly after that Plato stated in his “Phaedo” that he believed the Earth has a spherical surface (Emlyn-Jones & Preddy, 2017; Verdenius, 1958). During the same period the also Greek philosopher Theophrastos made the first recorded observations of Sun spots when studying weather phenomena (Hardy, 1991). In 350 BC Aristotle argues for the spherical shape of the Earth referring to the circular shadow of the Earth on the Moon (MacPherson, 1916). Aristarchus, who lived from 310–230 BC, was the first to publish a calculation of the size of the Sun and the Moon in combination with their distances from Earth. Although the calculations were off by a factor of 20 his methods in terms of observation and mathematics were already very advanced (Heath, 2013). First observations of Halley’s Comet have been recorded by Chinese astronomers in the year 239 BC (Hughes D. W., 1987). Around 240 BC Eratosthenes used the shadows of vertical objects in Alexandria and Syene to calculate the Earth’s circumference to 252,000 stadia (Schaubach, 1802). Unfortunately the exact measure of a stadion is not known, but it has been reconstructed from historical records to be in the range of 150–200 m (Engels, 1985), thus Eratosthenes’ calculation already was very accurate with an error of at most 20%. Eratosthenes is also credited with the invention of the “armillary sphere” briefly before that (Gangui et al., 2014) which was extended by Hipparchos with a sight tube shortly after 200 BC, creating the first device for measuring the positions of stars in the equatorial system (Truffa, 2018). The “Almagest” by Ptolemy from roughly 150 AD contains the first detailed description of the instrument (Lu, 2015). Hipparchos achieved several milestones in ancient astronomy. By careful observations of the stars and planets, he recognized the precession of the Earth’s rotational axis, determined the inclination of the ecliptic up to  $5'$  accuracy, measured the average lunar parallax and much more. Finally, around 120 BC he finished his star catalog with the positions of 1080 stars (General Notes, 1906).

Around 150 AD Claudius Ptolemy compiled the “Almagest” in which he not only provided a table of measurements of the position of stars but also elaborated on the geocentric view of the world and the motion of the planets according to the epicycle theory which was treated as a definitive work until the 17th century AD (Hetherington & Ronan, 1984; Fomenko et al., 1989).

In the “Surya Siddhanta”, a treatise about astronomy from roughly 400 AD, the Hindu gave the length of the year according to their calendar as accurate as some minutes compared to modern measurements of the sidereal year (Daphne, 2010).

In 499 AD the Indian astronomer and mathematician Aryabhata identified that a force between the celestial objects is responsible for them holding their orbits (presumably around the Earth in the geocentric view) (Gagandeep Kaur, 2017). Another astronomer from India, Brahmagupta, used the term “gurutvaakarshan” to refer to gravity as a force (Gagandeep Kaur, 2017).

The Persian astronomer Abd al-Rahman al-Sufi authored his “Book on the Constellations of the Fixed Stars” in 946. He was the first to recognize the Andromeda Galaxy and described it as a “nebulous spot” (Iatkhah sahabiya) in the form of a big Arabic fish. This was the first recorded observation of an extragalactic object (Kumitzsch, 1987).

On the 4th of July 1054 a supernova explosion in the constellation of Taurus occurred, creating the today well known supernova remnant and pulsar wind nebula designated the “Crab Nebula”. The explosion was witnessed by Chinese and Japanese astronomers who reported a new star appearing which could even be seen during the day (Mayall, 1939).

During his lifetime from 1473 until 1543 Nicolaus Copernicus compiled a work of six books entitled “De revolutionibus orbium coelestium” (On the Revolutions of the Heavenly Spheres) in which he, among other astronomically related work, describes the heliocentric system. Although this work was finished in 1530 he decided to publish it 13 years later in 1543 only after being convinced by friends. It marked the beginning of a shift of acceptance away from the geocentric model towards the heliocentric model (Holmes, 1916).

Shortly after that in 1584 Giordano Bruno published “De l’infinito, universo et mondi” (On the Infinite, Universe and Worlds) as part of his “Italian Dialogues” in which he suggested that all the stars in the night sky are of the same nature as the Sun and other planets such as the Earth could revolve around them (Gil, 2018).

In the year 1598 Tycho Brahe published a catalogue with the positions and magnitudes of 1004 stars. Modern analyses show that the overall width of the error distribution of his position measurements is

## 2 A Brief History

just 2' (Verbunt & van Gent, 2010). Shortly after that in 1609 Johannes Kepler published a book called "Astronomia Nova" in which he presented a very detailed examination of Mars' orbit. As a result of this analysis he concluded that the planet has an elliptical orbit with the Sun at one of the focal points and that "the force that moves a planet circularly weakens with distance from the source". Later in the same work he also stated a relation between the duration of the planet to pass an arc on the ellipse and the area covered by the cord from the planet to the Sun which is the same relation as the later one. He generalized these conclusions for all planets and both statements are known as Keplers first and second law today. In another work called "Harmonices Mundi" published in 1619 he found that the ratio between the cube of the semi-major axis and the square of the orbital period is a constant for all planets which has become known as Keplers third law. It is of no doubt that Keplers discoveries mark a milestone in the development of modern astronomy (B. et al., 1955; Aiton, 1969).

Between the publication of *Astronomia Nova* and *Harmonices Mundi* in 1608 the Dutch spectacle-maker Hans Lippershey tried to file the first patent for a refracting telescope (Murdin, 2000). Shortly after that when Galileo Galilei found out about this new invention he built one himself and applied some improvements. In this way he was able to create a scientific instrument with a magnification factor of up to 20 (Gingerich, 2011). Using this instrument he conducted observations of the Moon in January 1610 and discovered a very hilly landscape. Observations of the Milky Way and nebulae revealed that these were also made of countless individual stars. During a particular observation when Jupiter was close to the Moon he also observed this planet and discovered a line of three stars in the ecliptic very close to Jupiter. Observations on the following days revealed that the number of these little stars changed in the range from two to four and their positions with respect to Jupiter varied. This was in fact the discovery of Jupiter's four brightest Moons, today know as Io, Europa, Ganymede and Callisto but still often called Galilean moons. He wrote up a description of his telescope and his findings about Earth's Moon, the stars and Jupiter's Moons (christened Medicean Stars by him) and published it in March 1610 (Finocchiaro, 2010; Gingerich, 2011).

The first recorded construction of a reflecting telescope was done by the Italian Jesuit, physicist and astronomer Niccoló Zucchi in 1616, and is described in his "Optica Philosophica" which he published in 1652 (Geisler, 1807). Sir Isaac Newton recognized about 1665 the limitations of an optical system made from lenses enforced by chromatic aberration and therefore decided to build a reflecting telescope instead. In 1668 Newton built his first reflecting telescope and in 1671 a larger one which was sent to the Royal Society in the same year for inspection (Rupert Hall & Simpson, 1996). In 1687 Newton published his "Philosophiæ Naturalis Principia Mathematica" (Mathematical Principles of Natural Philosophy), a collection of three books which laid the foundation for what is these days known as classical mechanics. Most notably in this work he presented his three laws of motion, about inertia, the force exerted on a body being proportional to its acceleration and mass and all forces on an object existing in equal magnitude and opposite directions. He also gives a description of gravity which states that the strength of this force is proportional to the inverse square law of the distance between the attracting bodies. In the third book of the collection he applied these laws of motion to the trajectories of celestial objects in a heliocentric model of the solar system (Ginzburg, 1987).

In 1705 Sir Edmund Halley published his "Synopsis of the Astronomy of Comets" in which he recognized that the comets from the years 1531, 1607, and 1682 had very similar orbits, thus he claimed that it indeed was the same comet and predicated "that it will return again in the year 1758" (Halley, Edmond, 1705). This prediction turned out to be correct, and thus the comet was named after him: Halley's Comet (Hughes D. W., 1987).

Immanuel Kant described in "Allgemeine Naturgeschichte und Theorie des Himmels" (Universal Natural History and Theory of the Heavens) from 1755 anonymously how larger systems of stars such as the Milky Way and the Andromeda Galaxy behave in the same way as the planets in the solar system. He also speculated about how other systems of stars similar to the Milky Way might look from a distance and suggested that the up to this point unidentified nebulous patches in the sky might be just that, other galaxies. In the last part of this work he even speculated about the inhabitants of other planets (Richter, 1997).

When searching for new comets starting from the mid-18th century the French astronomer Charles Messier started taking notes on nebulous objects which are not comets. In 1771, he published this list, containing 45 objects at that time, in *Mémoires de l'Académie des sciences* (Messier, Charles, 1771). In Cooperation

with Pierre Méchain the catalog was extended to contain 70 objects in 1780, published in the French yearly publication of astronomical ephemerides “*Connaissance des temps*” in 1783 (Messier, Charles, 1783), and one year later to 103 objects, which was published the same way in 1784 (Messier, Charles, 1784). Later several additions were made by Méchain and others. Today the catalog contains 110 objects and is still widely used in astronomy (Shapley & Davis, 1917; Watson, 1949; Sawyer, 1948; Hockey et al., 2014).

During observations on 13th of March in 1781 near the star  $\eta$  Geminorum William Herschel noted an object with a measurable extent. First mistaken for a comet, he discovered the planet Uranus (Herschel & Watson, 1781; Cunningham, 2018).

While examining the quality of telescopes Joseph von Fraunhofer refracted light and discovered hundreds of dark lines in the spectrum of the Sun. This discovery laid the foundation of stellar spectroscopy (Fraunhofer, 1817).

In the first third of the 19th century Friedrich Wilhelm Bessel made a variety of important contributions to astronomy, physics in general and mathematics. Most notably he stated that comets consist of volatile matter which explained their trails, determined the masses of Jupiter and Saturn using the motion of their moons, analyzed the proper motion of stars, developed a theory on how to treat errors in measurements, created a catalog of 75,011 stars, hypothesized that another planet beyond Uranus must exist, calculated the parallax and therefore the distance of the double star system 61 Cygni as 10.4 light-years (Bessel, 1838) and determined that Sirius and Procyon must have invisible companions (Hockey et al., 2014).

Samuel Heinrich Schwabe conducted detailed observations of the Sun for 17 years and noticed a roughly ten-year cycle in the Sun’s activity according to the number of spots on its surface (Schwabe, Samuel Heinrich, 1843; Schwabe, 1844).

In 1845 William Parsons started to conduct observations with his six-foot reflector. An immediate result was the discovery of the spiral arms in the Whirlpool Galaxy M51 (of Rosse, 1968).

Urbain Le Verrier calculated a position where he expected another planet beyond Uranus from perturbations of its orbit in 1846 and notified Johann Gottfried Galle of his findings in a letter which arrived on September 23. The same night Dr. Galle set out to search for a disk-like object at this position using the academic observatory to Berlin. The observation was successful, the planet Neptune was found (Galle, 1846).

In August 1872 Henry Draper took a first spectrum of the star Vega and identified dark lines caused by the absorption of Hydrogen (Barker, 1887; Cannon, 1915).

In 1879, using an experimental setup with a fast rotating mirror, Albert A. Michelson measured the speed of light for the first time (Michelson, 1879).

After Draper’s death in 1882 his widow Mary Anne Palmer Draper funded Edward Pickering’s research under the name “Henry Draper Memorial”, a spectroscopic survey of stars. As a first result of this survey the “Henry Draper Catalogue of Stellar Spectra” was published by Pickering (1890). It contains spectroscopic classifications of 10,351 stars north of Declination  $-25^\circ$ . The classification was performed under the administration of Williamina Fleming using a subdivision of the classifications developed by Angelo Secchi in 1867 (Barker, 1887; Cannon, 1915; Hoffleit, 2002). In 1911 Annie Jump Cannon and Edward Pickering started their work on the “Henry Draper Catalogue”. Published in 9 volumes over the years from 1918 to 1924, it contains magnitudes, positions and spectral classifications of 225,300 stars. For the classification in the catalog Annie Jump Cannon used the Draper Sequence with the classes A through M for stars, O especially for Wolf-Rayet stars, P for planetary nebulae and Q for other spectra (Cannon & Pickering, 1918a,b, 1919a,b, 1920, 1921, 1922, 1923, 1924). They also noticed that almost all spectra fell into the classes B, A, F, G, K, and M, which, together with class O, form the modern Harvard Sequence.

In 1912 Henrietta Swan Leavitt recognized a relationship between the period and luminosity of Cepheid variables which later on could be used to determine the distance to other galaxies (Leavitt & Pickering, 1912).

Based on work of Enjar Hertzsprung from 1905, Henry Norris Russell found a relation between the spectral type and the brightness of most stars in 1913. When organizing stars in a diagram having these two axis a continuous band emerged. This very important diagram has become know as the “Hertzsprung-Russell diagram” and the striking band in the diagram was named “main sequence” (Russell, 1914a,b; Arp, 1959).

During a solar eclipse on May 29, 1919, Arthur Stanley Eddington noticed a deflection of light from the stars surrounding the event. It could be explained using Einstein’s theory of relativity and therefore gave

proof for this theory (Eddington, 1919a,b).

In 1925 Edwin Hubble used Cepheid variables to measure the distance to certain nebulae and therefore showed that these objects are of extragalactic origin (Hubble, 1925a,b). In the following year he published his classification scheme for these objects, identified as galaxies (Hubble, 1926). Another three years after that he found a linear correlation between the distance to a galaxy and its radial velocity. With this discovery the expansion of the universe became known (Hubble, 1929).

During a series of experiments on atmospherics on short wavelengths over two years Karl Jansky noticed that the location of a particular radio source is constant with respect to the sky. In this way he performed the first detection of radio waves from outer space (Jansky, 1933a,b).

After World War II in 1957 the U.S.S.R. launched the first artificial satellite Sputnik 1, opening the door to outer space (Wächtler, 1957; Schilling & Sterne, 1957) and only four years later on April 12th 1961 Yuri Gagarin entered space as the first human being on the Vostok 1 spacecraft launched from the Baikonur Cosmodrome (Bizony, 2011).

## 2.2 Black Holes and Accretion Physics

Although the modern term “black hole” was only developed much later, Michell (1784) already realized from considerations about the effect of gravity on the speed of light, and how to use this effect to measure the star’s mass, that for a star with the same density of the Sun but 500 times its size “all light emitted from such a body would be made to return towards it, by its own proper gravity”. According to Michell, this mechanism would render the star invisible, thus his description is often considered the first one of a black hole. Michell (1784) even suggested that although no light can be directly measured from said star its gravitational influence on neighbouring stars might make it indirectly detectable. In his “Exposition du Système du Monde” Laplace (1796) similarly postulated that a body with the same density and 250 times the diameter of the Sun will be invisible due to the gravitational influence on the light and in Laplace (1799) he delivered a mathematical proof for that claim.

With Einstein’s publication of the general theory of relativity (Einstein, 1912, 1915a,b,c,d,e,f, 1916) the up to this point fundamental theoretical description of black holes was developed and only one month later Schwarzschild (1916) published a solution to the field equations of Einstein’s theory for the simple case of a non-spinning mass with no electrical charge. According to Schwarzschild’s solution in this case a theoretical boundary of spherical shape is expected to exist and if the mass itself would be completely contained inside this boundary, nowadays called the “event horizon”, light would not be able to emerge from the mass anymore. This is the first modern description of what came to be known as a black hole.

Kerr (1963) was able to find the solution to the field equations which also takes the rotation of black holes into account and predicted the effect of frame dragging. If an object is inside an area in the vicinity of the black hole denoted as the *ergosphere* its inertial frame itself starts to revolve around the rotating black hole (Thirring, 1918; Lense & Thirring, 1918; Thirring, 1921).

In theory the only other parameter a black hole could expose to the world outside the event horizon, apart from its mass and spin, is its electrical charge. The solution to Einstein’s field equations for a non-rotating but charged black hole was developed by Reissner (1916), Weyl (1917), Nordström (1918), and Jeffery (1921) and is called the *Reissner–Nordström solution* while the solution including rotation and charge was found by Ezra T. Newman in 1965 (Newman & Janis, 1965; Newman et al., 1965) and is often called *Kerr–Newman solution*. In practice however, the material entering the event horizon of black holes is in general expected to be neutral, thus a charged black hole is not expected to be observed.

Because nothing is expected to leave a black hole on its own it cannot be observed directly but Salpeter (1964) theorized that interstellar matter attracted by a massive object, a process called *accretion*, might do so accompanied by the release of energy in form of electromagnetic radiation via processes such as bremsstrahlung and synchrotron radiation. Lynden-Bell (1969) suggested that the radiation observed from quasars might be generated by gravity and not, as assumed before that, by nuclear fusion and consequently when Shvartsman (1971) worked on possible observational properties of accreting black holes he found that they should appear as “faint optical stars with no lines” while also emitting hard radiation in the X-ray and gamma-ray regime which are also expected to undergo fluctuations on sub-second timescales and outbursts in intervals of months to tens of years. They also noticed that the angular momentum of the infalling

material plays an important role in the mechanism behind accretion and the resulting spectrum. Shapiro (1973a,b) considered spherical accretion onto a non-rotating black hole to only be fed by the material present in the interstellar medium and came to the conclusion that under such a scenario the resulting luminosity is very small, hinting that for an observable black hole a donor star providing material would be necessary (Pringle et al., 1973). Based on the fact that almost half of all stars evolve in binary systems (Pringle, 1989) Shakura & Sunyaev (1973b) calculated that if due to angular momentum material is accreted onto a black hole, originating in the stellar wind of a donor star, is expected to form a disk, called the *accretion disk*. Under these circumstances if the rate of mass accretion is in the range of  $10^{-9}$  to  $3 \times 10^{-8} M_{\odot} \text{ year}^{-1}$  this object can be a source of X-ray emission with corresponding photon energies in the range of 1 to 10 keV and luminosities of  $10^{37}$  to  $10^{38}$  erg/s. This model introduced a free parameter,  $\alpha$ , which characterizes the efficiency of the transport of angular momentum in the outward direction of the disk, there it is often called “ $\alpha$ -disk model”. The transport of angular momentum in this direction is necessary for material to be able to enter the event horizon of the black hole and made possible by magnetic fields and turbulent motion in the disk, which is assumed to be geometrically thin and optically thick. Because of viscosity the particles in the disk lose angular momentum and according to the virial theorem half of that energy is converted into kinetic energy and the other half into thermal energy, making this process very efficient. In this description the only parameters determining the irradiated spectrum and the bolometric luminosity is the mass accretion rate,  $\dot{M}$ . When defining  $\eta$  as the efficiency of the release of gravity the resulting luminosity of that process,  $L$ , can be written as

$$L = \eta \cdot \dot{M} c^2 \quad (2.1)$$

where  $\eta$  depends on the geometry and efficiency. For a stationary and non-rotating black hole  $\eta \simeq 0.06$  while a rapidly spinning black hole can raise  $\eta$  up to  $\simeq 0.4$ . However, Eddington (1916a) already realized that under the simple assumption of spherical accretion the outgoing force resulting from radiation pressure of the infalling gas will at some critical mass accretion rate,  $M_{\text{cr}}$ , be in equilibrium with the gravitational force, thus higher accretion rates are not possible in this scenario. The corresponding luminosity is called *Eddington luminosity*,  $L_{\text{cr}}$ , and although in practice spherical accretion is not expected due to the conservation of angular momentum it is often used to characterize the radiation power of astronomical X-ray sources. Eddington (1916a) calculated this parameter for stars as

$$L_{\text{cr}} = 10^{38} \frac{M}{M_{\odot}} \text{ erg/s} \quad (2.2)$$

with a corresponding mass accretion rate of

$$\dot{M} = 3 \times 10^{-8} \frac{M}{M_{\odot}} M_{\odot} / \text{yr} \quad (2.3)$$

According to the theory of Shakura & Sunyaev (1973b), if an accreting black hole was to exceed the Eddington luminosity, a massive outflow of matter with high velocities is to be expected which was the first theoretical prediction of an outflow of matter from a black hole binary system. Shortly after the  $\alpha$ -disk model was published Novikov & Thorne (1973) presented the first relativistic version of this model.

Starting from this point a variety of different empirical and physical models describing the spectra of accretion disks have been developed, some of which will be outlined in the course of this thesis.



### 3 Active Galactic Nuclei

Active galactic nuclei (AGN) are arguably one of the most extreme phenomenon observed in the universe. Harboring supermassive black holes (SMBHs) with masses in the range from  $10^6$  to  $10^{10} M_{\odot}$  (solar masses) they have total bolometric luminosities from  $10^{43}$  to  $10^{47}$  erg/s (Woo & Urry, 2002). Observations of AGN from the radio to the gamma-ray regime have revealed that these objects can have several different appearances even though their fundamental properties are the same. Driven by this realization a single model to describe the geometry of these sources and the main radiation processes, called the *unified model of AGN*, was developed.

As the name suggests, AGN are extragalactic objects observed at distances of up to  $z = 7.085$  (Mortlock et al., 2011). In very simple terms they are galaxies hosting SMBHs which accrete matter at a rate of roughly one solar mass per year (Delvecchio et al., 2015). The overall efficiency of this process as determined from observations is roughly 10% (Bian & Zhao, 2003) and generates radiation in all wavelength regimes.

After taking an optical spectrum of NGC 1068 using the 36 inch Crossley telescope with a total exposure time of 13 h and 34 min, Fath (1909) found not only absorption but also emission lines. Hubble (1925a,b) was able to show that these objects, to be known as galaxies, are of extragalactic origin and indeed entire stellar systems on their own. Furthermore, the main source of emission of these galaxies could be identified to be right at their core. Upon further spectroscopic observations and their analyses Seyfert (1943) recognized that the optical emission lines show Doppler broadening corresponding to high velocities of up to 8500 km/s, mainly in Balmer emission lines of hydrogen. He also noticed a variety of narrow lines corresponding to forbidden transitions in the spectra. The term *forbidden* at that time referred to the fact that these spectral lines were not reproduced in laboratory conditions on Earth. It has, however, already been recognized by Bowen (1927) that under conditions of extremely low density in the interstellar medium (ISM) these transitions from metastable states to lower states are indeed possible and the origin of forbidden lines in optical spectra.

Over the last decades a wide variety of different aspects of AGN have been discovered which are used to assign specific sources to classes. Some of the most important of these classes will briefly be described while comprehensive reviews are available in Netzer (2015), Padovani et al. (2017), and Blandford et al. (2019).

The central SMBH of an AGN is the driving force behind a variety of emission regions with different characteristics. An accretion disk around the black hole is releasing thermal and non-thermal X-rays while part of the accreted material is accelerated perpendicularly to the disk away from the black hole. This optically thin gas is the source of the observed forbidden line transitions and therefore called narrow line region (NLR). As proposed by Antonucci (1993) and Urry & Padovani (1995), if this construct is embedded into neutral and optically thick gas at larger distances the view towards the central region around the SMBH can be obscured. This region far in the gravitational well of the black hole is the source of the broadened optical emission lines due to the orbital motion of the gas in the accretion disk and hence called broad line region (BLR). If the line of sight from the observer towards the central region around the black hole is not obstructed by the outer optically thick gas then both, the NLR and BLR are visible, creating a Seyfert type I AGN. If, however, the BLR is obscured, then only narrow lines can be observed, rendering the object a Seyfert type II AGN (Osterbrock, 1977). Over time objects have been discovered whose spectra show mainly narrow emission lines with small contributions from broad lines. Depending on the ratio of their relative intensities they have been denoted to be of Seyfert type 1.2, 1.5, 1.8 and 1.9 (Osterbrock, 1981). Seyfert I galaxies with comparatively narrow HI lines are called narrow line Seyfert I (NLS1) galaxies (Osterbrock & Pogge, 1985).

Another distinction among AGN can be drawn from the observed radio emission. According to Wilson & Colbert (1995) three main features correlating with the presence of radio emission from AGN or lack thereof can be named. AGN showing radio emission, therefore called radio-loud, produce large scale radio jets and accompanying lobes. The first source where this was observed is M87. Curtis (1918) performed an extensive

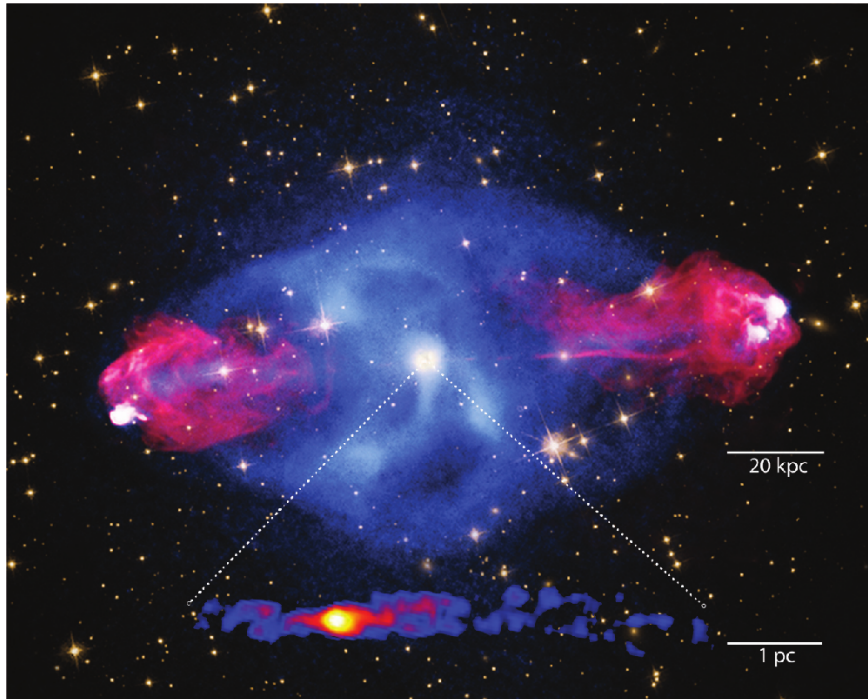


Figure 3.1: Composition of the radio (red), X-ray (blue) and optical (mainly foreground stars) emission of the radio galaxy Cyg A. The inset shows the jet emerging directly from the central SMBH. The diffuse X-ray emission around the galaxy is caused by heating and soft shock fronts from the jet termination lobes. Optical data comes from the Hubble Space Telescope (*HST*) (NASA/STScI), X-ray data from Chandra (NASA/CXC/SAO) and radio from the Very Large Array (*VLA*) (NSF/NRAO/AUI/VLA). Taken from Blandford et al. (2019).

photographic survey of 762 nebulae, curiously also using the Crossley reflector as Fath (1909), and noted for M87 (also known as NGC4486) that a “straight ray lies in a gap in the nebulosity [...] connected with the nucleus by a thin line of matter”. Radio jets similar to the one Curtis captured on the photographic plates is a typical feature of radio-loud AGN. These collimated outflows of matter reach scales on the order of megaparsecs into the intergalactic medium and are often terminated by a lobe-like structure on both ends which, depending on the inclination towards the observer, might both be visible or not (Blandford et al., 2019). A nice example for this situation is the radio-loud galaxy Cygnus A, shown in Fig. 3.1 with its emission in the radio, optical and X-ray regime. Not only is the central SMBH of the galaxy bright in all wavelengths but also the termination of the radio jets in the form of large scale lobes which demonstrates that the radio jets generate a significant portion of the total bolometric luminosity of AGN (Wilson & Colbert, 1995). The gas of the lobes feeds back into the medium surrounding the host galaxy and heats it via soft shock fronts causing diffuse X-ray emission which can also be seen in Fig. 3.1. For radio-quiet AGN on the other hand, observed radio jets are generally very weak and do not provide significant energy to their overall luminosity. According to Wilson & Colbert (1995), they are mostly hosted by spiral galaxies whose recent evolution was unaffected by other galaxies whereas radio-loud AGN are often contained in elliptical galaxies which have undergone recent mergers. Additionally, the space density for radio-loud galaxies is roughly a magnitude higher at the same luminosity compared with radio-quiet ones.

The central core of AGN can have a much higher brightness in the optical regime than the remaining components of its hosting galaxies, mainly being stars. This radiation can also be variable and combined with a strong ultraviolet (UV) component. Optical emission lines show the characteristics of Seyfert galaxies and are redshifted because of their distances. Owing this point-like appearance similar to stars these objects have been called quasi-stellar objects (QSOs) (Burbidge, 1967). Some of them are paired with strong radio emission, making them quasi-stellar radio sources (QSRs) (Blandford et al., 2019).

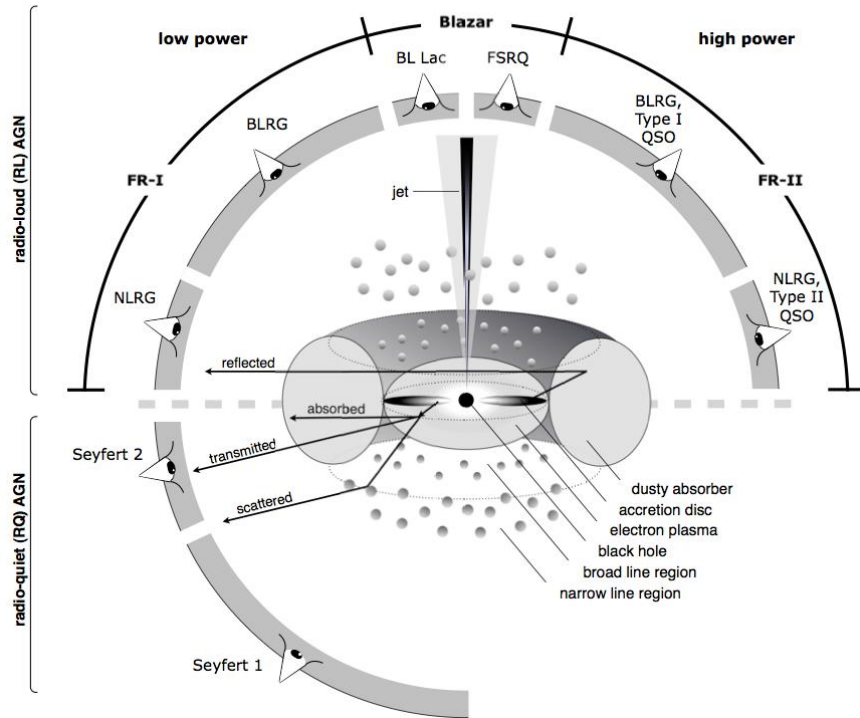


Figure 3.2: Sketch of an AGN under the aspect of the unified theory. Depending on the inclination of the viewing angle of the observer towards the central region and the gaseous absorber the object appears as a different class of source. Credit: Beckmann & Shrader (2012), taken from Britto et al. (2016)

Another interesting view of AGN emerges when the direction of their outflow is aligned with the line of sight towards the observer, thus the material is moving with high velocities close to the speed of light towards them. In this case a compact, strong radio source with a flat spectrum is visible. Optical and radio radiation is strongly polarized and accompanied by gamma radiation. All of these spectral components vary with a high amplitude over all timescales. Roughly 3500 of these objects called *blazars* are known to date<sup>1</sup> (Massaro et al., 2009). Depending on the appearance of emission lines blazars are further divided into two subclasses. If the optical spectrum of a blazar shows only very weak or no emission lines it is classified as a BL Lacertae (BL Lac) object. The accretion rate onto the SMBH at the center of these objects is believed to be very low due to a lack of material in its surroundings, depleting the BLR. If, however, the optical spectrum shows broad emission lines similar to these of QSOs the object is classified as Flat Spectrum Radio Quasar (FSRQ). For Steep Spectrum Radio Quasars (SSRQs) the index of the powerlaw describing the spectrum is much higher (Yuan et al., 2018). Observations show that FSRQs are more powerful than BL Lacs (Romero et al., 2017). Together with the fact that BL Lacs tend to be more concentrated in the local universe compared to FSRQs (Dunlop & Peacock, 1990; Rector et al., 2000; Ajello et al., 2014) the first are interpreted to be an evolutionary stage of the latter when the accretion of the SMBH subsides.

An additional distinction of radio-loud AGN can be achieved by considering the intensity and morphology of their radio lobes. Fanaroff & Riley (1974) divided a set of 57 AGN into two classes based on the ratio between the distance of the two locations showing the highest intensity and the total extent of the source. If this ratio is lower than 0.5 the source is said to be of class I while if it is higher class II. These classes have become known as Fanaroff–Riley (FR) classes in honor of their inventors and are important because they characterize the energy transport from the inner region of the AGN to the radio lobes (Blandford et al., 2019).

The largest group of AGN is formed by low-ionisation nuclear emission line region (LINER) galaxies.

<sup>1</sup>3561 at the time of writing this thesis according to the Roma BZCAT website (<https://www.asdc.asi.it/bzcat/>)

### 3 Active Galactic Nuclei

Their luminosity is low compared to that of other AGN classes and their spectra show emission lines from weakly ionized atoms (Singh et al., 2013; Mazengo et al., 2021). How these spectral properties are created is not yet clear, however, it has been proposed that the central SMBH which causes photoionization in the surrounding gas (Groves et al., 2004a,b), shock-heated gas (Heckman, 1980; Dopita & Sutherland, 1995, 1996) or photoionization by hot O-type stars (Filippenko & Terlevich, 1992) or post-asymptotic giant branch stars could play a role (Binette et al., 1994; Stasińska et al., 2008). Especially the latter case would of course mean that these objects are no AGN at all (Coldwell et al., 2018).

A descriptive sketch of the different classes of sources emerging from the described geometries and radio properties is shown in Fig. 3.2. The bottom part of this figure demonstrates how the two different types of Seyfert galaxies emerge by not showing radio emission and either obscure the BLR or not. In the upper part of the figure the emergence of the different types of radio-loud AGN is shown with the distinction according to the radio luminosity taken into account by the FR classes. The additional presence of the radio jet gives rise to the FSRQ class in the high luminosity case and BL Lac class in the low luminosity case. Narrow line radio galaxies (NLRGs) and broad line radio galaxies (BLRGs) essentially correspond to Seyfert type II and type I galaxies from the FR I class due to the additional low power radio emission. In the high power FR II case a quasi stellar radio source is additionally observed.

## 3.1 Black Holes

The driving forces behind the power unleashed by AGN are the SMBHs at their center. To understand how these objects are able to generate the intense observed radiation and accelerate particles in jets closely to the speed of light I will give a brief overview of the physics of black holes based on the illustrations by Longair (1994) and Meier (2012).

### 3.1.1 Field Equations

Einstein's general theory of relativity (Einstein, 1912, 1915a,b,c,d,e,f, 1916) is governed by its field equations which link the spatial distribution of matter with the curvature of four-dimensional spacetime, which can be written as

$$\mathcal{G} = 8\pi \frac{G}{c^4} \mathcal{T} \quad (3.1)$$

In this equation  $c$  is speed of light and  $G$  the gravitational constant from Newton's law of gravity. The Einstein tensor,  $\mathcal{G}$ , is composed of the Ricci curvature tensor,  $\mathcal{R}$ , its trace,  $\mathcal{R}$ , and the metric,  $\mathbf{g}$ , as

$$\mathcal{G} = \mathcal{R} - \frac{1}{2} \mathcal{R} \mathbf{g} \quad (3.2)$$

The metric,  $\mathbf{g}$ , is a four-dimensional tensor describing how space and time are linked together to form the four-dimensional spacetime and is essential for the description of black holes. By denoting the coordinate in spacetime using the four-vector,  $x^\mu$ , and the corresponding gradient,  $dx^\mu$ , the square of a line element,  $ds$ , can be calculated using the metric,  $\mathbf{g}$ , as

$$ds^2 = g_{\mu\nu} dx^\mu dx^\nu \quad (3.3)$$

This spacetime interval gives the distance between two events in curved spacetime and is invariant under certain conditions. In special relativity this is the case under Lorentz transformation and in general relativity under more general coordinate transformations. The metric for flat spacetime is called *Minkowski metric*, often denoted  $\eta$ , and defined as

$$\eta = \begin{pmatrix} -1 & 0 & 0 & 0 \\ 0 & 1 & 0 & 0 \\ 0 & 0 & 1 & 0 \\ 0 & 0 & 0 & 1 \end{pmatrix} \quad (3.4)$$

Depending on the convention the signs might be flipped. This metric results in the invariant line element

$$ds^2 = c^2t^2 - x^2 - y^2 - z^2 \quad (3.5)$$

where, again, the signs might be flipped when using a different convention for the signs of  $\eta$ . This metric, and therefore the invariant line element, is the one used in special relativity. Because the metric determines the line element,  $ds$  is often used as a proxy for the metric.

$\mathcal{R}$  can be expressed using the double-dot-product defined as  $\mathcal{A} : \mathcal{B} = A_{ij}B_{ij}$  (Einstein summation convention applies) between the inverse of the metric and the Riemann curvature tensor,  $\mathfrak{R}$ , as

$$\mathcal{R} = \mathbf{g}^{-1} : \mathfrak{R} \quad (3.6)$$

$\mathfrak{R}$  can be used to calculate the curvature of a Riemann manifold, such as the metric  $\mathbf{g}$ .

$\mathcal{T}$  is the stress-energy tensor which, in general, describes the direction and amount of the fluxes of energy and momentum in four-dimensional spacetime in the form of a 4x4 tensor. In case of only the electromagnetic field described by the electromagnetic field tensor,  $\mathcal{F}$ , from Maxwell's equations  $\partial_\mu F^{\mu\nu} = \mu_0 j^\nu$  existing next to the gravitational force the stress-energy tensor becomes

$$T^{\mu\nu} = \frac{1}{\mu_0} \left( F^{\mu\alpha} F_\alpha^\nu - \frac{1}{4} g^{\mu\nu} F_{\alpha\beta} F^{\alpha\beta} \right) \quad (3.7)$$

which means that  $\mathcal{T}$  has the form

$$\mathcal{T} = \begin{pmatrix} \frac{1}{2} \left( \epsilon_0 E^2 + \frac{1}{\mu_0} B^2 \right) & \frac{S_x}{c} & \frac{S_y}{c} & \frac{S_z}{c} \\ \frac{S_x}{c} & \sigma_{xx} & \sigma_{xy} & \sigma_{xz} \\ \frac{S_y}{c} & \sigma_{yx} & \sigma_{yy} & \sigma_{yz} \\ \frac{S_z}{c} & \sigma_{zx} & \sigma_{zy} & \sigma_{zz} \end{pmatrix} \quad (3.8)$$

where  $E^2$  and  $B^2$  are the strengths of the electric and magnetic field squared.  $S_i$  are the entries of the three-dimensional classical Poynting vector,  $\vec{S} = \vec{E} \times \vec{B} / \mu_0$ , which gives the energy flux of the electromagnetic field, and  $\sigma_{ij}$  are the entries of the classical Maxwell stress tensor given by

$$\sigma_{ij} = \epsilon_0 E_i E_j + \frac{1}{\mu_0} B_i B_j - \frac{1}{2} \delta_{ij} \left( \epsilon_0 E^2 + \frac{1}{\mu_0} B^2 \right) \quad (3.9)$$

where  $\delta_{ij}$  is the Kronecker delta which is 1 if  $i = j$  and 0 otherwise. From these entries it can be seen how  $\mathcal{T}$  mixes the interaction between the momentum and the fields with the energy and its flux.

### 3.1.2 Metrics of Black Holes

Finding metrics which solve Einstein's field equations is a central task for the application of general relativity. Because these metrics describe the geometry of spacetime itself it can also give direct insight into the fundamental properties of the universe.

#### Non-Rotating Black Holes: The Schwarzschild Metric

Shortly after Einstein published the initial version of the general theory of relativity in 1915 Schwarzschild (1916) found and published a metric which solves the field equations for a non-rotating and not charged point mass  $M$ . In his honor this metric has been named *Schwarzschild metric*. It is given by

$$\mathbf{g} = \begin{pmatrix} -c^2 \left( 1 - \frac{2GM}{c^2 r} \right) & 0 & 0 & 0 \\ 0 & \left( 1 - \frac{2GM}{c^2 r} \right)^{-1} & 0 & 0 \\ 0 & 0 & r^2 & 0 \\ 0 & 0 & 0 & r^2 \sin^2 \theta \end{pmatrix} \quad (3.10)$$

### 3 Active Galactic Nuclei

The coordinate system used in this case is expressed in spherical coordinates due to spherical symmetry. Calculating the line element yields

$$ds^2 = \left(1 - \frac{2GM}{c^2 r}\right) dt^2 - \frac{1}{c^2} \left( \frac{dr^2}{1 - \frac{2GM}{c^2 r}} + r^2(d\theta^2 + \sin^2\theta d\phi^2) \right) \quad (3.11)$$

The radius

$$r_S = \frac{2GM}{c^2} \quad (3.12)$$

carries special meaning and is called *Schwarzschild radius*. It simplifies the line element to

$$ds^2 = \left(1 - \frac{r_S}{r}\right) dt^2 - \frac{1}{c^2} \left( \frac{dr^2}{1 - \frac{r_S}{r}} + r^2(d\theta^2 + \sin^2\theta d\phi^2) \right) \quad (3.13)$$

For  $r$  being very far from  $r_S$ , i.e.,  $r \rightarrow \infty$ , the metric approaches the Minkowski metric again, for which the line element in spherical coordinates is

$$ds^2 = -c^2 dt^2 + dr^2 + r^2 d\theta^2 + r^2 \sin^2\theta d\phi^2 \quad (3.14)$$

This reflects the fact that very far away from the central mass the spacetime becomes flat and therefore the gravitational influence of the mass disappears. The same is true if the mass vanishes, i.e.,  $M \rightarrow 0$ . Curvature in this geometry only occurs along the  $t$  and  $r$  coordinates which means that the gravitational force only acts radially.

For radii smaller than the Schwarzschild radius ( $r < r_S$ ) an important effect can be observed. In this case the first two elements on the diagonal of the matrix change sign

$$\mathbf{g} = \begin{pmatrix} c^2 \left(\frac{r_S}{r} - 1\right) & 0 & 0 & 0 \\ 0 & -\left(\frac{r_S}{r} - 1\right)^{-1} & 0 & 0 \\ 0 & 0 & r^2 & 0 \\ 0 & 0 & 0 & r^2 \sin^2\theta \end{pmatrix} \quad (3.15)$$

The time component has become positive, the radius component negative, and they have reversed their roles with respect to the constraints on motion in spacetime. Outside the Schwarzschild radius masses are always constraint to move forward in time while inside this border the motion is constraint towards the central mass  $M$ . This is particularly true for light itself. Because not even light can escape this geometry no information about events beyond it can reach an observer on the outside, thus the resulting border is called *event horizon* and the object is called *black hole* due to the lacking emission of light.

Solving the equations of motion in this metric yields some interesting results. The radial component of the velocity becomes

$$v_r = -c \frac{m_0 c^2}{\mathcal{E}} \sqrt{\left(\frac{\mathcal{E}}{m_0 c^2}\right)^2 - 1 + \frac{r_S}{r}} \quad (3.16)$$

where  $\mathcal{E}$  is the relativistic energy of the particle and  $m_0$  its rest mass. When the particle crosses the event horizon, meaning when  $r = r_S$ , the radial velocity becomes exactly the speed of light,  $v_r = -c$ , which is negative because the motion is towards the origin of the coordinate system. This holds independently of the initial conditions of the particle. The situation is the same if it is located at infinity and has initial momentum or if it is placed just outside the event horizon at rest.

When also taking angular momentum into account, the particle will orbit around the black hole with the gravitational and centrifugal forces in equilibrium. Longair (1994) show that in the equatorial plane

( $v_r = 0$ ,  $v_\theta = 0$  and  $\sin\theta = 1$ ) the angular motion,  $v_\phi$ , can be written as

$$v_\phi = \sqrt{\frac{GM}{r - r_S}} \quad (3.17)$$

which has a surprising consequence: The angular velocity at exactly the event horizon, i.e.,  $r \rightarrow r_S$ , becomes infinite. Solving the equations of motion for the radius at which the angular velocity becomes the speed of light gives the *photon orbit radius*,

$$r_{\text{ph}} = \frac{3GM}{c^2} = \frac{3}{2}r_S \quad (3.18)$$

Photons can be on unstable orbits around a black hole at this radius.

An additional constraint emerges for massive particles: The speed must always be smaller than the speed of light. This can be adhered to by introducing a Lorentz factor,  $\gamma$ , of the form

$$\gamma = \frac{1}{\sqrt{1 - \frac{v^2}{c^2}}} \quad (3.19)$$

Setting  $v = v_\phi$  yields

$$\gamma = \sqrt{\frac{r - r_S}{r - \frac{3}{2}r_S}} \quad (3.20)$$

which becomes infinite at  $r_{\text{ph}}$ . The relativistic angular momentum,  $L$ , can be calculated in spherical coordinates using this Lorentz factor to

$$L = \gamma m_0 v_\phi r \sin\theta = \sqrt{\frac{r_S}{2r - 3r_S}} m_0 r c \quad (3.21)$$

and the relativistic energy,  $\mathcal{E}$ , becomes

$$\mathcal{E} = \sqrt{1 - \frac{r_S}{r}} \gamma m_0 c^2 = \frac{r - r_S}{\sqrt{r(r - \frac{3}{2}r_S)}} m_0 c^2 \quad (3.22)$$

If this energy is smaller than the rest energy,  $m_0 c^2$ , of a particle the orbit of the particle is bound to the central mass. In this case both  $L$  and  $\mathcal{E}$  have a minimum at the radius of the innermost stable circular orbit (ISCO),

$$r_{\text{ISCO}} = \frac{6GM}{c^2} = 3r_S \quad (3.23)$$

At this radius the energy is  $\mathcal{E}_{\text{ISCO}} = 2/3 \sqrt{2} m_0 c^2 \simeq 0.9428 m_0 c^2$  and the angular momentum  $L_{\text{ISCO}} = 2\sqrt{3} GMc/\mu_0$ . The binding energy can be calculated by subtracting the particles rest energy

$$\mathcal{E}_{\text{bind}} = -(\mathcal{E}_{\text{ISCO}} - m_0 c^2) \simeq 0.0572 m_0 c^2 \quad (3.24)$$

This binding energy is equivalent to the energy which can be released in the form of kinetic and thermal energy by accreting mass onto a black hole. Expressing the efficiency of energy conversion,  $\eta$ , of the process with respect to the rest energy gives

$$\eta \simeq 6\% \quad (3.25)$$

for accretion onto a black hole in the Schwarzschild metric, that is ignoring the spin of such an object. For comparison the efficiency of nuclear fusion of hydrogen to helium will be considered. In a very simple

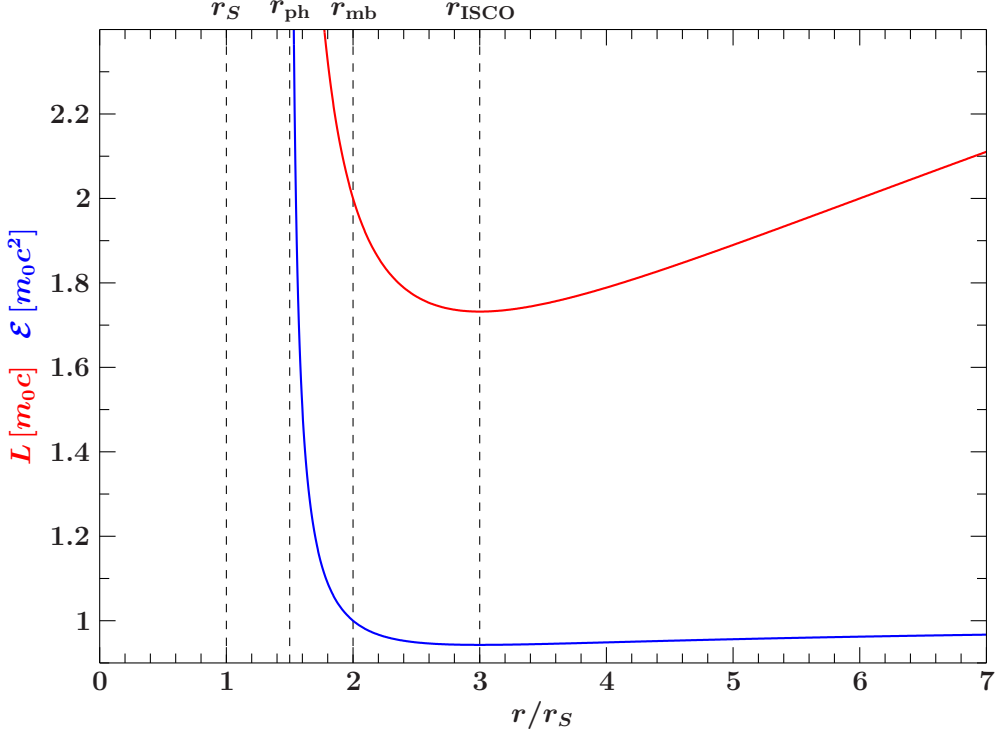


Figure 3.3: Total relativistic energy,  $\mathcal{E}$ , and relativistic momentum,  $L$ , of a particle orbiting a black hole in the Schwarzschild metric depending on the orbital radius,  $r$ , in units of the Schwarzschild radius,  $r_S$ . Both,  $\mathcal{E}$  and  $L$ , have a minimum at  $r_{\text{ISCO}}$  where especially  $\mathcal{E} < 1$ . It is unity again at the marginally bound orbit,  $r_{\text{mb}}$ . Energy and angular momentum diverge towards infinity when approaching the photon orbit radius at  $r_{\text{ph}}$ .

picture the total reaction equation for this process is



with  $\text{}^1_1\text{H}$  essentially being protons,  $e^+$  positrons,  $\nu_e$  electron neutrinos and  $\text{}^4_2\text{He}$  the resulting helium core. For the energy balance the masses of the neutrinos will be neglected.  $\eta$  then becomes

$$\eta = 1 - \frac{m_{\text{He}} + 2m_e}{4m_p} = 0.63\% \quad (3.27)$$

with the masses given by Particle Data Group et al. (2020). Accretion onto a non-rotating black hole is therefore roughly ten times more efficient in releasing energy than nuclear fusion.

The total relativistic energy at  $r_{\text{ISCO}}$  is smaller than then rest mass of the particle itself but rises again for smaller radii. It is identical to the rest mass at the radius of the *marginally bound orbit*,

$$r_{\text{mb}} = \frac{4}{GM}c^2 = 2r_S \quad (3.28)$$

Between  $r_{\text{mb}}$  and  $r_{\text{ISCO}}$  the particle can only be on unstable orbits. For smaller radii the binding energy becomes negative, thus more than the rest mass is necessary for the particle to stay on a circular orbit. Conclusively all particles below  $r_{\text{ISCO}}$  will eventually lose all their kinetic energy and angular moment and will spiral into the black hole if not accelerated outward by some mechanism. The energy and angular momentum in units of  $r_S$  are shown in Fig. 3.3 with the relevant radii as discussed above.

### Rotating Black Holes: The Kerr Metric

The Schwarzschild metric does not consider that black holes can rotate, meaning they can have angular momentum themselves. Still following Longair (1994) and Meier (2012), I will demonstrate how the Kerr metric (Kerr, 1963) considers this aspect and which effects arise from it. Another remaining property black holes can expose to the outside world would be their electrical charge. A metric describing such a black hole including all three aspects, mass, rotation and charge, is the Kerr-Newmann solution (Newman et al., 1965; Newman & Janis, 1965), but because the material entering the black hole is expected to be electrically neutral on average only the Kerr metric is expected to play a practical role. Compared to the Schwarzschild metric it has the form

$$\mathbf{g} = \begin{pmatrix} -\left(1 - \frac{2r_g r}{\rho^2}\right) c^2 & 0 & 0 & -\frac{\omega \Sigma^2 \sin^2 \theta}{\rho^2} \\ 0 & \frac{\rho^2}{\Delta} & 0 & 0 \\ 0 & 0 & \rho^2 & 0 \\ -\frac{\omega \Sigma^2 \sin^2 \theta}{\rho^2} & 0 & 0 & \frac{\Sigma^2}{\rho^2} \sin^2 \theta \end{pmatrix} \quad (3.29)$$

where multiple terms have been substituted for the sake of simplicity.  $r_g$  is the gravitational radius defined as half of the Schwarzschild radius,  $r_g = r_S/2$ . The spin of the black hole is expressed using the dimensionless spin parameter,  $j$ , defined as the fraction the angular momentum,  $J$ , of the black hole has with respect to the maximum angular momentum

$$j = \frac{J}{\frac{GM^2}{c}} \quad (3.30)$$

Here the denominator  $GM^2/c$  is the theoretically maximal possible value for the angular momentum.  $j$  can take values from -1 to 1, where  $j > 0$  means prograde rotation, i.e., the observer is rotating in the same direction as the black hole, and  $j < 0$  means retrograde motion, the opposite of prograde motion. Using these two expressions  $\Sigma$  is defined as

$$\Sigma = \sqrt{(r^2 + j^2 r_g^2)^2 - j^2 r_g^2 \Delta \sin^2 \theta} \quad (3.31)$$

$\Delta$  is a term similar to the first two terms on the diagonal of the Schwarzschild metric and also contains the spin parameter

$$\Delta = r^2 - 2r_g r + r^2 j^2 \quad (3.32)$$

Similar to  $r$ ,  $\rho$  gives a distance in radial direction with the difference that the surfaces are oblate

$$\rho = \sqrt{r^2 + j^2 r_g^2 \cos^2 \theta} \quad (3.33)$$

The distance from the rotational axis is given by

$$\frac{\Sigma \sin \theta}{\rho} \quad (3.34)$$

and can be identified in the Kerr metric.  $\omega$  is a contribution by the angular velocity of space itself,

$$\omega = \frac{2r_g^2 r c}{\Sigma^2} j \quad (3.35)$$

Importantly, if the black hole is not rotating, meaning  $\omega = j = 0$  and therefore  $\rho = r$ ,  $\Sigma = r^2$  and  $\Delta = (r - 2r_g)r$ , the Schwarzschild metric can be obtained again.

For the Schwarzschild metric the location of the event horizon could be determined using the first two elements of the diagonal. The contribution of time had to go to zero and that of the radius to infinity. In the Kerr metric however the two resulting radii under these conditions do not coincide. The second condition

### 3 Active Galactic Nuclei

is met if  $\Delta \rightarrow 0$  which is satisfied at

$$r_H = r_g \left( 1 + \sqrt{1 - j^2} \right) \quad (3.36)$$

In four-dimensional spacetime this event horizon is spherical as it was for the Schwarzschild metric, however, the radius of this sphere now depends on the angular momentum. For a non-spinning black hole it is again equal to the Schwarzschild radius while for maximally spinning black holes it is half as large and equal to the gravitational radius. With the constraint of the time component being zero one obtains

$$r_E = \left( 1 + \sqrt{1 - j^2 \sin^2 \theta} \right) r_g \quad (3.37)$$

$r_E$  is called the radius of the *ergosphere* and is identical to the radius of the event horizon at the pole of the black hole but larger otherwise, so the ergosphere forms an oblate spheroid. For non-spinning black holes the ergosphere and the event horizon coincide again in form of a sphere with the Schwarzschild radius.

For the region  $r_H < r < r_E$  both components of the metric become positive. The time coordinate of spacetime itself is aligned with the rotational direction of the black hole in this area and influenced by the off-diagonal element in the first column of the metric. All massive particles must rotate along the black hole because spacetime itself is rotating faster than the speed of light, so a particle which is not rotating would have to move faster than the speed of light against local spacetime, which is impossible. Because rotating spacetime “drags” all massive particles along this effect is called *frame-dragging*. It is, however, possible by having enough kinetic energy to leave the ergosphere again.

Conserved quantities such as the relativistic angular momentum,  $L$ , in the Kerr metric becomes

$$L = \gamma m_0 v_\phi \frac{\Sigma \sin \theta}{\rho} \quad (3.38)$$

and the relativistic energy

$$\mathcal{E} = \frac{\rho \sqrt{\Delta}}{\Sigma} \gamma m_0 c^2 + \gamma m_0 v_\phi \frac{\Sigma \sin \theta}{\rho} \omega \quad (3.39)$$

with  $v_\phi$  being the third component of the velocity in spherical coordinates. The angular momentum resembles the one resulting from the Schwarzschild metric but instead of the regular radius from spherical coordinates the cylindrical distance resulting from the Kerr metric takes its place. For a non-rotating black hole ( $j = 0$ ), it follows that  $\rho = r$  and  $\Sigma = r^2$  which restores the angular momentum obtained for the Schwarzschild metric.

The relativistic energy is now composed of two individual terms, the first of which is equivalent to the result for the Schwarzschild metric but with modifications resulting from the angular momentum. Indeed for  $j = 0$ , again  $\rho = r$ ,  $\Sigma = r^2$  and additionally  $\Delta = r^2 - 2rr_g = r^2 - rr_S$  which results in the same expression as for the Schwarzschild metric. The second term results from the rotation of spacetime itself and is an additional result emerging from the Kerr metric.

An interesting effect can be observed when considering the total balance of energy, angular momentum and mass when a spinning particle, i.e.,  $v_\phi \neq 0$ , is absorbed by an also spinning black hole. In case the particle’s motion is prograde with respect to the black hole the energy, mass and angular momentum of the black hole increases when the particle passes the event horizon. If, however, the motion of the particle is retrograde the effect on the black hole depends on the initial energy of the particle. In any case the total energy amounted for by rotation is reduced and for  $\mathcal{E} > 0$  also the mass of the black hole is increased. The situation is different for retrograde motion with high velocity, that is

$$-\frac{v_\phi}{c} > \frac{p^2 \sqrt{\Delta} c}{\Sigma^2 \sin \theta \omega} = \frac{\rho^2 \sqrt{\Delta}}{2j r_g^2 r \sin \theta} \quad (3.40)$$

In this case for the particle  $\mathcal{E} < 0$  for  $r \rightarrow \infty$  which results in a negative balance of the energy of the black hole, meaning upon absorption of the particle the black hole loses energy and the particle contributes more

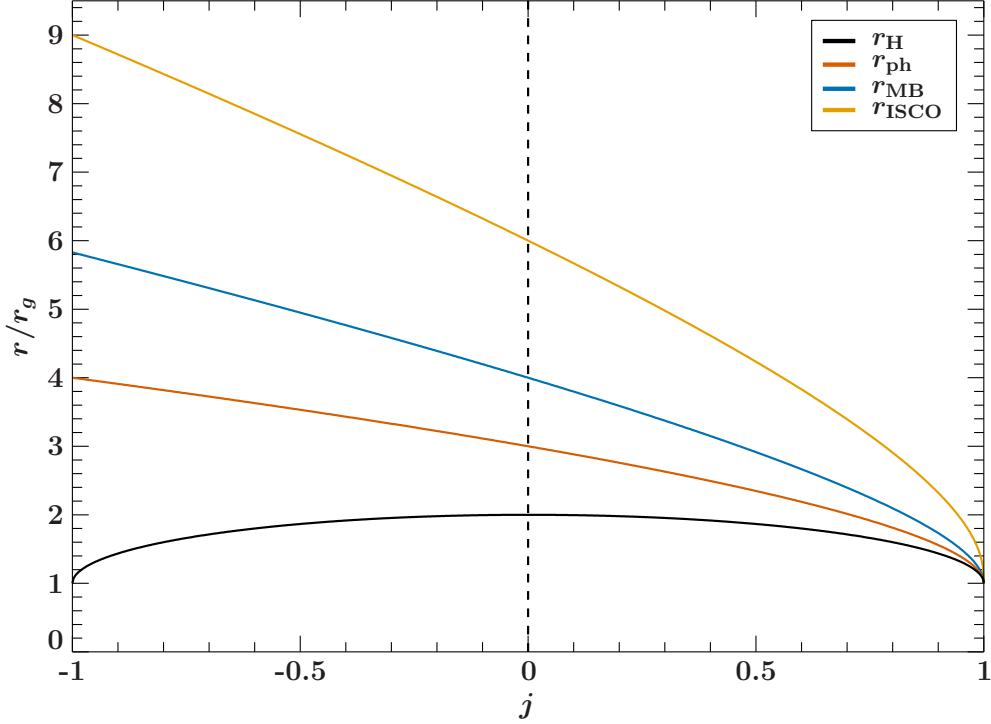


Figure 3.4: Important radii depending on the spin parameter of a Kerr black hole in units of the gravitational radius  $r_g$ .  $j < 0$  denote retrograde motion of a test particle. The radius,  $r_H$ , of the spherical event horizon is maximal for a non-spinning black hole, i.e.,  $j = 0$ , the Schwarzschild case. All other radii decrease from  $j = -1$  towards  $j = 1$  where they all coincide at  $r_g$ .

than its rest energy in the process which results in an efficiency of the extraction of energy of  $\eta > 100\%$ . The excess in energy making this possible comes directly from the rotation and therefore the total energy of the black hole. Still, the constraint  $v_\phi < c$  has to be obeyed which is true for trajectories which satisfy  $r < R_E$ , so this motion is only possible inside the ergosphere. As this mechanism was first recognized by Penrose (1969) it was subsequently named the *Penrose process*. In principle, it could play a role for the accretion of highly energetic particles with retrograde motion and the formation of relativistic jets (Gariel et al., 2010).

Calculating the radial velocity for a particle placed at rest at infinity gives

$$v_r = -\sqrt{\frac{2GM}{r} \frac{r \sqrt{r^2 + j^2 r_g^2}}{\Sigma}} \quad (3.41)$$

which has a similar shape as for the Schwarzschild metric and also in this case the particle always has  $v_r = -c$  when passing through the event horizon. Also, similarly as done for the Schwarzschild metric, the equilibrium of the gravitational and centrifugal forces can be used to calculate the orbital velocity,  $v_\phi$ , for a circular motion in the equatorial plane

$$\frac{v_\phi}{c} = \frac{\Sigma^2}{\sqrt{\Delta}(r^3 - j^2 r_g^3)} \left( \pm \sqrt{\frac{r_g}{r}} - j \frac{r_g^2}{r^2} \right) - \frac{2j r_g^2}{r \sqrt{\Delta}} \quad (3.42)$$

which is much more complicated than in the non-rotating Schwarzschild metric but still, when setting  $j = 0$  this case can be recovered again. The reference frame is rotating along with the particle so in the last term the rotation of spacetime itself is subtracted again. The first term contains the contributions of classical orbital motion and an additional centrifugal force resulting also from the rotation of spacetime.

### 3 Active Galactic Nuclei

By means of setting  $v_\phi = c$  the photon orbit radius can be calculated to

$$r_{\text{ph}} = 2r_g \left( 1 + \cos \left( \frac{2}{3} \arccos(\mp j) \right) \right) \quad (3.43)$$

which gives the same result of  $r_{\text{ph}} = 3r_g$  as in the Schwarzschild metric for  $j = 0$ . The negative and positive signs correspond to prograde and retrograde motion of photons, respectively, so photons moving along the rotation of the black hole can reach up to  $r = r_g$  while in the other case only up to  $r = 4r_g$  while still being able to escape the gravitational attraction.

Again, the radius  $r_{\text{mb}}$  of the marginally bound orbit can be found by setting  $\mathcal{E} = m_0c^2$  which results in

$$r_{\text{mb}} = \left( 1 + \sqrt{1 \pm j} \right)^2 r_g \quad (3.44)$$

with the same applying for the signs as for  $r_{\text{ph}}$  which gives  $r_{\text{mb}} = r_g$  for the prograde case and  $r_{\text{mb}} = (3 + 2\sqrt{2})r_g$  for the retrograde case. So for prograde motion  $r_{\text{ph}}$  and  $r_{\text{mb}}$  coincide at  $r_g$  for a maximally spinning black hole where also the event horizon is located.

As a last important radius, the ISCO can be computed by inserting the angular velocity into the angular momentum and finding the local minimum. Performing this calculation yields

$$r_{\text{ISCO}} = \left( h \mp \sqrt{\frac{-h^3 + 9h^2 - 3(6 - j^2)h + 7j^2}{h - 3}} \right) r_g \quad (3.45)$$

with  $h$  used as an abbreviation for

$$h = 3 + \sqrt{3 + j^2 + \sqrt[3]{1 - j^2} \left( (3 - j)\sqrt[3]{1 + j} + (3 + j)\sqrt[3]{1 - j} \right)} \quad (3.46)$$

For the retrograde motion around a maximally spinning black hole  $r_{\text{ISCO}} = 9r_g$  while once again, for the prograde case,  $r_{\text{ISCO}} = r_g$  coinciding with  $r_H$ ,  $r_{\text{mb}}$  and  $r_{\text{ph}}$ . This result is very important for the formation and emitted radiation of accretion disks around spinning black holes because it determines the location of the inner edge of the disk.

All these radii depending on the spin parameter,  $j$ , for circular motion in the equatorial plane are shown in Fig. 3.4. It is important to note however, that in practice the spin of a black hole can never be  $j = \pm 1$ . Thorne (1974) showed that under more realistic conditions given by accretion the highest value for the spin is  $j \simeq 0.998$  because photons with retrograde trajectories are preferably absorbed by the black hole since  $r_{\text{ph}}$  is smaller for those. Thus, the net angular momentum transfer of the photons onto the black hole will always be in the opposite direction of that of the black hole spin. Thorne (1974) was able to determine that under this constraint the maximum efficiency which can be achieved by accretion is roughly 30%.

## 3.2 Accretion Disks

Black holes themselves, as described in the previous section, cannot be observed since, because of the geometry of spacetime, nothing can escape the event horizon, not even light. The origin of the high energy radiation observed from AGN lies in the conversion of potential energy to other forms such as thermal and kinetic energy when matter is captured by the gravitational well of the black hole. This process is called *accretion* and can be extremely efficient in the conversion of energy as also outlined in the previous section.

Under the assumption that the matter falling towards the black hole has no intrinsic angular momentum and is doing so isotropically in the non-relativistic case, the entire potential energy is converted into kinetic energy

$$\frac{1}{2}mv^2 = \frac{GMm}{r} \quad (3.47)$$

where  $v$  is the velocity of a test particle,  $m$  its mass,  $M$  the mass of the central object and  $G$  the gravitational

constant. As described by Longair (1994), assuming that this entire energy can be converted, the resulting luminosity,  $L$ , which is the amount of energy emitted per unit of time, can simply be calculated from the mass accretion rate,  $\dot{m}$ ,

$$L = \frac{1}{2}\dot{m}v^2 = \frac{GM\dot{m}}{r} \quad (3.48)$$

Using the Schwarzschild radius of the central body, as defined in equation 3.12, this can be converted to

$$L = \frac{1}{2}\dot{m}c^2\frac{r_g}{r} \quad (3.49)$$

which conveniently introduces the speed of light next to the mass which gives the rest energy of the particle according to  $E = mc^2$ . When interpreting the accretion process as the conversion of this rest mass to kinetic energy by the gravitational potential and ultimately to radiation the luminosity can be written as

$$L = \eta\dot{m}c^2 \quad (3.50)$$

where the parameter  $\eta$ , again, gives the efficiency of this process. In combination with equation 3.49 in this simple case  $\eta$  can be identified as

$$\eta = \frac{1}{2}\frac{r_g}{r} \quad (3.51)$$

If, however, such a large amount radiation was released by the infalling material the radiative pressure driving the matter outward again is also expected to rise. This radiation force onto a test particle takes the form

$$F = \frac{\sigma S}{c} \quad (3.52)$$

where  $S = L/(4\pi r^2)$  is the flux and  $\sigma$  the cross-section of the particle in question. This force must be smaller than the gravitational force such that matter can still be accelerated inward,

$$\frac{\sigma L}{4\pi r^2 c} < \frac{GMm}{r^2} \quad (3.53)$$

so in particular

$$L = \frac{4\pi GMmc}{\sigma} \quad (3.54)$$

This upper limit for the luminosity in the simple case of spherical accretion is the Eddington luminosity,  $L_{\text{Edd}}$ , as already briefly mentioned in Section 2.2 (Eddington, 1916b). By neglecting the Thomson cross-section of electrons compared with that of protons, as suggested by Longair (1994), this becomes

$$L_{\text{Edd}} \simeq 1.3 \times 10^{38} \text{ erg s}^{-1} \frac{M}{M_{\odot}} \quad (3.55)$$

Using the relation 3.50, an upper limit of the mass accretion rate,  $\dot{m}$ , can be given in this way as

$$\dot{m} = \frac{L_{\text{Edd}}}{\eta c^2} \quad (3.56)$$

which is often called *Eddington rate*. As will be seen shortly this very simple picture of spherical absorption of pure and fully ionized hydrogen gas cannot hold in reality. The Eddington luminosity and Eddington rate are however often used to characterize the accretion behavior of certain objects. Ultraluminous X-Ray Sources (ULXs) for example show luminosities equal to or above the Eddington limit (Kaaret et al., 2017).

Specifically for AGN, but also for most other accreting objects such as white dwarfs, neutron stars

### 3 Active Galactic Nuclei

or protostars, the infalling material is expected to have some angular momentum. As a result of the conservation of angular momentum an isolated test particle can be on a stable orbit around the central object and not lose any energy. Considering the same situation but with a multitude of particles, for example a plasma, the particles would organize their orbits in a plane around the central object. This construct is called an *accretion disk*. In order for particles to decrease their orbital velocity and move closer to the center of the disk angular momentum must be transported outward via interactions between the particles.

Pringle (1981) gives an overview of the mechanisms providing the redistribution of angular momentum in thin accretion disks. The following considerations are based on a summary of these mechanisms by Longair (1994). The mass of the accretion disk is assumed to be negligible compared with the mass of the central object and the disk itself, even if being thin, has a final thickness which can be justified by hydrostatic support given by the gradient of the pressure,  $p$ , along the  $z$ -axis

$$\frac{\partial p}{\partial z} = -\frac{GM\rho \sin\theta}{r^2} \quad (3.57)$$

where  $M$  is again the mass of the central object,  $r$  the distance to its center and  $\rho$  the density. The scale height or also called “half width” is a measure for the extent of the disk in  $z$ -direction. For a thin disk this must be much smaller than the radius,

$$H \ll r \quad (3.58)$$

The *one-zone approximation* can be used to obtain another expression for the pressure gradient. It states that the pressure gradient is constantly distributed among the scale height of the disk as

$$\frac{\partial p}{\partial z} = \frac{p}{H} \quad (3.59)$$

Additionally, because the disk is assumed to be thin, the angle  $\theta$  (in spherical coordinates) is always very small and under this small angle approximation it can be used that

$$\sin\theta \simeq \frac{z}{r} \quad (3.60)$$

Combining all of these aspects yields the much simpler relation

$$\frac{p}{H} = \frac{GM\rho H}{r^3} \Leftrightarrow \frac{GM}{r} = \frac{p}{H^2} \frac{r^2}{\rho} \quad (3.61)$$

Furthermore, the orbital velocity,  $v_\phi$ , in the plane of the disk is expected to be much larger than the radial velocity,  $v_r$ , of the particles, which is the speed at which they move closer to the center. Because of that the orbit of all particles can be assumed to be of Keplerian nature which means that the gravitational and centrifugal forces need to be in balance,

$$\frac{mv_\phi^2}{r} = \frac{GMm}{r^2} \quad (3.62)$$

Substitution with the result of equation 3.61 gives

$$\frac{p}{\rho} = v_\phi^2 \frac{H^2}{r^2} \quad (3.63)$$

The speed of sound,  $c_s$ , in an ideal gas is

$$c_s = \sqrt{\gamma \frac{p}{\rho}} \quad (3.64)$$

where  $\gamma$  is the adiabatic index (Demtröder, 2008). So under the assumption that the gas is isothermal

( $\gamma = 1$ ) it holds that  $c_s^2 = p/\rho$  and therefore

$$\frac{H}{r} \simeq \frac{c_s}{v_\phi} = \frac{1}{\mathcal{M}} \quad (3.65)$$

which is expressed using the *Mach number*,  $\mathcal{M}$ . This means that for the disk to be sufficiently flat the rotational velocity must be much higher than the speed of sound in the accreted material. In this way the pressure gradient is low enough that the disk does not get inflated.

The assumption of Keplerian orbits has an important consequence in that the angular velocity is not constant with increasing radii, meaning differential rotation occurs. Angular momentum can be transported in the outward direction of the disk if some interaction between matter at two adjacent points is possible. Viscosity is expected to provide this interaction and shall further be investigated to make predictions about the behavior of the matter in the disk. In the simple case of a fluid flowing in one dimension but with a velocity gradient perpendicular to the direction of motion the force,  $F$ , between two adjacent layers of constant velocity,  $v$ , is given by

$$F(y) = \mu \frac{\partial v}{\partial y} \quad (3.66)$$

where the *shear viscosity*,  $\mu$ , is a parameter specific to the material. If the flow is not aligned with one axis in both dimensions, in this case  $x$  and  $y$ , it has to be considered that

$$F(x, y) = \mu \left( \frac{\partial v_x}{\partial x} + \frac{\partial v_y}{\partial y} \right) \quad (3.67)$$

Transforming this expression to polar coordinates and without loss of generality evaluating at  $\phi = 0$  yields

$$F = \mu r \frac{\partial \omega}{\partial r} \cdot A \quad (3.68)$$

where  $\omega$  is the angular velocity and  $A$  the area among which the force is distributed. In case of a disk this area is the cylindrical surface for which is

$$A = 2\pi r H \quad (3.69)$$

Using these relations the torque,  $D$ , at radius  $r$  can be calculated as

$$D = F \cdot r = \mu r \frac{\partial \omega}{\partial r} \cdot 2\pi r H \cdot r = \mu r (2\pi r^2 H) \frac{\partial \omega}{\partial r} \quad (3.70)$$

Using this as the inner boundary of an annular cylinder the total torque on the outer boundary at an infinitesimally higher radius  $r + dr$  is given by

$$D(r + dr) = D(r) + \frac{\partial D(r)}{\partial r} dr \quad (3.71)$$

which shows that the differential torque,  $dD$ , can be written as just

$$dD = \frac{\partial D(r)}{\partial r} dr \quad (3.72)$$

The torque is the derivative with respect to time of the angular momentum,  $L$ ,

$$\frac{dL}{dt} = \frac{\partial}{\partial r} \left( \mu r (2\pi r^2 H) \frac{\partial \omega}{\partial r} \right) dr \quad (3.73)$$

On the other hand, the angular momentum can be calculated using the momentum of the cylindrical element

### 3 Active Galactic Nuclei

which has a mass given by the density,  $\rho$ , and the volume  $V = 2\pi r^2 H$  and a circular velocity,  $v_\phi$ ,

$$L = 2\pi r^2 H \rho v_\phi dr \quad (3.74)$$

Taking the derivative and inserting into equation 3.73 results in

$$\frac{\partial v_\phi}{\partial t} = \frac{\nu}{r^2} \frac{\partial}{\partial r} \left( r^3 \frac{\partial v_\phi}{\partial r} \frac{1}{r} \right) \quad (3.75)$$

where the kinematic viscosity,  $\nu = \mu/\rho$ , was introduced.

An important parameter for the behavior of fluids is the Reynolds number,  $\mathcal{R}$ , which is directly relating the speed of the fluid to the viscosity over a length  $l$ ,

$$\mathcal{R} = \frac{vl}{\nu} \quad (3.76)$$

$\mathcal{R}$  can be used to directly determine the behavior of a fluid with respect to turbulence. For low Reynolds numbers the flow is laminar while for high numbers it becomes increasingly turbulent. The tipping point is around  $\mathcal{R} \simeq 1000$ . This can be used to make estimates about the behavior of the flow inside the accretion disk. Using the mean free path,  $\Lambda$ , of particles in the gas and their mean velocity, which in this case is assumed to be the speed of sound,  $c_s$ , the kinematic viscosity can directly be calculated as

$$\mu = \frac{1}{3} c_s \Lambda \quad (3.77)$$

(Demtröder, 2008) which means that

$$\mathcal{R} = \frac{3vl}{\rho c_s \Lambda} \quad (3.78)$$

Continuing from this point, Longair (1994) carries out an estimate of this value for a neutron star by making some further assumptions, such as the mass of the object being one solar mass and the region of the highest luminosity of the disk being at  $10r_g$ . The procedure concludes with the result of

$$\mathcal{R} = 10^{12} \quad (3.79)$$

The only possible conclusion which can be drawn from this value for  $\mathcal{R}$  is that the flow in the accretion disk must be highly turbulent. For this type of motion the *eddy viscosity* takes over the role of kinematic viscosity which results in the motion of particles not being constraint to the assumed Keplerian orbits, but some are able to move outwards in the disk and therefore transport angular momentum in this direction. Because charged particles of the plasma are moving in these eddies chaotic magnetic fields can be generated which provide an additional mechanism to contribute to this effect.

Analytical solutions are not able to capture all of these effects, so complicated simulations including magnetohydrodynamics have to be performed to study the formation of accretion disks under these aspects (see e.g., Hawley et al., 1996; Armitage, 1998; Fragile et al., 2007).

With this result recognized, Shakura & Sunyaev (1973a) introduced a way to include all of these effects in a single parameter  $\alpha$  which captures the transport-efficiency of angular momentum and relates to the turbulent viscosity as

$$\nu = \alpha c_s H \quad (3.80)$$

This parameter gave the entire model its name: the  $\alpha$ -disk model.  $\alpha$  is constrained to values between 0 and 1. With the entirety of physics related to the correct description of the processes occurring in the accretion disk hidden in this parameter it is possible to proceed with predictions of the observational aspects of such phenomenon. The proper values for  $\alpha$  can then be empirically determined from the observed data.

In this manner other parameters of the disk will now be estimated to finally arrive at predictions of

important fundamental properties of the disk such as the temperature and the dissipation of energy. To this end, it is assumed that the accretion process is in a steady state, meaning that only the viscosity  $\nu$  determines the drift speed,  $v_r$ , of matter in  $r$ -direction and the amount of matter passing through a radial layer in the disk is

$$\dot{m} = 2\pi r v_r \int \rho dz \quad (3.81)$$

which is constant. Using the definition of the kinematic viscosity and interpreting the height of the accretion disk as  $H = \int dz$  equation 3.70 can be written as

$$D = 2\pi r^3 \nu \int \rho dz \frac{\partial \omega}{\partial r} = 2\pi r^3 \nu \Sigma \frac{\partial \omega}{\partial r} \quad (3.82)$$

where the surface density,  $\Sigma = \int \rho dz$ , was introduced. By definition the angular momentum is  $L = m v_\phi r$ , so its transport can also be expressed in terms of the mass transfer rate,

$$\dot{L}(r) = \dot{m} v_\phi r = 2\pi r v_r \Sigma v_\phi r = 2\pi r^3 \Sigma v_r \omega(r) \quad (3.83)$$

where it was considered that  $v_\phi = \omega r$  and the definition of the surface density was inserted. The same holds for the outer radius of the finite layer,

$$\dot{L}(r + \Delta r) = 2\pi (r + \Delta r)^3 \Sigma v_r \omega(r) \quad (3.84)$$

Taylor expansion and subtracting both equations yields for the difference in angular momentum

$$\Delta L = 2\pi \Delta r \frac{d}{dr} r^3 \Sigma v_r \omega \quad (3.85)$$

For a layer with finite thickness  $\Delta r$ , it follows from equation 3.71 that

$$D(r + \Delta r) - D(r) = \frac{\partial D}{\partial r} \Delta r \quad (3.86)$$

Because the torque,  $D$ , describes the change of angular momentum the last two equations can be set equal to obtain

$$\frac{dD}{dr} = 2\pi \frac{d}{dr} r^3 \Sigma v_r \omega \quad (3.87)$$

and over integrating after  $r$

$$D = 2\pi r^3 \Sigma v_r \omega + c \quad (3.88)$$

with a constant of integration,  $c$ . Using the direct relation to  $D$ , as given in equation 3.82, the result takes the form of

$$\nu \Sigma \frac{d\omega}{dr} = -\Sigma v_r \omega + \frac{c}{2\pi r^3} \quad (3.89)$$

where the direction of the flow is now considered to be towards the center of the disk, thus  $v_r \rightarrow -v_r$ . The integration constant now has to give the boundary condition which determines at which point the accretion flow is terminated at the inner edge of the disk and is the transport of angular momentum into this boundary layer. For black holes it is given by the ISCO of the particles which in turn is determined by the spin of the black hole. Ignoring relativistic effects, according to the virial theorem, the rotational energy at this border

### 3 Active Galactic Nuclei

must be lower than half the gravitational potential of the black hole,

$$\frac{L^2}{2I} < \frac{GMm}{2r_{\text{ISCO}}} \quad (3.90)$$

with the moment of inertia,  $I$ , which in this case is  $I = mr_{\text{ISCO}}^2$ . Solving after  $L$  results in

$$L < m\sqrt{GMr_{\text{ISCO}}} \quad (3.91)$$

so the rate of angular momentum transport,  $\dot{L}$ , expressed in terms of the mass transfer rate is

$$\dot{L} < \dot{m}\sqrt{GMr_{\text{ISCO}}} \quad (3.92)$$

which is exactly the condition for the rate of transport at the boundary, hence the integration constant,  $c$ . Because the orbit is assumed to be Keplerian the angular velocity and its derivative after  $r$  are

$$\omega = \sqrt{\frac{GM}{r^3}} \Rightarrow \frac{d\omega}{dr} = -\frac{3}{2}\sqrt{GM}r^{-5/2} \quad (3.93)$$

Inserting this and the boundary condition into equation 3.88 yields

$$-\frac{3}{2}\nu\Sigma\sqrt{GM}r^{-5/2} = -\Sigma v_r\sqrt{GM}r^{-3/2} + \frac{c}{2\pi r^3} = -\Sigma v_r\sqrt{GM}r^{-3/2} + \frac{\dot{m}\sqrt{GMr_{\text{ISCO}}}}{2\pi r^3} \quad (3.94)$$

$\Sigma v_r$  can be expressed using the definition of the surface density in equation 3.81

$$-\frac{3}{2}\nu\Sigma r^{-5/2} = -\frac{\dot{m}}{2\pi r}r^{-3/2} + \frac{\dot{m}\sqrt{r_{\text{ISCO}}}}{2\pi r^3} \quad (3.95)$$

$$\Rightarrow \nu\Sigma = \frac{\dot{m}}{3\pi} \left(1 - \sqrt{\frac{r_{\text{ISCO}}}{r}}\right) \quad (3.96)$$

where the term  $\sqrt{GM}$  was eliminated. The dissipation of energy,  $\dot{E}$ , of an incompressible fluid caused by internal friction can be calculated in spherical coordinates as

$$\dot{E}(r) = \frac{1}{2}\nu\Sigma r^2 \left(\frac{d\omega}{dr}\right)^2 \quad (3.97)$$

(Pringle, 1981), where finally the result of equation 3.95 and the angular velocity of the orbit can be inserted to obtain for the disk

$$\dot{E}(r) = \frac{3}{8\pi} \frac{GM\dot{m}}{r^3} \left(1 - \sqrt{\frac{r_{\text{ISCO}}}{r}}\right) \quad (3.98)$$

This very important result can now be used to predict in which way accretion disks generate radiation and what spectrum this radiation follows.

## 3.3 Radiation Processes

### 3.3.1 Blackbody Emission

One of the initial assumptions about the thin accretion disk in this model was that it is also optically thick which means that each element of the disk will radiate a blackbody spectrum. From this the total luminosity of the disk and its spectrum can be calculated if the temperature distribution is known. From the assumption of a blackbody spectrum follows that the temperature,  $T$ , and total luminosity,  $\mathcal{L}$ , per unit

area are correlated via the Stefan-Boltzmann law as

$$\mathcal{L} = \sigma T^4 \quad (3.99)$$

where  $\sigma$  is the Stefan-Boltzmann constant. Conveniently the energy dissipation rate,  $\dot{E}$ , is exactly this quantity, the energy released by a unit area per unit time, so both can be set equal and solved for  $T$ . It has to be taken into account, however, that the disk has two sides over which the energy is dissipated which results in

$$T(r) = \sqrt[4]{\frac{3}{8\pi} \frac{GM\dot{m}}{r^3\sigma} \left(1 - \sqrt{\frac{r_{\text{ISCO}}}{r}}\right)} \quad (3.100)$$

so for regions sufficiently far away from the center ( $r \gg r_{\text{ISCO}}$ ) this results in the basic dependency of the temperature on the radius,

$$T \propto r^{-3/4} \quad (3.101)$$

From this the temperature at any radius can be given in terms of the central temperature,  $T_{\text{in}}$ , and radius,

$$T(r) = T_{\text{in}} \left(\frac{r}{r_{\text{ISCO}}}\right)^{-3/4} \quad (3.102)$$

where

$$T_{\text{in}} = \sqrt[4]{\frac{3}{8\pi} \frac{GM\dot{m}}{\sigma r_{\text{ISCO}}^3}} \quad (3.103)$$

The spectrum,  $S_p(f, T)$ , i.e., the amount of power emitted at a given frequency,  $f$ , and temperature,  $T$ , of a blackbody is described by Plack's law,

$$S_p(f, T) = \frac{2hf^3}{c^2} \frac{1}{e^{hf/(kT)} - 1} \quad (3.104)$$

where  $h$  is the Planck and  $k$  the Boltzmann constant. The overall spectrum can be calculated as a continuous composition of the blackbodies with different temperatures depending on the radii and starting from the inner edge up to an outer radius,  $r_{\text{out}}$ , over the surface of the disk,

$$S(f) = \int_{r_{\text{ISCO}}}^{r_{\text{out}}} S_p(f, T(r)) 2\pi r dr \quad (3.105)$$

As suggested by Longair (1994), the variable of integration can be changed to  $1/T$  to obtain

$$S(f) = \int_{T_{\text{ISCO}}}^{T_{\text{out}}} \frac{2hf^3}{c^2} \frac{1}{T^{5/3}} \frac{1}{e^{hf/(kT)} - 1} d\left(\frac{1}{T}\right) \quad (3.106)$$

and further by setting it to  $x = hf/(kT)$ ,

$$S(f) = \frac{2h}{c^2} f^{1/3} \int_{x_{\text{ISCO}}}^{x_{\text{out}}} \frac{x^{5/3}}{e^x - 1} dx \quad (3.107)$$

Analytical solutions to this integral are inherently difficult, however, the frequency,  $f$ , is not part of it anymore, thus it can be stated that

$$S(f) \propto f^{1/3} \quad (3.108)$$

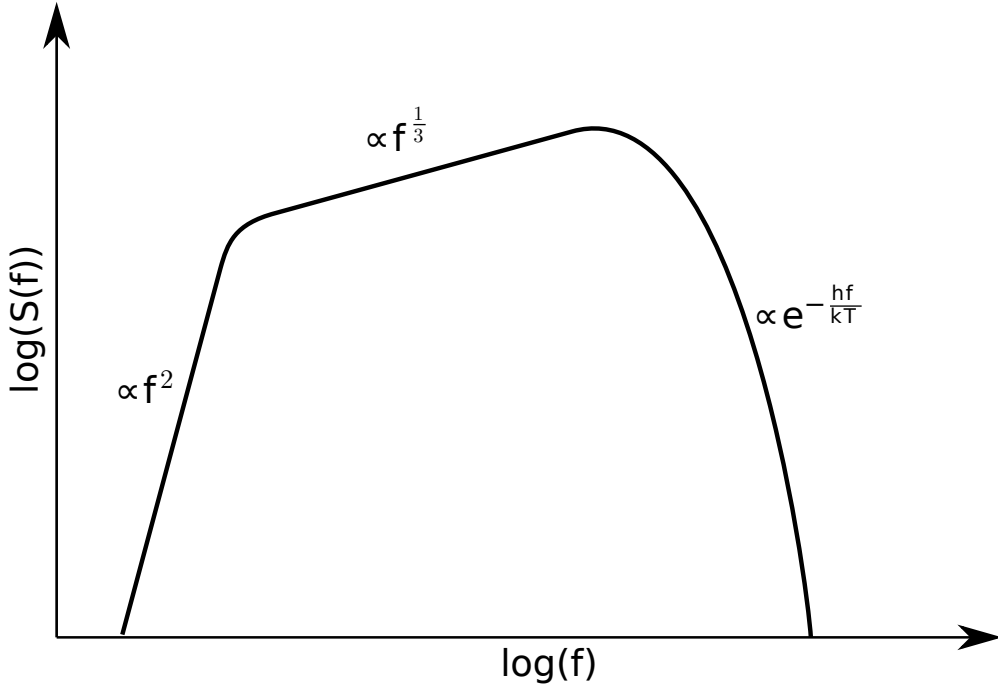


Figure 3.5: Sketch of the resulting spectrum of a multi temperature disk blackbody. After Longair (1994)

for a disk blackbody spectrum for all radii which lie between  $r_{\text{ISCO}}$  and  $r_{\text{out}}$ . For frequencies corresponding to temperatures below  $T(r_{\text{out}})$  the spectrum approaches the shape given by the Rayleigh-Jeans approximation

$$S(f) \propto f^2 \tag{3.109}$$

and for temperatures higher than  $T(r_{\text{ISCO}})$  the exponential part dominates,

$$S(f) \propto e^{-hf/(kT)} \tag{3.110}$$

The resulting spectral distribution is sketched in Fig. 3.5. Variations of this model spectrum with slightly different boundary conditions were successfully applied to galactic black hole binaries for which  $r_{\text{ISCO}}$  is much smaller than for the SMBHs at the center of AGN. Examples for such analyses are given in Mitsuda et al. (1984), Makishima et al. (1986), Kubota et al. (1998), and Zimmerman et al. (2005). The name of a widely used implementation of such a model is `diskbb`.

Finally, by taking into account that two sides are radiating energy, the total luminosity,  $\mathcal{L}$ , of the disk can be calculated by integrating over two entire surfaces to extending to infinite radii

$$\mathcal{L} = \int_{r_{\text{ISCO}}}^{\infty} 2 \cdot \dot{E} 2\pi r \, dr = \frac{GM\dot{m}}{2r_{\text{ISCO}}} \tag{3.111}$$

This result indicates that half of the gravitational energy of the infalling material can be converted into radiation under the assumed model of an optically thick and geometrically thin accretion disk which is terminated at an inner radius with a zero-torque boundary condition.

### 3.3.2 Inverse Compton Scattering

During the first systematic observations of a multitude of AGN the accretion disk model could be tested on these objects. As it turns out, the overall spectral shape of Seyfert type I galaxies is better described by a

much simpler model which only assumes a powerlaw shaped spectrum of the form

$$S(E) = N \cdot E^{-\Gamma} \quad (3.112)$$

where now the photon energy,  $E$ , is used instead of the frequency.  $N$  is a normalization factor and  $\Gamma$  the spectral index, or photon index. When shown in a plot with logarithmic axes a powerlaw model becomes just a straight line with the parameter  $-\Gamma$  giving the slope of this line, thus this parameter is just called the “slope” of the powerlaw. Studies discovering this behavior have been carried out in the eighties, for example using First *High Energy Astronomy Observatory (HEAO-1)*, Second *High Energy Astronomy Observatory (HEAO-2)* (Rothschild et al., 1983; Mushotzky, 1984) and *European X-ray Observatory Satellite (EXOSAT)* (Turner & Pounds, 1989), and found the slope to be roughly  $\Gamma = 0.7$ . Turner & Pounds (1989) specifically did find deviations from this shape for soft X-ray photons from 0.1 to 2 keV which were interpreted as originating from the superimposed blackbody component, verifying that indeed accretion plays a role for the generation of radiation in these objects, but most of the spectrum, being the “hard tail” provided by the powerlaw up to hundreds of keV, could not be explained by thermal emission.

There are, however, more processes involved in generating the observed radiation for which the photons from the blackbody emission only provide the seed. An important mechanism is the interaction between these photons and the highly energetic electrons contained in the plasma, either in and around the accretion disk itself or above the black hole (see Chapter 3.5 for details on this geometry). When these two particles scatter via the electromagnetic interaction, energy can be transferred from one to the other. This effect is called *Compton effect* after Arthur Holly Compton who discovered this phenomenon when scattering X-ray photons off electrons at rest (see Compton, 1923, for the original publication). In this case a photon with an initial energy,  $E_{\gamma 1}$ , has an energy of

$$E_{\gamma 2} = \frac{E_{\gamma 1}}{1 + \frac{E_{\gamma 1}}{m_e c^2} (1 - \cos \theta)} \quad (3.113)$$

after the scattering, where  $\theta$  depicts the scattering angle. The theoretical description of the differential cross-section for this interaction has been developed by Klein & Nishina (1929) from the first order approximations of quantum electrodynamics (QED) as

$$\frac{d\sigma}{d\Omega} = \frac{1}{2} \left( \frac{\alpha \hbar}{m_e c} \right)^2 \left( \left( \frac{E_{\gamma 2}}{E_{\gamma 1}} \right)^3 + \frac{E_{\gamma 2}}{E_{\gamma 1}} - \left( \frac{E_{\gamma 2}}{E_{\gamma 1}} \sin \theta \right)^2 \right) \quad (3.114)$$

where  $\alpha = e^2/4\pi\epsilon_0\hbar c$  is the fine structure constant and  $d\Omega$  the solid angle element into which the particle is scattered with the infinitesimal cross-section  $d\sigma$ .

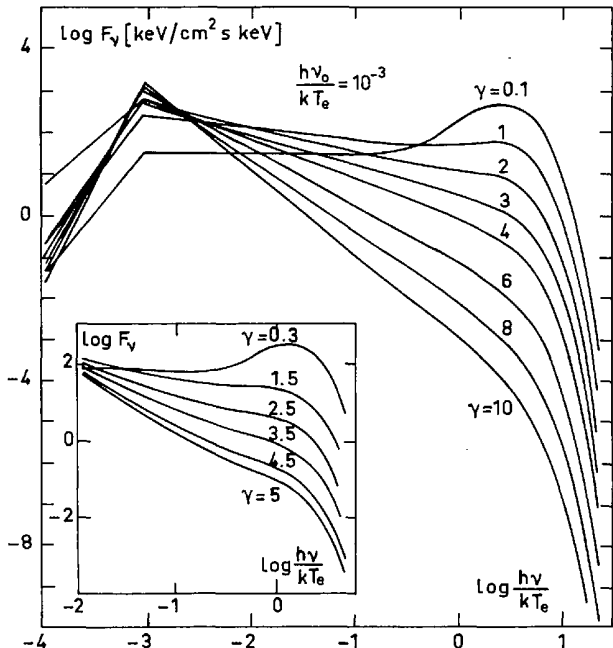
To properly describe the situation where the electron is not at rest the Klein-Nishina cross-section can be used after the frame of reference is changed to the electron’s frame of rest via Lorentz transformation. In this frame the electron is stationary again, and the scattering can be carried out after which the energy of the photon is transformed back to the original reference frame again. In case the electron has a sufficiently high energy and that of the photon is sufficiently low a net energy transfer from the electron to the photon is possible in the initial reference frame. This phenomenon is called *inverse Compton effect* because the roles of the donor and acceptor of energy are reversed.

The low energy photons for this process are supplied by the thermal blackbody emission from the accretion disk. They are scattered off highly energetic electrons contained in hot plasma of the *X-ray corona*, the mentioned plasma located around the accretion disk or concentrated above the poles of the SMBH. The velocity distribution of the electrons in the plasma is assumed to follow a Maxwellian distribution of the form

$$n(v) dv = n \left( \frac{m}{2\pi kT} \right)^{3/2} 4\pi v^2 e^{-mv^2/(2kT)} dv \quad (3.115)$$

which gives the number density,  $n(v)$ , of particles in a velocity element,  $dv$ , where  $n$  is the number density of particles and  $m$  their respective mass (Demtröder, 2008). Depending on the optical depth of the plasma

Figure 3.6: Spectral shape of electromagnetic radiation emerging from a hot plasma after multiple inverse Compton scatterings as calculated by Sunyaev & Titarchuk (1980). The initial energy of the seed photons is  $hf = 10^{-3}kT_e$ . The parameter  $\gamma = \pi^2 m_e c^2 / 3(\tau_0 + \frac{2}{3})^2 kT_e$  with the optical depth,  $\tau_0$ , is a measure for the number of scatterings the photons undergo until they escape the plasma (high  $\gamma$  means low optical depth, so fewer scatterings). As a result the spectra show the typical powerlaw shape with a high energy rolloff and for low  $\gamma$  the Wien hump.



multiple scatterings can occur between a photon and an electron until it escapes the plasma towards the observer. When the time for the photons to escape the plasma is much longer than the time in between scatterings, meaning that the photons scatter a large number of times, this *Comptonization* process is said to be *saturated*. In the other case it is considered *unsaturated*.

The theoretical description of this process is given by the partial differential equation developed by Kompaneets (1957) for this purpose,

$$\frac{\partial n}{\partial y} = \frac{1}{x^2} \frac{\partial}{\partial x} \left( x^4 \left( \frac{\partial n}{\partial x} + n + n^2 \right) \right) \quad (3.116)$$

where  $n$  now depicts the photon number density.  $x$  is the ratio between the photon energy and thermal energy of the electron corresponding to  $T_e$ ,

$$x = \frac{hf}{k_B T_e} \quad (3.117)$$

with the Boltzmann constant,  $k_B$ , and  $y$  is the *Kompaneets parameter* defined as

$$y = \frac{k_B T_e}{m_e c^2} n_e \sigma_T c t \quad (3.118)$$

with the Thomson cross-section for electrons,  $\sigma_T$ , and the number density of electrons,  $n_e$ . The contribution of  $n$  in equation 3.116 can be interpreted as originating from recoil effects in the scattering procedure,  $n^2$  as induced emission and  $\partial n / \partial x$  as the influence of Doppler motion. It is emphasized that Kompaneets's equation has been developed specifically for the description of the inverse Compton effect. In this case the energy of the photon is much smaller than the energy of the electron, i.e.,  $hf \ll k_B T_e \Leftrightarrow x \ll 1$ .

In simplified cases equation 3.116 can be solved analytically (see for example Jones, 1968; Pomraning, 1972; Sunyaev & Titarchuk, 1980; Haardt, 1993; Titarchuk, 1994) but for more general considerations numerical Monte Carlo simulations of the scattering processes are necessary. Early results of these are presented for example by Pozdnyakov et al. (1983) and Belmont et al. (2008) provide a much more sophisticated method which also takes other effects into account such as synchrotron self-absorption and electron-positron pair-production and annihilation. The results of both methods, analytical calculations and simulations, show that

the emerging spectrum of electromagnetic radiation leaving the plasma follows a powerlaw with a “rolloff”, a steep decrease in intensity, at higher energies with a “rolloff”, a steep decrease in intensity, at higher energies<sup>2</sup>. If the optical depth is high, meaning the photons undergo numerous scatterings until emerging from the plasma, an additional excess called *Wien hump* at energies just below the rolloff is expected. Spectra showing all these effects resulting from the analytical calculations by Sunyaev & Titarchuk (1980) are shown in Fig. 3.6. In the energy range of moderate X-rays (0.1 to 10 keV) typically only the powerlaw section is present, explaining the observed behavior of AGN. The rolloff can be directly observed in hard X-rays to gamma-rays (Zdziarski et al., 2000) and indirectly inferred from effects observed in lower energy X-rays (García et al., 2015).

### 3.3.3 Fluorescent Line Emission

Up to this point only the two continuum components provided by thermal blackbody emission and Comptonization were discussed. In the considerations for the Comptonization process only the interaction of thermal photons with free electrons was considered, but the accreted material can also contain atomic nuclei. At large radii the accretion disk is expected to be cool and therefore not or only weakly ionized (Netzer, 2015). When illuminated by X-rays from the central region of the system near the black hole energy can be deposited in this material leading to the transition of electrons to energetically higher orbitals via photoabsorption. After a certain lifetime, usually given in terms of the average lifetime,  $\tau$ , the electron will transition to lower energy states. From the difference in energy either a photon is emitted (radiative transition) or the dissipation occurs via another process, for example the ejection of an electron from the atom via the Auger effect, creating an ion (non-radiative transition). In the first case the photon emitted upon the relaxation of the electron can have at most the same energy as the initially absorbed photon due to the conservation of energy. Another constraint on the emitted photon is given by the fact that the electron can only transition between the discrete energy levels of the orbitals and furthermore the selection rules of the transitions between these quantum mechanical states given by the conservation of angular momentum. As a result of this process called *fluorescence* the material in the cold accretion disk is expected to radiate a spectrum of distinct emission lines specific to each element and its corresponding abundance in the gas.

Even though the possible energies of these fluorescent lines are discrete the emerging emission lines are not infinitely thin but broadened. In part, this can be attributed to the Heisenberg uncertainty principle which creates a relation between the width of the emission line,  $\Gamma$ , and the corresponding lifetime of the initial state according to

$$\Gamma \cdot \tau \geq \hbar \Leftrightarrow \Gamma \geq \frac{\hbar}{\tau} \quad (3.119)$$

giving a lower limit for the resulting width of the emission line (Bambynek et al., 1972). The total decay width,  $\Gamma$ , is composed of the widths of the radiative and non-radiative transitions where only the first one can be measured using the emerging electromagnetic radiation. With the ratio between the total energy emitted and absorbed the *yield* of the fluorescent transition is defined. Additional broadening of the fluorescent line is caused by the thermal motion of the emitting particles.

Fig. 3.7 shows in red the emerging spectrum when an unionized accretion disk is illuminated by a powerlaw spectrum with spectral index  $\Gamma = 1.7$  and an exponential rolloff at 300 keV, shown in black. The blue spectrum is a superposition of both components. It was calculated using the `xillver` model developed by García et al. (2013) and setting the ionization parameter to zero while the inclination under which the accretion disk is viewed is  $20^\circ$ . For iron the abundance in the material is set to the solar value. As a result of fluorescence in this reflection process<sup>3</sup> multiple narrow emission lines are present of which the major ones have been marked with the according element in Fig. 3.7. Because of the combination of fluorescence yield and elemental abundance the most prominent emission line is that of the Fe  $K\alpha$  transition (Miller,

<sup>2</sup>This rolloff is often modelled using an exponential function, as for example in the `cutoffpl` model, which owes its name to the fact that “cutoff” is also often used to refer to the decrease in intensity. However, the name “cutoff” would imply a discontinuity in the flux and was therefore considered a misnomer in this thesis and the term “rolloff” was used instead.

<sup>3</sup>Actually the entire process consists of the absorption, reprocessing and reemission of photons, but is in the literature mostly referred to as *reflection*, even though it is not the same process as conventional reflection as described in Section 4.1.2

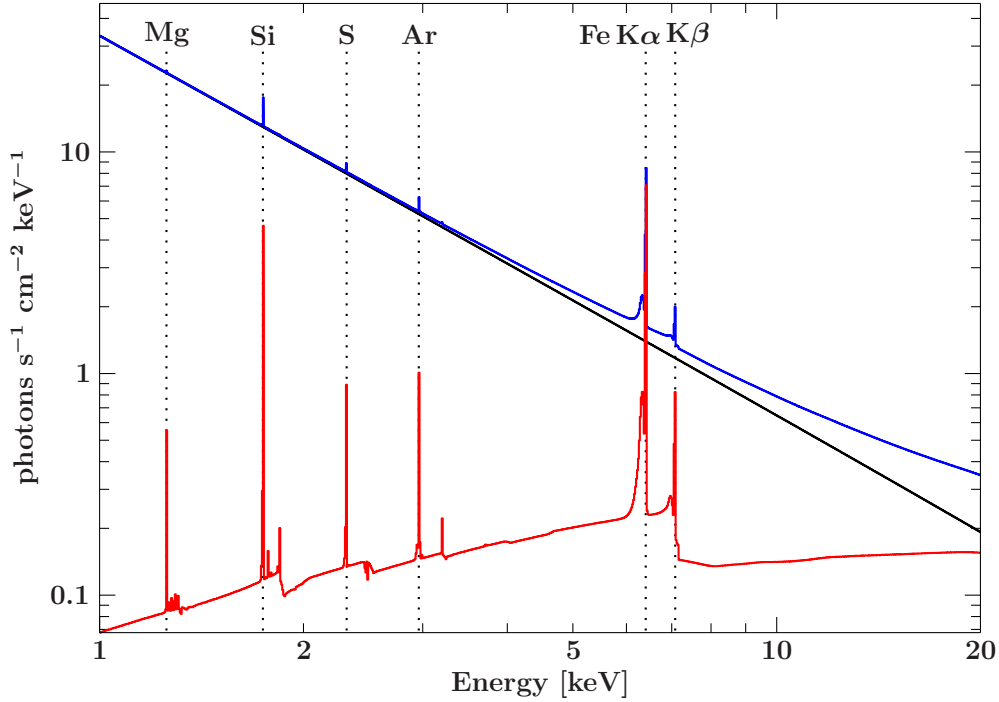


Figure 3.7: Reflected spectrum (red) off an ionized one-dimensional slab of material calculated using the `xillver` model (García et al., 2013) from an incident powerlaw with photon index  $\Gamma = 1.7$  (black) and the total spectrum as a superposition of both (blue). The elements and energies of major fluorescent lines have been marked.

2007). Corresponding to the transition of an electron from the 2p to 1s orbital the line is a superposition of two transitions at 6.391 keV and 6.404 keV with a probability of 1:2 (Bambynek et al., 1972). According to George & Fabian (1991), each of the lines has a natural width of  $\Delta E \simeq 3.5$  eV given by the uncertainty principle. The thermal broadening can be estimated using

$$\Delta E \simeq 0.4 \sqrt{\frac{T}{10^6}} \text{ eV} \quad (3.120)$$

For cold material the intrinsic width of the fluorescent emission lines is therefore only on the order of a few electronvolts. As will be explained later, the observed shape of especially the Fe  $K\alpha$  line does not resemble this expected narrow shape. Studying this deformation of the initially narrow fluorescent line provides a powerful method of probing the physical effects in the central region of the accretion disk close to the SMBH of an AGN.

### 3.3.4 X-ray Absorption

When the radiation generated by an AGN embarks on its journey towards the observer, for example an X-ray telescope in space such as *eROSITA*, it will not reach this destination unaffected but will at least interact with the ISM in the Milky Way which imprints an effect of energy dependent absorption onto the resulting spectrum. The overall cross-section of this process is a combination of the cross-sections of the elements forming the ISM with their respective abundances and the different phases in which this material can be present: atomic gas, molecules and grains. Calculating these cross-sections is a complicated process heavily relying on the understanding of atomic physics and the involved approximations without which the actual calculations would be unfeasible. Absorption by the ISM is implemented for example by the `phabs` model provided as a built-in model of the X-ray data analysis package `xspec` (Arnaud, 1996). It

uses the method of obtaining the photoelectric absorption cross-section developed by Balucinska-Church & McCammon (1992) who give polynomial fit coefficients for functions up to eight degrees approximating the cross-sections of 17 astrophysically relevant elements as given by experimental data provided by Henke et al. (1982). Because the coefficients have been determined for the cross-sections of all elements individually their relative abundances can be varied. This model, however, does not include the effects caused by molecules such as  $\text{H}_2$ , dust grains and the absorption by ionized material. The improved model `tbabs` developed by Wilms et al. (2000) provides handling of dust grains and molecular  $\text{H}_2$  gas. In their publication they also discuss the problem of determining the correct elemental abundances. One feature of both models is the possibility to vary these relative abundances, but this creates 17 additional parameters. Because of this it was suggested to use abundances measured in the solar photosphere or from meteorites, as done for example by Anders & Ebihara (1982), Grevesse & Anders (1989), Anders & Grevesse (1989), and Shull (1993), also for the absorption of X-rays caused by the ISM. `phabs` and `tbabs` provide this in the form of simplified versions with the former reproducing the total cross-section as determined in the previous work by Morrison & McCammon (1983) which was also based on the individual cross-sections from Henke et al. (1982) and abundances given by Anders & Ebihara (1982). For the latter one Wilms et al. (2000) used improved abundance values for carbon from Cardelli et al. (1996), for nitrogen from Meyer et al. (1997) and for oxygen from Meyer et al. (1998) while for magnesium, silicon, sulfur, calcium, titanium, chromium, iron and nickel the values were adopted from Snow & Witt (1996). The main difference of these abundances are given by measurements suggesting that in the ISM these values are 20% to 30% lower than the solar value (see for example Sofia et al., 1994; Snow & Witt, 1996; Savage & Sembach, 1996). For all other elements, being helium, neon, sodium, aluminum, chlorine, argon and cobalt 70% of the solar abundances were used, following these indications. In the meantime a new and improved version of `tbabs`, named `tbnew`, was published<sup>4</sup> which implements finer grids for the structure of the absorption edges and provides much better computational performance.

Although in this work only the `tbabs` model in its form with default abundances was used, note that Gatuzz et al. (2015) developed a model named `ISMabs` which compiles more recent atomic data and also takes a variety of singly and doubly ionized elements into account.

To specify the amount of absorption the *equivalent hydrogen column density*,  $N_{\text{H}}$ , is a widely used parameter. It relates the observed, energy dependent intensity,  $I_{\text{obs}}(E)$ , to the source intrinsic intensity,  $I_{\text{source}}(E)$ , with the total cross-section,  $\sigma_{\text{ISM}}$ , of the ISM as

$$I_{\text{obs}}(E) = I_{\text{source}}(E) \cdot e^{-\sigma_{\text{ISM}}(E) \cdot N_{\text{H}}} \quad (3.121)$$

where it is emphasized that  $\sigma_{\text{ISM}}$  also depends on the photon energy and is the focus of the above-mentioned models. Figuratively speaking, the equivalent hydrogen column density gives the number of hydrogen atoms per square centimeter causing the same amount of absorption as the composition of elements with their respective abundances in the ISM. The effect of absorption by the ISM with different values for  $N_{\text{H}}$  as calculated using the `tbabs` model on a powerlaw with  $\Gamma = 1.7$  is depicted in Fig. 3.8. Atomic transitions of the elements cause strong absorption edges which have been marked. It is clearly visible that the effect of absorption increases strongly towards softer X-rays and is amplified for higher values of  $N_{\text{H}}$ .

### 3.4 Ionized Reflection

When the hot inner region of the accretion disk is illuminated by the hard X-ray emission of the corona photoionization of the matter in the disk can occur (Ross & Fabian, 1993). The degree of ionization of the disk is usually expressed using the *ionization parameter*,  $\xi$ , defined by Tarter et al. (1969) as

$$\xi = \frac{4\pi F_x}{n} \quad (3.122)$$

where  $F_x$  is the incident flux on the disk and  $n$  its density. A low value of  $\xi \simeq 1$  corresponds to very weakly ionized or neutral material. When the material is close to fully ionized  $\xi$  approaches  $10^4$  or greater. Because

<sup>4</sup>It is available on <https://pulsar.sternwarte.uni-erlangen.de/wilms/research/tbabs/index.html>

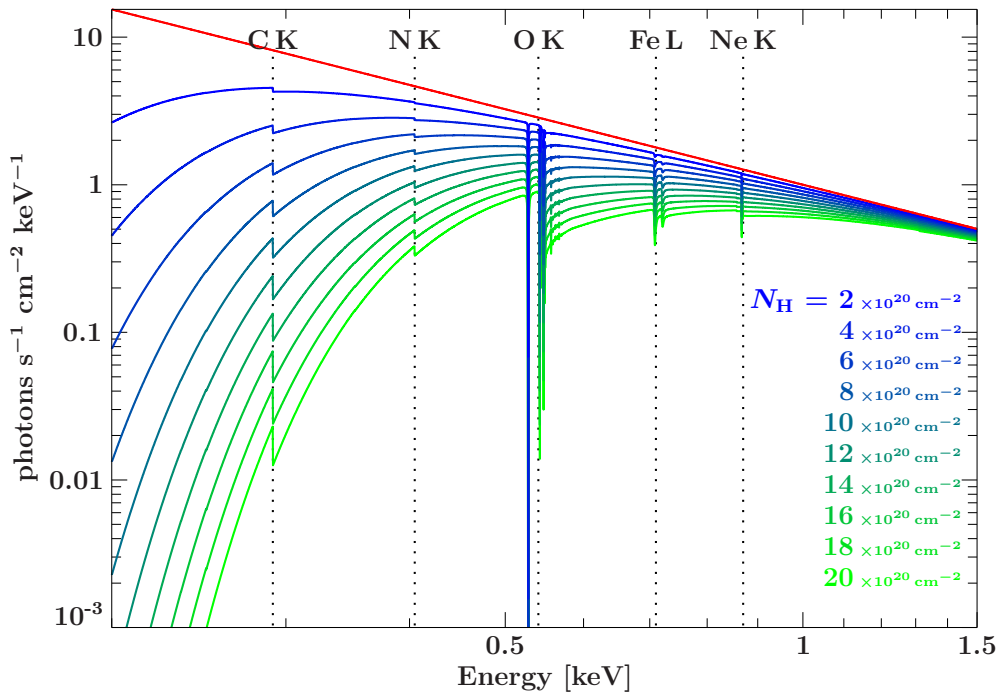


Figure 3.8: Effect of X-ray absorption by the ISM on a powerlaw spectrum with photon index  $\Gamma = 1.7$  (red) for different values of the equivalent hydrogen column density,  $N_{\text{H}}$ , calculated using the `tbabs` model with default elemental abundances. Major absorption edges are marked with their corresponding atomic transitions.

of this broad range and to account for more subtle changes of the parameter in its lower range often the logarithm of  $\xi$ ,  $\log \xi$ , is used to express the ionization stage.

Tarter et al. (1969) initially calculated the reaction of an optically thin gas to the illumination by X-rays following a thermal bremsstrahlung spectrum. Further effort was put into investigating the imprint of the reflection by ionized matter on non-thermal emission for example by Lightman & White (1988), Ross & Fabian (1993), Zycki et al. (1994), Ross et al. (1999), and Ross & Fabian (2005), which also includes the calculation of expected spectra for different ionization stages. One of the main features predicted by these analyses is an excess in X-ray flux at 30 keV which has been confirmed in the spectra of several AGN, for example NGC 1365 (Walton et al., 2014; Kara et al., 2015b), SWIFT J2127.4+5654 (Marinucci et al., 2014; Kara et al., 2015b), Mrk 335 (Parker et al., 2014) and MCG-5-23-16 (Zoghbi et al., 2014).

García & Kallman (2010) developed the `xillver` model which solves the equations of radiative transfer, energy balance and ionization equilibrium in the one-dimensional case and applies this for rings of constant radius and density in the material of the accretion disk for an incident spectrum consisting of a powerlaw with an exponential rolloff. Importantly, `xillver` takes up-to-date atomic data such as energy levels, line wavelengths and transition probabilities as provided for a broad range of ionic states of several elements by the `xstar` database (Bautista & Kallman, 2001) into account. An updated version of the model has also been published by García et al. (2013). It provides the calculated reflected powerlaw spectra for photon indices in the range of  $1.2 \leq \Gamma \leq 3.4$  with rolloffs from 5 to 1000 keV and ionization states in the range of  $1 \leq \log \xi \leq 4$ . Additionally, these spectra have been calculated for different abundances,  $A_{\text{Fe}}$ , of iron from 0.5 to 10 in units of the solar abundance and angles of inclination of the line of sight towards the accretion disk in the range from  $5^\circ$  to  $85^\circ$ . The intensity of the reflected spectrum is expressed using the reflection fraction,  $f_{\text{refl}}$ .

Fig. 3.9 shows a set of reflected spectra calculated using the `xillver` model in the energy range from 0.1 to 10 keV for different ionization stages. The incident powerlaw with photon index of  $\Gamma = 1.7$  and a rolloff at 300 keV is shown in red. As seen under an inclination of  $i = 20^\circ$  the reflected spectra cover a range of

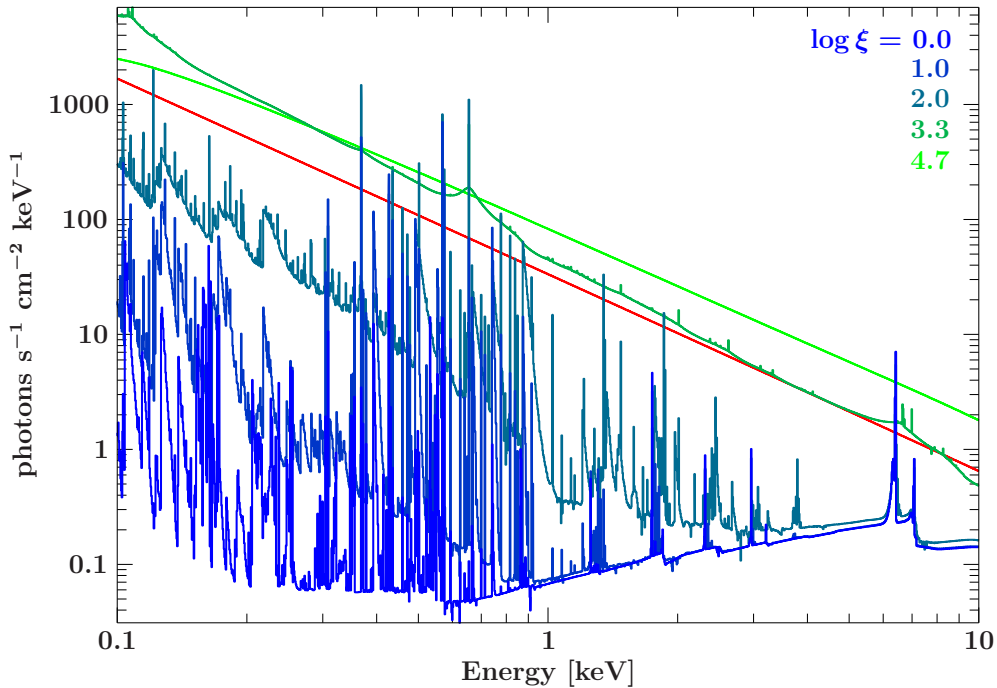


Figure 3.9: Reflected spectra off an ionized accretion disk with different ionization stages as described by the ionization parameter,  $\log \xi$ , calculated using the `xillver` model. The incident spectrum, a powerlaw with photon index  $\Gamma = 1.7$  and a rolloff at 300 keV is shown in red. The abundance of iron is set to the solar value and the disk is viewed under an inclination of  $30^\circ$ .

ionization from neutral ( $\log \xi = 0$ ) to heavily ionized with  $\log \xi = 4.7$  which is the highest available value for the model. In the completely neutral case the spectrum is identical to the one shown in Fig. 3.7 but this plot has been extended to energies one magnitude lower to show the forest of absorption and fluorescence emission lines caused by a variety of different elements in the accretion disk. As the ionization increases the intensity of the reflected spectrum increases as well and the strength of the spectral lines goes back while their width grows. In the heavily ionized cases the lines vanish almost completely and the reflected spectrum mostly resembles the incident one. The effect of ionization is nicely illustrated by the distortion and change in flux of the Fe  $K\alpha$  line at 6.4 keV and the accompanying absorption edge next to the also visible Fe  $K\beta$  line.

### 3.5 The Lamp-post Model

Even when taking all the effects mentioned in the previous sections such as thermal emission, Comptonization and ionized reflection into account still effects can be observed in the spectra of AGN which cannot be explained. One of the most striking examples is the shape of the Fe  $K\alpha$  emission line. Fig. 3.10 shows how this spectral feature is smeared across multiple keV. The data shown in this plot were obtained by a 325 ks observation with *XMM-Newton* (Fabian et al., 2002b) and a 347 ks observation with *Suzaku* (Reeves et al., 2006; Miniutti et al., 2007). To make the profile of the line visible a foreground-absorbed powerlaw was fitted as a continuum model below the line energy from 3 to 4 keV and above from 7.5 to 12 keV. The spectrum was then divided by the resulting powerlaw with a photon index of  $\Gamma = 2.0$ . The peak energy of the line is still located at the 6.4 keV, but it also has a red wing extending to roughly 3.5 keV and a smaller blue wing up to  $\simeq 7$  keV. This shape can be explained by taking the relativistic effects in the extreme environment in the vicinity of the SMBH into account. When the Comptonized radiation is emitted by the X-ray corona its trajectory and energy is subject to the influence of distorted spacetime caused by the mass and rotation of the SMBH as explained in Section 3.1. Additionally, the reflecting matter of the accretion disk is moving

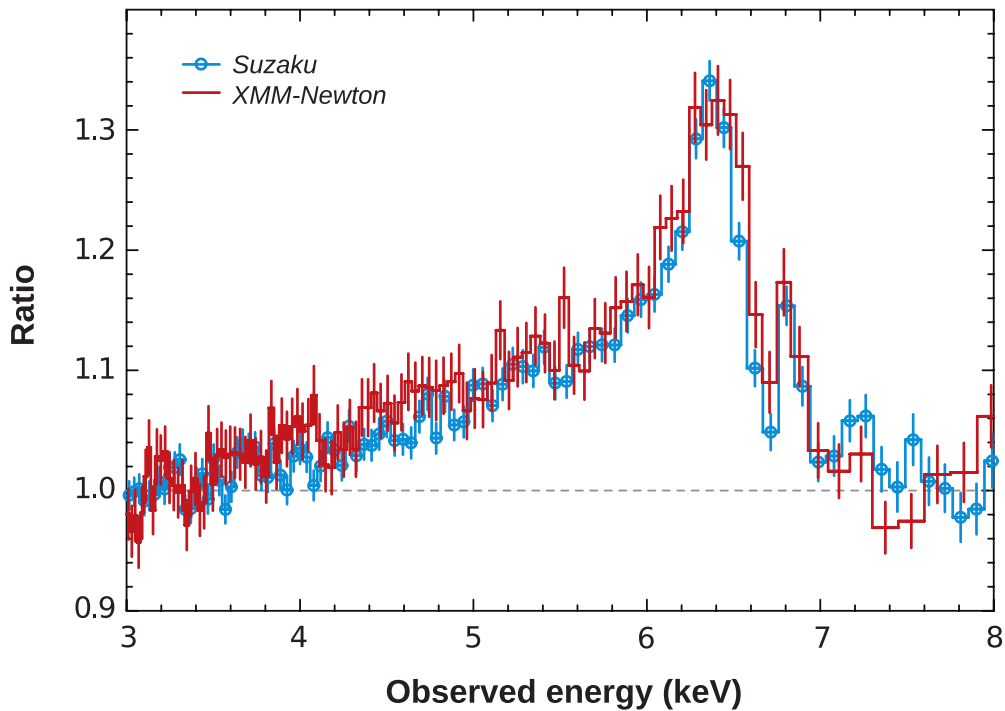


Figure 3.10: Relativistic profile of the Fe  $K\alpha$  emission line from MCG-6-30-15 as observed by *X-ray Multi-Mirror Mission* (XMM-Newton) and *Suzaku*. For this figure the continuum below the line from 3 to 4 keV and above it from 7.5 to 12 keV was fitted with a powerlaw subject to galactic foreground absorption and the data were divided by it. Taken from Miller (2007) who adopted it from Reeves et al. (2006) and Miniutti et al. (2007)

with relativistic velocities which causes an additional shift in energy of the reflected component.

### 3.5.1 Geometry

To properly account for these effects it is important to consider the path of the photons in this environment which is determined by the location of emission and the geometry of spacetime given by the mass and spin of the central black hole. Shakura & Sunyaev (1973a) already suggested that the thermal photons coming from the accretion disk are up-scattered by hot, evaporated material from the disk located above and below it. This idea was further pursued and elaborated on by for example Haardt (1993) and Dove et al. (1997). The profile of the Fe  $K\alpha$  line can be used to test this hypothesis. It is influenced by the intensity distribution of the radiation reflected by the disk. When assuming a standard  $\alpha$ -disk and that the intensity hitting the disk from the corona is directly proportional to the intensity of the thermal radiation, then according to equation 3.98 this *emissivity profile* should also follow the relation

$$I(r) \propto r^{-3} \quad (3.123)$$

However, high resolution spectroscopy of the Fe  $K\alpha$  line from a variety of AGN, for example MCG-6-30-15 (Wilms et al., 2001; Fabian et al., 2002b; Brenneman & Reynolds, 2006), 1H 0707-495 (Fabian et al., 2004; Zoghbi et al., 2010; Dauser et al., 2012), IRAS13224-3809 (Ponti et al., 2010), NGC 7383 (Brenneman et al., 2011), and Mrk 79 (Gallo et al., 2011), indicate that this profile is much steeper than predicted by an X-ray corona located at the surface of the accretion disk.

An alternative location for the primary X-ray source is above the rotational axis of the black hole from where it irradiates the disk (Martocchia & Matt, 1996). Because of the similarity of the corona to a lamp, illuminating the accretion disk similar to a street, this geometry is called the *lamp-post geometry*. In Fig 3.11

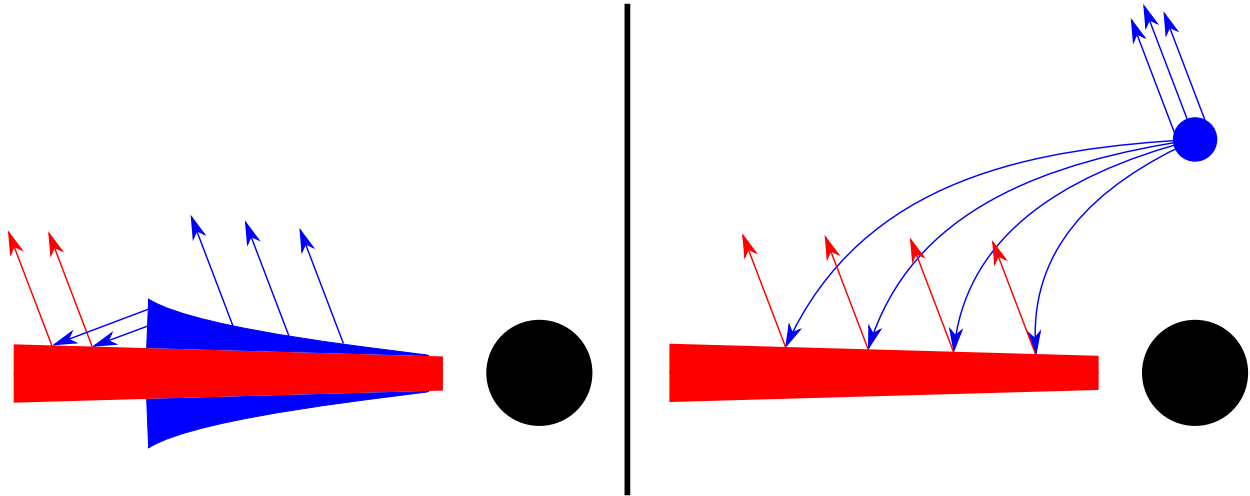


Figure 3.11: Two different geometries for the X-ray corona. **Left:** Classical corona at the surface of the accretion disk. **Right:** The corona as a compact source above the black hole on its rotational axis. In both cases the corona (blue) emits the primary radiation of which a part goes directly in the direction to the observer, indicated by the blue arrows towards the upper left-hand side. Another portion of the primary radiation hits the accretion disk (red) and is reflected. Part of this reflected component also travels towards the observer, indicated by the red arrows. In the lamp-post case the photon trajectories are curved to illustrate the relativistic effects caused by the black hole.

a comparison between the classical corona located on the accretion disk and the lamp-post model is shown. In the classical case the photons are up-scattered by the blue corona from which a portion of the resulting powerlaw spectrum travels directly towards the observer. The emissivity profile in this case is expected to correspond to the above-mentioned  $I \propto r^{-3}$  relation. In the lamp-post case the compact source above the black hole on its rotational axis also generates a powerlaw spectrum from which a fraction goes directly to the observer. Another fraction of the photons travels to the bottom towards the accretion disk and is influenced by the curved spacetime around the black hole. As will be outlined in the next section the resulting emissivity profile is much steeper and a variety of other relativistic effects are imprinted onto the resulting spectrum.

### 3.5.2 Models considering Relativistic Effects

In order to predict resulting spectra for radiation emitted in and passing through the relativistic environment several models have been developed in the past. Fabian et al. (1989) developed an analytical model named `diskline` to describe the observed line profile in spectra of Cyg X-1. It does not consider the rotation of the central black hole but different emissivity profiles, inner and outer radii of the relativistic accretion disk and the inclination of the disk to the line of sight towards the observer.

The now called `laor` model by Laor (1991) was the first one able to calculate the shape of emission lines under the influence of a maximally spinning black hole, but this model cannot be used to test for slower rotating black holes using observed Fe  $K\alpha$  lines. It was however able to provide theoretical spectra for different emissivity profiles by varying the exponent of this powerlaw distribution, different inner and outer radii of the accretion disk and inclinations of the observer towards the surface of the disk while also accounting for the effect of limb-darkening (George & Fabian, 1991). Because of its age the number of pre-calculated spectra limits the applications of this model in the modern age (Dauser, 2010).

A subsequent model named `kyrline` was developed by Dovčiak et al. (2004) and provides a much finer grid of pre-calculated spectra for two different limb-darkening laws, the same assumed by Laor (1991) and another one by Haardt (1993). `kyrline` can calculate the emission line profile for a black hole with an arbitrary angular momentum and again for different inclinations and inner and outer disk radii. The

### 3 Active Galactic Nuclei

emissivity profile is given by a broken powerlaw with two different indices changing from one to the other at an also changeable radius.

All the above-mentioned models can only consider prograde motion of the accretion disk with respect to the spin of the black hole. To also include the retrograde case, and improve upon several other aspects, Dauser et al. (2010) implemented the `relline` model. It can take arbitrary emissivity profiles and limb-darkening into account while not relying on a large sample of pre-computed spectra, especially compared to the `kyrline` model. The model parameters are essentially the same as for the `kyrline` model but different limb-darkening laws are available. As an extension, the `relline_lp` model was created by Dauser et al. (2013) which is capable of carrying out the calculation of the observed spectrum for a stationary and moving lamp-post source by assuming a primary powerlaw emitter with a photon index and the height above the black hole as additional parameters. From this constellation the emissivity profile onto the accretion disk can be directly calculated in a self-consistent way, eliminating the artificial broken powerlaw of the previous models.

The `kyrline` and `relline` models also provide the possibility to convolve another arbitrary model spectrum to obtain the resulting observed spectrum with the imprinted effects of the relativistic environment. In this mechanism only the average of the intensity over each solid angle is considered. This problem was addressed by García et al. (2014) by implementing the angle-dependent emission calculated by the `xillver` model (compare Section 3.4) directly into the ray tracing capabilities of the `relline` model. The resulting model is named `relxill`<sup>5</sup>. In the classical corona configuration the model assumes an incident powerlaw with exponential rolloff (the powerlaw index and energy of the rolloff are model parameters) and calculates the angle-dependent reflection off the accretion disk while properly handling the relativistic light bending of the photon trajectories. García et al. (2014) emphasize that this yields a different result than a convolution of a spectrum generated by `xillver` through `relconv`, the convolutional model of the `relline` family. The `relxill` model then also incorporates the ionization parameter,  $\log \xi$ , and the iron abundance,  $A_{\text{Fe}}$ , of the accretion disk from the `xillver` model. The reflection fraction,  $f_{\text{refl}}$ , as another model parameter gives the strength of the reflected component and is defined as the fraction of photons emitted towards the accretion disk and towards the observer in the frame of the primary source (Dauser et al., 2016a). As explained by García et al. (2014) comparisons, with the previous models indicate that these may have overestimated the iron abundance by up to a factor of two.

Another variety of the `relxill` model, named `relxill_lp`, performs the calculation of the resulting spectrum under the lamp-post geometry as described by Dauser et al. (2013). The lamp-post model is especially attractive because it is capable of predicting the reflection fraction directly from the given geometry of the source (Dauser et al., 2014) which is also true for the emissivity profile. In this way a more consistent way of modelling the observed spectrum with less empirical parameters is possible. To summarize, a list of all parameters of the `relxill_lp` model is given in the following:

- `norm`: Normalization of the total flux
- `h`: Height of the compact source above the black hole, lamp-post height in short
- `a`: Dimensionless spin parameter from -0.998 (maximal retrograde rotation) to 0.998 (maximal prograde rotation)
- `$\theta$` : Inclination of the accretion disk with respect to the line of sight towards the observer
- `$R_{\text{in}}$` : Inner radius of the accretion disk
- `$R_{\text{out}}$` : Outer radius of the accretion disk
- `$\Gamma$` : Photon index of the incident powerlaw
- `$E_{\text{cut}}$` : Energy of the exponential rolloff of the incident powerlaw
- `$z$` : Cosmological redshift of the source
- `$\log \xi$` : Ionization parameter (compare Section 3.4)

<sup>5</sup>Available for download at [www.sternwarte.uni-erlangen.de/research/relxill/](http://www.sternwarte.uni-erlangen.de/research/relxill/)

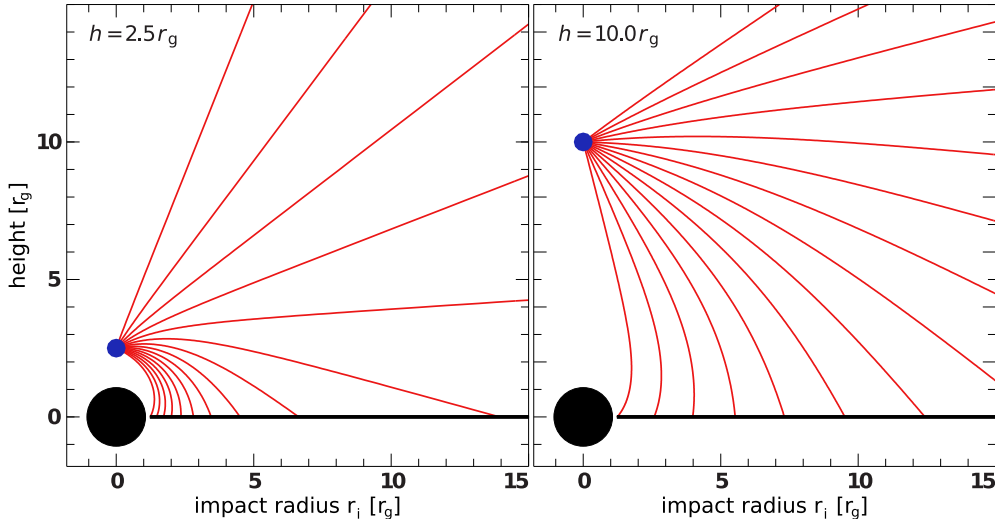


Figure 3.12: Illustration of the trajectories of photons emitted from a compact lamp-post source above a maximally prograde spinning black hole ( $a = 0.998$ ) for two different lamp-post heights,  $h$ , towards the accretion disk. Note that the distribution of photons hitting the disk is significantly influenced by the gravity of the central black hole. The effect is much more pronounced for a primary source closer to the black hole. Taken from Dauser (2010).

- $A_{\text{Fe}}$ : Abundance of iron in the accretion disk, given in solar values
- $f_{\text{reff}}$ : Reflection fraction as defined above

### 3.5.3 Manifestation of Relativistic Effects

The relativistic effects imprinted on the spectrum seen by the observer, after being reflected off an accretion disk and propagating through curved spacetime, is extensively discussed by Dauser (2010) and Dauser (2014). Based on these publications I will give an overview of the most important aspects regarding the lamp-post geometry.

Fig. 3.12 illustrates the effect of the gravitational pull on the trajectories of the photons emitted by the lamp-post source. Their path is bent towards the black hole which results in a more concentrated distribution of photons near the inner edge of the accretion disk, thus a much steeper emissivity profile is naturally created. This effect becomes very pronounced for low lamp-post heights. When the photons travel towards the observer they also have to leave this potential well which causes a decrease in their energy due to gravitational redshift. In Fig. 3.13 the apparent image of the accretion disk and the energy shift of the photons travelling from each location to the observer is depicted. This shift is not only caused by the gravitational redshift but also by the relativistic Doppler effect. It causes an energy increase of the photons from the left side of the disk, which is moving towards the observer, and an additional decrease for the photons on the right side, moving away.

In the calculated spectrum the changes of parameters manifest themselves most prominently in the shape of Fe  $K\alpha$  emission line around 6.4 keV. Fig. 3.14 shows this effect for changes to the lamp-post height,  $h$ , and the spin of the black hole,  $a$ . The closer the source is to the black hole and the faster the black hole is spinning in prograde motion the stronger the distortion of the line is. For the spin this can be mainly explained by the influence of  $a$  on the ISCO of particles in the accretion disk. For higher values of  $a$  the inner edge of the disk is much closer to the black hole and therefore the contribution to the overall spectrum from this area more affected by the gravitational effects is larger. In case of the lamp-post height being closer to the black hole the emissivity profile is much steeper as depicted in Fig. 3.12, thus also the contribution of radiation from this inner area is higher. In the extreme case of  $a$  being close to the maximal value and  $h$  being very low the resulting shape can hardly still be called an emission *line*. On its blue side it decreases

### 3 Active Galactic Nuclei

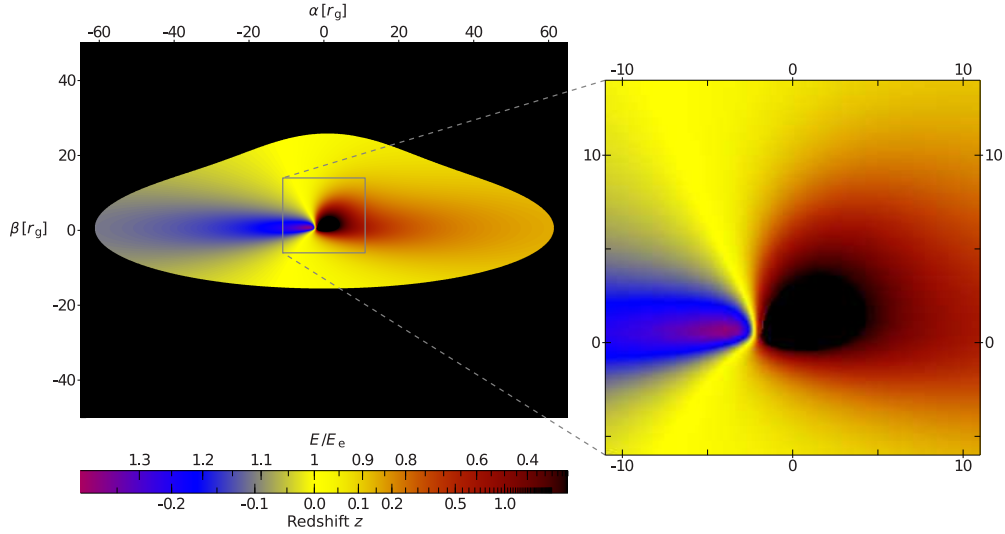


Figure 3.13: Color coded map of the energy shift of photons reaching the observer from an accretion disk viewed under an inclination of  $\theta = 75^\circ$  from above. The coordinates are chosen to be perpendicular to the line of sight. The accretion disk behind the black hole at the center appears to be lifted upwards due to the bending of light from behind it towards the observer. On the left the accretion disk is moving towards the observer, generating blue-shifted photons, on the right it is moving away, thus creating red-shifted photons. Taken from Dauser (2014).

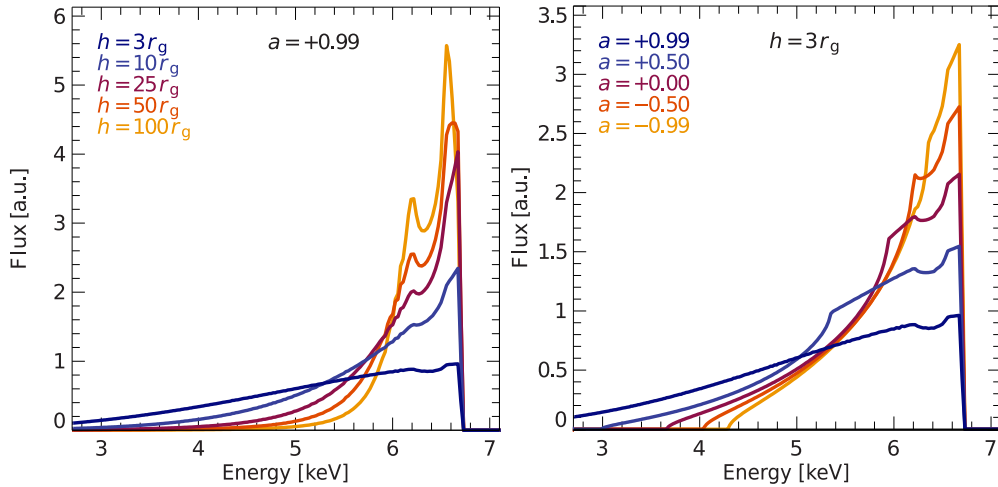


Figure 3.14: **Left:** Influence of the lamp-post height,  $h$ , on the shape of the Fe  $K\alpha$  emission line. The black hole is assumed to be spinning with  $a = 0.99$ , so close to the theoretically highest possible value. The closer the source gets to the black hole, the more the emission line is distorted. **Right:** The shape of the emission line is influenced by the spin of the black hole. In this case the lamp-post height is set to three gravitational radii. For retrograde motion ( $a < 0$ ) the distortion is minimal while for maximal prograde motion the line is distorted the most. In all cases the inclination is set to  $\theta = 30^\circ$  and the inner orbit is given by the ISCO. As can be seen, in most cases the emission line has a large wing towards lower energies and a much sharper boundary towards higher energies. Taken from Dauser et al. (2013).

rapidly while on the other side having a red wing at lower energies which can be recognized even below 3 keV. Another characteristic feature which is most pronounced for large lamp-post height and rapid spin is the double horned shape of the line. It is most prominent in this parameter configuration because the large

### 3.5 *The Lamp-post Model*

lamp-post height causes a gentle emissivity profile on the disk which reaches close to the central black hole.



# 4 X-ray Astronomy

## 4.1 Detecting and Measuring X-rays

In a sense optical light is extraordinarily suited for astronomical observations. Apart from deviations caused by atmospheric seeing and effects emerging in the modern age such as light pollution and bright satellites optical light from astronomical objects can be captured with traditional ground based telescopes employing mirrors or lenses. Photons of the X-ray regime, however, are much more challenging to observe. Not only are traditional telescopes employing large primary mirrors unable to reflect X-ray photons but these photons also do not reach the surface of the Earth in the first place. In the following these challenges and the techniques to circumvent them will be discussed.

### 4.1.1 The Need to go to Space

As described in the previous sections, X-ray observations were started using rocket and balloon experiments evolving into spacecraft carrying sophisticated measurement devices. To understand why observational X-ray astronomy must be carried out in space a very simple model of the interaction of X-rays with an atmosphere based on planet Earth will be considered. The atmosphere is for simplicity assumed to consist of 79% molecular nitrogen and 21% molecular oxygen gas. Assuming an ideal gas the pressure  $P$  at an altitude  $z$  can be calculated as

$$P(z) = P_0 \cdot e^{-z/H} \quad (4.1)$$

where  $P_0$  is the pressure at altitude 0 km and  $H$  is the scale height which is determined by the gravitational acceleration,  $g$ , and the temperature,  $T$ , as

$$H = \frac{R \cdot T}{M \cdot g} \quad (4.2)$$

with the ideal gas constant,  $R$ , and the mean molar mass,  $M$ , of the involved particles (Léna et al., 1998).

To express the attenuation of a beam of X-ray photons with an initial intensity,  $I_0$ , in a certain material the absorbed power,  $dI$ , can be specified as

$$dI = -I\mu dx \quad (4.3)$$

where  $\mu$  is called the attenuation coefficient. The solution to this problem is an exponential decay of the intensity with the travelled distance,

$$I(x) = I_0 \cdot e^{-\mu x} \quad (4.4)$$

When ignoring scattering the attenuation coefficient  $\mu$  is identical to the absorption coefficient which depends on the particle density,  $n$ , and their corresponding absorption cross-sections,  $\sigma$ ,

$$\mu = n \cdot \sigma \quad (4.5)$$

which can be used to express the remaining intensity,  $I(x)$ , as

$$I(x) = I_0 \cdot e^{-\mu x} = I_0 \cdot e^{-\alpha/\rho \rho x} = I_0 \cdot e^{-\kappa \rho x} \quad (4.6)$$

where  $\rho$  is the mass density and therefore  $\rho \cdot x$  gives the total amount of mass penetrated by the radiation.

## 4 X-ray Astronomy

$\kappa$  is called the mass absorption coefficient (Demtröder, 2009b).

Because the atmosphere is assumed to be an ideal gas the ideal gas equation can be used to calculate the density to

$$\rho = P \cdot \frac{M}{R \cdot T} \quad (4.7)$$

Equation 4.1 can be used to retrieve the pressure at a given height,  $z$  (Demtröder, 2009b), therefore the density at this height is

$$\rho(z) = P_0 \cdot e^{-z/H} \cdot \frac{M}{R \cdot T} \quad (4.8)$$

The relative amount of radiation,  $I/I_0$ , which can pass unabsorbed through a vertical layer of atmosphere of thickness  $\Delta z$  can thus be calculated as

$$\frac{I}{I_0} = e^{-\kappa \rho \Delta z} = \exp\left(-\kappa \cdot P_0 \cdot e^{-z/H} \cdot \frac{M}{R \cdot T} \cdot \rho \cdot \Delta z\right) \quad (4.9)$$

The molar mass can be calculated with Avogadro's number,  $N_A$ , and the particle mass,  $m$ ,

$$M = N_A \cdot m \quad (4.10)$$

For simplicity the mass of the electrons will be ignored and the protons and neutrons are considered to have the same mass of  $m_p = 1.67 \times 10^{-27}$  kg while Avogadro's number is taken as  $N_A = 6.022 \times 10^{23}$  (Particle Data Group et al., 2020). The molar mass of oxygen then is 0.032 kg/mol and that of nitrogen is 0.024 kg/mol. Taking the fractions of both gases, the combined molar mass is 0.02568 kg/mol. The pressure on ground is assumed to be 101300 Pa and the temperature 250 K which results in a scale height of 7178 m. National Institutes of Standards and Technology (NIST)<sup>1</sup> provides the values for the mass absorption coefficients at 1 keV of oxygen as  $459.0 \text{ m}^2/\text{kg}^2$  and of nitrogen as  $331.1 \text{ m}^2/\text{kg}^3$ . As a combined value for the entire gas the arithmetic mean of both values weighted with their contributions is taken as  $357.959 \text{ m}^2/\text{kg}$ .

Starting at a height of 200 km the relative amount of radiation at 1 keV penetrating layers of thickness  $\Delta z = 100$  m can be calculated. The result is shown in Fig. 4.1. Initially, up to around 150 km, the attenuation does not affect the intensity very heavily, but directly below the remaining radiation drops rapidly until at around 90 km almost no intensity remains.

This shows that X-ray observations have to be carried out above an altitude of at least 150 km to provide enough flux of the astrophysical sources reaching the instruments. In Fig. 4.1 also the altitude where the optical depth, defined as  $\ln(I_0/I)$ , reaches one is marked with a dashed line. Materials having such an optical depth for a specific wavelength of light are considered opaque. This also demonstrates that the atmosphere is opaque to X-rays which is one of the aspects making the development of life on Earth possible.

With increasing photon energy  $\kappa$  decreases which results in less atmospheric absorption. Thus, in the hard X-ray regime above 10 keV balloon experiments which can reach altitudes of  $\sim 50$  km can be used to provide enough flux of astrophysical sources to the detectors. Much higher altitudes can be reached by sounding rockets such as the one used by Giacconi et al. (1962). They operate above 100 km up to roughly 500 km and can enable observations of softer X-ray photons. Both methods provide only very temporary observations of at most weeks for balloons and only below 1 h for sounding rockets. To provide enough time above the Earth's atmosphere to do a survey of the entire sky in X-rays such as the one by *eROSITA*, the only option is to use a spacecraft which can operate for multiple years in outer space.

### 4.1.2 Focusing High-Energy Photons

When performing observations of the sky it is crucial to identify the location where the observed radiation is emerging from. Over time several technologies to accomplish this have been developed. In the case of

<sup>1</sup><https://www.nist.gov/pml>

<sup>2</sup><https://physics.nist.gov/PhysRefData/XrayMassCoef/ElemTab/z08.html>

<sup>3</sup><https://physics.nist.gov/PhysRefData/XrayMassCoef/ElemTab/z07.html>

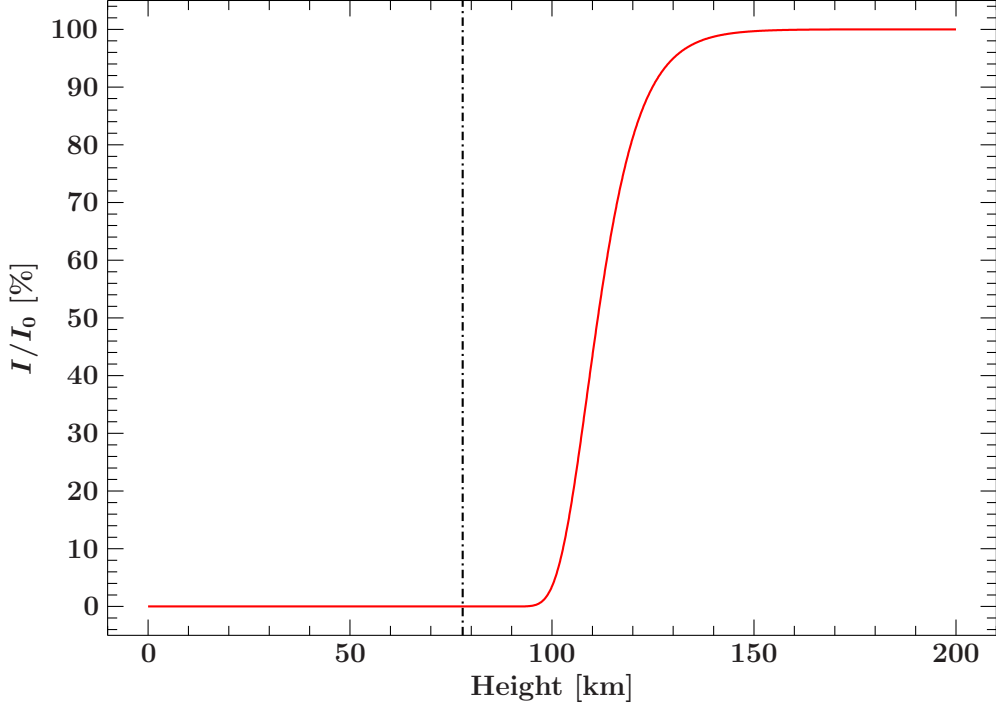


Figure 4.1: Amount of radiation not absorbed by an atmosphere of 79% nitrogen and 21% oxygen gas based on the planet Earth at 1 keV and 250 K depending on height above the ground. The dashed-dotted line marks where the optical depth reaches 1 at 77.9 km.

high energy photons from the X-ray regime and above this task proves to be more difficult than for example for optical light in which case traditional telescopes with mirrors or lenses can be used to create an image in the focal plane. These optical elements are mostly placed almost perpendicular to the path of the light falling into the system. While lenses work based on refraction when the light enters the glass, mirrors use the phenomenon of reflection. In this case the path of the photon after the reflection is solely determined by the angle of incidence. This angle with respect to the normal of the reflecting surface is identical before and after the reflection but on opposite sides of the normal.

To show how this mechanism works and how this applies to X-rays I will follow the exploration of this aspect from Demtröder (2009a), starting with Maxwell's equations describing the behavior of electric and magnetic fields. In matter these equations take the form

$$\vec{\nabla} \times \vec{E} = -\frac{\partial \vec{B}}{\partial t} \quad (4.11)$$

$$\vec{\nabla} \times \vec{H} = \vec{j} + \frac{\partial \vec{D}}{\partial t} \quad (4.12)$$

$$\vec{\nabla} \cdot \vec{D} = \rho \quad (4.13)$$

$$\vec{\nabla} \cdot \vec{B} = 0 \quad (4.14)$$

where  $\vec{E}$  and  $\vec{B}$  are the electric and magnetic fields, respectively. The displacement field,  $\vec{D} = \epsilon_0 \vec{E} + \vec{P}$ , considers also the dipole moment,  $\vec{P}$ , as a response of the penetrated material and the magnetizing field,  $\vec{H} = (\vec{B} + \vec{M})/\mu_0$ , includes the response in form of the magnetization vector,  $\vec{M}$ .  $\epsilon_0$  and  $\mu_0$  are the permittivity and permeability of vacuum, respectively.  $\vec{j}$  is the current density and  $\rho$  the charge density. Assuming that the responses of the material to penetration by the electric field is linear with the electric susceptibility,  $\chi$ , it can be written as  $\vec{D} = \epsilon_0(1 + \chi)\vec{E} = \epsilon\vec{E}$ , where  $\epsilon = \epsilon_0\epsilon_r$  is the total permittivity with

#### 4 X-ray Astronomy

the relative permittivity,  $\epsilon_r = 1 + \chi$ . The same can be done with  $\vec{B}$  and  $\vec{H}$  to obtain  $\vec{B} = \mu_0\mu_r\vec{H}$ . Assuming a non-conducting material it holds that  $\vec{j} = 0$  which delivers the wave equation

$$\Delta\vec{E} = \frac{1}{v^2} \frac{\partial^2\vec{E}}{\partial t^2} \quad (4.15)$$

in which  $\Delta$  denotes the Laplace operator,  $\Delta = \vec{\nabla}^2$ , and  $v = 1/\sqrt{\epsilon_r\epsilon_0\mu_r\mu_0}$  is the speed of light in the material. Considering that  $c = 1/\sqrt{\epsilon_0\mu_0}$  it follows that  $v = c/\sqrt{\epsilon_r\mu_r}$  and with  $v = c/n$  and the assumption that the material is not magnetic, i.e.,  $\mu_r = 1$ ,

$$n = \sqrt{\epsilon_r} \quad (4.16)$$

In case of a wave travelling in  $z$ -direction the amplitude in  $x$ -direction given as a solution of the wave equation is

$$E_x(z, t) = E_0 \cdot e^{i(\omega t - kz)} \quad (4.17)$$

With such a wave travelling through a non-conductive material, which has a linear electric susceptibility, the polarization can be calculated as

$$P_x(z, t) = N \cdot \alpha \cdot E_x = N \cdot \alpha \cdot E_0 \cdot e^{i(\omega t - kz)} \quad (4.18)$$

With the volume density of induced dipoles,  $N$ , and their polarizability,  $\alpha$ . Inserting this relation into the wave equation yields

$$-k^2 E_x = -\frac{\omega^2}{c^2} E_x - \frac{\omega^2 N \alpha}{\epsilon_0 c^2} E_x \quad (4.19)$$

and therefore finally

$$n^2 = 1 + \frac{N \alpha}{\epsilon_0} \quad (4.20)$$

for the refractive index of the material. Treating the electrons in the material as dampened harmonic oscillators, the electric dipole moment,  $p$ , of these electrons can be expressed as

$$p = \frac{e^2 E}{m(\omega_0^2 - \omega^2 + i\gamma\omega)} \quad (4.21)$$

With  $p = \alpha(\omega) \cdot E$  this becomes

$$\alpha = \frac{e^2}{m(\omega_0^2 - \omega^2 + i\gamma\omega)} \quad (4.22)$$

with which the refractive index can be calculated as

$$n^2 = 1 + \frac{e^2 N}{\epsilon_0 m(\omega_0^2 - \omega^2 + i\gamma\omega)} \quad (4.23)$$

In case of conducting material, i.e.,  $\vec{j} = \sigma \cdot \vec{E} \neq 0$ , the wave equation has an additional term containing the conductivity,  $\sigma$ ,

$$\Delta\vec{E} = \frac{1}{v^2} \frac{\partial^2\vec{E}}{\partial t^2} + \mu_r\mu_0\sigma \frac{\partial\vec{E}}{\partial t} \quad (4.24)$$

A solution for propagation in  $z$ -direction is given by a dampened wave of the form

$$E(z, t) = E_0 e^{-\alpha/2z} e^{i(\omega t - kz)} \quad (4.25)$$

where  $E_0$  is the amplitude,  $\alpha$  the absorption coefficient,  $k$  the wave vector and  $\omega$  the frequency. In case of conducting materials (for example the surface of a mirror) and high frequencies free charge carriers in form of electrons in the metal contribute the major part to the refractive index. In this case the restoring force of these electrons in the electron gas can be considered zero, thus taking  $\omega_0 = 0$  one obtains for the refractive index

$$n^2 = 1 - \frac{Ne^2}{\epsilon_0 m \omega^2 - i\gamma\omega} \quad (4.26)$$

The frequency of the oscillation of the electrons with a particle density,  $N$ , is called *plasma frequency*,  $\omega_p$ , and is defined as

$$\omega_p = \sqrt{\frac{ZNq^2}{\epsilon_0 m}} \quad (4.27)$$

where  $Z$  denotes the atomic number (Jackson, 2014). Using this relation the following expression is obtained for  $n$

$$n^2 = 1 - \frac{\omega_p^2}{\omega^2 - i\gamma\omega} = 1 - \frac{\omega_p^2}{\omega^2 \left(1 - \frac{i}{\omega\tau}\right)} \quad (4.28)$$

where  $\tau = 1/\gamma$  is the mean time between two interactions.

The complex refractive index is  $n = n_r + i\kappa$  for which it can be identified that

$$n_r^2 - \kappa^2 = \frac{1 + \tau^2 (\omega^2 - \omega_p^2)}{1 + \omega^2 \tau^2} \quad (4.29)$$

$$2n_r \kappa = \frac{\omega_p^2 \tau}{\omega(1 + \omega^2 \tau^2)} \quad (4.30)$$

For the electrons the equation of motion is assumed to be dampened without a restoring force but under the influence of a periodic electric field. The ansatz  $\vec{v} = \vec{v}_0 e^{-i\omega t}$  gives

$$\vec{v}_0 = \frac{e\vec{E}_0}{m} \frac{1}{\gamma - i\omega} \quad (4.31)$$

The mean current density can be written as  $\vec{j} = \sigma \vec{E} = Nev_0$  from which the electrical conductivity can be obtained as

$$\sigma = \frac{Ne^2}{m} \frac{\tau}{1 - i\omega\tau} = \epsilon_0 \omega_p^2 \frac{\tau(1 + i\omega\tau)}{1 + \omega^2 \tau^2} \quad (4.32)$$

Comparing this to the complex refractive index one can see that

$$n_r^2 - \kappa^2 = 1 - \frac{\text{Re}(\sigma)}{\frac{\epsilon_0}{\tau}} \quad (4.33)$$

$$2n_r \kappa = \frac{\text{Im}(\sigma)}{\epsilon_0 \omega^2 \tau} \quad (4.34)$$

X-ray photons can be considered having a high energy and therefore a high frequency. An approximation

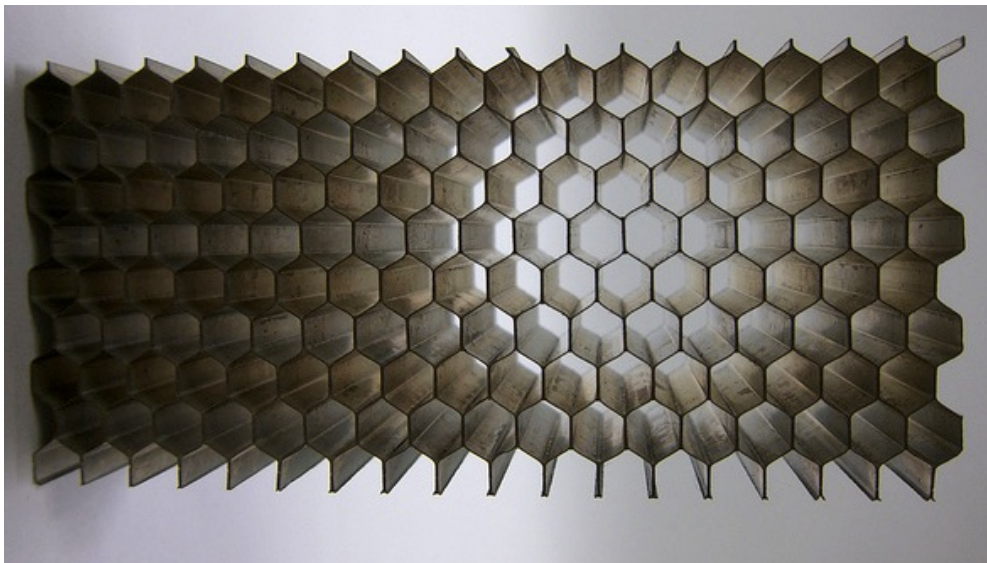


Figure 4.2: A collimator made of hexagonal tubes developed for Rossi X-ray Timing Explorer (*RXTE*) (C. B. Markwardt, N. Shaposhnikov, HEASARC<sup>4</sup>)

can therefore be made with  $\omega_p \tau > \omega \tau \gg 1$ ,

$$\sigma \simeq i\epsilon_0 \frac{\omega_p^2}{\omega} \quad (4.35)$$

Together with equation 4.28 this yields

$$n^2 = 1 - \frac{\omega_p^2}{\omega^2} \quad (4.36)$$

which has some important consequences. In case the frequency of the incoming photon is smaller than the plasma frequency, i.e.,  $\omega < \omega_p$ , it is  $n^2 < 0$  and therefore  $n = n_r + i\kappa$  is fully imaginary which means in particular  $n_r = 0$ , thus, apart from an evanescent part of the wave which penetrates the material to a certain depth, the incoming wave is totally reflected. This is the case for optical light on a metallic surface, for example a mirror of a telescope with an evaporated layer of metal. If, however, the frequency of the incoming light is higher than the plasma frequency ( $\omega > \omega_p$ ) the refractive index,  $n$ , becomes real, or in other words, the medium is transparent to this wavelength of light, no reflection occurs. The primary mirror of the *HST* for example is coated with a 65 nm thick layer of aluminum (Robberto et al., 2000) which has a measured plasma frequency of  $3.63 \times 10^{15}$  PHz corresponding to a photon energy of 15 eV (Langley et al., 2009). This energy lies scarcely above the UV regime in the very soft X-rays. All harder radiation, being the entirety of X-rays and gamma-rays, are not reflected by the material rendering this technology useless for the application in X-ray telescopes.

### Collimators

The explained non-reflexibility of X-rays can also be used to recover spatial information of incident radiation by restricting the opening angle from a detector towards the sky. The intensity,  $I$ , of a beam of light, X-ray photons in this case, is decaying exponentially with distance,  $x$ , when entering a material. The absorption coefficient,  $\mu$ , of the material determines the exact shape of this function,

$$I(x) = I_0 \cdot e^{-\mu x} \quad (4.37)$$

<sup>4</sup><https://heasarc.gsfc.nasa.gov/docs/xte/pca/doc/rmf/pca-arf-2011/>

where  $I_0$  denotes the intensity of the incident beam. So to absorb the X-rays as quickly as possible a material with a high absorption coefficient should be chosen. Note that in general this value also depends on the energy of the incident radiation. For high energy radiation, such as X-rays and gamma-rays, heavy metals proved to provide the highest absorption coefficients. However, for the usage on spacecrafts low mass is of importance. For this reason lighter metals are used. The Proportional Counter Array (PCA) onboard *RXTE* for example uses an alloy made of beryllium and copper to form a so called *collimator* (Jahoda et al., 1996) (compare Fig. 4.2). With different designs used for other detectors, the purpose of collimators is to provide a narrow angle in front of the instrument under which incident radiation can reach the detector. Photons arriving from angles outside this window are absorbed by the metallic walls of the collimator. Because of the non-zero size of the detector below the collimator usually not a single large opening is used, but the collimator is split up into a multitude of tubes. To not waste any space an efficient honeycomb pattern of hexagonal tubes is often preferred, for example for the PCA in which case the walls of the tubes are 0.069 mm thick and the distance between opposite sides of one tube is 3.2 cm. The entire collimator is 20 cm high which provides a FOV of  $1^\circ$  full width at half maximum (FWHM) (Jahoda et al., 2006).

### Wolter Optics

Even though collimators ensure that only radiation from a particular region of the sky falls onto the detector, they do not focus the X-rays onto a focal plane to create a real image of the photons projected onto the sky. Another technology can be employed to accomplish this task. Although, as described above, X-ray photons pass through most material when hitting it perpendicularly, total reflection can still occur if the angle of incidence is very small. This is a result of Snell's law which states that when light is refracted at the interface of two materials the product of the refractive indices,  $n_{1/2}$ , and the sine of the respective angles,  $\theta_{1/2}$ , towards the normal of the surface is identical,

$$n_1 \cdot \sin(\theta_1) = n_2 \cdot \sin(\theta_2) \Leftrightarrow \sin(\theta_1) = \frac{n_2}{n_1} \sin(\theta_2) \quad (4.38)$$

From  $\sin(\theta_{1/2}) \leq 1$  it follows that also

$$\sin(\theta_1) \leq \frac{n_2}{n_1} \quad (4.39)$$

If, however, the materials involved provide refractive indices such that under a range of incident angles this relation is not satisfied, then no refraction occurs and all radiation is reflected. For most materials the refractive index is higher for higher densities, thus this effect can occur when light is passing through a more dense medium and hitting the interface towards a less dense medium. In these cases, for example the interface between water and air, this effect is called *total internal reflection* (Demtröder, 2009a). As demonstrated above, the refractive index of a material differs for light of different wavelengths with major influence by the plasma frequency. For X-rays the refractive index of metals is lower than 1, for gold for example  $n = 0.8787$  at 50 eV (Werner et al., 2009). With  $n = 1$  in vacuum, an X-ray photon hitting gold will transition from an area of higher refractive index into one with a lower one. This again enables total reflection but because the photon is not emerging from the denser material but is reflected off it, this process is called *total external reflection*.

From Snell's law the critical angle,  $\theta_{\text{crit}}$ , for total internal/external reflection can be obtained as

$$\sin(\theta_{\text{crit}}) = \frac{n_2}{n_1} \quad (4.40)$$

Expressing the angle not with respect to the normal but with respect to the surface, i.e.,  $\theta_{\text{crit}} \rightarrow \theta_{\text{crit}} + 90^\circ$ , and considering that  $n_1 = 1$  this becomes

$$\cos(\theta_{\text{crit}}) = n_2 \quad (4.41)$$

so the critical angle only depends directly on the refractive index of the reflecting material. With Equa-

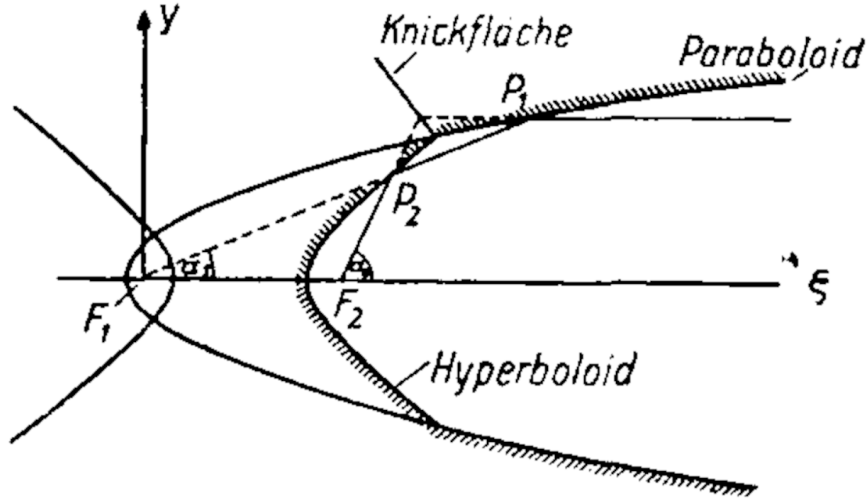


Figure 4.3: Drawing of the Wolter type I mirror design from the original publication by Wolter (1952a). Photons enter from the right and are first reflected by the paraboloid at  $P_1$  towards focus point  $F_1$  and then by the hyperboloid at  $P_2$  towards the final focus point  $P_2$ . The border between the two geometries is labeled “Knickfläche”.

tion 4.36, the fact that  $\omega = 2\pi c/\lambda$  and  $q = -e$  it can be written as

$$n = \sqrt{1 - \frac{NZe^2}{\epsilon_0 m 4\pi^2 c^2} \lambda^2} \simeq 1 - \frac{1}{2} \frac{NZe^2}{\epsilon_0 m 4\pi^2 c^2} \lambda^2 \quad (4.42)$$

so finally

$$\cos(\theta_{\text{crit}}) = n = 1 - \delta \quad (4.43)$$

where  $\delta$  is the second term of equation 4.42. The contribution of  $\delta$  is expected to be much smaller than one, so the Taylor expansion of the cosine can be used to arrive at

$$\theta_{\text{crit}} = \sqrt{2\delta} \quad (4.44)$$

Assuming that the number of neutrons in the cores of the atoms is the same as the number of protons, the density of the material,  $\rho$ , can be introduced as

$$\delta = \frac{1}{2} \frac{\rho e^2}{2m_p \epsilon_0 m 4\pi^2 c^2} \lambda^2 \quad (4.45)$$

Calculating the constants finally yields for the critical angle

$$\theta_{\text{crit}} = 5.6' \left( \frac{\rho}{1 \text{ g cm}^{-3}} \right)^{1/2} \frac{\lambda}{1 \text{ nm}} \quad (4.46)$$

(Wilms, 2017)

With gold, which is used for the mirrors of *eROSITA* and *XMM-Newton*, this angle is roughly  $0.41^\circ$  with respect to the surface and therefore often called *grazing angle*. As with optical telescopes, for example Newtonians, paraboloid mirrors can be used to focus the photons which hit the surface of such a mirror with an angle lower than the grazing angle onto a focal plane. Owing to the shape of the paraboloid this is only given for off-axis radiation and the inner area of the mirror is therefore useless. This effect can be compensated by removing this part of the mirror and inserting another paraboloid as a shell inside

the first mirror followed by subsequent shells of decreasing radii. To decrease the resulting focal length, a second reflecting surface in the shape of a hyperboloid is used and integrated in the same shell as the paraboloid surface which then has a break. This optical design is called *Wolter telescope* after Hans Wolter who developed this system initially for X-ray microscopy (Wolter, 1952a,b). The described design, where both reflections happen towards the inside of the assembly, is called Wolter type I optics but two other ways to arrange the mirrors are possible. In case of Wolter type II optics the light is again reflected off the inside of the paraboloid but then hits the outside of hyperboloid and in the type III case it hits the outside of a paraboloid and then the inside of an ellipsoid. The type I design is most efficient in terms of consumed space and resulting effective area by nesting multiple shells, thus they are the preferred design for X-ray telescopes. In practice the reflective layer is deposited onto a mandrel and then the carrying substrate, for example nickel, is electroformed onto this layer from the outside.

### Coded Aperture Masks

For hard X-ray and gamma-ray photons the grazing angle becomes so small that Wolter mirror assemblies become impractical. In this case a coded aperture mask can be used to recover spatial information. It blocks the incoming light in a known geometric pattern which causes uneven illumination in the focal plane resulting from absorption of photons in the paths blocked by the mask. The material which can be used for the mask has to be chosen according to the targeted wavelength. For the WFC onboard *BeppoSAX*, which operated in the range from 2 to 28 keV, the mask was created from stainless steel (Jager et al., 1997).

### 4.1.3 Detectors for X-rays

After the X-ray photons entering the aperture of the optical system are focused or selected according to the optical system in place, they need to be registered and quantified. During this operation the amount of photons of a given energy and optionally their location on the sensor have to be determined. Several technologies with different characteristics have been developed to accomplish this task and will be discussed.

#### Proportional Counters

Proportional counters use the ionization of gas caused by incident X-rays to measure their energy. A detailed description is given by Knoll (2000). As material in the detector usually a noble gas such as xenon is used because of its low threshold for ionization. When an X-ray photon enters the chamber through a dedicated entrance window it ionizes the gas which leaves positively charged ions and their corresponding negatively charged electrons. One or multiple anodes and cathodes are placed in the chamber, often in the form of wires. Between these an electrical potential is created by an applied voltage in the range from hundreds to thousands of volts. After the incident photon generated ions and electrons they start to drift towards the cathodes and anodes, respectively. During this acceleration the detector gas is further collisionally ionized causing a cascade which forms a plasma discharge. The ions can be in an electrically excited state and emit UV photons upon transitioning to a lower state which increases the duration of the cascades. To absorb these photons additional gas such as  $\text{CH}_4$  is introduced into the chamber. However, under the constant plasma discharges this gas forms free radicals which in turn can cause polymers to form on the anode and cathode wires causing the detector to age.

When the charges are drained through the anodes and cathodes a pulse in voltage can be measured. The height of this pulse is proportional to the number of collected ions and electrons and therefore the energy of the incident photons, hence the name of the device. Depending on the dead time of the detector, that is the time, until the cascade subsides, very high time resolution can be accomplished by proportional counters. This is why they were used as detectors for *RXTE* in form of the PCA which could achieve a time resolution of only  $1 \mu\text{s}$  (Jahoda et al., 1996).

When the voltage of the anode is measured at both ends of a wire which has a substantial amount of resistance the charge is separated between the two points from which the location where on the wire the discharge occurred can be reconstructed, giving also spatial resolution in one dimension. Adding a perpendicular set of wires working with the same principle gives full spatial resolution in for example the focal plane of a Wolter type I telescope. These devices are then called position position sensitive

proportional counters (PSPCs) and were for example used for the *ROentgen SATellite* (*ROSAT*) mission as primary imaging devices (Briel & Pfeffermann, 1986).

### Scintillators

Harder X-rays do not create enough ions and electrons by interacting with the detector material which renders proportional counters useless in this energy range. Alternatively, more dense material can be used, either in the form of highly pressurized gas or solid crystals, for example consisting of NaI. An incident X-ray photon can interact with the contained atoms and cause electron excitation. This electron is still bound by the Coulomb potential of the atom and subsequently transitions to a lower state under the emission of a photon which has much less energy than the initial X-ray photon, for example from the UV or optical regime. This process is called *scintillation* and the detectors are therefore called *scintillators*.

The secondary photons created by the scintillation process can then be registered by a device sensitive to UV or optical light. Often photomultiplier tubes (PMTs) are used for this purpose. The entrance to the PMT is covered by a photocathode from which the low energy photon is absorbed, and a free electron is created via the photoelectric effect. This electron is focused by an electric field onto a dynode which has a positive voltage applied. Upon impact the accelerated electron deposits its energy and more free electrons are created which are then accelerated onto a subsequent dynode with a higher applied voltage. This process is repeated several times until in the end a final anode absorbs the electrons and provides a point to measure the created charge which amplified the initial signal by a factor of  $10^5$  to  $10^7$ .

In this way the energy of the incident high energy X-ray photon can be measured (Knoll, 2000). Scintillators, in combination with PMTs, have for example been used for High Energy X-Ray Timing Experiment (HEXTE) onboard *RXTE* in the energy range from 12 to 250 keV and could achieve a spectral resolution of 15% at 60 keV (Rothschild et al., 1998).

### Microchannel Plate

The fundamental operating principle behind microchannel plates is the same as for PMTs but they do not use individual dynodes. Instead, the wall of the tube is coated with a conducting material to which a gradient of electric potential is applied. An initial photoelectron entering the tube is accelerated towards the wall of the tube and releases more secondary electrons which subsequently are accelerated towards the opposite wall. This process is repeated until the shower of electrons reaches the end of the tube where the signal is amplified by five to six orders of magnitudes.

Assembling hundreds or thousands of these channels with diameters in the range of tens of micrometers yields a *microchannel plate*. Using such a device in combination with a crossed grid charge detector results in a position sensitive measurement device (Knoll, 2000). This design was used for the High Resolution Imagers (HRIs) onboard the *Einstein* (Giacconi et al., 1979) and *ROSAT* (Zombeck et al., 1990) probes.

### Charge Coupled Devices

Semiconductors have a unique property which makes them suitable for X-ray detectors by providing not only moderate spectral resolution but simultaneously good spatial resolution. The property in question is the width of the energy gap between the valence band and the conduction band. For isolators this gap is more than 3 eV wide and for metals it is practically non-existent, but for semiconductors it sits right in between and is very narrow at  $\sim 1$  eV. Silicon for example has a band gap of 1.11 eV and germanium only 0.66 eV (Demtröder, 2009b). This energy is just below the value for optical light. Red light at 700 nm has a photon energy of 1.77 eV and blue light at 400 nm has 3.1 eV. Therefore an electron in the valence band can, upon absorption of an optical photon, gain enough energy to transition to the conduction band. Upon this happening the lack of the electron in the band structure of the atomic lattice in the valence band creates a virtual positively charged particle called an *electron hole* or just *hole*. The transitioned electron, in combination with the resulting hole, is often called the *electron-hole pair*.

For higher photon energies multiple electron-hole pairs can be created, depending on the energy of the

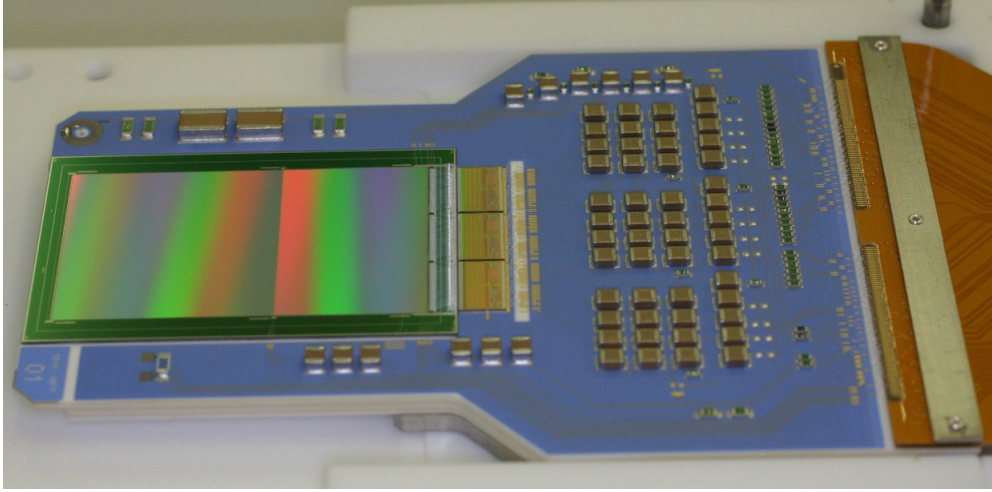


Figure 4.4: Individual Charge-Coupled Device (CCD) assembly for *eROSITA*. The sensor itself is the square area on the left-hand side of the reflecting surface to the left. The remaining rectangular area of this component is the frame store area which is used to hold the accumulated electrons during readout and is shielded from X-rays. The readout electronics is located on the blue printed circuit board and the connection to the remaining electronics system is provided by a rigid flex printed board connection on the right. Taken from Meidinger et al. (2011).

absorbed photon. In an easy model this number can be calculated as

$$N = \frac{E_{\text{ph}}}{E_{\text{gap}}} \quad (4.47)$$

where  $E_{\text{ph}}$  is the energy of the incident photon and  $E_{\text{gap}}$  is the width of the band gap. When X-ray photons around 1 keV hit a silicon crystal about 909 electrons will transition into the conduction band. Measuring this free charge can thus be used as a proxy for the energy of the incident photon, but in regular semiconductors the electrons will immediately recombine with the holes.

To work around this problem the band structure can be manipulated by introducing foreign atoms into the atomic lattice, a process called *doping*. The effect of this manipulation depends on the electron configuration of the introduced atoms. If the additional atoms have an excess of electrons in the outer orbital, compared with the semiconductor itself, additional electrons will enrich the electron gas, thus these atoms are called *donors* and the resulting material is called *n-type semiconductor* because of the increase in negative charge carriers. The opposite can be achieved by introducing *acceptors* which can bind more electrons and create a *p-type semiconductor* with an excess of positive charge carriers in the form of holes.

In case of a p-type semiconductor the additional electrons lower the band structure while in an n-type material it is raised. Bringing a p- and an n-type semiconductor, for example silicon, together creates a *pn-junction* with an intrinsic field gradient inside the material. Electrons from the n-type region diffuse to the p-type region and vice versa where they recombine and vanish. Because of the lack of holes and electrons this area is called *depletion region*.

A Charge-Coupled Device (CCD) utilizes this mechanism to enable position resolved spectroscopy. A few hundred micrometers thick silicon wafer is modified such that most of the bottom area consists of undepleted p-doped material. Above this is a fully depleted p-doped layer followed by a very thin n-doped layer. The top of the sensor is insulated using  $\text{SiO}_2$  and in the silicon material highly p-doped columns are inserted which prevent the diffusion of electrons in horizontal direction, called *p-stops*. On top of the insulation layer horizontal electrodes are located ranging across the entire surface. These electrons can be used to create wells in the electric potential of the n-doped layer and thus collect the released electrons. In combination with the p-stops the wells divide the silicon material into a grid of individual cells sensitive to radiation. Conventionally these are called *picture elements* or *pixels*. The number of electrodes is usually three times

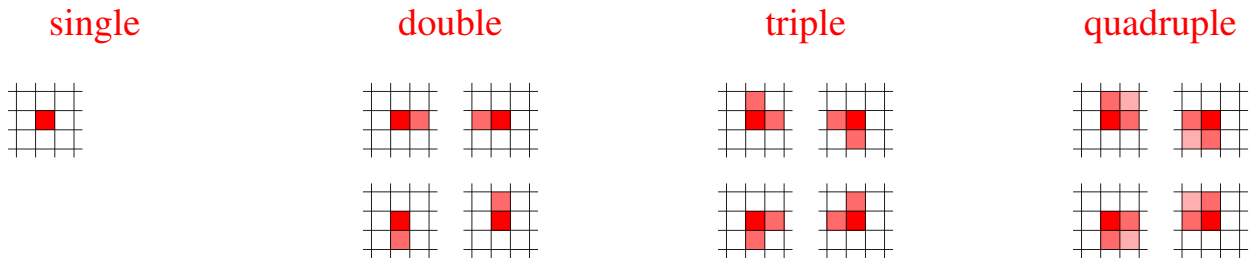


Figure 4.5: Possible valid patterns for the detection of an individual event on a CCD. The amount of charge in each pixel is represented by the saturation of the red color in the pixels. Taken from Schmid (2012).

higher as the number of p-stops to enable the readout process.

A time interval during which photons are absorbed by the detector material and electrons are accumulated in the potential is called *exposure time*. For X-ray spectroscopy very short exposure times are targeted such that only a single photon can be registered in each pixel, hence the accumulated number of electrons directly corresponds to the energy of the photon. Typical exposure lengths are on the order of tens of milliseconds (*eROSITA*: 50 ms, EPIC-pn: 68.7 ms), followed by the readout process.

During this procedure the accumulated charges are shifted through the semiconductor material by an alternating pattern of voltage, called *drive pulses*, applied to each set of three electrodes which causes the potential wells, and therefore the electrons, to shift row by row to one side of the sensor. At this side one or multiple anodes are located by which the electrons are drained, and the signal is amplified followed by a quantization procedure. In this way the number of charges in each pixel, and therefore the amount of energy deposited, can be measured. The efficiency of this charge shifting mechanism is very high with negligible losses (Knoll, 2000).

The overall efficiency of CCDs is mainly determined by the amount of photons interaction with the semiconductor material. For lower energy photons a limiting factor can be whether they penetrate the sensor through the structures on the surface while higher energy photons might pass through the substrate entirely. The efficiency can be greatly increased to more than 90% by using the backside of fully depleted substrate as the side exposed to the radiation. All cameras of *eROSITA* (Meidinger et al., 2010, 2011, 2012, 2014) and the EPIC-pn camera onboard *XMM-Newton* (Strüder et al., 2001) use back-illuminated CCD sensors.

The entire readout procedure takes a significant amount of time compared to the typical exposure time, for example for *eROSITA* cameras 9.18 ms versus 50 ms. During this time, when the charges are shifted, photons can still enter the detector and deposit their energy, hence create additional electrons which are then not assigned to the correct pixels. These events are therefore called *out-of-time events* and usually manifest themselves in the form of bright streaks along the readout direction of the CCD emerging from bright sources. This effect can for example be seen in the EPIC-pn camera (Strüder et al., 2001). A possible technique to mitigate out-of-time events is the usage of a *frame store area* which is an additional set of the same number of pixels directly next to the sensor in the same substrate material to which all charges are shifted in a very short time immediately after the exposure. This area is shielded against incident radiation and therefore the probability for out-of-time events is greatly reduced. The readout electronics operates then on the charges stored in this location instead of the imaging sensor itself.

A photon entering the substrate and depositing enough energy to release a number of charges above a certain threshold is called an *event*. Depending on the size of the pixels and other characteristics of the sensor, the free charges created by an event may not be contained within a single pixel but spread out over multiple adjacent ones. The way in which the charge is distributed among these pixels is called *pattern*. Single event patterns are only registered in a single pixel while double event patterns are possible in two neighbouring pixels. For triple event patterns the charge is distributed among three pixels which are arranged in an angle of  $90^\circ$  and for a quadruple pattern event a block of four directly adjacent pixels is affected. These four types of event patterns and their distribution of charges are shown in Fig 4.5 and are the only ones possible for the impact of a single photon. All other types of patterns are considered invalid because at least two photons must have contributed to their creation which renders the reconstruction of

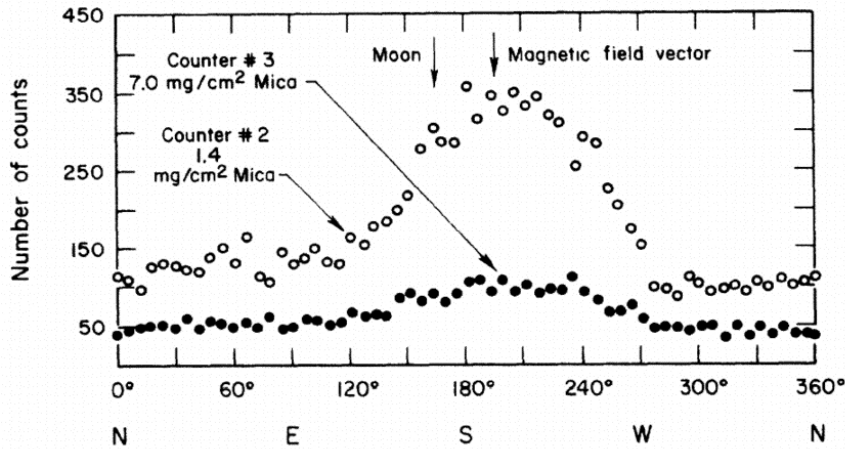


Figure 4.6: Number of counts versus the azimuth angle of the detectors onboard the Aerobee rocket. Marked is the direction towards the Moon and along the magnetic field lines of the Earth. The main peak of the count-rate does not coincide with the Moon and was therefore interpreted as originating from outside the solar system. Taken from Giacconi et al. (1962).

energy impossible. This effect is called *pattern pileup*. If, however, two or more photons generate a valid pattern, e.g., two photons hit two adjacent pixels mimicking a double pattern event, the reconstructed energy will be wrong but not be identified as such, an effect called *energy pileup*. During the analysis of data obtained by CCDs event selection using pattern analysis has to be performed to minimize the influence of pileup on the obtained spectral data.

## 4.2 Historical X-ray Observations of Astrophysical Sources

### 4.2.1 Rocket Experiments

Herbert Friedman in 1949 equipped a V-2 rocket with Geiger counters which were able to detect X-ray emission from then Sun above 87 km (Friedman et al., 1951).

Similarly, in 1962 Riccardo Giacconi initiated a program to use an Aerobee 150 sounding rocket equipped with three Geiger counters to measure the proposed X-ray flux of the Moon. X-ray photons originating from the Sun were expected to cause fluorescence on the lunar surface which in turn would create a measurable amount of X-rays. Giacconi et al. (1962) estimated the count-rate by which this flux would register in the detectors to 0.1 to 1 cts/s.

On June 18th, 1962, 23:59 MST, the rocket was launched from the White Sands Missile Range, New Mexico. At this point in time the Moon was  $35^\circ$  above the horizon and only one day past full. After the launch the highest point of the rocket's trajectory was 225 km, and it spent 350 s above 80 km while covering a distance of roughly 120 km, almost due north. During the flight the rocket was spinning about two times a second around its longitudinal axis while two of the Geiger counters (the third one was malfunctioning) were scanning the sky in an angle of  $55^\circ$  to said axis. The aperture of both detectors were covered by mica of different thickness and the count-rates measured by each detector with respect to the orientation, being the azimuth, are shown in Fig. 4.6.

Most notably the peak of count-rate located at  $\sim 195^\circ$  does not coincide with the marked position of the Moon but is shifted by roughly  $35^\circ$  westwards. By calculating the expected angular distribution of counts for a unidirectional beam of electrons and comparing it to the observed data Giacconi et al. (1962) concluded that the measured radiation does also not stem from particle background. The detectors were shielded against ultraviolet and visible light, which was verified by the fact that the Moon, which is a strong source

## 4 X-ray Astronomy

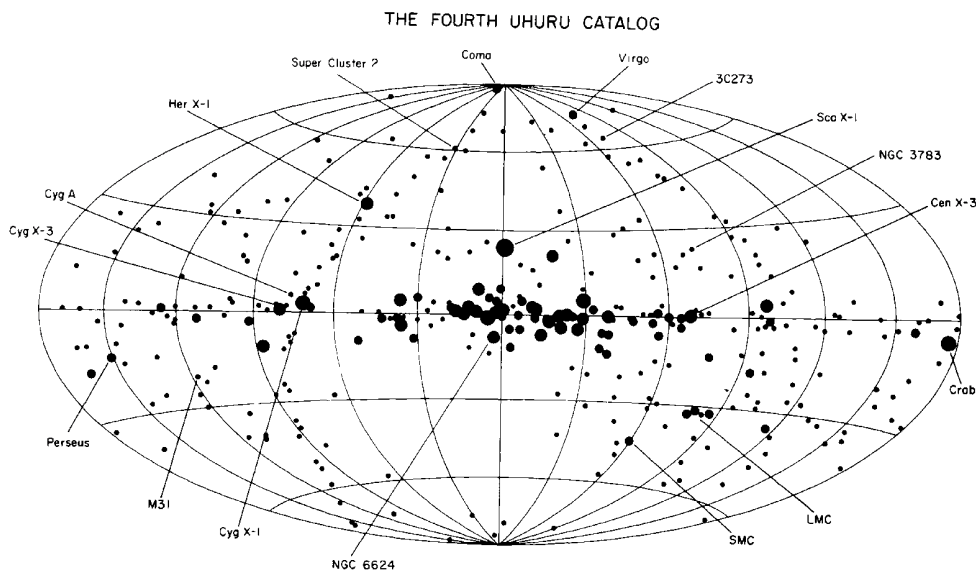


Figure 4.7: Sources of the original 4U catalog from the *UHURU* satellite in the galactic coordinate frame. The sizes of the dots is proportional to the logarithm of the peak intensity as measured of the sources. Taken from Forman et al. (1978).

of visible light and the Moon and the Virgo cluster, both being sources of ultraviolet light, went through the FOV of the detectors but were not registered. Thus it was concluded that the registered radiation was indeed electromagnetic in nature, part of the soft X-ray regime and not originating from inside the solar system.

This X-ray source was later identified to be a neutron star and designated as Sco XR-1 (Morton, 1964; Shklovsky, 1967, its modern designation is Sco X-1), meaning the first X-ray source to be discovered in the constellation of Scorpius.

A variety of balloon experiments carrying X-ray detectors were performed in the decades after that which, in addition to rocket based observations, revealed tens of new X-ray sources from outside the solar system (Ubertini, 1983).

### 4.2.2 X-ray Observatories in Space

The successful balloon campaigns in the 1960s helped to convince the government to fund the development and construction of satellites, and on December 12th, 1970, the *UHURU* X-ray observatory was launched into space. Equipped with two large area proportional counter arrays its mission was to perform the first survey of the entire sky in X-rays in the energy range of 1 to 20 keV (Jagoda et al., 1972). With this very similar objective, in a sense, *UHURU* can be considered as the oldest relative of *eROSITA*. Apart from important discoveries like X-ray emission from extragalactic sources such as M87 (Kellogg et al., 1971b), Seyfert galaxies such as NGC1275 and NGC4151 (Gursky et al., 1971a,b) and the galactic center region (Kellogg et al., 1971a), the first X-ray transients (Matilsky et al., 1972) and pulsations X-ray sources such as Cyg X-1 (Oda et al., 1971; Holt et al., 1971), Cen X-3 (Giacconi et al., 1971) and Her X-1 (Tananbaum et al., 1972) a cohesive catalog of 125 sources was published by Giacconi et al. (1972). After a revised version with 161 sources (Giacconi et al., 1974) the fourth and final version of the catalog containing 339 X-ray sources was published by Forman et al. (1978). The designations of these sources start with the letters “4U”, indicating the version of the catalog and the letter “U” for the spacecraft. For the most prominent sources these are still widely used to this day. In March 1973 contact to the satellite was lost, ending the successful mission (Forman et al., 1978).

The 7th *Orbiting Solar Observatory* (*OSO-7*) was launched on September 29th, 1971, and carried two sets of proportional counters sensitive from 1 to 60 keV (McClintock, 1975), an X-ray telescope designed for

hard radiation in the regime of 7 to 550 keV and a gamma-ray monitor (Higbie et al., 1972). While also performing a survey of the entire sky it observed sources from the 3U catalog and discovered new sources, generating a catalog with 185 entries (Markert et al., 1979). Among other results it found a 4.8 h period of Cyg X-3 in the range from 6 to 21 keV but not from 21 to 98 keV (Ulmer et al., 1974) and a 9-day period in the radiation from Vela X-1 (Ulmer et al., 1972).

On August 21st, 1972, the *Orbiting Astronomical Observatory C (OAO-C)* was launched as the third of a row of four space observatories. After the successful launch its designation changed to *Orbiting Astronomical Observatory 3 (OAO-3)* and subsequently to *Copernicus* in honor of Nicolaus Copernicus on the 500th anniversary of his date of birth. In addition to an ultraviolet telescope with a mirror of 80 cm diameter it carried the University College London X-ray Experiment (UCLXE), which consisted of four X-ray telescopes, three using mirror optics and one collimator module, sensitive in the range of 1 to 10 keV (Sanford, 1974). During its operation until February 1981 several important discoveries were made by *Copernicus*, among which are the large amplitude variability of the X-ray flux of Centaurus A (Davison et al., 1975), long period pulsation of X-ray pulsars such as X Per (White et al., 1976) and absorption events recognized in the variable spectrum of Cyg X-1 (Sanford et al., 1975).

Another two years later on October 15th, 1974, the satellite *Ariel V* was launched which was a dedicated X-ray observatory. It was equipped with six instruments designed to constantly monitor the X-ray sky in the energy range from 0.3 to 40 keV. Four of these instruments were aligned with the rotational axis of the satellite around which it was rotating with a period of 6 s while the other two were oriented perpendicular to this axis and scanned the entire sky. In this way long and continuous observations of sources were possible as well as monitoring of the entire sky to detect X-ray transient events (Smith & Courtier, 1976; Holt, 1976; Villa et al., 1976). All sources detected by this mission were coherently published in two catalogs with a differentiation by galactic latitude where  $|b| = 10^\circ$  is the limit. 109 sources are part of the first part of the catalog for  $|b| < 10^\circ$  (Warwick et al., 1981) and 142 sources are contained in the second part for  $|b| > 10^\circ$  (McHardy et al., 1981). *Ariel V* was able to discover multiple X-ray transients, for example A0620–00 (Elvis et al., 1975), A1742–28 (Eyles et al., 1975b) and A0535+26 (Rosenberg et al., 1975), monitored the outbursts of known transients such as Cyg X-1 (Eyles et al., 1975a), Cir X-1 (Coe et al., 1976) and Aql X-1 (Kaluziński et al., 1977), while also finding long pulse periods on the timescale of minutes to hours and even days in a variety of sources (Ives et al., 1975; Serlemitsos et al., 1976; Holt et al., 1976b,a; Owens, 1977; Kemp et al., 1978; Molteni et al., 1980; Blissett et al., 1981; Priedhorsky et al., 1983). Additionally, *Ariel V* enabled the association of Seyfert galaxies with X-ray sources (Cooke et al., 1976; Burnell & Culhane, 1979; Hayes et al., 1980a,b) and was able to measure iron line emission in extragalactic sources (Mitchell & Culhane, 1977; Berthelsdorf & Culhane, 1979; Hayes et al., 1980a; Fabian & Ross, 1981). After a successful mission the satellite decayed during the reentry in Earth's atmosphere on March 14th 1980.

The *Astronomische Nederlandse Satelliet (ANS)* was launched on August 30, 1974 (Brinkman et al., 1974). Equipped with an ultraviolet telescope, proportional counters as detectors for soft X-rays from 1 to 7 keV (den Boggende & Lafleur, 1975) and for hard X-rays from 1.5 to 30 keV and the so called “Bragg Crystal Assembly” (BCA) for the detection of silicon lines (Gursky et al., 1975) it was able to detect soft X-ray emission from stellar coronae, for example from Capella and Sirius (Mewe et al., 1975a,b, 1976). It also discovered X-ray flares from the stars UV Ceti and YZ CMi (Heise et al., 1975) and very short X-ray bursts lasting for only seconds mainly from sources in globular clusters (Grindlay et al., 1976; Heise et al., 1976; Cooke, 1976; Shklovskii, 1976a,b).

Although the main objective of the 8th *Orbiting Solar Observatory (OSO-8)*, which was launched on June 21st, 1975, was to obtain solar spectra using the Graphite Crystal X-ray Spectrometer (Kestenbaum et al., 1976), this instrument, working in the energy range from 2 to 8 keV, was used at satellite night in combination with the Goddard Space Flight Center Cosmic X-Ray Spectroscopy Experiment (GCXSE), consisting of three proportional counters working in the range from 2 to 60 keV, the High Energy Celestial X-ray Experiment, a spectrometer working from 0.01 to 1 MeV, and the Soft X-ray Background Radiation experiment, employing proportional counters sensitive in the range from 0.15 to 45 keV, to investigate cosmic sources of X-rays. The GCXSE was able to determine a blackbody shaped spectrum of X-ray bursts (Swank et al., 1977) and show the iron line emission from clusters of galaxies (Serlemitsos et al., 1977).

On May 7, 1975, the Third *Small Astronomy Satellite (SAS-3)* was launched. With its four instruments sensitive in the X-ray regime the main goals were to search for transient phenomena such as flares, bursts or

novae, identify the position of bright X-ray sources to an accuracy of  $15''$  and investigate specific sources in the energy range from 0.1 to 55 keV. The first instrument to accomplish this goal was made of two rotating modulation collimator systems which were in front of proportional counters sensitive from 2 to 6 keV and 6 to 11 keV. Using this instrument positions of sources could be determined accurately up to  $15''$ . A large area of the sky was monitored by three slat collimators each with a proportional counter perpendicularly to the rotational axis of the satellite which was spinning with a period of 95 min. These proportional counters operated in the energy range from 5 to 15 keV while one Xenon counter was added to one detector which increased the response to 60 keV. These detectors had a large FOV and could be used to determine the coarse position of sources. Three tube collimators with the same energy range but a much smaller FOV were used for detailed timing and spectral analyses of specific sources. A low-energy detector system consisting of four reflection concentrators equipped with two gas-flow counters each could be used to detect X-rays in the range from 0.15 to 1 keV (Mayer, 1975). *SAS-3* discovered the so called “Rapid Burster”, designated as MXB 1730–335, a X-ray source which shows bursts in intervals of only seconds to minutes (Lewin et al., 1976a; Grindlay & Gursky, 1977; Ulmer et al., 1977; van Paradijs et al., 1979; Marshall et al., 1979; Loznikov & Iamburenko, 1982; Basinska et al., 1980), among other bursting sources (Lewin et al., 1976b; Hoffman et al., 1976; Clark et al., 1976; Jernigan et al., 1977; Li et al., 1977). It also found X-ray emission from the isolated white dwarf HZ 43 (Hearn et al., 1976a), the multiple star system Algol (Schnopper et al., 1976) and the cataclysmic variable AM Her (Hearn et al., 1976b; Hearn & Richardson, 1977) while additionally performing a survey of the soft X-ray background from 0.1 to 0.28 keV which was shown to be anti-correlated to the neutral hydrogen column density (Marshall & Clark, 1984). With the detection of MR2251–178 a quasi stellar object was discovered via its X-ray emission (Ricker et al., 1978).

The up to this point heaviest satellite was placed in orbit on August 12th, 1977 and was named *HEAO-1* indicating the dedicated mission to study astrophysical sources of highly energetic radiation such as X-rays. *HEAO-1* was equipped with four instruments with designations A-1 through A-4. A-1, the Large Area Sky Survey experiment (LASS), operated with seven proportional counter modules with large apertures in the energy range from 0.25 to 25 keV to create a catalog of X-ray sources during the survey operation of *HEAO-1* (Wood et al., 1984). With six proportional counters of different types the Cosmic X-ray Experiment (A-2) could cover a total energy range from 0.15 to 60 keV and its main incentive was to study the diffuse X-ray background (Rothschild et al., 1979). The MIT/SAO scanning Modulation Collimator (A-3) instrument was composed of two proportional counters each having a grid of four collimators. It was sensitive in the range from 0.9 to 13.3 keV and its purpose was to measure the position of X-ray sources over the entire sky with precision up to  $7''$  (Gursky et al., 1978). Using seven inorganic scintillation detectors the UCSD/MIT Hard X-ray/Low-Energy Gamma-Ray Experiment (A-4) was used to measure the temporal behavior and spectra of discrete sources from the hard X-ray to gamma-ray regime (10 keV to 10 MeV) (Matteson, J. L., 1978). For these experiments a dedicated catalog of sources was created (A-1: Wood et al. (1984), 842 sources; A-2: Nugent et al. (1983), 114 sources; A-3: 654 sources<sup>5</sup>; A-4: Levine et al. (1984), 73 sources). *HEAO-1* was able to study the variability of Cyg X-1 on the timescale of milliseconds (Meekins et al., 1984).

The next iteration of the *High Energy Astronomy Observatory (HEAO)* satellites was the *HEAO-2* which was launched on November 12th, 1978 and renamed *Einstein* probe thereafter. Apart from using the Monitor Proportional Counter (MPC) to constantly record the count-rate of the currently observed object it was the first mission to use dedicated X-ray focusing optics consisting of Wolter Type I grazing incidence mirrors to achieve high spatial resolution. The focus could be placed on one of four different instruments (Giacconi et al., 1979). The MPC was sensitive in the energy range from 1 to 20 keV (Gaillardetz et al., 1978) while the Imaging Proportional Counter (IPC) in the focal plane provided spectral and spatial information with resolution of  $1'$  in the energy range from 0.4 to 4 keV (Harvey et al., 1976). Much higher spatial resolution of up to  $2''$  was provided by the HRI which was achieved by the generation and multiplication of free electrons by two microchannel plates and the subsequent detection by a crossed grid charge detector (Giacconi et al., 1979). Spectral information was provided by the Solid State Spectrometer (SSS) in the range from 0.5 to 4.5 keV with a resolution of 150 eV which consisted of a cooled Si(Li) crystal (Joyce et al., 1978) and the Focal Plane Crystal Spectrometer (FPCS) which used six Bragg crystals to diffract the focused X-rays onto two imaging proportional counters, providing a spectral coverage from 0.2 to 2.6 keV with a resolution from

<sup>5</sup>No referred publication of this catalog exists, but it is available through the W3Browse interface of HEASARC at <https://heasarc.gsfc.nasa.gov/cgi-bin/W3Browse/w3table.pl?0bservatory=HEAO1#>

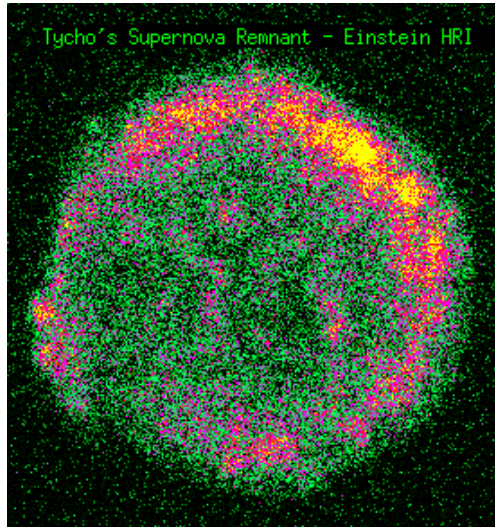


Figure 4.8: The Tycho supernova remnant as seen by the High Resolution Imager onboard the Einstein probe. (From the HEASARC website <https://heasarc.gsfc.nasa.gov/Images/einstein/tycho.gif>)

50-100 for  $E < 0.4$  keV and 100-1000 for  $E > 0.4$  keV (Giacconi et al., 1979; Lum et al., 1992). With its high spatial resolution *Einstein* was able to identify X-ray jets aligned with radio jets in the galaxies M87 (Schreier et al., 1982) and Cen A (Schreier et al., 1979) and perform morphological studies of supernova remnants such as the Tycho supernova remnant shown in Fig. 4.8 (Long & Helfand, 1979; Murray et al., 1979; Tuohy, 1980; Fabian et al., 1980; Reid et al., 1982; Tuohy et al., 1982).

The on June 2nd, 1979, launched *Ariel VI* was equipped with two X-ray instruments sensitive in soft and hard X-rays apart from cosmic ray detectors. As a result of heavy interference from ground the radio communication to the satellite was unreliable and the battery charger and tape recorder did not work properly, thus the scientific results of this mission was severely limited (Pounds, 1986).

*CORSA-b* was another satellite dedicated to X-ray observations launched on February 21st, 1979, after which it was renamed *Hakucho*. It carried four units of proportional counters sensitive in the range from 0.1 to 0.2 keV, called Very Soft X-ray experiment (VSX), six units of proportional counters operating in the range from 1.5 to 30 keV, called Soft X-ray experiment (SFX), and a scintillator for the detection of hard X-rays in the regime from 10 to 100 keV. The main objectives of the mission were to survey the sky in X-rays to discover and monitor X-ray bursting and transient sources and their temporal and spectral behavior (Inoue et al., 1979; Hakucho Team et al., 1979a,b,c,d). *Hakucho* was able to discover 2 Hz oscillations in the radiation from the Rapid Burster (Tawara et al., 1982) and bursts from the known transients Aql X-1 (Koyama et al., 1981), Cen X-4 (Matsuoka et al., 1980) and GX 3+1 (Makishima et al., 1983).

On September 20, 1979, Third *HEAO* (*HEAO-3*), the third and last mission of the High Energy Astronomy Observatory Program, was launched. Equipped with two experiments for the analysis of cosmic rays it also carried the High Resolution Gamma-Ray Spectrometer (HRGRS), a germanium based spectrometer working in the range from hard X-rays beginning at 50 keV up to the gamma-ray regime at 10 MeV (Mahoney et al., 1980). It performed a survey of the sky in the search for narrow line hard X-ray and gamma-ray emission which was found for sources such as the galactic center and a variety of hard X-ray and gamma-ray transients (Ramaty et al., 1981).

The *EXOSAT* was launched on May 26, 1983, and stationed in a highly inclined and eccentric orbit with a period of 90 h (White & Peacock, 1988). To target low energy X-rays in the range of 0.05 to 2 keV a Wolter type I telescope was used which could focus the radiation onto the Channel Multiplier Array (CMA) for imaging purposes with an on-axis resolution of  $18''$  or with the Transmission Grating Spectrometer (TGS) in the optical path for spectroscopy. Alternatively the Position Sensitive Detectors (PSD), being proportional counters, could be placed at the focal point, however, they failed early in the mission (de Korte et al., 1981). Eight proportional counters working in the energy range from 1 to 50 keV were called the Medium Energy

(ME) instrument and provided spectral and timing information in this regime (Turner et al., 1981). The third instrument onboard was the Gas Scintillation Proportional Counter (GSPC) operating in the energy range from 1 to 80 keV in four different modes (Peacock et al., 1981). *EXOSAT* was able to discover quasi period oscillations (QPOs) in low mass X-ray binaries and pulsars (Stella, 1988) and performed extensive studies of the spectra and variability of extragalactic objects such as AGN (McHardy, 1988; Maraschi & Maccagni, 1988; Pounds & Turner, 1988).

*Tenma*, before its launch on February 20, 1983, known as *ASTRO-B*, carried the GSPC instrument consisting of 10 of said devices sensitive from 2 to 60 keV. Complementary to this were the X-ray Focusing Collector, a set of two position sensitive proportional counters operating in the range from 0.1 to 2 keV, the Transient Source Monitor (TSM) and the Radiation Belt Monitor/Gamma-Ray Burst Detector (RBM/GBD). The TSM itself consisted of the Hadamard X-ray telescope, a pair of position sensitive proportional counters with a Hadamard mask in front, and a scanning counter system and performed constant monitoring of a 100° diameter FOV. Two scintillation counters constitute the RBM/GBD system which was used for background monitoring to protect the satellite from radiation belts and to record GRBs (Tanaka et al., 1984; Anderson, 1983). Using these instruments it was possible to detect iron line emissions from a variety of sources, such as low mass X-ray binaries (Suzuki et al., 1984; Hirano et al., 1986), high mass X-ray binaries (Ohashi et al., 1984; Matsuoka et al., 1986b), Seyfert galaxies (Matsuoka et al., 1986a) and even galactic emission nebulae such as M42 (Agrawal et al., 1986). *Tenma* also discovered absorption lines at 4 keV in the spectra of X-ray bursts of X1636–536 (Waki et al., 1984).

The subsequent mission *ASTRO-C* was launched on February 5th, 1987, after which it was renamed *Ginga*. Its main instrument was the Large Area Proportional Counter (LAC) sensitive from 1.5 to 37 keV and consisting of eight multi-cell proportional counters (Turner et al., 1989). It also carried the All-Sky Monitor (ASM) which consisted of two gas proportional counters operating in the range from 1 to 20 keV over a FOV of 180° in which way it could discover new transient sources and monitor known sources (Tsunemi et al., 1989a). Additionally, it was equipped with the Gamma-Ray Burst Detector (GBD). This instrument used proportional counters and scintillation spectrometers with a wide FOV to detect radiation from 1.5 to 500 keV (Murakami et al., 1989). It discovered cyclotron lines in the spectra of the pulsars 4U 1538–52 (Clark et al., 1990), X0331+53 (Makishima et al., 1990) and Cep X-4 (Mihara et al., 1991), a variety of new X-ray transient sources (Kitamoto et al., 1989; Tsunemi et al., 1989b) and iron line emission from the galactic center (Yamauchi et al., 1990) and Seyfert I galaxies (Pounds et al., 1989).

With the launch of *International Astrophysical Observatory (GRANAT)* on December 1st, 1989, a dedicated X-ray and gamma-ray observatory with seven instruments in total entered orbit. These instruments, a combination of coded mask detectors, proportional counter spectrometers, an all sky monitor and three experiments to detect gamma-ray bursts, covered an energy range from 2 keV up to 100 MeV (Brandt et al., 1990; Roques et al., 1990; Siunjaev et al., 1990; Terekhov et al., 1991). It performed a very deep survey of the galactic center region (Sunyaev et al., 1991) and discovered electron-positron annihilation lines in the Nova Muscae (Gilfanov et al., 1991) and low mass X-ray binary 1E1740.7–2942 (Bouchet et al., 1991).

The *Broad Band X-ray Telescope (BBXRT)* was brought into orbit as part of the *ASTRO-1* payload with the Space Shuttle Columbia mission STS-35 in December 1990. With its two five-segmented solid state spectrometers in the focal planes of two X-ray telescopes it was able to obtain spectra in the range from 0.3 to 12 keV and a resolution of 90 eV at 1 keV and 150 eV at 6 keV (Serlemitsos et al., 1984). *BBXRT* was able to resolve the iron K-alpha line in the spectra of Cyg X-2 (Smale et al., 1993) and Cen X-3 (Audley et al., 1996) and detected line broadening in the Seyfert galaxy NGC 4151 (Weaver et al., 1992).

### 4.2.3 ROSAT - The Predecessor of eROSITA

When the *ROSAT* was launched on June 1st, 1990, a mission started its operation which can be regarded as the direct predecessor to *eROSITA*. The goal of the *ROSAT* mission was to first do a survey of the entire sky using its X-ray telescope in the energy range from 0.1 to 2.5 keV after which a phase of pointed observations of dedicated sources was planned (Truemper, 1982). With an additional instrument the energy range could be extended down towards 0.06 keV (Pye, 1984).

Using four 500 mm long Wolter type I mirrors with an outer aperture of 835 mm and a focal length of 2400 mm it could achieve an on-axis resolution of 5". Taking the entire collection area of the four mirror

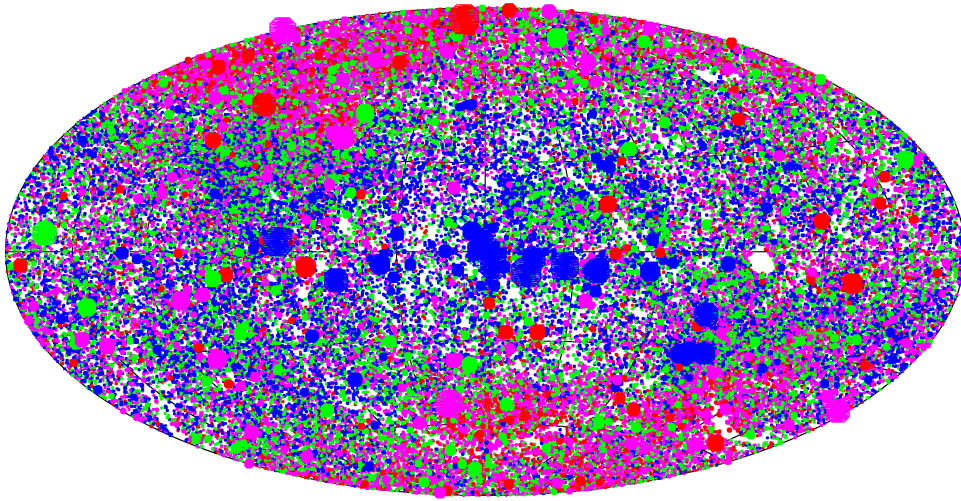


Figure 4.9: Map of the sources in the 2RXS catalog in galactic coordinates using the Hammer-Aitoff projection. The sizes of the dots are proportional to the sources count-rate while the color is a measure for the hardness of the radiation of the source. (Credit: Boller et al. (2016))

shells results in  $1141 \text{ cm}^2$  while the effective area was  $400 \text{ cm}^2$  (Aschenbach et al., 1982).

In the focal plane a carousel was located which housed three instruments: Two redundant position sensitive proportional counters (PSPCs) and the HRI. By rotating the carousel the active instrument could be exchanged.

Each PSPC covered a total FOV of  $2^\circ$  in diameter and consisted of two separate proportional counters. One anode with two cathodes were used as the positioning sensors while another anode as an anticoincidence unit to reject background events. The anodes were made from gold-plated tungsten wires while the cathodes consisted of platinum-iridium ones. All wires were placed in a grid inside a glass ceramic support frame. An X-ray photon passing through the entry window of the detector, made from  $1 \mu\text{m}$  thick polypropylene coated with carbon and polycarbonate, was absorbed by the counter gas, a mixture of 60% argon, 20% xenon and 20% methane, producing a free electron via the photoelectric effect. This electron interacted with the counter gas again, losing energy and creating an electron cloud in the process, which drifted towards the electrodes where they could be registered. Because X-ray photons were absorbed by the counter gas with a probability of almost 100% the quantum efficiency was determined by the energy dependent transmissivity of the entrance window which was 50% at 0.93 keV. By on-axis illumination of the X-ray telescope the instrument could achieve a spatial resolution of  $30''$ . In total four PSPC instruments were built, named PSPC-A through PSPC-D, where PSPC-B and PSPC-C were used on *ROSAT* while the other two acted as flight spare units and were used for calibration measurements on ground (Pfeffermann & Briel, 1982; Briel & Pfeffermann, 1986; Pfeffermann et al., 1986; Stephan & Englhauser, 1986; Briel et al., 1988).

The third instrument in the carousel, the HRI, was based on the instrument of the same name of the *Einstein* observatory but had improved quantum efficiency and detector background. It could achieve a spatial resolution of  $1.7''$  over a FOV of  $38'$  (Zombeck et al., 1990, 1995b).

An additional instrument, coaligned with the primary telescope, was the extreme ultraviolet (XUF) Wide Field Camera (WFC) operating in the energy range from 0.06 to 0.15 keV. It consisted of a small telescope with a micro channel plate acting as the photon detector and provided the first all sky survey in this band (Pye, 1984).

From the data collected during the six-month survey period, using mostly the PSPC-C instrument, two catalogs were been produced. The *ROSAT* all-sky survey bright source catalogue (RASS-BSC) contains 18811 sources, which have a count-rate of at least 0.05 cts/s in the PSPC in the energy band from 0.1 to 2.4 keV, a detection likelihood of at least 15 and 15 source counts or more. All sources have also been verified visually and flagged if appropriate by the criteria of nearby sources, having positional errors, being

extended, having complex emission structures or being not detected by the software used for processing. The catalog has also been released under the designation 1RXS (Voges et al., 1999).

As a complementary catalog the *ROSAT* all-sky survey faint source catalog (RASS-FSC) contains 105924 sources having at least six source counts and a detection likelihood of at least seven in the same energy band as the RASS-BSC (Voges et al., 2000).

On February 12, 1999, the *ROSAT* mission ended, and the satellite reentered the Earth's atmosphere on October 23rd 2011.

Motivated by the advanced processing capabilities of modern technology Boller et al. (2016) created a revised version of the 1RXS catalog, subsequently denoted the 2RXS catalog. This newer version contains 135118 sources detected in the energy range from 0.1 to 2.4 keV with a detection likelihood of 6.5 or higher. With these results “the 2RXS catalogue provides the deepest and cleanest X-ray all-sky survey catalogue in advance of eROSITA” (Boller et al., 2016).

#### 4.2.4 Between *ROSAT* and *eROSITA*

*Advanced Satellite for Cosmology and Astrophysics (ASCA)* was launched on February 20, 1993, and carried four X-ray telescopes with 3.5 m focal length in the focal plane of which one of two sets of two identical instruments could be used (Inoue, 1991). The first set were Imaging Gas Scintillation Proportional Counters (PGSPCs) and consisted of gas chambers filled with Xenon and position sensitive photomultipliers. These could achieve a spatial resolution of  $30''$  at 5.9 keV over a FOV of  $50'$  in the energy range from 0.7 to 20 keV while the effective area of the instruments was  $50 \text{ cm}^2$  for photons of energy 1 keV and the energy resolution 8% at 5.9 keV (Ohashi et al., 1991; Kohmura et al., 1993). The other instrument housed the first CCDs used for a X-ray observatory and was called Solid-state Imaging Spectrometer (SIS). Each of these detectors had an array of four  $420 \times 420$  square pixel areas covering a FOV of  $23 \times 23'$ . Having an effective area of  $105 \text{ cm}^2$  it offered a spatial resolution of  $30''$  while simultaneously providing a spectral resolution of 2% at 5.9 keV (Burke et al., 1993, 1994; Inoue, 1993). With its high sensitivity and good spectra resolution *ASCA* was not only able to resolve broad iron lines in a variety of galaxies (Yaqoob et al., 1995; Iwasawa et al., 1996a; Nandra et al., 1996; Weaver et al., 1997; Nandra et al., 1997b; Yamashita et al., 1997; Terashima et al., 1998) but also show their variability (Iwasawa et al., 1996b; Guainazzi et al., 1996; Nandra et al., 1997d; Iwasawa et al., 1997; Nandra et al., 1997c; Finoguenov & Chernyakova, 1998). *ASCA*, using X-ray spectroscopy, could show that the coronae of active stars have much lower metallicities than the solar value (Singh et al., 1996; Mewe et al., 1996; Favata et al., 1997). It also discovered non-thermal emission from the supernova remnant 1006 (Koyama et al., 1995; Reynolds, 1996) and its data were used to determine the role of type II supernovae for the abundance of heavy elements found in the hot gas of galaxy clusters (Mushotzky et al., 1996; Loewenstein & Mushotzky, 1996; Tamura et al., 1996; Gibson et al., 1997; Fukazawa et al., 1998).

On December 30, 1995, the Rossi X-ray Timing Explorer (*RXTE*) was launched. It was equipped with two instruments for X-ray observations with high temporal resolution and an additional wide field detector for monitoring of large areas of the sky. Operating in the energy range from 2 to 60 keV the Proportional Counter Array (PCA) consisted of five proportional counters filled with xenon with a total effective area of about  $6500 \text{ cm}^2$ . It offered an unprecedented time resolution of only  $1 \mu\text{s}$  and the FOV of the collimators was  $1^\circ$  at FWHM (Zhang et al., 1993; Gruber et al., 1996). HEXTE consisted of two arrays of four scintillation detectors sensitive in the energy range from 12 to 250 keV. Each array had a collecting area of  $800 \text{ cm}^2$ , a time resolution of  $8 \mu\text{s}$  and the FWHM of the FOV was also  $1^\circ$  in diameter. Both detectors could be pointed  $1.5$  or  $3^\circ$  off the target position every 16 to 128 s to take measurements of the background (Rothschild et al., 1998). Using three position sensitive proportional counters behind coded aperture masks the ASM could monitor roughly 80% of the sky every 90 min in the energy range from 2 to 10 keV. The spatial resolution of the instrument was  $3 \times 15'$  which arises from the slit shaped apertures each of which covered a  $6 \times 90^\circ$  segment of the sky. All three detectors of the ASM had a combined collection area of  $90 \text{ cm}^2$  (Levine et al., 1996). Among other important results regarding variability of X-ray sources *RXTE* discovered fast quasi periodic oscillations on the timescales of milliseconds in a variety of sources (Berger et al., 1996; Smale et al., 1996; Jernigan et al., 1999; Cui et al., 2000; Strohmayer, 2001; Altamirano et al., 2008).

The Satellite per Astronomia a raggi X (ital., Satellite for X-ray Astronomy, abbrev. SAX), which was named *BeppoSAX* in honor of the Italian physicist Giuseppe “Beppo” Occhialini, was launched on April

30, 1996, and carried four X-ray telescopes with two spectrometers in their focal plane, a gas scintillation proportional counter, a phoswich detector system and two coded mask proportional counters (Boella et al., 1997a). The Low-Energy Concentrator Spectrometer (LECS) consisted of a position sensitive gas scintillation detector (PSGSD), was in the focal plane of the X-ray telescopes and was sensitive to photons in the energy range from 0.1 to 10 keV while it provided a spatial resolution of  $9.7'$  over a FOV of  $37'$  with an effective area of  $22\text{ cm}^2$  (Parmar et al., 1997). The second instrument in the focal plane was the Medium Energy Concentrator Spectrometer (MECS) which consisted of three individual PSGSDs with a total effective area of  $150\text{ cm}^2$  and a FOV of  $56'$ . The spatial resolution of that instrument was  $75''$  (Boella et al., 1997b). Another gas scintillation proportional counter named High Pressure Gas Scintillator Proportional Counter (HPGSPC) was not located in the focal plane of the telescope but used a collimator for retrieval of spatial information. It was sensitive from 4 to 120 keV with an effective area of  $240\text{ cm}^2$  and provided a FOV of  $1^\circ$  in diameter (Manzo et al., 1997). The Phoswich Detection System (PDS) consisted of four phoswich scintillators with an effective area of about  $600\text{ cm}^2$  and a FOV of  $1.3^\circ$  (Frontera et al., 1997). Two Wide Field Cameras (WFCs) were used to image the X-ray sky in the energy range from 2 to 28 keV over a FOV of  $20 \times 20^\circ$  with an effective area of  $140\text{ cm}^2$  and an angular resolution of  $5'$  (Jager et al., 1997). *BeppoSAX* was able to detect a variety of GRBs and perform follow-up observations of these events to detect their X-ray afterglow and determine their position with arc minute accuracy (in 't Zand et al., 1998, 1999; Nicastro et al., 1999; Kuulkers et al., 2000; Frontera et al., 2000; Antonelli et al., 2000).

On October 9th, 2000 the High Energy Transient Explorer (*HETE-2*) was launched. The satellite carried three instruments to detect and localize GRBs. The Wide Field X-ray Monitor (WXM) was sensitive in the range from 2 to 25 keV and could achieve a spatial resolution of  $10''$  using two perpendicular one dimensional coded aperture masks. Photons were detected by PSPCs and the total effective area of the instrument was  $175\text{ cm}^2$  (Shirasaki et al., 2003; Nakagawa & Hete-2 Collaboration, 2009). The Soft X-ray Camera (SXC) used a similar coded mask setup but CCDs as photon detectors which could achieve a spatial resolution of  $33''$  and were sensitive in the range from 0.5 to 10 keV over an effective area of  $72\text{ cm}^2$  (Kawai et al., 2001; Nakagawa & Hete-2 Collaboration, 2009). Sensitive to photons in the range from 6 to 400 keV, the French Gamma-ray Telescope (FREGATE) with an effective area of  $120\text{ cm}^2$  was used to detect gamma radiation (Kawai et al., 2001; Nakagawa & Hete-2 Collaboration, 2009). *HETE-2* was able to discover and localize a variety of gamma-ray and X-ray bursts and automatically alert other facilities for follow-up observations (Hurley et al., 2009) while also providing data for extensive spectral analyses of these events (Nakagawa & Hete-2 Collaboration, 2009).

With the launch of the Advanced X-ray Astrophysics Facility (AXAF) on July 23, 1999, an observatory started its mission which, at the point of writing this thesis is still operating. It was renamed Chandra X-ray Observatory (*CXO*, short: *Chandra*) in honor of Subrahmanyan Chandrasekhar. The High-Resolution Mirror Assembly (HRMA) of the X-ray telescope is composed of four shells of a lithium-aluminosilicate glass-ceramic compound coated with iridium for high reflectivity of X-ray photons and has a focal length of 10 meters (Weisskopf et al., 2002). Two different sets of gratings can be inserted into the optical path for spectroscopy purposes. The Low Energy Transmission Grating (LETG) is sensitive for photons from 0.08 to 6 keV (Mendez, 2003) and the High Energy Transmission Grating (HETG) from 0.5 to 10 keV (Flanagan et al., 2003). Two instruments are located in the focal plane of the HRMA. The Advanced CCD Imaging Spectrometer (ACIS) consists of ten CCDs subdivided into two groups, ACIS-I and ACIS-S. The ACIS-I is used for imaging purposes over a FOV of  $16 \times 16'$  with a spatial resolution of  $0.5''$ . It is sensitive in the range from 0.2 to 10 keV and each sensor has an effective area of  $110\text{ cm}^2$ . Six CCDs aligned in a row provide the ACIS-S which is designed to be used with the spectroscopic gratings (Garmire et al., 2003). The High Resolution Camera (HRC) is the second instrument which can be inserted into the focal plane and is also divided into two parts. The HRC-I is a square shaped 90 mm detector of microchannel plates capable of imaging over a FOV of  $30 \times 30'$  with a resolution of  $0.5''$  and an energy range from 0.1 to 10 keV while having an effective area of  $225\text{ cm}^2$ . For the HRC-S the detector has a square shape of  $7 \times 97'$  and is designed for use with the LETG (Zombeck et al., 1995a; Kenter et al., 2000; Kraft et al., 2000). With its unprecedented spatial resolution in the X-ray regime *Chandra* can show small scale features of X-ray sources such as supernovae remnants. A prominent example is SN 1987A. This structure is only slightly larger than  $1''$  but *Chandra* is not only able to resolve it but also can monitor its expansion (Park et al., 2007; Garmire et al., 2003).

*XMM-Newton* was launched on December 10, 1999, and is also still operating. Because data of this observatory was used for this thesis it is discussed in more detail in Chapter 6.

The European Space Agency (ESA) launched the International Gamma-Ray Astrophysics Laboratory (INTEGRAL) satellite on October 17, 2002. It is still operating and equipped with a variety of instruments covering the optical, X-ray and  $\gamma$ -ray regime (Winkler et al., 2003). The INTEGRAL Spectrometer (SPI) operates from 20 keV to 8 MeV and has an energy resolution of 2.5 keV at 1.3 MeV. Its coded aperture mask made of tungsten has a collecting area of  $\sim 500 \text{ cm}^2$ . A set of 19 germanium blocks operate as detectors providing a spatial resolution of  $\sim 2.5^\circ$  and a timing resolution of  $52 \mu\text{s}$  (Vedrenne et al., 2003). It is complemented by the imaging system IBIS which also uses a tungsten coded aperture mask. IBIS has two detector arrays with a total collecting area of  $2600 \text{ cm}^2$  and provides a FOV of  $9 \times 9^\circ$  and a spatial resolution of  $12'$ . Over an energy range from 15 keV to 10 MeV it achieves an energy resolution of 9% to 10% and a timing resolution of  $61 \mu\text{s}$  (Ubertini et al., 2003). Another coded mask instrument is the Joint European X-ray Monitor (JEM-X). This instrument operates from 3 to 35 keV and uses gas chamber detectors with an energy resolution of 1.37 keV at 10 keV, an angular resolution of  $3.35'$  and a timing resolution of  $122 \mu\text{s}$  over a FOV of  $4.8^\circ$  (Lund et al., 2003). The Optical Monitoring Camera (OMC) is a refracting telescope with an aperture of 50 mm and a focal length of 153.7 mm making it a fast optic with a focal ratio of 3.1. A CCD is located in the focal plain which has  $1024 \times 2048$  pixels with an edge length of  $13.3 \mu\text{m}$ . Because it is operating in frame transfer mode only half of this area is sensitive to light. OMC can obtain optical data over a FOV of  $5 \times 5^\circ$  and detect point sources down to a V-band magnitude of 18 mag with a positional accuracy of  $6''$  (Mas-Hesse et al., 2003). Being a versatile instrument, INTEGRAL enables studies of, among other phenomena, GRBs, galactic and extragalactic black holes, electron-positron annihilation and nucleosynthesis in the Milky Way and supernova remnants. Winkler et al. (2011) gives an overview of the science highlights achieved by INTEGRAL during its first nine years of operation. These include the first all-sky map in the light of the 511 keV electron-positron annihilation line, the discovery of a new class of X-ray binary and the detection of polarized high energy radiation of cosmic origin.

To further investigate the origin of GRBs the National Aeronautics and Space Administration (NASA) launched the *Swift* observatory on November 20, 2004. In honor of the project's principal investigator Neil Gehrels, who passed away in 2017, it was renamed Neil Gehrels *Swift* Observatory in 2018. The Burst Alert Telescope (BAT) is a coded mask instrument with a large FOV of 1.4 steradians (half coded) and a detecting area of  $5240 \text{ cm}^2$ . It is sensitive from 15 to 150 keV with an energy resolution of  $\sim 7 \text{ keV}$  and a spatial resolution of 1 to  $4'$ . With these capabilities it detects and localizes new GRBs in the FOV in 20 seconds and triggers an autonomous slew of the spacecraft to the GRB's position for more detailed observations using *Swift*'s other instruments (Barthelmy et al., 2005). The X-ray telescope (XRT) uses Wolter type I mirrors and a CCD of the same type as the *XMM-Newton* MOS CCDs. It operates over an energy range from 0.2 to 10 keV and has an effective area of  $120 \text{ cm}^2$  at 1.5 keV and a FOV of  $23.6 \times 23.6'$ . After the position of a new GRB was acquired by the spacecraft XRT can determine the exact location of the event with an accuracy of a few arc seconds within 100 s of its beginning (Burrows et al., 2005). Photons of less energy are detected by Ultra-Violet/Optical Telescope (UVOT). It operates at wavelength from 170 to 600 nm and uses a modified Ritchey-Chrétien telescope with an aperture of 30 cm and a focal length of 3.8 m, giving the optics a focal ratio of 12.7. The micro channel plate intensified CCDs in the focal plan provide a FOV of  $17 \times 17'$ . 11 filters can be used to cover different wavelength bands, two grisms enable low resolution spectroscopy in the UV and optical regime and a four times magnifier can quadruple the focal length of the telescope. UVOT can determine the location of GRBs with sub arc second accuracy (Roming et al., 2005). After *Swift* detected a new GRB it continues to monitor its afterglow in regular intervals. Apart from investigating the origin of GRBs *Swift* produced a survey map in hard X-rays, discovers new X-ray transients and monitors known X-ray sources (Markwardt, 2004).

After the launch failure of the *Astro-E* satellite in February 2000, the Institute of Space and Astronautical Science of Japan Aerospace Exploration Agency in collaboration with NASA initiated a recovery mission named *Astro-E2*. After its successful launch on July 10, 2005, it was renamed *Suzaku*. Three instruments onboard enabled studies of astrophysical objects from 0.2 to 600 keV (Mitsuda et al., 2007). Unprecedented spectral resolution of 7 eV was achieved by the X-ray Spectrometer (XRS) which consisted of an array of 36 microcalorimeters sensitive in the range from 0.3 to 12 keV. To achieve this the pixels which are  $624 \mu\text{m} \times 624 \mu\text{m}$  in size were cooled to 60 mK. Unfortunately three weeks into the mission the liquid helium necessary

for the cooling process was vaporized, rendering the instrument inoperable (Kelley et al., 2007). In contrast, the X-ray Imaging Spectrometer (XIS) utilized four CCDs in the focal planes of four mirror assemblies named X-ray Telescopes (XRT) with a focal length of 4.75 m (Serlemitsos et al., 2007). In combination with the CCDs which have  $1024 \times 1024$  square,  $24 \mu\text{m}$  large pixels a FOV of  $18 \times 18'$  was realized. One of the CCDs is backside illuminated, the other front-side, yielding an effective area of  $370 \text{ cm}^2$  and  $330 \text{ cm}^2$  at 1.5 keV, respectively. At 5.9 keV their energy resolution was 130 eV while they were sensitive in the range from 0.2 to 12 keV (Koyama et al., 2007b). Complementing the XIS and XRS, the Hard X-ray Detector (HXD) detected photons with energies from 10 to 600 keV over a FOV of  $4.5^\circ$  at more than 100 keV and  $34'$  at less than 100 keV. Two types of detectors were used for this instrument. Diodes achieved an energy resolution of 3.0 keV and scintillators 12% at 511 keV. The total effective area of the instrument was  $260 \text{ cm}^2$  at 100 keV and the timing resolution  $61 \mu\text{s}$ . The active shielding of the HXD could be used as an all-sky monitor without spatial information (Takahashi et al., 2007). For the first time *Suzaku* was able to identify helium-like chromium and manganese in the intra-cluster medium of the Perseus cluster (Tamura et al., 2009), detected hard X-ray pulsations from an accreting white dwarf (Terada et al., 2008), studied the diffuse emission from the galactic center in great detail (Koyama et al., 2007a) and put constraints on the era of most active iron formation in the universe (Werner et al., 2013).

Installed on the Japanese Experiment Module - Exposed Facility of the International Space Station (ISS) the Monitor of All-sky X-ray Image (MAXI) started operations in August 2009. It uses two slit cameras with a gas proportional counter sensitive from 2 to 30 keV and CCDs operating from 0.5 to 12 keV (Mihara et al., 2011; Tomida et al., 2011). During the roughly 90 min long orbit of the ISS MAXI scans large portions of the sky and can identify transient X-ray events. It monitors the long-term variability of known sources, creates X-ray catalogs and maps the diffuse X-ray emission (Matsuoka et al., 2009).

When the Nuclear Spectroscopic Telescope Array (*NuSTAR*) was launched on June 13, 2012, the first focusing hard X-ray observatory started its operation. It uses two sets of grazing incidence mirrors with a focal length of 10.14 m mounted on an extendible mast. The orientation of the mirrors is measured with respect to the optical bench with the X-ray detectors using two laser metrology units. In combination with information from star trackers the original position of incident X-ray photons can be calculated on ground. A set of four CdZnTe detectors in the focal plane of each mirror module provide a FOV of  $12 \times 12'$ . Each detector has  $32 \times 32$  0.6 mm large square pixels, each of which is equipped with its own discriminator triggering a readout of itself and its eight surrounding pixels upon an interaction with an X-ray photon. *NuSTAR* achieves an angular resolution of  $18''$  (FWHM), a timing resolution of  $2 \mu\text{s}$  and an energy resolution of 400 eV at 10 keV. Bright sources can be localized with an accuracy of  $1.5''$ . The main goals of *NuSTAR*'s mission are the investigation of non-thermal emission originating from young supernova remnants, simultaneous observations of blazars with other facilities to study relativistic jets, observations of core-collapse supernovae in the Local Group and other nearby type Ia supernovae. It is also able to detect hard radiation emerging from obscured AGN and galactic compact objects (Harrison et al., 2013).

The first dedicated Indian astronomy satellite was constructed under the direction of the Indian Space Research Organization and launched on September 28, 2015. Named *Astrosat* it carries a total of five instruments for observations from the optical to the hard X-ray regime (Hutchings, 2014; Singh et al., 2014, 2016; Yadav et al., 2016; Ramadevi et al., 2017; Bhalerao et al., 2017). It can carry out variability studies from the soft to the hard X-rays including correlation studies down to the UV and optical band, search for cyclotron features in spectra of neutron stars and construct spectral energy distributions (SEDs) of a wide range of astrophysical objects.

Insight-HXMT (Hard X-ray Modulation Telescope) uses three sets of instruments to cover the energy range from 1 to 250 keV and delivers a timing resolution down to  $100 \mu\text{s}$ . The Chinese X-ray observatory has been launched on June 15, 2017, and performs temporal studies mainly of known, bright objects (Li et al., 2019).

Launched on June 3, 2017, NICER (Neutron star Interior Composition Explorer) was integrated into the systems of the ISS and started its operations on June 13. With 56 X-ray concentrators and silicon drift detectors it is sensitive from 0.2 to 12 keV with a peak effective area of  $1900 \text{ cm}^2$  at 1.5 keV. During each orbit of the ISS NICER tracks a variety of objects, focusing on neutron stars, and uses its unprecedented timing resolution of better than 100 ns to study the pulse profile of these objects and perform pulse-resolved spectroscopy. NICER is also testing the possibility of using pulsars for navigation in space (Arzoumanian

et al., 2014; Gendreau et al., 2016; Gendreau & Arzoumanian, 2017). The instrument detected the pulsar with the shortest known orbital period of 38 min (Strohmayer et al., 2018) and the brightest X-ray burst observed to date (Bult et al., 2019).

### 4.3 Working with X-ray Data

No instrument used to measure the spectra of X-ray sources in the sky can directly determine its real flux distribution. Following Arnaud et al. (2011) and Wilms (2017) I give an overview of how conclusions about the real nature of X-ray sources can be obtained. The actual quantity provided by the measurement is a variety of events for each of which the pulse height amplitude (PHA) was measured and digitized. Initially introduced for the operation of proportional counters, the term PHA refers to the maximal amplitude of a pulse in voltage caused by the detection of a single event (Knoll, 2000). The discrete energy intervals, corresponding to the discrete steps the PHA values have after the digitization process, are called *channels*. For each incident photon a variety of instrumental properties determine if and in which channel the event is registered. To characterize the overall efficiency of the instrument to detect photons at a given energy,  $E$ , the *effective area*,  $A(E)$ , can be used. It is defined as the virtual energy-dependent sensitive or collecting area the X-ray instrument itself would have if no other inefficiency would occur during the detection process. When X-ray photons are detected they do not necessarily get the PHA value corresponding to their energy assigned. The *response matrix*,  $R(c, E)$ , of the instrument gives the probability for a photon of energy,  $E$ , to be registered in a certain channel,  $c$ . From a theoretical real flux distribution,  $F(E)$ , of a source the count-rate,  $\dot{n}(c)$ , in each channel can then be calculated as

$$\dot{n}(c) = \int_0^{\infty} R(c, E) \cdot A(E) \cdot F(E) dE \quad (4.48)$$

In reality, due to the discrete width of the channels corresponding to discrete intervals in energy,  $\Delta E_i = E_{i+1} - E_i$ , this equation is used in a discretized form

$$N(c) = \Delta T \sum_i^{n_{\text{ch}}} A(E_i) \cdot R(c, E_i) \cdot F(E_i) \cdot \Delta E_i \quad (4.49)$$

which gives the total number of events registered in channel,  $c$ , over an observation lasting for the exposure time,  $\Delta T$ .  $F(E_i)$  is the theoretical flux of the source in the energy band with the width  $\Delta E_i$ . This total number of measured counts still includes the number of background counts,  $B(c)$ , not originating from the source. To recover the real number of counts,  $S(c)$ , originating from the source itself the background has to be subtracted,

$$S(c) = N(c) - B(c) \quad (4.50)$$

In practice, when X-ray focusing optics are used, the background data are taken from an area on the sensor close to source of interest. The error,  $\sigma(S(c))$ , can then be estimated under the assumption of Poisson statistics as

$$\sigma(S(c)) = \sqrt{\sigma(N(c))^2 + \sigma(B(c))^2} \quad (4.51)$$

A comparison between a theoretical flux distribution and a real measurement cannot be done directly but the model flux has first to be calculated on the grid given by the energy bins,  $\Delta E_i$ , and then convolved through equation 4.49.

To interpret an X-ray spectrum often a theoretical distribution,  $F(E)$ , correctly describing the observed data is sought. Usually the calculation of  $F(E)$  depends on additional parameters reflecting the physical mechanism expected to produce the spectral shape, for example the temperature of a blackbody distribution. How well a particular distribution  $F(E)$  calculated from a set of parameters fits to the observed data after

being convolved through equation 4.49 can be judged using a *likelihood function*. It can be defined as

$$\mathcal{L} = \prod_i^{n_{\text{ch}}} \text{Prob}(S(i)|M(i, \vec{\alpha})) \quad (4.52)$$

where  $\text{Prob}(S(i)|M(i, \vec{\alpha}))$  is the probability of finding the number of counts,  $S(i)$ , in the  $i$ th channel with the prediction by the model,  $M(i, \vec{\alpha})$ , calculated by a set of parameter,  $\vec{\alpha}$ , for this channel. Inserting the Poisson distribution

$$\text{Prob}(S(i)|M(i, \vec{\alpha})) = \frac{M(i, \vec{\alpha})^{S(i)} e^{-M(i, \vec{\alpha})}}{S(i)!} \quad (4.53)$$

and taking the logarithm yields the *log-likelihood*,

$$\ln(\mathcal{L}) = \sum_i^{n_{\text{ch}}} (-M(i, \vec{\alpha}) - \ln(S(i)!) + S(i)\ln(M(i, \vec{\alpha}))) \quad (4.54)$$

For numerous counts the Poisson distribution converges to the Gaussian distribution of the form

$$\text{Prob}(S(i)|M(i, \vec{\alpha})) = \frac{1}{\sigma(S(i))\sqrt{2\pi}} \exp\left(-\frac{(S(i) - M(i, \vec{\alpha}))^2}{2\sigma(S(i))^2}\right) \quad (4.55)$$

and therefore

$$\ln(\mathcal{L}) = \sum_i^{n_{\text{ch}}} \ln\left(\frac{1}{\sigma(S(i))\sqrt{2\pi}}\right) - \frac{1}{2} \sum_i^{n_{\text{ch}}} \frac{(S(i) - M(i, \vec{\alpha}))^2}{\sigma(S(i))^2} = \sum_i^{n_{\text{ch}}} \ln\left(\frac{1}{\sigma(S(i))\sqrt{2\pi}}\right) - \frac{1}{2}\chi^2 \quad (4.56)$$

where the chi-square ( $\chi^2$ ) statistic was introduced. The left part of this log-likelihood cannot be affected by changes in the set of model parameters,  $\vec{\alpha}$ , therefore often only  $\chi^2$  is used to judge the fit to the data and optimized the model parameters. The entire  $\ln(\mathcal{L})$  can be maximized by just minimizing  $\chi^2$ . This task can be achieved by a variety of computerized algorithms to find the optimal fit of the model to the data, a process often called *spectral fitting*. Using the value of  $\chi^2$  divided by the number of degrees of freedom the quality of the fit can be judged. The resulting value is called reduced chi-square,

$$\chi_{\text{red}}^2 = \frac{\chi^2}{N_{\text{dof}}} \quad (4.57)$$

where  $N_{\text{dof}}$  can be calculated from the number of bins,  $n_{\text{bins}}$ , minus the number of free parameters,  $n_{\text{free}}$ , of the set  $\alpha$ ,

$$N_{\text{dof}} = n_{\text{bins}} - n_{\text{free}} \quad (4.58)$$

If  $\chi_{\text{red}}^2$  is much higher than one then the model in its current set of parameters,  $\vec{\alpha}$ , is not describing the data accurately and large deviations are present. On the other hand, if  $\chi_{\text{red}}^2$  is much smaller than one (but above zero), then the model is over predicting the observed data and possibly describing features which originate in statistical noise. Only when  $\chi_{\text{red}}^2 \simeq 1$  the model can be considered as describing the data accurately within the limits imposed by the statistical errors from the measurement.

Another statistic to judge the goodness of a fit was introduced by Cash (1979)

$$C = 2 \sum_i^{n_{\text{ch}}} (M(i, \vec{\alpha}) - S(i)\ln(M(i, \vec{\alpha}))) \quad (4.59)$$

As shown by Cash (1979) this fit-statistic is better suited to describe data with low-count statistics while in the asymptotic limit of many counts per bin it reproduces the  $\chi^2$ -statistic. Throughout this thesis several datasets with a very low signal-to-noise ration (SNR) will be analyzed, therefore, mostly the  $C$ -statistic is

#### 4 *X-ray Astronomy*

used.

## 5 The X-ray Survey Instrument *eROSITA*

extended ROentgen Survey with an Imaging Telescope Array (*eROSITA*) is the primary instrument onboard the *Spectrum-Roentgen-Gamma* (*SRG*) mission. It has been designed and constructed to perform an all-sky survey in the energy band from 0.1 to 10 keV with a FOV of  $1^\circ$ . *eROSITA* is expected to discover millions of AGN and hundreds of thousands of galaxy clusters and will therefore provide new insight into the structure of the universe on cosmological scales. Apart from this primary incentive it can also discover and characterize variable sources in the X-ray sky like X-ray binaries, GRBs and stars because it observes each position in the sky in intervals of 4 h during at least six consecutive visits every six months. To quickly identify these transient events and enable rapid additional investigations in the form of follow-up observations the author of this thesis, in collaboration with other members of the Remeis observatory, developed the *eROSITA* Near Real-Time Analysis (NRTA) pipeline. To highlight the most important aspects and some results of this software a summary of the *eROSITA* instrument, and the *SRG* mission in general, is given, its main objectives are discussed, after which the NRTA is described in detail and one particular transient event detected by it is presented as an exemplary result.

### 5.1 The *Spectrum-Roentgen-Gamma* Mission

The *SRG* mission consists of three major components. Mikhail Pavlinsky Astronomical Roentgen Telescope – X-ray Concentrator (*ART-XC*) and *eROSITA* are the scientific payload which is carried on the infrastructural *Navigator* platform. A detailed description of *ART-XC* and *Navigator* can be found in Sunyaev et al. (2021). To provide context for the entire mission a brief description of *ART-XC* and *Navigator* based on this publication is presented.

*Navigator* was developed and built by NPO Lavochkin (NPOL) and has already been used for the scientific Radioastron (*Spektr-R*) mission and the first of the two meteorological *Electro-L* satellites. *Spektr-R* was an orbit based radio telescope with a ten-meter dish working in conjunction with ground based radio telescopes to perform Very Large Baseline Interferometry (VLBI) (Alexandrov et al., 2012a,b). It has been slightly modified to adjust for the requirements of the *SRG* mission which is not orbiting the Earth. Most notably a new and more powerful X-band radio complex was installed which is necessary to provide reliable communication between the spacecraft located at Langrange point two (L2) and the radio antennas on ground. *Navigator* also houses the solar panels which can be reoriented towards the Sun and are the main source of electricity of the spacecraft. It is predicted that the solar panels will be able to provide 1870 W of power at the end of their lifetime which is more than the nominal total power consumption of 1700 W of all systems on the spacecraft combined. Until their deployment after the launch a 55 Ah battery provided enough power for the control systems. For attitude control reaction wheels are used. Over time the angular momentum of these devices can built up. Eight small thrusters providing 0.5 N of force can be used to dump this angular momentum with an additional eight thrusters for reserve. A set of larger thrusters with 5 N of force can be engaged for larger adjustments of the spacecraft’s trajectory. All thrusters are fueled by two tanks initially containing 360 kg of hydrazine in total. By combining data from the onboard star trackers and gyroscopes, *Navigator* can determine its attitude within a margin of  $10''$  and control its angular velocity with an accuracy of  $0.72''/s$ . The nominal survey rate is  $0.025^\circ/s$ . Scientific data can be transferred to ground by the radio complex at a rate of 512 Kbit/s while uploading of commands to the spacecraft is done at 500 Bit/s.

*ART-XC* was renamed to Mikhail Pavlinsky *ART-XC* in honor of the scientific advisor of Space Research Institute of the Russian Academy of Sciences (IKI) and principal investigator of *ART-XC* who passed away on July 1st, 2020, after the launch of *SRG*. The instrument was developed by IKI and All-Russian Scientific Research Institute for Experimental Physics (VNIIEF). It uses seven mirror modules with a focal length of 2700 mm built by NASA’s Marshall Space Flight Center (MSFC) to focus X-rays onto the focal plains of its

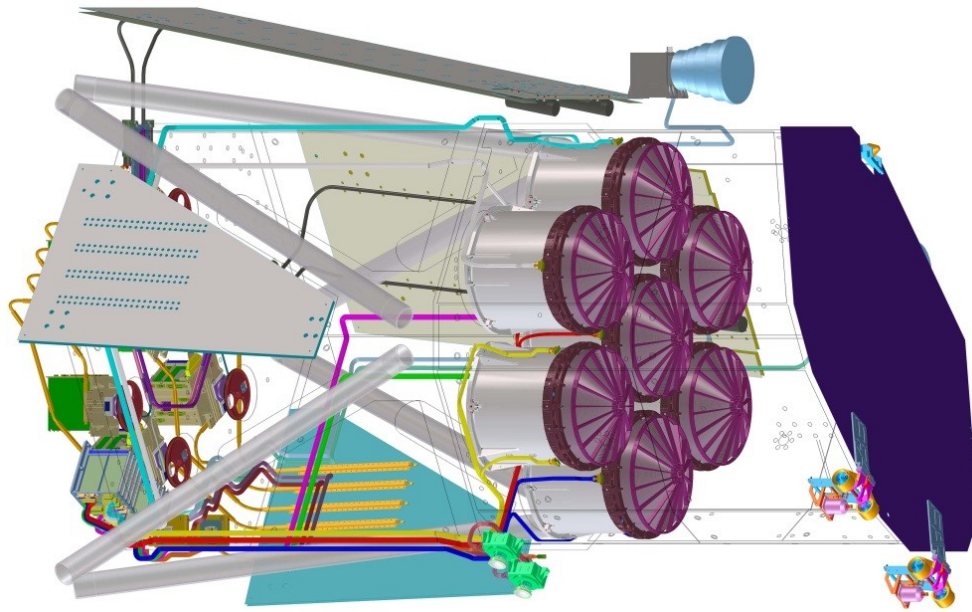


Figure 5.1: Drawing of the *eROSITA* instrument. On the right-hand side is the closed blue front cover which after release can swing down. To its left are the seven mirror modules inside the shaded hexagonal structure of the instrument with the baffles on top (wine red). On the top a front facing star tracker is visible (light blue) and on the very left three of the seven camera modules including the filter wheels (red) and electronic boxes (green) are visible. The outside of the structure is surrounded by four radiators. Taken from Predehl et al. (2021).

telescopes while being able to operate in the energy range from 4 to 30 keV. During the all sky survey the effective upper limit is expected to be around 12 keV. Detection of the X-rays in the focal planes is achieved by double-sided silicon strip detectors. These devices consist of an n-doped silicon wafer with highly p-doped and n-doped stripes in parallel on the top and bottom. The predominant direction of both sets of stripes are perpendicular to each other. When an X-ray photon hits the silicon and deposits its energy electron-hole pairs are created which propagate to the stripes and generate a measurable voltage corresponding to the photon's energy. Spatial information can be recovered by the distribution of voltage on the grid of stripes (Speller et al., 2001). The cadmium telluride based sensors of *ART-XC* use 48 stripes on each side over the  $30 \times 30$  mm large die and can achieve a spatial resolution of  $54''$  over a FOV of 0.3 square degrees while the overall effective area of the instrument is  $385 \text{ cm}^2$  at 8.1 keV and the time resolution  $23 \mu\text{s}$  (Pavlin et al., 2021).

## 5.2 The *eROSITA* Instrument

A comprehensive description of the *eROSITA* instrument is given in the instrumental paper by Predehl et al. (2021). Following this publication the main aspects of the instrument will be described.

The roughly hexagonal outside structure is about 1.9 m in diameter and 3.2 m in length and has a total weight of 808 kg. Until the instrument was in space and isolated from the carrier vehicle the front facing entrance for light was protected from debris by a large cover. Two star trackers are located at the front for an accurate determination of the attitude. Four radiators on the side provide cooling for the cameras and electronics (Eder et al., 2018).

### 5.2.1 Optical Tube Assembly

Focusing of X-rays onto the focal plane is accomplished by seven Wolter type I telescope modules with a focal length of 1600 mm. The 54 nickel shells of each mirror module are coated with gold on the side reflecting the X-rays and have an outer diameter of 360 mm. On ground an on-axis resolution of the mirror modules of  $16.1''$  was measured at 1.5 keV (Friedrich et al., 2008). Because of the Wolter type I design of the mirrors photons from sources just outside the FOV can be scattered onto the focal plane by single reflections. To mitigate this problem baffles were created which consist of 54 concentric cylindrical shells with increasing height towards larger radii. They are held in place by so called “spiders” which consist of 16 triangular shaped spacers spreading out from the center of baffles which were mounted on top of the mirror modules such that the shells of the baffles directly extend the shells of the mirrors (Friedrich et al., 2014). Cosmic particles of low energy entering the mirror assembly from the front, for example electrons, are redirected by magnetic deflectors. Fig. 5.1 shows the structure of the instrument in a schematic way. Each mirror assembly in combination with a camera in the focal plane is referred to as a Telescope Module (TM). The TMs are enumerated with numbers from 1 to 7.

### 5.2.2 Camera Modules

The CCDs of the telescope modules are located 0.4 mm closer to the mirror assemblies than the focal plane. A property of the Wolter type I mirrors is decreasing performance towards higher off-axis angles in the form of larger and butterfly-shaped point spread functions. By shifting the sensors slightly intra-focal the on-axis resolution of the instrument is decreased to  $18''$ , but the average overall resolution is increased to  $26''$ .

The CCDs are square shaped with an edge length of 28.8 mm and have  $384 \times 384$  square pixels with a size of  $75 \times 75 \mu\text{m}$ . This results in a square FOV of  $1.03 \times 1.03^\circ$  and a diagonal of  $1.45^\circ$  in combination with the mirror assembly with each pixel covering an angular segment of  $9.6 \times 9.6''$ . Base material of the back illuminated CCDs is  $450 \mu\text{m}$  thick silicon and the individual pixels are made of pn-diodes. The nominal exposure time of the system is 50 ms which has been chosen as a compromise between good time resolution at shorter exposure times and less heat dissipation in the focal plane at longer exposure times. With 50 ms the heat dissipation has been measured to be 0.7 W. After an exposure the entire array of charge clouds deposited in the silicon of the sensor is shifted in  $115 \mu\text{s}$  into the frame store area. This rectangular area directly next to the pixel array houses  $384 \times 384$  potential wells which can hold the charge clouds during the readout and digitization procedure. The individual elements of the frame store area are  $75 \times 51 \mu\text{m}$  in size and shielded against X-rays to reduce the amount of out-of-time events. The usage of the frame store area for the *eROSITA* cameras reduces the probability for such events by 99.8%. Additionally, a massive copper shield around the CCDs protects them from cosmic particles. If in turn a cosmic particle is absorbed in this shield X-ray fluorescence can occur producing additional background. To mitigate this problem another shield consisting of aluminium, beryllium, and boron-carbide is in place. Readout of the charge clouds from the frame store area is performed by three analog signal processors called CMOS Amplifier and MultipLEX chip (CAMEX) with 128 channels each (hence the  $3 \cdot 128 = 384$  columns of the sensor) in 9.18 ms and a depth of 14 bits. The readout noise of the sensor has been measured to 2.5 electrons using the root-mean-square while the energy resolution at 0.5 keV is 64 eV at FWHM decreasing linearly to 202 eV at 9.7 keV. Best mitigation of radiation damage is feasible at an operating temperature of  $-95^\circ\text{C}$  (Meidinger et al., 2014) although in practice the sensors are only cooled to  $-85^\circ$ . Each camera module is connected via a heat pipe to two redundant ring heat pipes transporting thermal energy to the four radiators on the outside of the instrument (Fürmetz et al., 2008).

In front of the sensors filter wheels (FWs) are located which have four different positions. First, the FWs are set to CLOSED, meaning the FW itself is blocking the path towards the sensor. In this position the CCDs are protected while the instrument is on ground and in space it can be used to measure the intrinsic instrumental background. To completely vent the gas from the instrument the FWs can be set to the OPEN position. For calibration purposes the CALIB position can be set. In this position a radioactive  $^{55}\text{Fe}$  is located which creates spectral emission lines at energies of 5.9 keV and 6.5 keV. Additional emission lines at 4.5 keV and 1.5 keV are created by fluorescence of the radiation in an aluminum and titanium target. For most of the observing time the FILTER position is being used where a polyimide foil of 200 nm thickness is located in front of the sensor. This foil provides blocking of UV light. To prevent optical light from hitting



Figure 5.2: Launch of the *SRG* spacecraft from launch site 81 of the Baikonur Cosmodrome on July 13th, 2019, 12:31 UTC onboard a Proton-M rocket. Taken from IKI's webpage<sup>1</sup>; Image credit: TsENKI/Roscosmos.

the sensor and generating false signal the sensors of TMs 1, 2, 3, 4 and 6 are evaporated with a 100 nm thick layer of aluminium while for TMs 5 and 7 this layer is evaporated onto the polyimide foil in the FW (Meidinger et al., 2010, 2011, 2012, 2014).

Connected to the cameras are seven sets of Camera Electronics (CE) responsible for supplying power to the cameras, timing and onboard data processing during which fixed offsets are applied to the readout data and events caused by cosmic particles are rejected. After that the valid events are encoded and written into telemetry frames together with housekeeping data, consisting of infrastructural information such as temperatures and voltages. The CEs communicate with the central Interface and Thermal Controller (ITC) which writes the telemetry frames into the mass memory. The ITC is also responsible for supplying power to the cameras and send commands to them while it in turn is connected to the power distribution and communication system of the *Navigator* platform.

### 5.3 Launch and Commissioning

*SRG* was launched on July 13th, 2019, 12:31 UTC from the Baikonur Cosmodrome in the desert of Kazakhstan on launch site 81. A Proton-M rocket with three stages was used as the launch vehicle with a BLOK-DM03 space tug as a fourth stage. After roughly two minutes the first stage separated, after roughly five and a half minutes the second stage and after roughly nine and a half minutes the third stage which subsequently separated from the BLOK-DM03 module. The space tug then inserted *SRG* into a trajectory towards L2 and exactly 2 h after the launch separated from the spacecraft. Eight minutes after the separation first telemetry from *eROSITA* was received and decoded on ground. On July 22 the *Navigator* platform performed the first maneuver to correct the trajectory and a day later the front cover of *eROSITA* was opened successfully. During this operator the swinging cover introduced additional angular momentum to the spacecraft which caused its pointing to deviate from the nominal position. Data from the first of the two star trackers of *eROSITA* during this occurrence is shown in Fig. 5.3 where it can also be seen how the spacecraft's attitude control system recovers the pointing. After the cover was opened the outgassing of the instrument started. During this time all remaining gas was vented from the inside of the instrument. To support this process and to prevent any residue from building up on the CCDs the cooling system of the cameras stayed inactive. A second trajectory correction was carried out on August 6 and on August 22 the cooling system of the cameras was switched on which marked the start of the commissioning phase of the

<sup>1</sup><https://www.roscosmos.ru/media/gallery/big/26563/3434770793.jpg>

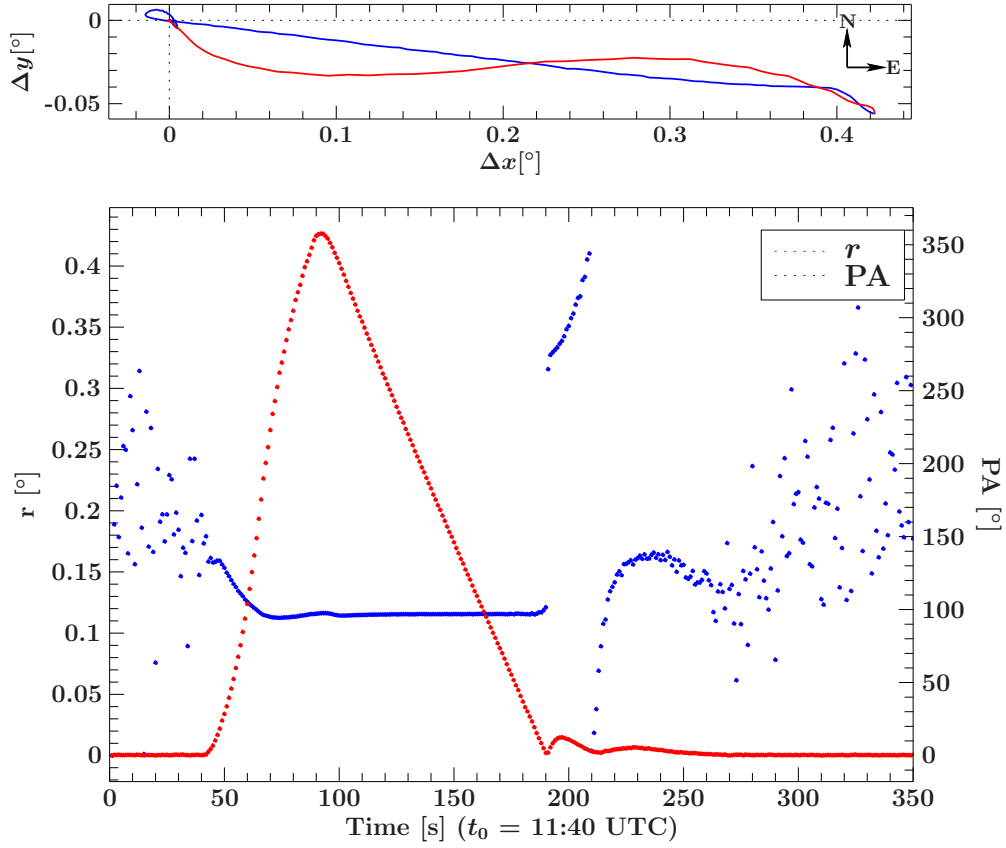


Figure 5.3: Deviations from the nominal pointing of *SRG* due to the angular momentum introduced when *eROSITA*'s protective cover was opened.

**Top:** Path of the spacecraft's pointing on the sky with respect to the nominal position at the origin of the coordinate system. Red points indicate that the pointing was moving away from the nominal position and blue points that it was moving back towards it.

**Bottom:** Same data but represented in form of the angular separation (red) and position angle (blue) of the pointing with respect to the nominal pointing in dependence of time. The attitude control of *SRG* was able to correct for this effect in less than five minutes. The data were measured by the first of two star trackers on *eROSITA* and extracted from the housekeeping data using the NRTA web front end.

instrument. During this phase, on August 10, a CE unit experienced a processor crash and several settings regarding control voltages of the cameras were found changed without being commanded. For the purpose of investigation and to minimize the risk of damage to the hardware the commissioning phase was extended. The so called "commissioning first light" was carried out with only two TMs on September 15 and targeted the supernova remnant SN 1987A in the Large Magellanic Cloud (LMC). The commissioning phase ended when in the time from 16th to 18th of October all seven cameras were switched on and revisited SN 1987A for the official first light of the instrument. After that the Calibration and Performance Verification (CalPV) phase followed during which pointed observations of several known targets were carried out. During this phase the initial in-orbit calibration of the instrument was performed, which was especially aided by simultaneous observations of other instruments, and expectations from the tests on ground were verified. A third correction to the trajectory of the spacecraft was performed on October 21 and the CalPV phase ended on December 8. Five days later the all-sky survey began.

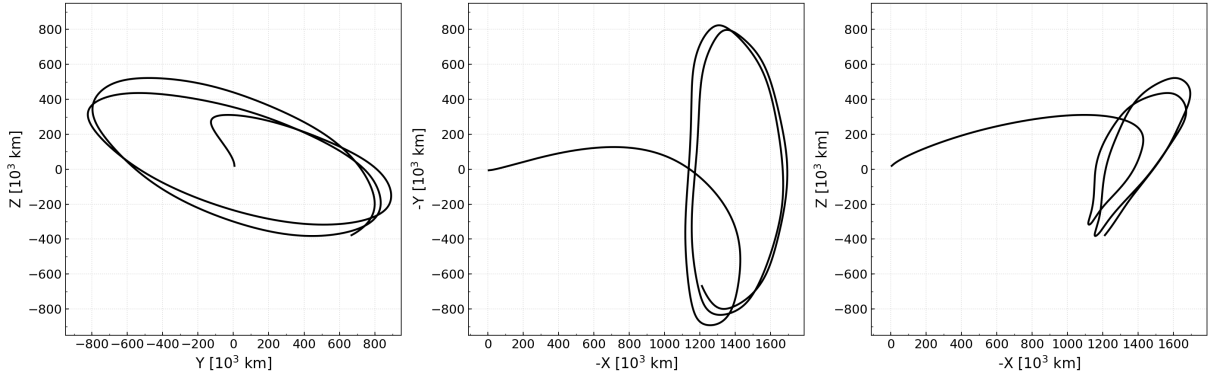


Figure 5.4: Trajectory of *SRG* for 450 days after the launch. Ecliptic projection was used to show the data in Geocentric Solar Ecliptic coordinates. In the  $X$ - $Y$  and  $X$ - $Z$  planes the 100-day-long journey of *SRG* to the area around  $L2$  is visible. Taken from Predehl et al. (2021).

## 5.4 Orbit and Mission Planing

*SRG* is orbiting a special point in the gravitational system created by the Sun and the Earth, the Lagrange point two ( $L2$ ). In total five Lagrangian Points are created by two orbiting masses. The effective potential created by these two massive bodies can be calculated by superposition of both gravitational potentials and the potential created by the centrifugal force. The Lagrangian points manifest themselves in the form of five local maxima in this effective potential, hence the gradient of this potential and therefore the force acting on a third and much smaller mass is zero. The first Lagrangian Point is located between the Earth and the Sun, roughly 1.5 million kilometers from Earth. Solar observatories such as *Solar and Heliospheric Observatory (SOHO)* are suitably located at this position (Domingo et al., 1995). Other non-solar observatories are preferably located at  $L2$  which is located on the same virtual line from the Sun to the Earth but 1.5 million kilometers beyond the Earth's orbit. Notable examples utilizing this point are the *Herschel* infrared observatory (Harwit, 2004), the microwave observatories targeting the cosmic microwave background *Wilkinson Microwave Anisotropy Probe (WMAP)* (Bennett et al., 2003) and *Planck* (Tauber et al., 2010a,b) and the astrometric Gaia mission (Gaia Collaboration et al., 2016). The  $L3$ ,  $L4$  and  $L5$  points are located on the path of Earth's orbit around the Sun with  $L3$  being exactly at the opposite side of the Earth, rendering it useless for the placement of any spacecraft.  $L4$  and  $L5$  are situated at an angle of  $60^\circ$  off the connection between  $L3$  and the Sun.

To precisely communicate the orientation of the spacecraft and relative directions to it, a distinct coordinate system is defined. In the direction of the line of sight of the telescopes the  $X$ -axis is oriented. The solar panels are defined to be extended in the  $Y$ -direction. Perpendicular to both is the  $Z$ -axis which is the main rotational axis of the spacecraft. The antenna complex is pointed in this direction. Two main constraints are imposed by a variety of factors on the orientation of the spacecraft. The beam width of the antenna complex is  $48^\circ$  in total therefore the  $Z$  axis can only deviate  $24^\circ$  or less from the direction towards the Earth for communication purposes. To provide enough power the normal of the solar panels can span an angle of  $20^\circ$  at most with the Sun which is also required to prevent solar stray light from entering the telescopes apertures and to maintain the cooling capabilities of the radiators. Other limitations require the Sun to be within  $13^\circ$  of the  $X$ - $Z$  plane, therefore this lower limit is in place for the angle of the  $Z$ -axis towards the Sun.

*SRG*'s orbit consists of a motion around  $L2$  with a period of half a year and a semimajor axis of 750000 km. Along with the Earth,  $L2$  also moves around the Sun which results in a constantly changing orientation of *SRG*'s orbit to comply with the given restrictions. During the all-sky survey *SRG* is rotating with a rate of  $0.025^\circ/\text{s}$  around the  $Z$ -axis which is called *scan rate*. This rate corresponds to a rotational period of 4 h which is also used as a unit of time specific to the *eROSITA* instrument, called the eroday. One eroday corresponds to the duration of one nominal rotation of the *SRG* spacecraft around its  $Z$ -axis and is 4 h =

14400 s long. eroday 1 is defined to be on January 1, 2000 at 00:00 UTC. A specific point on the celestial sphere spends about 40 s in the FOV. Because of the movement of L2 along the Earth’s orbit, in combination with the restrictions on the orientation of the  $Z$ -axis, this axis also rotates with a period of

$$\frac{360^\circ}{365.24 \text{ d}} \simeq 1.0 \text{ deg day}^{-1} = \frac{10'}{4 \text{ h}} \quad (5.1)$$

called the *survey rate*, meaning each subsequent great circle is shifted by  $10'$  and overlaps with the previous one by  $52'$  at the equator of the rotation, given by the FOV of  $1.03^\circ$ . At the equator a point in the sky is scanned six times until it is revisited again after six months. The rotational axes of *SRG* are pointing towards the *survey poles* which have been chosen to be aligned with the ecliptic poles. In total eight individual all-sky surveys are planned which will take four years. After this pointed observations of dedicated targets will be carried out. During one survey 200 s of exposure at the ecliptic equator are accumulated while for the constantly scanned ecliptic poles this value is as high as 4000 s. When the planned eight surveys are finished the total exposures will be 1600 s and 30000 s, respectively.

*SRG* has contact to several radio antennas on ground every day for roughly 4 h in total. The main ones in use are located in Bear Lake and Ussuriysk and the time of each ground contact is split between operation of the spacecraft itself by NPOL and operation of and dumping science data from *ART-XC* by IKI and *eROSITA* by Max Planck Institute for Extraterrestrial Physics (MPE). Roughly 60% of these 4 h are dedicated to the *eROSITA* operations team which performs monitoring of the central infrastructure of the instrument, such as power distribution and thermal control, and the health of the cameras via housekeeping parameters and real time transmission of events. Commands are sent to the instrument and executed either in real-time or scheduled to a later point which is not during the ground contact. The science data are dumped from mass memory at a rate of roughly 400 MB per session.

## 5.5 Data Ownership and Release

The two space agencies involved in the project are Roscosmos from the Russian side and Deutsches Zentrum für Luft- und Raumfahrt (DLR) from the German side. All data obtained by *eROSITA* is considered proprietary and split between both participants as determined by two hemispheres in galactic coordinates. The border between both hemispheres is defined as the great circle with constant galactic longitude passing through the position of Sgr A\*, located at  $l = 359.94423568^\circ$  and  $b = -00.04616002^\circ$ .<sup>2</sup> Ownership of the data originating from the hemisphere westwards from this location ( $l \in [180.05576432^\circ, 359.94423568^\circ]$ ) lies with MPE which has the responsibility to manage the access rights and scientific exploitation of it in the German *eROSITA* collaboration. All data held by the German *eROSITA* collaboration is planned to be eventually publicly available through a variety of data releases. End of June 2021 the data taken during the CalPV phase was released to the public accompanied by 35 scientific publications by members of the German *eROSITA* collaboration. Data accumulated during the first all-sky survey is planned to be released in 2022, from the first four all-sky surveys in 2024 and all the data from the full set of eight all-sky surveys in 2026. After the eight all-sky surveys are completed the *SRG* mission will carry out pointed observations which can be proposed by the scientific community.

## 5.6 Instrument Performance

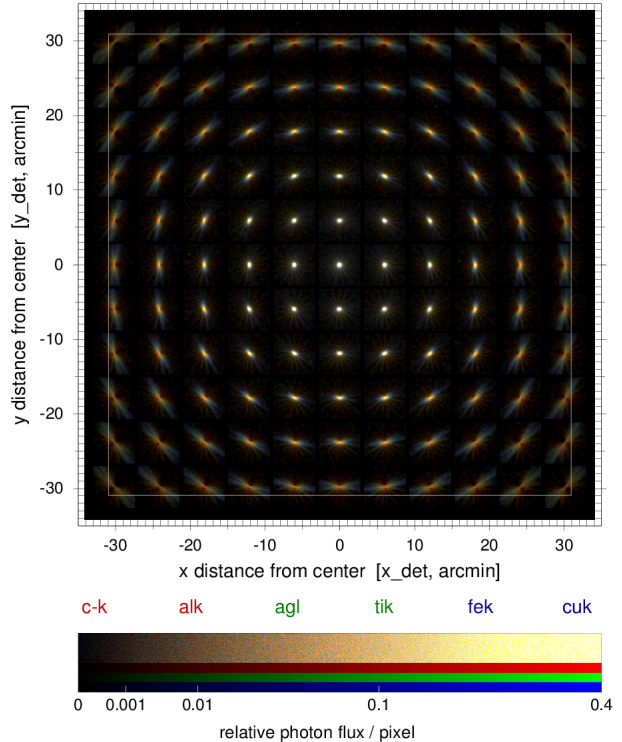
In the following the performance of the *eROSITA* instrument as theoretically calculated and measured on ground and in space will be discussed. Tests on ground were performed at MPE’s X-ray test facilities PUMA and PANTER. PUMA<sup>3</sup> is a six meter long evacuated vacuum chamber on one side of which an X-ray source with multiple targets made of different elements is located. The X-rays are absorbed by these elements which then emit radiation at specific energies from 0.28 keV for carbon up to 8.04 keV for copper. This radiation is then used to test the optics and/or detectors. PANTER<sup>4</sup> works similarly but provides a

<sup>2</sup>According to the SIMBAD database (Wenger et al., 2000) [http://simbad.u-strasbg.fr/simbad/sim-id?Ident=Sgr+A\\*](http://simbad.u-strasbg.fr/simbad/sim-id?Ident=Sgr+A*)

<sup>3</sup><https://www.mpe.mpg.de/resources/HE/PUMA/main.html>

<sup>4</sup><https://www.mpe.mpg.de/heg/panter>

Figure 5.5: Point Spread Function (PSF) measurements taken with TM1 at different positions on the detector and energies. As shown by the color scale the brightness corresponds to the photon flux in each pixel and the color is used as a measure for the hardness. This is achieved by combining the photons from the C-K (0.227 keV) and Al-K (1.49 keV) emission lines into the red channel, from the Ag-L (2.984 keV) and Ti-K (4.51 keV) lines into the green channel and from the Fe-K (6.40 keV) and Cu-K (8.04 keV) lines into the blue channel. Taken from Predehl et al. (2021).



beam line of 130 meters through a vacuum tube with a diameter of one meter. At the end of this tube the test chamber is located with a diameter of 3.5 meters. The completely assembled *eROSITA* instrument was tested inside this chamber.

### 5.6.1 Point Spread Function

The Point Spread Function (PSF) describes the response of an optical system to the illumination by a point source. In other words, the PSF is the picture of a point source generated in the focal plane of an optical system. Generally, the PSF for a telescope with a finite aperture cannot be only a point in the focal plane but has some extent. This effect caused by diffraction at the telescope's aperture. If the aperture is of circular shape and otherwise now flaws are present the picture of a point source is an airy disk. In practice however, and especially for X-ray telescopes employing Wolter optics, the PSF can have a much more complicated shape which also varies across different off-axis angles. To calibrate the PSF for *eROSITA* the PANTER facility was used to illuminate the telescope's optics with a quasi-parallel beam of photons at different energies and from different angles covering the entire FOV of  $1^\circ$  in diameter. The resulting PSF map for TM1 is shown in Fig. 5.5. As can be seen, the on-axis PSF at the center of the frame is point-like in shape but has some extent and upon close inspection the diffraction spikes generated by the spacers of the baffles can be seen. The FWHM has been measured for all TMs in the range from 7.0 to 9.3'' at 1.49 keV and from 5.7 to 7.9'' at 8.04 keV. The further off-axis the beam was oriented the more pronounced the for Wolter type I telescopes typical butterfly shape emerges. This effect can also be seen in Fig. 5.5 where one can recognize from the color coded hardness of the radiation that photons of higher energies lie further out in the wings of the shape.

### 5.6.2 Effective Area

Multiple steps are necessary for an X-ray photon entering the aperture of the telescope to be detected by the sensor in the focal plane. A measure for the overall effectiveness of this procedure is the *effective area*. First, due to the geometry of Wolter telescopes, photons are not focused over the area of the entire aperture.

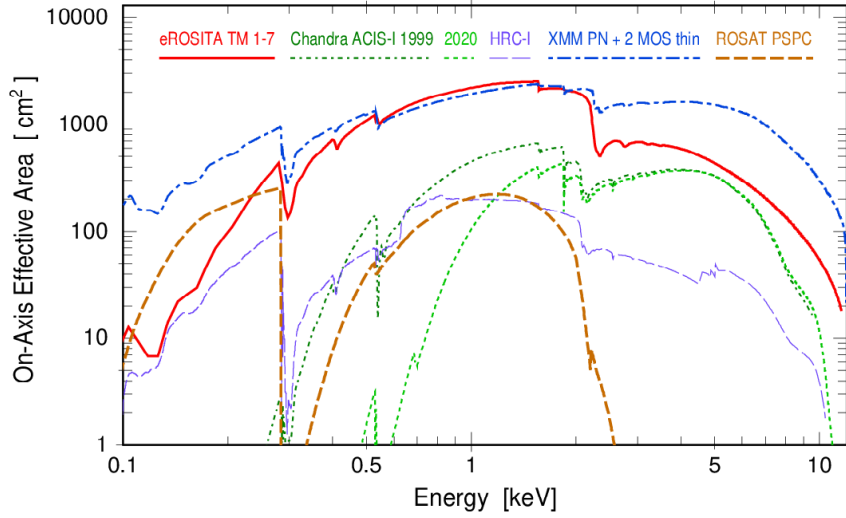


Figure 5.6: Effective area for all seven TMs of *eROSITA* combined (red) compared to a selection of other X-ray observatories. Taken from Predehl et al. (2021).

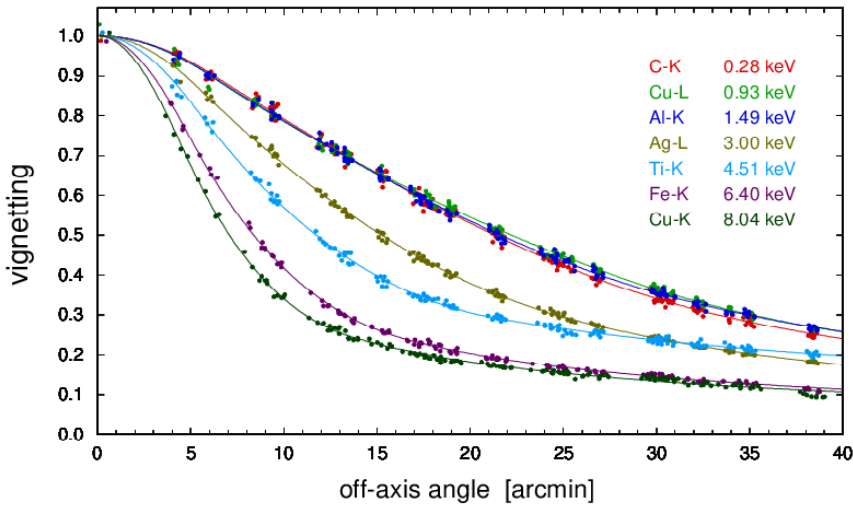


Figure 5.7: Vignetting measurements for TM1 at seven different energies. Taken from Predehl et al. (2021).

When they are reflected off the mirrors also losses can occur. Those hitting the detector are only registered with a certain probability which is the quantum efficiency. All of these processes depend on the energy of the incident photon. The effective area can be used as a proxy for all of these effects combined in that it gives the virtual area of the aperture to use for any calculations regarding properties of sources. The effective area of *eROSITA* is shown in Fig. 5.6. From this diagram it becomes apparent that the sensitivity of *eROSITA* is mainly present in the energy range from 0.1 to 10 keV. Also, characteristic absorption edges of material used in the CCDs, such as silicon, can be seen in the effective area.

### 5.6.3 Vignetting

The effective area, as described before, is only valid for sources which are exactly on-axis at the center of the FOV. For deviations from the central position the flux measured of a given source is smaller. This effect called vignetting has also been quantified with the same measurement done as for the PSF and has

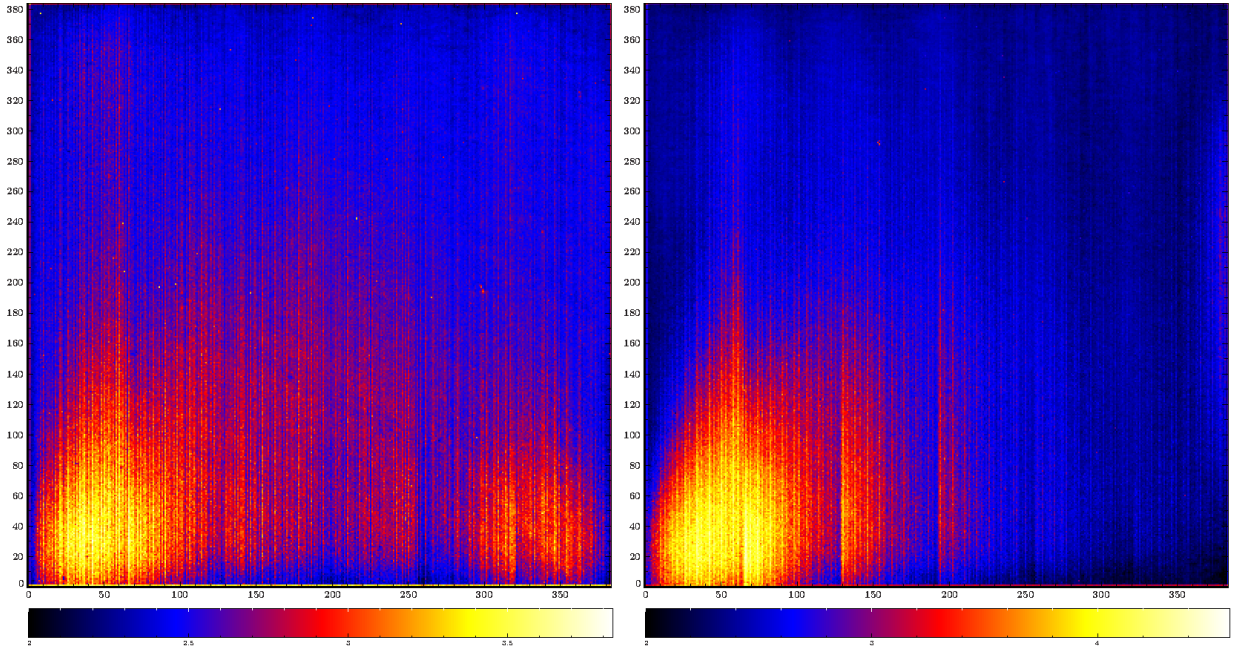


Figure 5.8: Raw detector images of TM5 (left) and TM7 (right) of erodays 43900 to 43999 in logarithmic scale. The large scale patterns with more illumination on both bottom corners for TM5 and on the bottom left corner for TM7 caused by optical light entering the camera bodies and reaching the CCDs. During this particular period the extent of the leak was more pronounced for TM7.

to be taken into account when calculating properties of sources and effective exposure maps. To specify the amount of vignetting in dependence of the off-axis angle the total flux inside a circle of  $8'$  in diameter was measured and compared with the flux measured in the corresponding circle for the on-axis PSF. Dividing the first by the latter gives a value between zero (100% vignetting) and one (no vignetting). These vignetting curves have been measured at different energies from 0.28 keV (C-K line) to 8.04 keV (Cu-K line) and are shown in Fig. 5.7. For all energies the amount of vignetting increases towards larger off-axis angles. Up to a photon energy of 1.49 keV the curves are almost identical while for higher energies the amount of vignetting is higher (i.e., the ratio is lower) and also drops more rapidly for increasing off-axis angles.

#### 5.6.4 Optical Light Leak

As explained in Section 5.2.2, TMs 5 and 7 are not equipped with on-chip filters to block optical light from causing wrong signal in the CCDs but have the film of aluminum for this purpose on the polyimide foil in the FW which is responsible for blocking UV light. During the commissioning phase it was recognized that these two TMs show strongly elevated levels of signal in the low energy regime. In Fig. 5.8 I show the accumulated data in raw detector coordinates for both TMs over a period of 100 erodays (2.5 days) in logarithmic scale. An excess of signal in both bottom corners for TM5 and the bottom left corner for TM7 can be recognized. In both cases the amount of signal in these bright areas is about a magnitude larger than in the remaining image. This behavior can be explained by optical light leaking into the area of the CCDs via some other way. The amount of additional signal strongly depends on the orientation of the spacecraft with respect to the sun. To prevent the available telemetry from being consumed by this effect the energy thresholds for events from these cameras to be valid has been raised from 80 eV to 125 to 140 eV. By analyzing the dependence of this effect on several factors strategies are being developed to increase the tolerance for this problem. As the amount of additional signal strongly depends on the angle towards the sun and follows an already recognized pattern (see Fig. 18 in Predehl et al., 2021) it might be possible to mitigate this problem by setting additional constraints on the angle of the spacecraft towards the sun. Furthermore, this effect is non-uniformly distributed across the entire surface of the CCDs, thus

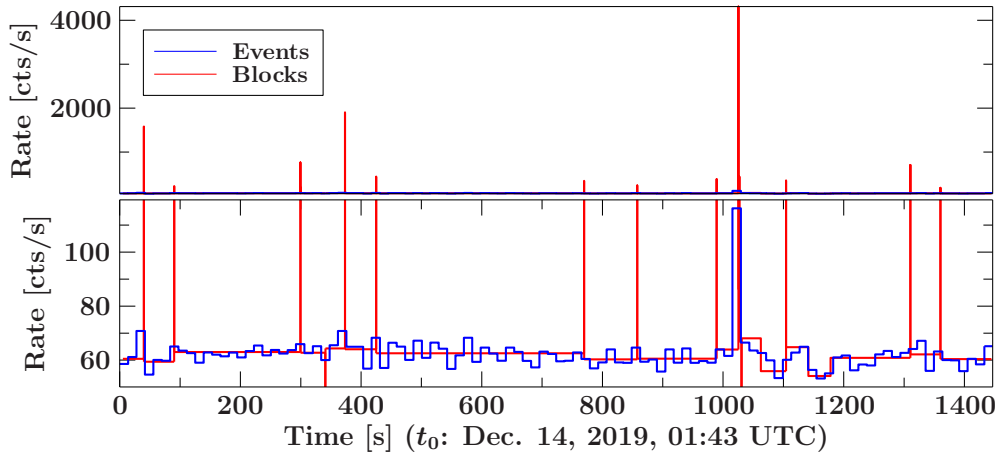


Figure 5.9: Count rate (blue) and corresponding Bayesian blocks (red) of a single telemetry file containing 24 minutes of data from TM1. The bins of the count-rate are 14s long. The upper panel shows the entire data including the blocks with the highest count-rate while the lower panel shows the same but only the range of the binned count-rate on the y-axis. Several short periods of very high count-rate are determined by the Bayesian block algorithm and manifest themselves in the form of short peaks in the Bayesian blocks.

threshold maps could be used to specifically omit low energy events from the more affected areas on the bottom of the sensors while still accepting events from the less affected ones.

### 5.6.5 Impacts of Cosmic Rays on Camera Electronics

As described in Section 5.3, the CE unit of TM5 experienced a processor crash on August 20, 2019. After this crash control voltages of the camera have been found changed although no such change was instructed via commands from ground. Two other CEs experienced similar situations which led to an extension of the commissioning phase and an investigation of the problem. It was concluded that these crashes were most likely caused by an ionizing cosmic particle causing a single-event upset (SEU) in the CE which are not implemented as a triple redundant system. SEUs can present themselves for example in the form of bit-flips in memory or processor registers. Because the CE is of the same construction for all seven TMs these events can occur across all these instruments. Indeed, on average one incidence of this kind is recorded per week across all seven CEs. Each affected camera resumes operation after a reset commanded during a ground contact session. The ITC is built using the same components as those in which most likely the SEUs of the CEs occur but is implemented in the form of full triple redundancy which strongly decreases the probability of SEUs. However, one crash of the ITC was recorded during the first ten months of the mission.

### 5.6.6 MIP Rejection and Corrupt Frames

The *eROSITA* NRTA implements a mechanism to identify bright sources passing through the FOV of the instrument. While details of the NRTA will be discussed in Chapter 5.8, this mechanism identified an additional characteristic of the data generated by *eROSITA* which is therefore briefly explained.

When a bright source enters the FOV the overall count-rate of the detector is expected to increase significantly. These periods of elevated count-rate can be identified by using a Bayesian Block segmenting algorithm operating on the time tagged events registered by the detector and generating the most likely segmentation of this detector light curve (Scargle, 1998; Scargle et al., 2013a,b). When one of these segments, called a block, is considered valid, source detection on the events contained in this block can be performed with subsequent automatic characterization of the detected sources and potentially alerts can be generated. During pointed observations in the CalPV phase the NRTA frequently triggered source detection which was unexpected because no bright sources were passing through the FOV. Alerted by this behavior, I analyzed

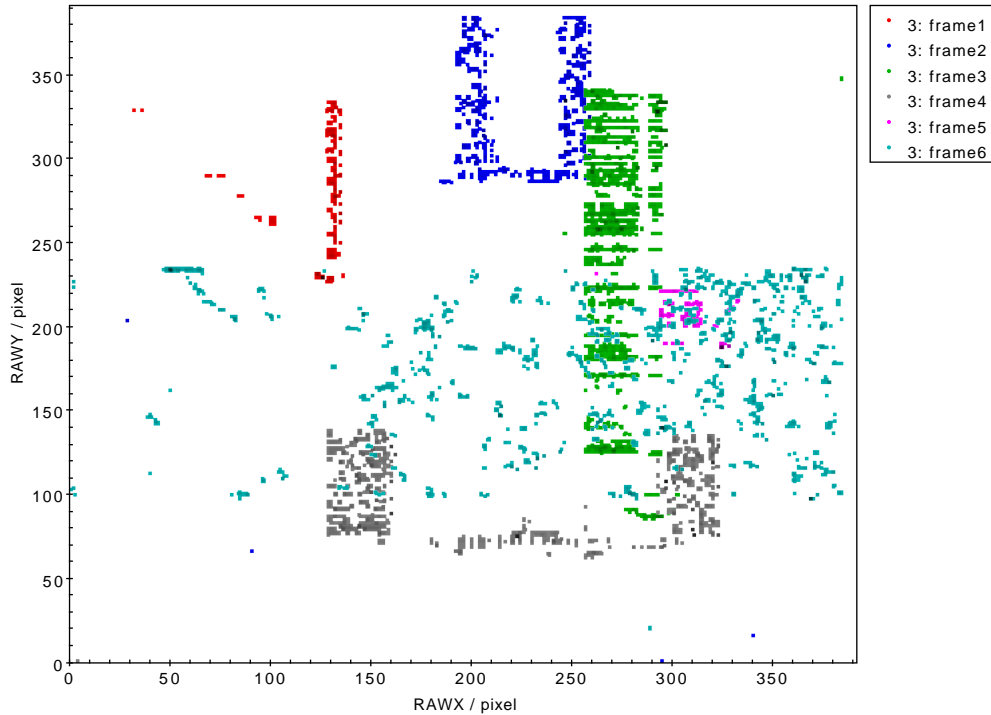


Figure 5.10: Six individual CCD frames, each causing a sharp peak in the detector light curve

several of these occurrences to understand their origin and developed an empirical technique to quantify and characterize the affected data. The results of this analysis are discussed in this section.

Figure 5.9 shows the detector light curve of TM1 over period of 24 minutes with 14s bins in blue. The Bayesian Block algorithm of the NRTA was used to segment this detector light curve into blocks of constant count-rate which are shown in red. Both panels show the same data, however, the  $y$ -axis of the lower panel has been adjusted such that the histogram of the lightcurve becomes visible. The  $y$ -axis of the upper panel is scaled to contain the entire magnitude of the blocks. From this figure it can be seen that the count-rate over the entire detector is on average at around 60 cts/s, but the Bayesian Block algorithm has determined multiple very short intervals of constant count-rate in the range of several thousand cts/s. These occasions were then further analyzed by the NRTA using a variety of source detection algorithms from the eROSITA Science Analysis Software System (eSASS) but no astrophysical source of X-ray emission could be detected. Furthermore, the Bayesian Blocks algorithm triggered source detection frequently even during pointed observations which is unexpected because, apart from the intrinsic variability of X-ray sources in the FOV and possible background flaring events, the count-rate of the detector is expected to be constant during the observation. Further investigation of the time series showed that these very short spikes in count-rate are caused by single CCD frames containing tens to hundreds of events. In combination with the nominal exposure time of 50 ms this results in a count-rate of hundreds to thousands of cts/s for a twentieth of a second. Because of the significance of this high count-rate the Bayesian Block algorithm assigns dedicated segments to these periods which got interpreted by the NRTA as a very bright source passing through the FOV for a brief period of time.

To further understand this behavior the appearance and other properties of individual corrupted frames was investigated. Fig. 5.10 shows the patterns emerging directly from the CCD for six isolated corrupted frames. The patterns seem to consist of either a single rectangular shape or a combination of three rectangles forming a “U”-like shape. These structures are filled with numerous almost randomly illuminated pixels which tend to be organized in rows or columns. Because of this characteristic they are called “bar code events”. The density of illuminated pixels inside the shapes and the size of the rectangles can differ, compare for example frame 5 and frame 6, while the events contained in these patterns correspond to energies of soft

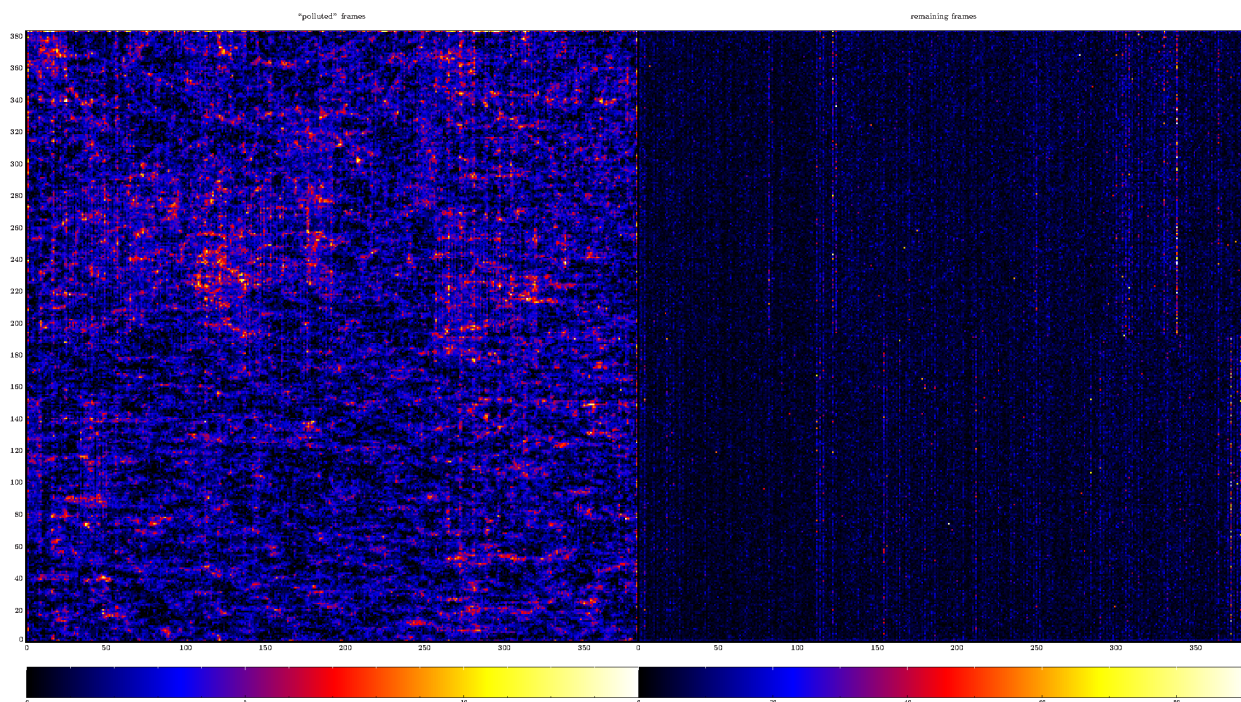


Figure 5.11: **Left:** All events from TM3 captured during eroday 43390 and identified as being corrupt from the outlined criteria combined in one image.

**Right:** Detector image of the remaining events.

X-rays around and below 200 eV.

To investigate the distribution of these corrupt frames over time and their intrinsic properties empirical criteria had to be found from which corrupt frames could automatically be recognized. It was found that all TMs show similar behavior in their detector lightcurves, but the spikes are larger for TM4. Because initially the events were recognized by frames containing many events a lower limit was determined for how many events a single frame must contain to be considered corrupt. Investigation of multiple detector lightcurves suggested a limit of 40 counts per frame corresponding to a count-rate of 800 cts/s. Additionally, numerous events were found which had PHA values exceeding 12288 which, according to the specifications of the CEs, cannot come from detections of real photons. Other criteria were already captured using a bit mask which could be used to set complementary constraints on the events such as the pattern of the event on the CCD to be valid or to not come from or be located next to a defect pixel.

The result of applying this filtering approach to the data taken by TM3 during the commissioning phase on eroday 43390 is shown in Fig. 5.11. On the left-hand side all events from all frames being identified as corrupt are combined and on the right-hand side the image consisting of all remaining events is shown. Individual bar code events can still be identified in the image of the removed frames but additional patterns emerge. The image is polluted by a variety of seemingly randomly oriented streaks. A possible origin of these tracks are minimum ionizing particles (MIPs) passing through the semiconductor material of the CCDs and depositing their energy. They consist of cosmic particles and solar protons. The firmware running on the CEs employs certain algorithms to detect tracks caused by MIPs onboard after the readout of a frame and removes the corresponding events directly such that they are not stored in the telemetry. However, as explained in the section before, MIPs appear to be able to disturb the processing electronics and cause processor crashes. The unnatural shape of bar code events suggests that the corrupt frames are also results of cosmic particles influencing the onboard processing.

When examining single CCD frames a third unusual pattern can be identified. It consists of single, mainly horizontal and short streaks in individual frames. They are called “space invaders” and cannot be automatically identified by the outlined procedure because of the lower implied count-rate. However,

the processing software used to calibrate the event files on ground and prepare them for further scientific applications has been adjusted to include a screening mechanism which recognizes most of the described corrupt frames and events by analyzing external housekeeping parameters supplied by the onboard processing electronics. In total about 1% of the frames captured by the CCDs are corrupted and the events in these corrupt frames can take up roughly 5% to 20% percent of the entire data in the telemetry. Information about these corrupted frames was published in the context of the early data release (EDR) and a description is available at MPE's website<sup>5</sup>.

## 5.7 Science Objectives

The *eROSITA* Science Book (Merloni et al., 2012) gives a detailed description of the scientific goals pursued by the *eROSITA* mission which are briefly summarized.

### 5.7.1 Sensitivity & Expected Detections

The instrument performance of *eROSITA* in space has been shown to be compatible with the theoretical expectations. It is therefore assumed that the theoretical predictions of the sensitivity to point and extended sources will still hold. However, the background has already been reported to be several times higher than predicted for energies above 2 keV, although being consistent with the predictions for energies below 2 keV (Predehl et al., 2021). The effective area of the instrument (see Fig. 5.6) might suggest that most of *eROSITA*'s power to detect sources is given below a major absorption edge which coincidentally is also located at roughly 2 keV. Predehl et al. (2021) also suggests that because of the current solar minimum the amount of particle background caused by cosmic radiation of galactic origin is higher than anticipated and will therefore decrease with the rise of the Sun's activity in the coming years. The flux limit for the detection of point sources over the full all-sky survey is given by Predehl et al. (2021) as  $1.1 \times 10^{-14}$  erg/s/cm<sup>2</sup> (0.2 to 2.3 keV) and  $2.5 \times 10^{-13}$  erg/s/cm<sup>2</sup> (2.3 to 8 keV) for the total accumulated exposure at the ecliptic equator. For the polar regions with much higher exposure these values are  $2.5 \times 10^{-15}$  erg/s/cm<sup>2</sup> and  $4 \times 10^{-14}$  erg/s/cm<sup>2</sup> respectively. The number of detected sources across multiple source classes is estimated from these values to a few million AGN and roughly 700000 active stars. Next to a broad variety of other galactic sources such as black hole and neutron star binaries *eROSITA* will, at the end of the eight all-sky surveys, have at least 100000 galaxy clusters detected.

### 5.7.2 Cosmology with Galaxy Clusters

Clusters of galaxies are the largest gravitationally bound structures in the universe Sarazin (1986). They typically consist of multiple hundred galaxies and are tens of millions of light-years in size while having total masses beyond  $5 \times 10^{14} M_{\odot}$ . Sounding rockets were able to identify X-ray emission from galaxies such as M87 and Cygnus A first in 1966 (Byram et al., 1966a,b) and subsequent discoveries of X-ray sources were made in the Coma (Meekins et al., 1971) and Perseus clusters (Fritz et al., 1971) leading to the suggestion that galaxy clusters in general were sources of X-ray emission (Cavaliere et al., 1971). With the results from the *UHURU* and *Ariel V* missions this hypothesis was confirmed, and it was established that galaxy clusters are non-variable sources (Elvis, 1976) of extended bright X-ray emission with luminosities ranging from  $10^{43}$  to  $10^{45}$  erg/s (Kellogg et al., 1972a,b,c; Forman et al., 1972). Spectral analysis of these sources showed that the origin of this soft radiation lies within thermal bremsstrahlung occurring in the low density and high temperature gas within the cluster containing  $10^{-3}$  atoms/cm<sup>3</sup> at  $10^8$  K (Sofia, 1973).

One of the main goals of the *eROSITA* instrument is to map the distribution of galaxy clusters in the observable universe by their soft X-ray emission. When this distribution is known important cosmological parameters can be constrained one to two orders of magnitude better than previously possible through X-ray cluster samples. Examples for such parameters are the normalized mean density parameter for normal matter, the amplitude of linear matter density fluctuations and parameters regarding the equation-of-state of dark matter. The spectra of individual nearby clusters, which are therefore relatively bright, can be well

<sup>5</sup><https://erosita.mpe.mpg.de/edr/eROSITAIssues/dataartefacts.html>

resolved by *eROSITA* making it possible to study the dynamic structure of these objects. It is also feasible to study the chemical enrichment of intra-cluster gas with heavy elements by supernovae in dependence of the cosmological redshift.

### 5.7.3 Active Galactic Nuclei

As outlined above, *eROSITA* is expected to detect multiple millions of AGN. A detailed description about how these objects generate X-ray emission and what properties this radiation has is given in Chapter 7. With this large sample size extensive population studies become possible. One of the most studied characteristics of the AGN population is the luminosity function. It relates the galaxy's X-ray to its optical and UV luminosity and its evolution over cosmological timescales can be measured by selecting AGN of different eras of redshift. This approach provides insight into the growth of SMBHs and the interaction between them and their hosting galaxies and therefore galaxy formation in general (Soltan, 1982; Haiman & Menou, 2000; Yu & Lu, 2004; Mahmood et al., 2005; Hopkins et al., 2005b,a, 2007; Silverman et al., 2008; Ebrero et al., 2009; Aird et al., 2010; Hirschmann et al., 2012b; Ross et al., 2013; Enoki et al., 2014; DiPompeo et al., 2014; Dotti et al., 2015; Fotopoulou et al., 2016; Rosas-Guevara et al., 2016; Kulkarni et al., 2019) while it is also the testing ground for the predictions of cosmological simulations (Hirschmann et al., 2012a, 2014; Sijacki et al., 2015). With the AGN catalog produced by *eROSITA* it will therefore be possible to study the history of black hole evolution in unmatched detail while also the clustering properties of close AGN with a redshift of up to roughly two can be studied in a new way. By determining the X-ray luminosities of AGN in its sensitive energy range, *eROSITA* is providing the possibility to set the SED of AGN in relation to other properties such as the host galaxy type and the redshift. Also, distinct spectral features can be analyzed with respect to these properties. *eROSITA* is expected to detect more exotic types of AGN, for example at very high redshifts and highly obscured ones and the detection of tens of thousands obscured AGN in general will enable studies of the relation between the accretion onto the SMBHs and their hosting galaxies.

### 5.7.4 Compact Galactic Sources

At the time of writing this thesis, seven isolated neutron stars (INSs) are known which have been discovered in the *ROSAT* data (Walter et al., 1996; Haberl et al., 1997, 1998; Schwobe et al., 1999; Motch et al., 1999; Haberl et al., 1999; Zampieri et al., 2001). It is estimated that *eROSITA* can increase the number of detected INSs from seven to somewhere in the range from 240 to 1500 (Turner et al., 2010). Also, white dwarfs are known to be emitter of X-rays under certain conditions, for example when accreting material from a companion star. *eROSITA* can systematically study the population of accreting white dwarfs in the Milky Way and measure their luminosity functions as well the one of accreting neutron stars. Combined with black hole binaries the total number of newly detected compact X-ray sources inside the Milky Way is expected to be around 3000. As final compact sources of X-ray emission stars have to be taken into account. Indeed, stars will represent the largest portion of galactic X-ray sources in the all-sky survey with roughly multiple thousands of detections. They generate X-rays by wind-shocks or strong magnetic activity in their atmosphere (Güdel, 2004; Güdel & Nazé, 2009). Using *eROSITA*, it is possible to extensively study the X-ray properties of stellar populations and identify young stellar objects in star formation regions. Depending on their orbits, *eROSITA* will also study comets as probes for the composition of the solar wind.

### 5.7.5 Diffuse Emission

Next to the variety of compact sources in the Milky Way also diffuse gas can generate high energy photons in the X-ray regime. The driving mechanisms behind this are stellar explosions and stellar winds creating supernova remnants and a variety of bubbles from which shock fronts propagate into the inhomogeneous ISM. With a temperature of around  $10^6$  to  $10^7$  K these structures of plasma generate soft X-rays in the form of continuum and line emission and can therefore ideally be mapped with an imaging X-ray telescope survey, as performed by *eROSITA*, to create a complete sample of galactic supernova remnants and determine the age and physical condition of the plasma of supernova remnants near the solar system, which are therefore largely extended, giving insight into the interaction of these structures with the surrounding ISM. Also, the

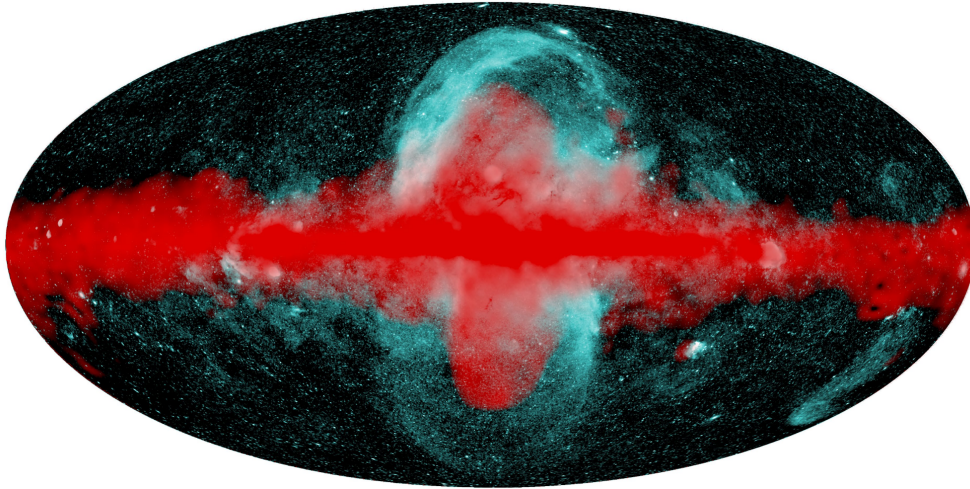


Figure 5.12: The *eROSITA* bubbles as seen in the 0.6 to 1.0 keV band (cyan) surrounding the Fermi bubbles (red). Taken from Predehl et al. (2020).

effect of solar winds and solar X-rays onto the ISM will be investigated. Because they are comparatively close to the Milky Way (compared to cosmological distances) these studies are also possible in the Magellanic Clouds, with the LMC being of special interest because it is actively undergoing star formation and therefore contains numerous supernova remnants and bubbles. Of particular interest are the so called “Fermi bubbles” which are two symmetrical bubbles of gamma-ray emitting plasma extending perpendicularly to the galactic plane from the galactic center and indicating possible AGN activity of the Milky Way in the past (see Fig. 5.12). It has already been reported that *eROSITA* discovered two accompanying bubbles, also shown in Fig. 5.12, surrounding this structure in X-rays (Predehl et al., 2020).

### 5.7.6 Variable Sources

Because of the sampling interval of at least six subsequent scans every six months *eROSITA* provides a unique strategy for detecting variability in X-ray sources. Apart from the variability of AGN, which occurs on long timescales, this specific topic is addressed by the NRTA and will therefore be discussed in Chapter 5.8.1.

## 5.8 The *eROSITA* Near-Real-Time Analysis Pipeline

As outlined above, *eROSITA* provides a unique sampling pattern for variability studies of astrophysical objects. Each position of the sky is scanned at least six times in a 4 h interval for roughly 40 s. For higher ecliptic latitudes the number of consecutive scans increases to the ecliptic poles which coincide with the poles of the survey. These positions are covered continuously in 4 h intervals. Because *eROSITA* progressively scans large portions of the sky the potential for covering time-critical events is greater than for most other missions, especially than for pointing observatories like *XMM-Newton* and *Chandra*. To harvest this potential I, in collaboration with other members of the Remeis observatory, developed a software pipeline named Near Real-Time Analysis (NRTA) which automatically analyzes the data immediately when they arrive on ground, already during the ground contact with *SRG*, and identifies important events as defined by a set of source specific criteria. This enables rapid follow-up observations with dedicated pointings of other observing facilities at all wavelengths.

### 5.8.1 Transient Events in the X-ray Sky

When investigating the sky on a clear night with their own eyes the resulting perception to humans is that the celestial sphere is a calm place. This, however, is not true when switching perspective to the X-ray regime. Compact sources, such as neutron stars and black holes, can show short term variability or momentary emission on every timescale, from milliseconds to years. In the following I give a short summary of the main classes of objects which are relevant as transients for eROSITA.

#### X-ray Binaries

Most stars do not evolve isolated but in systems of at least two stars (Pringle, 1989). The final state and rate of stellar evolution depends on the mass of each of these stars. More massive stars evolve more rapidly. If the initial mass of the star is below  $\sim 10 M_{\odot}$  its final stage will be a white dwarf, a compact object with a radius of less than 2% of the solar radius and less than 1.4 times the mass of the sun (Koester & Chanmugam, 1990). If the mass of the remaining core at the end of the red giant phase exceeds  $1.4 M_{\odot}$ , known as the Chandrasekhar limit (Chandrasekhar, 1931, 1935), gravity overcomes the force generated by electron degeneracy pressure and an object which consists of mostly neutrons is created, thus called *neutron star*. The radii of these dense objects are in the range from 10 to 12 km and they have masses from one to two solar masses. Because of the conservation of angular momentum during the collapse neutron stars have rotational periods of only seconds down to milliseconds (Vidaña, 2018). When the neutron star exceeds the Tolman-Oppenheimer-Volkoff limit of about 2.1 to  $2.2 M_{\odot}$  it collapses into a stellar mass black hole (Tolman, 1939; Oppenheimer & Volkoff, 1939; Özel et al., 2012; Rezzolla et al., 2018).

Depending on the configuration of the resulting binary system mass can be transferred from the less developed companion onto the compact object. When the companion star enters the red giant phase its volume increases (Clayton, 1983). If this volume exceeds the *Roche volume*, given by the potential resulting from gravity and the centrifugal force, mass can be transferred from the star to the gravitational potential of the compact object (Kuiper & Johnson, 1956). Alternatively, if the companion star is of type O or B and therefore very massive, it generates strong stellar winds with velocities of  $v \simeq 1000 \text{ km s}^{-1}$  and a mass loss rate of  $\dot{M} \simeq 10^{-6} M_{\odot} \text{ yr}^{-1}$ . Similarly, red giants show stellar wind with only  $v \simeq 10 \text{ km s}^{-1}$  but have a higher mass loss rates of  $\dot{M} \simeq 10^{-3} M_{\odot} \text{ yr}^{-1}$  (Lamers & Cassinelli, 1999). When this material enters the gravitational potential of the compact object an accretion disk is formed as outlined in Section 3.2. The termination mechanism of the disk at the inner edge depends on the compact object in the center. For black holes the accretion disk is only terminated at the ISCO while for white dwarfs and neutron stars not only the surface plays a role but also magnetic fields (Bhattacharyya, 2010; Mukai, 2017). Neutron stars in particular have strong magnetic fields ranging from  $10^8$  to  $10^{15} \text{ G}$  causing the accreted material to be deflected towards their poles (Konar, 2017).

These X-ray binaries are usually classified by of their donor star. The two main classes are low-mass X-ray binaries (LMXBs) and high-mass X-ray binaries (HMXBs). In LMXB systems the donor star is usually of spectral type A or later and less massive than the compact object and the mass transfer occurs by Roche lobe overflow (Reig, 2011). In case of HMXBs the mass transfer occurs through stellar wind and the donor stars are mostly of type O or B but also Wolf-Rayet stars are known (Kretschmar et al., 2019). Be/X-ray binaries are special HMXBs because of the properties of the optical companion which is of spectral type Be. These stars, which are massive B-type stars, have high rotational velocities causing a disk of gas to form around the equator of the star. Material can be accreted by the compact object, which in the case of Be/X-ray binaries are neutron stars, when passing through this disk of material (Reig, 2011).

When white dwarfs are the compact objects in these systems a variety of different classes of transient sources can emerge. The most common one are classical novae, recurrent novae and dwarf novae. They are caused by a buildup of accreted material on the surface of the white dwarf which can suddenly be ejected, driven by nuclear burning on the surface of the white dwarf. This phenomenon can be observed as an optical transient over days to months and when the line of sight towards the burning layer becomes transparent to X-rays a supersoft X-ray transient emerges. Supersoft sources are dominated by a thermal X-ray spectrum corresponding to temperatures from  $10^5$  to  $10^6 \text{ K}$  generated by the nuclear burning on the surface of the white dwarf (Galloway et al., 2017; Chomiuk et al., 2020).

For Be/X-ray binaries the main mechanism driving the changes in flux is the orbital motion of the compact

object with respect to the optical companion. So called type I outbursts follow a quasi-periodic pattern of increases in flux of about one order of magnitude, in line with their orbital period. During type II outbursts the X-ray luminosity increases by three to four orders of magnitude and can reach the Eddington luminosity of the neutron star. They occur on a much more irregular basis and last for a large portion of one orbital period or longer (Reig, 2011). The exact effects causing the variability observed from other HMXBs and LMXBs have not been clarified completely. According to the *eROSITA Science Book* by Merloni et al. (2012), the main cause in LMXB systems is a buildup of material on the accretion disk generated by Roche lobe overflow and a sudden increase in accretion rate triggered by an instability in the disk. In HMXBs the main reason is intrinsic variability of the stellar wind from the optical donor itself.

### Gamma-ray Bursts and their Afterglows

Gamma-ray bursts (GRBs) are short-lived pulses of intense gamma radiation observed in irregular intervals isotropically in the entire sky. They have been first detected in the late sixties by the *Vela* satellites which were deployed to monitor nuclear explosions on the surface of the Earth (Klebesadel et al., 1973). Kumar & Zhang (2015) give a comprehensive review of the observational properties of GRBs and theories aiming to explain their origin. The duration of these phenomena ranges from below 0.1 s to multiple minutes. Interestingly, two peaks in the distribution of the durations can be found at 0.3 s and 30 s which caused the introduction of the classification into short-GRBs with a duration of less than 2 s and long-GRBs with longer durations. The non-thermal broken powerlaw spectrum of pulses peaks at energies from 10 to  $10^4$  keV. Afterglows of GRBs can be observed from the X-ray to the radio regime and show a powerlaw spectrum with a photon index of roughly 0.4 to 1.4. The flux decays with a powerlaw index over time, following  $\sim t^{-1\dots-2}$ . A few GRBs are detected every day by gamma-ray monitoring instruments such as *Swift* BAT (see Section 4.2.4) or the Gamma-ray Burst Monitor (GBM) onboard the *Fermi* satellite (Meegan et al., 2009). With its more limited FOV, *eROSITA* is not able to provide sensitivity to the afterglow of GRBs over the entire sky but because of their rate of occurrence and isotropic distribution it is estimated that it will detect the afterglow of roughly four to eight of these events per year (Khabibullin et al., 2012). In these cases it can provide the exact location of the GRB down to arc second accuracy and measure the decay of the afterglow of these transient sources in intervals of 4 h.

### Tidal Disruption Events

As outlined in Section 3, SMBHs are located at the center of AGN. It is, however, becoming more evident that every galaxy, also inactive ones, harbor a SMBH (Kormendy & Gebhardt, 2001). In our own galaxy, the Milky Way, this black hole could be identified using infrared (IR) spectroscopy by determining the orbit of nearby stars (Eisenhauer et al., 2005) while its X-ray luminosity, apart from minor flaring activity, is several magnitudes lower compared to that of most other AGN (Padovani et al., 2017; Mossoux et al., 2020). When in those quiet galaxies a star passes within the *tidal radius* given by

$$r_T = R_* \left( \eta^2 \frac{M}{M_*} \right)^{1/3} \quad (5.2)$$

where  $R_*$  and  $M_*$  are the radius and mass of the star,  $M$  the mass of the black hole and  $\eta \simeq 1$  is a parameter depending on the structure of the star, the resulting tidal force will tear the star apart, a process named tidal disruption event (TDE) (Gezari, 2021). The subsequent accretion of the material onto the black hole creates an accretion disk and therefore an X-ray flaring event with a lightcurve following a powerlaw of the shape  $t^{-5/3}$ . According to the recent review by Gezari (2021), 56 of such candidates have been identified. The decay of the X-ray lightcurve can be observed over periods of years (Komossa & Greiner, 1999; Komossa & Bade, 1999; Komossa et al., 2004). Therefore, the all-sky survey conducted by *eROSITA* provides an ideal opportunity to not only search for the immediate outbursts in X-rays expected from TDEs but also to study their long-term lightcurves.

### Stellar Flares

Stars are not only constant sources of soft X-ray emission but also show occasional flares. These *stellar flares* are caused by magnetic reconnection events in coronae leading to heating of coronal plasma and therefore an increase in thermal X-ray emission. This increase in X-ray luminosity lasts for minutes to hours (Haisch et al., 1991; Favata & Micela, 2003; Güdel, 2004; Güdel & Nazé, 2009). An analysis of stars in the 2XMM serendipitous source catalog (Watson et al., 2009) conducted by Pye et al. (2015) found  $\sim 130$  flares originating from  $\sim 70$  stars. The continuous scanning of the X-ray sky preformed by *eROSITA* is also able to detect these flaring events as X-ray transients and measure their lightcurves.

### AGN

As outlined by Padovani et al. (2017), AGN show the most rapid variability in the high energy regime of X-rays and  $\gamma$ -rays. While the large scale amplitude variations increase on longer timescales also variability over just minutes was observed (McHardy et al., 2006; Ishibashi & Courvoisier, 2009; Padovani et al., 2017; Maughan & Reiprich, 2019). This intrinsic variability is mainly attributed to effects occurring in the inner region of the accretion flow and the X-ray corona (compare Section 3). It has been shown that these effects are expected to scale linearly with the mass of the central black hole which motivates efforts to find explanations applying simultaneously to the variability observed from galactic black hole X-ray binary systems on short timescales and that of AGN on longer ones (Ishibashi & Courvoisier, 2009; Padovani et al., 2017). Apart from this source-intrinsic variability, AGN have been found to show a change from Compton-thick to Compton-thin emission or vice versa (Matt et al., 2003; Bianchi et al., 2005; Piconcelli et al., 2007; Ballo et al., 2008; Risaliti et al., 2009; Ricci et al., 2016). Because of this property they are often called *changing-look* AGN, a term now also used for objects changing their optical classification (Denney et al., 2014; LaMassa et al., 2015; MacLeod et al., 2016; McElroy et al., 2016; Ruan et al., 2016; Runnoe et al., 2016; Gezari et al., 2017). These occurrences are attributed to variable obscuration along the line of sight towards the central emission region, variable accretion rate and TDEs in an active galaxy (Yang et al., 2018). Changes due to partial covering can take place rapidly on timescales below 1 h. A more detailed analysis of such an event is given in Chapter 7. With the expected total number of AGN detected by *eROSITA* around three million (Merloni et al., 2012), a systematic search for these events can be conducted. For further investigations rapid follow-up observations are necessary which requires a fast automated analysis of the data gathered by *eROSITA*.

### Unknown Transient Sources

When *eROSITA* scans the sky it will often be the only instrument observing a particular point in the sky. In case during one of these roughly 40 s long snapshots a previously unknown X-ray transient emerges which cannot be detected in follow-up observations and no counterpart can be identified at another wavelength, then it is very difficult to obtain information about the nature of this transient source. During one scan of *eROSITA* not nearly enough data are accumulated to enable a detailed spectral analysis to directly obtain information such as the cosmological redshift of the source or the underlying radiation process creating the continuum shape of the spectrum. Unless the transient emerges again and is observed by other instruments for a longer period of time the actual class of the source will remain a mystery. In fact, in Section 5.8.5 I will present such an event which was found by the *eROSITA* NRTA.

### Technical Aspects

As explained in Section 5.6.5, cosmic particles can cause SEUs in the CEs, making a reset of the affected module necessary. Experience has shown that after such a reset the internal timer of the affected CE can experience a jump of exactly 1 s, either forward or backward in time. When the positions of the X-ray photons detected by this particular module are then reconstructed from the attitude reported by the star trackers they will be offset exactly by an angle of

$$\theta = \pm 1 s \cdot \omega = 1.5' \quad (5.3)$$

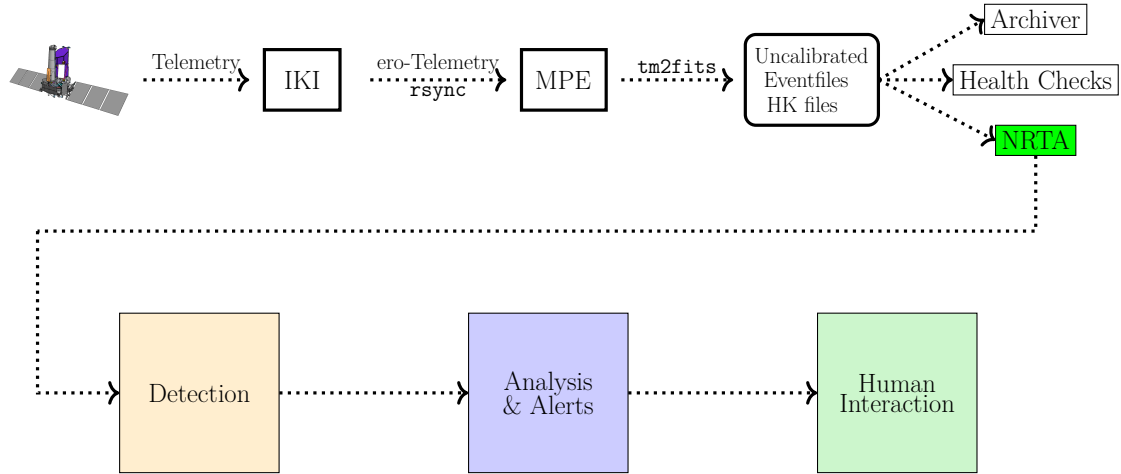


Figure 5.13: Schematics of the flow of data from *eROSITA* to the results of the NRTA

along the slewing direction of the instrument, where  $\omega$  is the scan rate (compare Section 5.4). Known, bright X-ray sources will therefore be shifted to one of these positions which can be calculated prematurely. Using the NRTA these positions can be routinely monitored and in case such a shift in position is recognized the responsible technical personnel can be informed.

Additionally, when new bright pixels are present on one of the CCDs those can also be detected by the NRTA as unknown X-ray sources as soon as the data arrive on ground and the appropriate action can be taken.

### 5.8.2 Implementation of the NRTA

For the creation of the X-ray catalog, as the final product of *eROSITA*'s all-sky survey, source detection must be performed for which a continuous set of data is necessary. This requirement, however, cannot be satisfied on a short notice after each telemetry downlink because the data do not arrive on ground in chronological order. Typically, 5 h are allocated to *eROSITA* during *SRG*'s daily ground contact sessions during which instrument health checks are performed by the operations team, necessary actions such as resetting CEs affected by SEUs are taken (compare Section 5.4) and data from the onboard mass memory are “dumped” to ground, a process taking roughly two to 3 h. They arrive at MPE as *telemetry files* in a binary format. Roughly 84 of these files are created for each 24 h of observation, each roughly 7.2 MB in size. Usually each telemetry files contains consecutive science and housekeeping data generated by the various instruments, sensors and electronics components. Science data are the events registered by the CCDs and housekeeping data are the readings of various sensors such as temperatures and voltages, the output of the star trackers in addition to diagnostic data from the seven CEs. The time covered by the data in each telemetry file depends on the number of events registered by the CCDs. On average, when assuming 84 files in 24 h, each file covers  $\sim 17$  minutes. With the scan rate of  $\omega \simeq 1.5' \text{ s}^{-1}$  this corresponds to an arc of  $25^\circ$  covered by the FOV of *eROSITA*. However, sources of very different luminosities pass through the FOV which causes the amount of events registered by the CCDs to vary strongly. When this rate of events is elevated the amount of time and therefore the arc covered by one telemetry file can be much shorter and in case of lower activity it can be much longer.

The immediate analysis of the data contained in the telemetry files, to find time critical events in the X-ray sky, needs a different approach than the standard source detection pipeline which is based on a consecutive set of data covering large areas in the sky taken during multiple scans without major gaps. This analysis can only be done multiple days after the data were dumped from space to ensure the entire data are available. To this end, I and the remaining team of the Remeis observatory designed and implemented the *eROSITA* NRTA, a software pipeline enabling very fast analysis of the data gathered by the instrument. We traded the sensitivity provided by the standard analysis pipeline, running days after the downlink, for

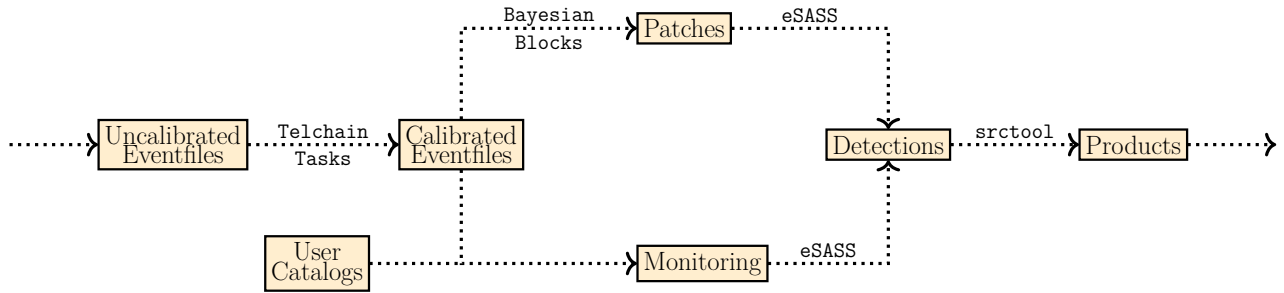


Figure 5.14: Flowchart depicting the first part of the processing conducted by the NRTA. Initially uncalibrated event files coming directly from the telemetry decoder are prepared for processing. Areas containing bright sources are identified by the Bayesian Block algorithm and external regions are supplied via user catalogs in addition to already known point sources for monitoring. By performing source detection the sources in the detection regions are identified and for all of these and the monitoring sources the products such as lightcurves and spectra are extracted.

increased speed and less waiting time by only focusing on the data on a per-scan basis.

Fig. 5.13 shows a sketch of the coarse flow of data from being generated onboard *eROSITA* to its various final locations. It is first sent from *eROSITA* via the radio complex to a ground antenna and temporarily stored as telemetry files at IKI which are transferred to MPE over the internet. A software developed by the Remeis observatory, named `tm2fits`, then splits the telemetry files into its various components of event files and housekeeping data and stores them as FITS files which can easily be read by a broad variety of software (Wells et al., 1981; Cotton et al., 1995; Pence et al., 2010). From this point three main things occur simultaneously. The archiver, which was also developed at the Remeis observatory, is responsible for consolidating all data in the *eROSITA* archive on which the final source catalog is based and all non-time critical analysis is performed. It ensures that no duplications are present in the time series and stores it as FITS files on a per-eroday basis (compare Section 5.4) with a slight overlap. Additionally, simple health checks are performed automatically by comparing values from the housekeeping data to predefined ranges considered as nominal. As a last branch the NRTA starts operating immediately on the FITS files created by `tm2fits`.

### Pipeline Layout

The event lists, also called event files, of each TM entering the NRTA pipeline are considered to be *uncalibrated*, which means that they only contain information which can directly be provided by the CE. These values are, among others, timestamps and counters identifying the CCD frame in which the events were registered, the location of the event on the sensor in pixels and the PHA values in analog-to-digital units (ADUs). A separate extension of the event files contains information about the good time intervals (GTIs). They specify the time intervals during which all parameters indicated nominal operation of the corresponding CE and the entire *eROSITA* instrument. Time periods during which conditions have been present which might indicate that the obtained data are unreliable are excluded from the GTI. In this way the data itself can be kept and is not deleted but is not considered in scientific analyses. Most of the other housekeeping parameters are stored in separate FITS files. These include the data from the star trackers, information about the onboard MIP rejection processing and the readings of all other sensors on the instrument and partially the spacecraft platform. These data are then used to prepare the event files for scientific analysis by flagging invalid events and calculating their physical properties. Before going further, the data are split in time into individual erodays if multiple ones are contained within one telemetry file.

After that two separate branches in the pipeline determine which regions covered by the FOV are to be analyzed in more detail. Bright sources passing through the FOV are identified by a Bayesian Block algorithm and predefined regions for source detection or point sources for monitoring are introduced by external catalogs. For all sources found on each of these branches source products, such as spectra and

lightcurves, are then created. After that the sources are matched against external reference catalogs to identify their known counterparts and, based on the source products, additional properties such as count-rates and hardness ratios are calculated. For each source the resulting properties are compared with specified trigger criteria and if they are met a science alert is generated which causes a notification of the trigger's owner via e-mail. All data generated by the NRTA, with minor exceptions for certain input catalogs and file types, are transferred to the dedicated NRTA archive. From this point on human interaction is required to validate the alert by investigating the source products in a browser based front end. After every ground session is completed, and the entire data dumped throughout this session has been processed by the NRTA, an additional analysis identifies the processed sources in the individual scans and checks for changes in predefined source properties over time. If such a change is found, as specified by a trigger criterion, again an alert is generated. This process enables the identification of sources changing over time.

### Preparing the Data

Before scientific analyses can be conducted the physical properties of the registered events, i.e., the energy and projected position on the sky, must be calculated and events which do not satisfy certain quality criteria must be identified as such. Erroneous events are not deleted, but each carries a 32 bit long mask in which specific attributes can be encoded. These include the ownership according to the data right policy and associations with the impact of a MIP, a defect pixel or a corrupt frame. This task is accomplished by a set of programs of the eSASS (Brunner et al., 2018) named `telchain` and is the first operation the NRTA performs on the event files, as depicted in the flow chart in Fig. 5.14. First step in this process is the calculation of the actual time-dependent attitude of *SRG* from the data obtained by the star trackers. After that basic checks and operations on the event data are performed which means that the events and their frames are sorted according to their time, adjustments listed in the calibration database (CALDB) are applied, events are flagged accordingly if being invalid or originating from a defect CCD frame, the times are corrected for jumps resulting from for example CE resets and events with impossible times are flagged, the event data is decompressed if the onboard algorithm used compression, all periods during which a problem was identified are excluded from the GTI and the dead time correction is calculated. After that events originating from or being next to bad pixels as listed in the CALDB are flagged after which the pattern analysis is performed (see Section 4.1.3) followed by the reconstruction of the energies of the events. During the pattern analysis events with invalid patterns are flagged. Finally, by considering the initially calculated attitude data of the spacecraft, the positions of the events projected onto the sky are calculated. At the end of the `telchain` the event files are considered *calibrated* and are ready for scientific analysis. Before that, however, the event files are split in time according to their containing erodays. This ensures that the sources are analyzed on a per-scan basis if multiple erodays are contained in a single telemetry file and enables the detection of changes on the short timescales given by subsequent visits by *eROSITA*.

### Bayesian Blocks

The NRTA is designed to address the most time critical events. Because of this only specifically targeted regions can be analyzed to keep the processing time short. Most of these regions are supplied via external *user catalogs* but an additional mechanism was implemented to search for bright sources in general to identify previously unknown, bright X-ray transients. It is based on the fact that when *eROSITA* is performing its survey with the nominal scan rate each source is in the FOV for approximately 40s at most. If the source is sufficiently bright the count-rate of the respective detector is elevated for this period of time compared to the base count-rate caused by for example faint background sources. A bright source passing through the FOV can therefore be interpreted as a significant excess in the rate of detected events. For ease of communication the rate of events detected by a certain CCD in dependence of time is named *detector lightcurve* in resemblance of lightcurves giving the time-dependent count-rate or luminosity of X-ray sources. The detector lightcurve can be interpreted as consisting of a superposition of blocks of constant count-rate, each caused by a source in the FOV. Note that this is an approximation because the true count-rate of an intrinsically constant source registered by the detector is not constant due to the changing vignetting of the source when it passes through the FOV (compare Section 5.6.3). This changing count-rate of a single source can however again be approximated by intervals of constant count-rates.

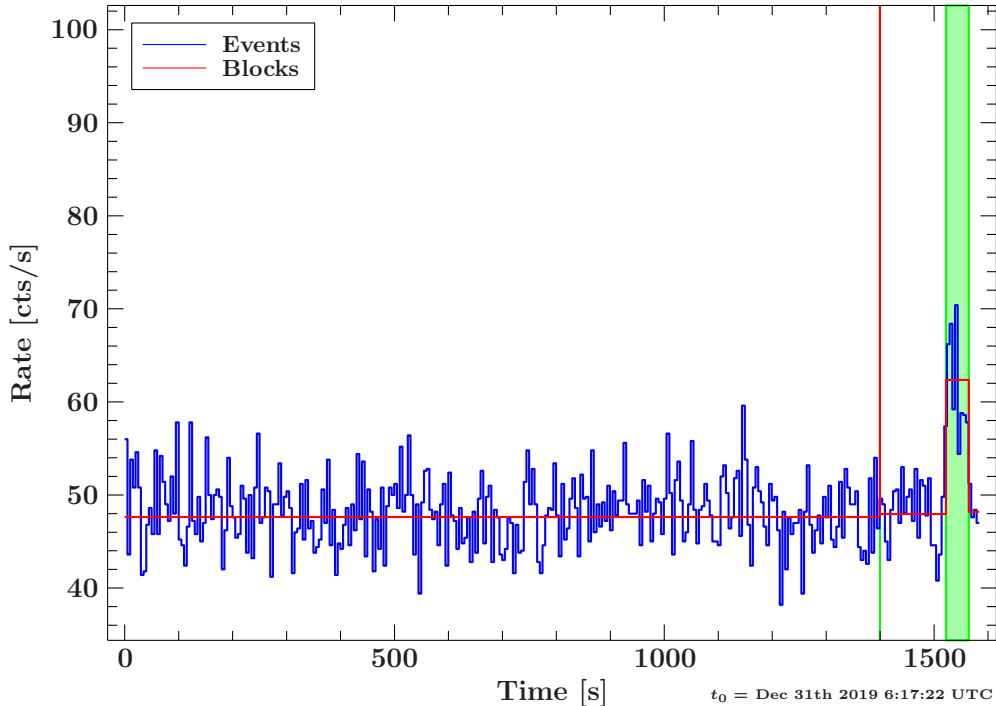


Figure 5.15: Exemplary detector lightcurve (blue) of TM6 of one telemetry file with bins 5 s in length. The segmentation created by the Bayesian Blocks algorithm is shown in red and the identified intervals of bright sources in the FOV are shaded green. Note that the very short block at  $t \sim 1400$  s was caused by a remaining corrupt frame similar to the ones shown in Fig. 5.9. The block of elevated count-rate towards the end of the lightcurve was caused by an unknown transient X-ray source detected on New Year’s Eve 2019.

An algorithm to find the optimal segmentation of time series data, such as events registered by the CCD detectors, into an optimally fitting model of piecewise constant blocks, was developed by Scargle et al. (2013b) and is named *Bayesian Block Algorithm*. Optimally fitting for discrete event data is interpreted as the distribution of blocks among the time tagged events maximizing the likelihood function of the Cash (1979) statistic. The algorithm described in Scargle et al. (2013b) was implemented by Bissinger (2016), who used it for the analysis of lightcurves from Be/X-ray binaries, in the **S-Lang** programming language for usage in Interactive Spectral Interpretation System (ISIS)<sup>6</sup> (Houck & Denicola, 2000) and is part of the **isisscripts**, a collection of functions useful for X-ray data analysis using ISIS maintained by the Remeis observatory<sup>7</sup>. A detailed analysis of how this segmentation algorithm can be used to detect bright transients using data from *eROSITA* is presented by Hain (2017). Based on these considerations I implemented the Bayesian Blocks algorithm of the **isisscripts** into the NRTA.

After the creation of calibrated event files by the **telchain** the algorithm is applied to the event data of each TM individually except TMs 5 and 7 because the optical light leak causes strong fluctuations in the detector lightcurves of these CCDs which results in strongly segmented piecewise constant models leading to misidentifications of bright sources. Events associated with bad pixels, corrupt frames (see Section 5.6.6), the impact of a MIP or invalid patterns are excluded by filtering for an appropriate bit mask. Also, only events with an energy higher than 0.05 keV are used because, although the effective area of *eROSITA* is very low at these energies, a large amount of events is registered. The algorithm also properly treats the GTIs and accepts a variety of input parameters assisting in the segmentation process. One of these is the minimal time difference between to subsequent events. This was set to 49 ms because the nominal exposure time is 50 ms. The maximal number of simultaneous events, being the maximal number of events in one

<sup>6</sup><https://space.mit.edu/cxc/isis/>

<sup>7</sup><https://www.sternwarte.uni-erlangen.de/isis/>

CCD frame, was set to 30000.

Output of the algorithm is a list of intervals of constant event-rates defined by *change points* which give the moments in time when the constant rate is changing abruptly. An exemplary detector lightcurve of TM6 for one telemetry file and the created optimal segmentation for it is shown in Fig. 5.15. The data contained in this particular file covered  $\simeq 26.4$  min and was taken starting from Dec 31, 2019 6:17:22 UTC. For the majority of the lightcurve a single block was created representing the constant base count-rate of  $\simeq 48$  cts/s. It is created by the multitude of background sources, diffuse emission from the Milky Way and background radiation. At  $t \simeq 1400$  s, however, a very short block was created by the segmentation algorithm even though no peak in the count-rate is visible. This effect was caused by a remaining corrupt frame which contains many defective events causing a very short period of extremely elevated count-rate due to the short exposure time. Because this single frame is contained in a bin of 5 s the effect is not noticeable in the histogram of the count-rate. Roughly  $\simeq 520$  s later an excess in the count-rate is visible which lasts for  $\simeq 40$  s and gave also rise to the creation of a separate block of this length. After that, for a short period of time, the count-rate drops again to the initial level which was also correctly recognized by the Bayesian Block algorithm.

In the resulting segmentation for each block the possibility for being caused by a real bright source must be evaluated. Hain (2017) developed several criteria to achieve this task which have been implemented into the NRTA and for which I will give a short summary of the relevant aspects. The elevated count-rate can only remain as long as the corresponding source is in the FOV. Because of that blocks exceeding this period can be discarded. A source passing through the FOV exactly along the grid of a CCD if *eROSITA* is visible on the sensor for  $\sim 41$  s when assuming the nominal scan rate of  $1.5'$ /s. In the extremely unlikely case that the path is exactly diagonal from one corner of the sensor to the other this time is  $\sim 58$  s. By also taking into account that the vignetting causes strong suppression of the count-rate towards these corners a compromise of 47 s was taken as the maximal allowed length for a block to be valid. The implementation of the Bayesian Block algorithm also provides the statistical error for the constant count-rate of a block. This can be used to calculate the SNR for this block and discard it if a certain value is not exceeded. Hain (2017) suggested applying a lower limit of 5, but we allowed a slightly lower value of 4 for the NRTA. Under some assumptions the background level can also be estimated using two different methods. The first is again based on the fact that a block generated by a bright source can only be of a limited length. If the block has a longer duration it can only contain background events. By taking all blocks not satisfying the minimum length criterion and calculating the arithmetic mean weighted by the block length an estimation for the average background rate can be given. The second method is based on the equally binned detector lightcurve and assumes that most of the time no bright source is in the FOV and the detector only measures background events. When then creating an equally binned lightcurve and subsequently a histogram of the values of the bins in this lightcurve the background count-rate should correspond to the highest bin in this histogram, i.e., the count-rate with the highest number of occurrences. This mechanism has two free parameters: The bin width of the detector lightcurve and the number of bins of the second histogram. Hain (2017) performed the analysis of this method based on 24 h long simulated observations and concluded that 60 bins in the lightcurve can achieve a good estimate of the background count-rate. However, this prerequisite is not true for the data worked on by the NRTA because the time covered by the data contained in one telemetry file is, as described in Section 5.8.2, on average only 17 min and can vary by a large amount. The width of one bin when taking 60 bins over 24 h is 24 min which itself is already longer than the entire lightcurve of one event file. Because of this we decided that the bins of the equally binned lightcurve should again reflect the fact that an upper limit for the time of a source in the FOV is present, and the bin width was set to 50 s. From this the number of bins of the lightcurve can be calculated. Hain (2017) did not state any suggestions for the number of bins in the second histogram. When assuming 17 min of data and 50 s bins then  $\sim 20$  bins are in the lightcurve. The lower limit of the second histogram is set to the lowest count-rate in the lightcurve and the upper limit to the highest one. If no bright source passes through the FOV a normal distribution in the second histogram is expected. If, however, a bright source did pass through the FOV the upper limit of this histogram is increased and the values of the background cluster towards its lower limit. As can be seen in Fig. 5.15, the base background count-rate is about 48 cts/s. Assuming Poisson statistics the uncertainty is then  $\sim 7$  cts/s. A clustering of more than one in at least one bin at the lower end of this histogram, for a source having double the count-rate of the constant background, is achieved if  $\sim 60$

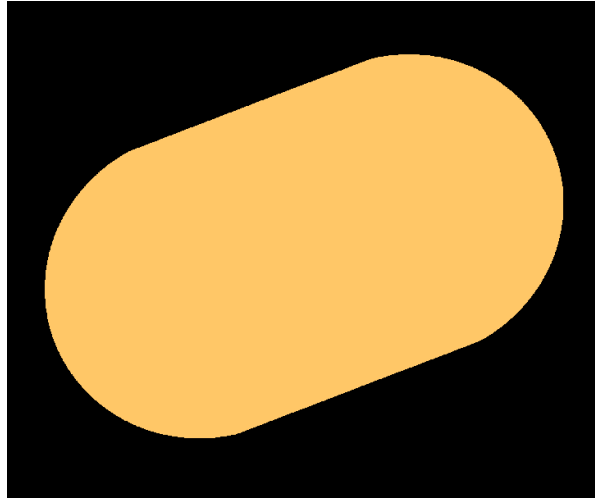


Figure 5.16: Detection mask of a patch identified to contain a bright source by the Bayesian Block algorithm

bins are chosen. Therefore, the number of bins in the second histogram was set to 60. The background count-rate is then extracted from this histogram by assuming a normal distribution around the highest bin, i.e., the count-rate with the highest number of occurrences, and taking the upper confidence limit of 95% of this normal distribution.

Each block is finally tested against all these criteria. If it has a SNR higher than the threshold, its count-rate is higher than these of both background estimates and its duration is not longer than the maximal possible time in the FOV it is declared as a valid block caused by a real bright source passing through the FOV. In the ideal case only a single block is created by the passage of the source, but it can also happen that, due to vignetting effects, the count-rate steadily rises when the source gets closer towards the center of the sensors and then steadily drops again until the source disappears. In this case the Bayesian Block algorithm might segment the passage itself into multiple blocks which are all valid. In such a case the NRTA concatenates all these subsequent blocks and marks the enclosed time period as qualified for source detection. After this these qualified time intervals found for each individual TM are combined into a single interval. Because of corrupt frames, which occasionally are not identified correctly, very short blocks of essentially only a single CCD frame are found by the segmentation algorithm and assigned a very high count-rate. Such an example can also be seen in Fig. 5.15. To avoid triggering source detection in such cases the NRTA drops all concatenated and combined intervals which have a length of less than 5 s.

The source detection procedure outlined in the next section needs spatial information about the targeted area in the sky. To provide this the NRTA extracts for each qualified interval the track on the sky covered by the FOV from the attitude data and calculates its center and the angular extent of the arc. A circular region is then positioned at this center with the diameter identical to the angular extent of the track. Somewhere in this region the identified bright source is located and can be identified by the source detection process. The imprint of the area covered by the entire FOV during the qualified interval corresponds to a roughly  $1^\circ$  broad region in the sky with two semicircles at the terminating ends and is named a *patch*. An example for such a region is shown in Fig. 5.16.

### User Catalogs

Some specific science cases cannot rely on the assumption that the source of interest is very bright and is recognized by the Bayesian Block algorithm. To also address these use cases the NRTA can be supplied by members of the German eROSITA consortium with external *user catalogs* which can contain either a list of regions which should be targeted by source detection or a list of already known point-like sources for which only the relevant data products such as images, spectra and lightcurves will directly be extracted. For the content of each telemetry file the NRTA calculates from the attitude data which of these regions or

Table 5.1: Energy bands used by the NRTA

$E_{\min}$ [keV]	0.2	0.5	1.0	2.2
$E_{\max}$ [keV]	0.5	1.0	2.2	10.0

sources were covered by the FOV during the scan and marks them to be processed as outlined in the next sections. Extended regions contained in user catalogs are designated *stamps*. The power of this mechanism lies in the fact that the user catalogs can be updated continuously in the background by custom programs on a regular basis to ingest newly discovered transients from other surveys or monitoring programs or other time-critical phenomena directly into the NRTA on a short notice.

### Source Detection

During the source detection process point-like and extended sources are identified in patches and stamps based on images created from the events originating from these regions in different energy bands. To perform source detection the NRTA heavily relies on the eSASS. I will briefly describe the steps it performs to find and characterize sources. First, the event files are filtered to only contain events originating from the targeted region and an event list for each defined energy band is created. The NRTA uses the four energy bands listed in Tab. 5.1, defined by the lower limit,  $E_{\min}$ , and upper limit,  $E_{\max}$ . For each energy band an image is created. Splitting the data into different energy bands is necessary because the effective exposure differs for different energies due to the energy-dependent vignetting function (compare Fig. 5.7) which results in different exposure maps calculated in the next step. Detection masks are generated from thresholds for the slope and values in the exposure maps and a sliding box algorithm identifies sources inside the images, confined by the detection masks. For each energy band a smooth background map is created from the event data by ignoring the sources found initially by the sliding box detection which is then repeated while taking the background estimates into account. For each source candidate found by the second sliding box detection finally the PSF (compare Section 5.6.1) is fitted to the event data. In this way a final list of sources is generated which contains information about source positions and their errors, time periods during which the respective source was visible, the extents of the sources including their likelihoods and errors, the source counts, count-rates and fluxes for each energy band individually and the total one, again including errors and finally the likelihoods of the detections.

### Source Products

For all sources found by the source detection process and specified as monitoring sources in user catalogs a variety of scientifically relevant files named *source products* are created using `srctool` which is also part of the eSASS. It analyzes each source and the corresponding background region to create lightcurves for each and the combined energy band, a source and background spectrum and the accompanying necessary auxiliary data, containing the response matrix and effective area. All these files are created for the data obtained by all TMs combined and for each individually in which case also event files containing the source and background events are generated. Because the auxiliary files containing the response matrix have a large size and are easily reproducible the ones for the individual TMs are deleted to save significant disk space.

### Source Properties

The next section of the processing conducted by the NRTA, as depicted in Fig. 5.17, characterizes the sources in more detail and, if applicable, generates an alert. To achieve this task a set of extended *source properties* is calculated for each source. These are, among others, the average count-rates in the different energy bands calculated from the lightcurves, the SNR for each individual TM, a variety of hardness-ratios, the total exposure in each energy band and the minimal distance to the center of the FOV. At this stage the source positions are also compared with a predefined blacklist containing regions in the sky for which, if a source lies in this region, no alert can be generated. This was made to, for example, prematurely

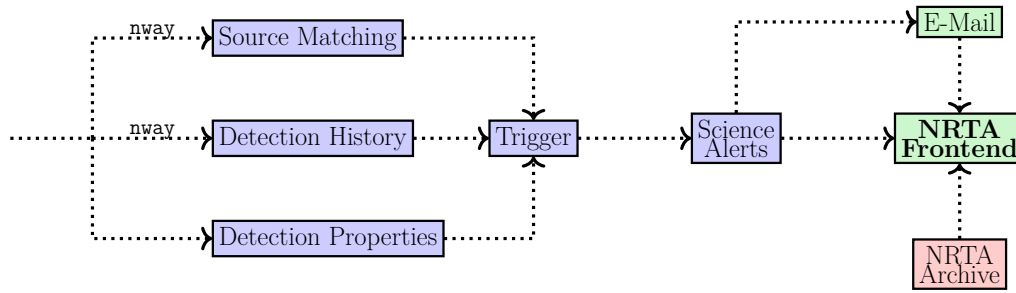


Figure 5.17: Flowchart depicting the second part of the processing conducted by the NRTA. The sources are identified in other catalogs containing sources in all wavelengths and a set of extended source properties is calculated. All these parameters are then evaluated according to predefined trigger criteria and if fulfilled an alert is generated. All obtained data are transferred to the final NRTA archive and the owner of the alert is notified via e-mail and the information about the source in the archive is made available in the web-based NRTA front end. When all data of a ground-contact session was processed the resulting detections and monitoring sources are identified in consecutive scans and the temporal behavior of the parameters is evaluated again according to the trigger criteria. If a criterion is fulfilled an alert is generated.

suppress the effect of stray light around very bright X-ray sources which can lead to a large amount of false detections. Source blacklisting can however be overruled again in the definition of the trigger criteria (compare Section 5.8.2).

### Source Matching

An important characteristic of a source is whether it is already known and listed in another catalog, also at a different wavelength, and if so which properties it has in this catalog. To provide this information for evaluation of the trigger criteria the NRTA performs a matching of sources between the source positions found during the processing and a set of external catalogs. The list of catalogs being matched against at the time of writing this thesis is given in Tab. 5.2. Identifying possible counterparts is a non-trivial task which has to take the positional uncertainties of the sources in both catalogs into account. Additionally, the matching process for the NRTA has to be performed in a short period of time. A novel approach to this problem is taken by the `nway` program developed by Salvato et al. (2018) and employs Bayesian statistics. It was therefore implemented into the NRTA and states for every detected source the probability that a counterpart was found and for all candidates individually the probability that it is the correct one. For more details see the work by Salvato et al. (2018) and Knies (2021, in preparation) who applied `nway` to the specific case of the NRTA.

### Generating Alerts

When all the information about the sources has been collected, being the source properties and the counterparts in other catalogs including the properties of these counterparts, and for those sources which were found during source detection also the parameters retrieved during this process, it is evaluated against a defined set of trigger criteria by a program designated *alerter*. It was initially developed by Bastian Falkner from the Remeis observatory to provide a large amount of flexibility when defining trigger criteria and expanded and is maintained by the author of this thesis. Each trigger is defined by a set of criteria which can logically be combined in an arbitrary manner with either **and** or **or**. All criteria defining a trigger are evaluated in the order of definition while short circuit logic applies, meaning the evaluation is terminated as soon as a definitive answer has been obtained. Because most sources do not satisfy all criteria of a trigger a large amount of processing time can be saved in this way. The criteria types are divided into two main categories: Those needing the source history (see following section) and those which don't. I will give a brief overview of the criteria types which do not rely on the source history.

<sup>8</sup><https://vizier.u-strasbg.fr/viz-bin/VizieR>

Table 5.2: External catalogs matched against by the NRTA as of writing this thesis

Name	VizieR <sup>8</sup>	Wavelength
agn_3lac_highlat	J/ApJ/810/14/highlat	gamma
agn_3lac_lowlat	J/ApJ/810/14/lowlat	gamma
egret	J/ApJS/123/79/3eg	gamma
fermi_3fgl	J/ApJS/218/23/table4	gamma
integral_krivonos	J/A+A/475/775/table1	gamma
linford_blazars	J/ApJ/726/16/table1	gamma
akari_fis	II/298/fis	ir_submm
alfalfa	J/AJ/142/170/table1	ir_submm
glimpse	II/293/glimpse	ir_submm
herschel	J/ApJ/811/145/table3	ir_submm
iras_point	II/125/main	ir_submm
msx6c	V/114/msx6_gp	ir_submm
planck	VIII/91/pccs1	ir_submm
sdwfs	J/ApJ/716/530/catalog	ir_submm
sefvert_deo	J/ApJ/705/14/catalog	ir_submm
allWISE	II/328/allwise	mid-IR
allWISE_xmmsl2	J/MNRAS/473/4937/xmmslew2	mid-IR_xray
BSC	V/50/catalog	optical
SDSS_quasars	VII/280/catalog	optical
Tycho2	I/259/tyc2	optical
gaia_dr2	I/345/gaia2	optical
euve	IX/35/survey	optical_uv
haberl	J/A+A/586/A81/table5	optical_uv
liu	J/A+A/469/807/lmxb	optical_uv
sefvert_koulouridis	J/ApJ/639/37/table1	optical_uv
uvex	J/MNRAS/420/1115/uvex	optical_uv
veron	VII/258/vv10	optical_uv
at20g	J/MNRAS/402/2403/at20gcat	radio
cgrabs	J/ApJS/175/97/table2	radio
crates	J/ApJS/171/61/table5	radio
gb6	VIII/40/gb6	radio
lofar	J/A+A/574/A73/lofarlb	radio
nvss	VIII/65/nvss	radio
pmne	VIII/38/pmne	radio
pmns	VIII/38/pmns	radio
pmnt	VIII/38/pmnt	radio
pmnz	VIII/38/pmnz	radio
vlsr	VIII/97/catalog	radio
WISEagn	J/ApJS/234/23/r90cat	uv_nir
3xmm	IX/55/xmm3r8s	xray
XMMSL2	IX/53/xmmsl2c	xray
XMMSL2_stellar	J/A+A/614/A125/catalog	xray
allWISE_2rxs	J/MNRAS/473/4937/2rxswg	xray
bat_agn	J/ApJ/749/21/table1	xray
csc	IX/45/csc11	xray
integral_ibis_agn	J/MNRAS/426/1750/tablea1	xray
rass_2rxs	J/A+A/588/A103	xray
rass_variable	J/A+A/403/247/table7	xray
ritterCV	B/cb/cbdata	xray
ritterLMXB	B/cb/lmxbdata	xray
sefvert1_zhou	J/ApJ/713/L11/table1	xray
sefvert2_poletta	J/ApJS/106/399/table1	xray
swift_bat_agn	J/ApJ/681/113/table1	xray
swxrt	J/A+A/551/A142/1swxrt	xray

The simplest criterion named “detection parameter criterion” compares a source property against a given range or a list of specific values. If the property has or has not, depending on the definition, exactly one of the defined values or lies in the given range the criterion is considered true.

Another simple criterion is the “blacklist criterion” (not to be confused with the general blacklisting described in Section 5.8.2). It checks whether a source is listed in an externally supplied file specifying a set of circles with varying radii at arbitrary locations in the sky. If the source position is not enclosed by

one of these circles the criterion is considered to be true.

The “match criterion” can be used to test for the presence or absence of a match in either a specified catalog or any catalog covering a certain wavelength regime. Upper and lower limits can be specified for the probability of the match derived by `nway` and its distance to the initial source position. Additionally, the candidates in the reference catalog can be dynamically filtered using an expression complying to the FITS *extended filename syntax*.

Lastly, properties of monitoring sources can be compared against arbitrary expressions supplied with their definition in the user catalog by the “user catalog criterion”. An expression can be given containing arithmetic operations to be performed on values in additional columns in the user catalog file which are taken from the row of the monitoring source. If the resulting value is lower or higher, depending on the criteria definition, than the specified source property the criterion is considered to be true.

```

=====
Checking trigger "LMC"
Criterion as string:
'LMC' by Frank Haberl (GAL) [silent] send alert to 'fwh@mpe.mpg.de':
  (ORGCAT in ['LMC']) & (0.1 <= 'CountRate_0') & (1.5 <= 'SNR') &
  ('RA' <= 88) & ('EXT_LIKE' <= 10) &
  (not in /NRTA/config/blacklists/LMC_exclude_alerts.fits)
Alerting even if source is blacklisted
Criteria for trigger: 6
1.: ORGCAT: LMC in ['LMC']
   ==> True
2.: CountRate_0: 1.8488327 above 0.1
   ==> True
3.: SNR: 137.06061 above 1.5
   ==> True
4.: RA: 86.67503889339355 below 88
   ==> True
5.: EXT_LIKE: 0.0 below 10
   ==> True
6.: Not blacklisted in file /NRTA/config/blacklists/LMC_exclude_alerts.fits
   ==> False
--> Trigger is not valid
=====

```

Listing 1: Example for the decision tree created by the alerter during the evaluation of a criterion checking whether a sufficiently bright source was located in the LMC. The trigger was supplied by Frank Haberl and consists of a set of 5 detection parameter criteria followed by a blacklist criterion which was not fulfilled, i.e., the source was located in one of the regions defined by the custom blacklist.

For each trigger evaluated on each source the alerter creates a log file called *decision tree*. Every step taken in the evaluation of the trigger is documented to assist in the subsequent assessment during human interaction. An example for such a decision tree is given in Listing 1.

If all criteria of a trigger are valid for a given source an alert is generated. By default, an e-mail is then sent to a list of responsible scientists defined by the trigger. However, this can be overridden for individual triggers.

## Source Tracking

The entire process described above is based on detections performed for each slew over a target individually. To characterize the behavior of sources across different erodays their individual detections must first be associated with each other. This task is again achieved by using `nway` as described in Knies (2021, in preparation) but can only be performed when the entire data of a ground-contact session have passed through the mechanism described above and all detections are present in the archive. The NRTA therefore monitors the processing of data and when for a total of 60 minutes no source detection was performed it assumes that all data of a ground-contact session was processed and launches the second part of the pipeline designated `postnrta`. It first performs source matching of all detections and monitoring sources of every

eroday between itself and the 15 erodays before. After this the alerter evaluates all triggers containing criteria relying on the source history. Two of these criteria are available.

The “history criterion” compares the value of a source property of the currently considered eroday against values of this property on an arbitrary set of past erodays. If the property changed by at least or at most a specified factor, depending on the definition, the criterion is considered true. Independent factors can be specified for arbitrary numbers of erodays back in time. Simultaneously the criterion can also check whether the past values lie in a given range or not.

Using the “deviation criterion” a source property of the currently considered eroday can be compared against some average calculated over a specified number of past erodays. It can be executed in strict context, meaning that the source must have been detected in the entire specified time range, or a minimum number of detections can be specified. To calculate the average the arithmetic mean and median are available. If the result of the calculation is in a given range or if the result compared with the value of the current eroday exceeds a specified fraction the criterion is considered true.

Again all decisions made by the alerter are documented in the form of a decision tree.

### 5.8.3 Browser-Based User-Interface

Running the `postnrta` concludes the processing performed by the NRTA with the notification of the relevant scientists. All data has been stored in the final NRTA archive and is made available for visual inspection in a web-browser based front end developed by the Remeis observatory which can be used by weekly assigned shifting personnel to validate the quality of the alerts, perform simple analysis tasks and communicate. It offers a broad variety of possibilities to inspect images, spectra, lightcurves, source lists, the decision tree, source matches and the source history. It also embeds an Aladin interface (Boch & Fernique, 2017) to compare the alert and image at hand to other all-sky surveys. A screenshot showing an example use case of the NRTA front end is shown in Fig. 5.18.

### 5.8.4 Statistics from the NRTA

From the beginning of the mission up to June 11th, 2021, the NRTA has analyzed the occurrences of 21.4 million possible sources. Roughly one million of these were found during source detection in patches or stamps while all remaining ones are monitoring sources. In total roughly 150 thousand alerts were generated and for the most relevant an Astronomer’s Telegram (Rutledge, 1998) was published to alert the scientific community and provide necessary information for follow-up observations (see for example Wilms et al., 2020; Gokus et al., 2020; Koenig et al., 2020b; Haberl et al., 2020; Rau et al., 2020; Grotova et al., 2020; Koenig et al., 2020a). It is emphasized that this high number of alerts is mostly caused by effects such as newly arising bright pixels and bright sources causing numerous spurious detections or trigger criteria which were initially to loosely defined. With the start of *eROSITA*’s fourth all-sky survey the NRTA is generating a few alerts per 24 h.

For most monitoring sources the nominal exposure time of only about 40 s is not enough to provide enough data for statistical evaluation. The situation is different for all sources found during the source detection procedure. To compare the brightness of monitoring sources to the ones found by source detection in patches and stamps the count-rate for every source is calculated from the lightcurves, a data product present in both cases. On the left-hand side in Fig. 5.19 the resulting cumulative distribution of count-rates calculated from the lightcurves for detected sources is shown in comparison to that determined by the maximum likelihood based PSF-fitting performed by the eSASS. Up to  $\sim 10$  cts/s the NRTA found more sources to have a lower count-rate compared to the PSF-fitting procedure. This effect might be caused by the influence of the asymmetric Poisson distribution at low count-rates which can lead to higher values calculated by the maximum likelihood based PSF-fitting procedure. To investigate this effect further a two-dimensional histogram showing the relation between both count-rates for all sources is shown on the right-hand side of Fig. 5.19. In this case the influence of Poisson statistics might cause the distribution to be spread out more towards the left on the  $x$ -axis. On the  $y$ -axis the distribution only extends down to  $\sim 0.1$  cts/s meaning for all sources the count-rates found by PSF-fitting are at least this high. When assuming a nominal exposure time of 40 s this corresponds to a total of at least four counts detected for each source during a single slew. This might indeed correspond to a lower limit necessary for the detection of point sources. However, in its

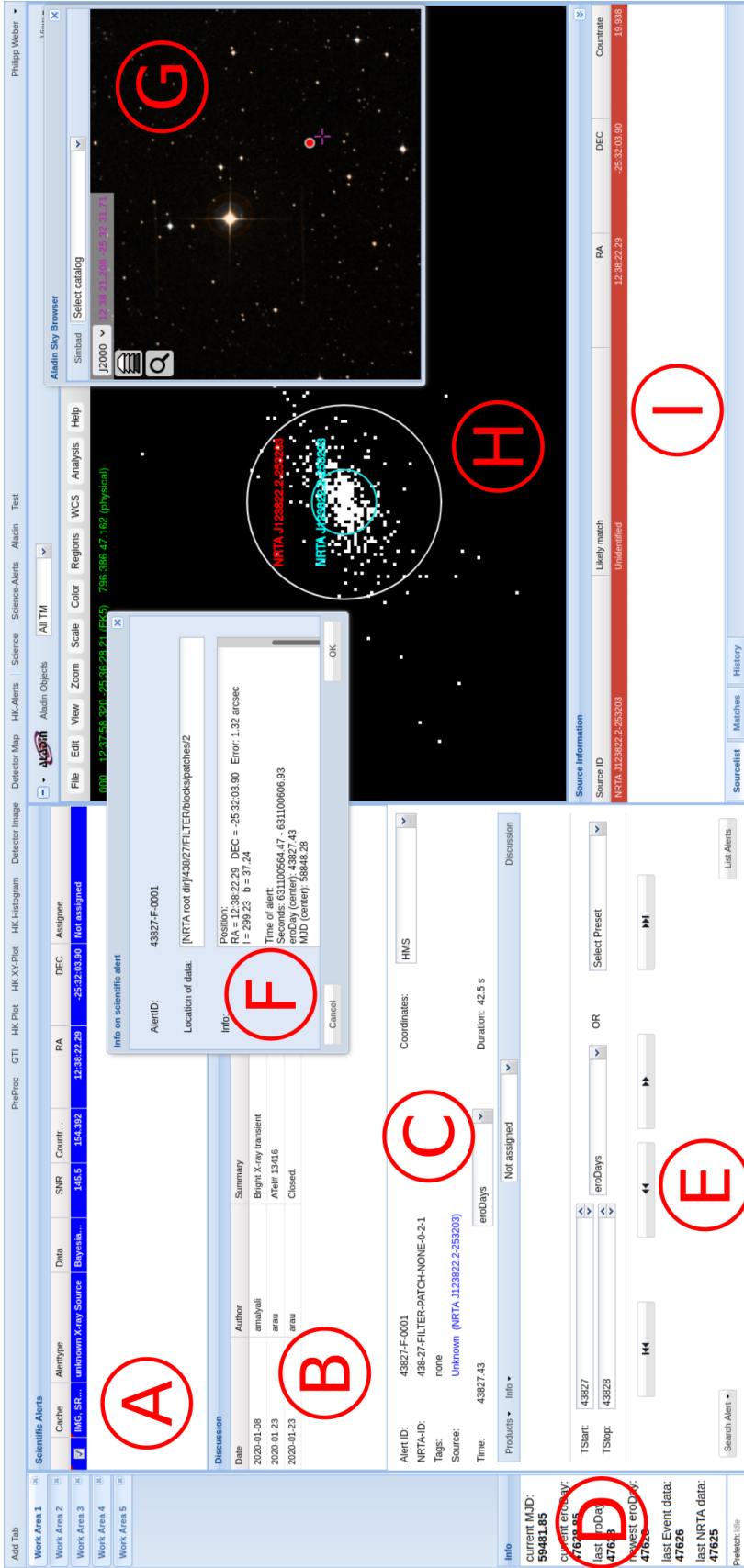


Figure 5.18: Screenshot of the NRTA web front end showcasing the main features.

- Ⓐ List of science alerts in the selected time period
- Ⓑ Discussion about the currently displayed alert
- Ⓒ Basic information about the currently displayed alert
- Ⓓ Information about the current time and data available in the NRTA archive
- Ⓔ Time period selection for Ⓐ and alert search
- Ⓕ Detailed information about the currently displayed alert (separate window)
- Ⓖ Aladin window currently displaying the Digitized Sky Survey (Lasker et al., 1990). The red dot in the window corresponds to the position of the alerting source
- Ⓗ Science analysis window displaying the image of the alerting source. It can also show lightcurves and spectra
- Ⓘ Window showing the list of sources found in the currently opened image, source matches and history

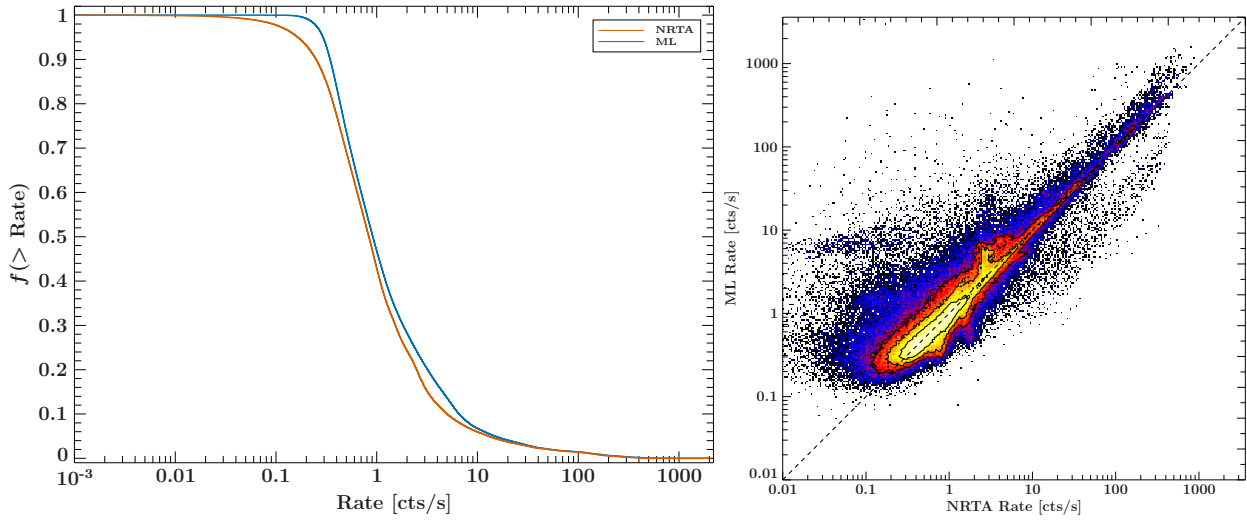


Figure 5.19: **Left:** Cumulative distribution of the count-rates of all sources detected by the NRTA during the all-sky survey as calculated from the lightcurves by the NRTA itself compared to the distribution found by maximum likelihood (ML) based PSF-fitting performed using the eSASS. On the  $y$ -axis the fraction of sources having a count-rate higher than that of the current value on the  $x$ -axis is shown. The NRTA found more sources to have a lower count-rate than the PSF-fitting up to  $\sim 10$  cts/s. This effect might be caused by the influence of Poisson statistics in the low count regime which is treated differently in the ML based PSF-fitting compared to the extraction of simple lightcurves.

**Right:** Two-dimensional histogram showing the relation between the count-rate from the NRTA and that from the PSF-fitting. Although the distribution from the NRTA is broader and tends towards lower count-rates the majority is concentrated on the diagonal implying an agreement between both methods.

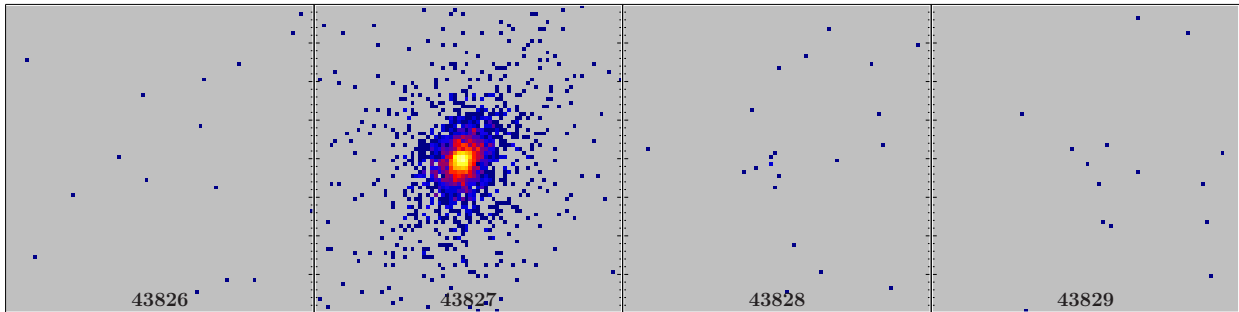


Figure 5.20: Images of the position where the bright transient source was detected for each scan by *eROSITA*, starting from one eroday before the event to two erodays after. The edges of the images correspond to an angle of  $160''$ . Only on eroday 43827 a very bright source is visible. On the following eroday a slight clustering of events is can be seen which was also identified by the detection process as a faint source.

entirety the distribution is concentrated on the diagonal in the histogram, marked with a dashed line, which indicates that for most sources the count-rates determined by both methods are in agreement.

### 5.8.5 Example: The New-Years-Eves Transient

On December 31, 2019, shortly after *SRG* finished its CalPV phase and started its all-sky survey, the NRTA generated an alert regarding an up to this point completely unknown and very bright X-ray source. The findings regarding this new X-ray transient have been published as Astronomer’s Telegram (ATel) #13416<sup>9</sup>

<sup>9</sup><https://www.astronomerstelegam.org/?read=13416>

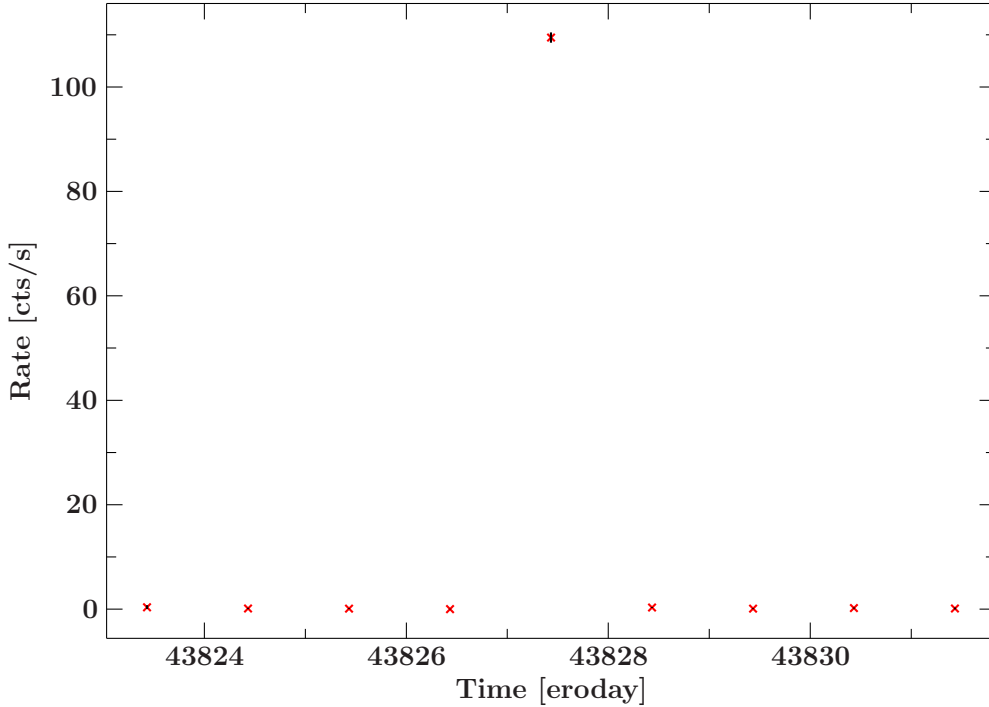


Figure 5.21: Lightcurve showing the count-rate measured by *eROSITA* from 0.1 to 10.0 keV at the position of the transient source in steps of erodays. Errorbars are included but very small.

by Wilms et al. (2020).

Source detection was triggered by the Bayesian Block algorithm on an interval of 42.5 s starting from 6:42:41 UTC which corresponds to eroday 43827. The detector lightcurve of TM 6 for the telemetry file containing the data and the period triggering the source detection are shown in Fig. 5.15. A clear excess in the count-rate is visible towards the end of the lightcurve. The source detection process identified a very bright source at  $\alpha = 12^{\text{h}} 38^{\text{m}} 22.2^{\text{s}}$  and  $\delta = -25^{\circ} 32' 06''$  with an estimated positional accuracy of  $10''$ , thus the source was designated SRGt J123822.3–253206. The images at this position of a  $160 \times 160''$  large area on the sky, from the slew before the event until two slews after, are shown in Fig. 5.20. Strikingly, the source suddenly appears on eroday 43827, and it is not visible on any prior or following scan. Only on eroday 43828 a slight clustering of events is visible at the position where the source was found which was also still detected as a point source.

A lightcurve showing this phenomenon in the 0.1 to 10.0 keV band is given in Fig. 5.21. During the slew covering the outburst of the source the count-rate jumped to  $109 \pm 1.0$  cts/s while for all other slews it was below 0.5 cts/s. The short term development of the count-rate in 1 s wide bins is shown in Fig. 5.22. Interestingly, the source was brightest when it entered the FOV with a count-rate between 200 cts/s and 250 cts/s apart from an isolated bin extending up to 300 cts/s. Over the first half of the  $\sim 40$  s long observation the count-rate dropped to a level between 50 cts/s and 100 cts/s.

Because of the high count-rate the data obtained by *eROSITA* is affected by pileup (see Section 4.1.3) causing it to be unreliable. Therefore, the count-rates can only be interpreted as lower limits. To estimate the real flux of the source a model has to be fitted to the data. However, the effect of pileup cannot be expected to affect photons of all energies equally, thus also the spectrum could be heavily affected, thus no conclusion can be drawn on the physical parameters of the source. The obtained spectrum from all TMs in the energy range from 0.5 to 7.0 keV is shown in Fig. 5.23. To give a lower limit of the source flux I applied a variety of simple empirical models consisting of a combination of galactic foreground absorption using `TBnew` with its default abundances, an update version of `TBabs` (Wilms et al., 2000), a `powerlaw` and an ordinary Planck function to describe `blackbody` emission or a `diskbb` component to account for the

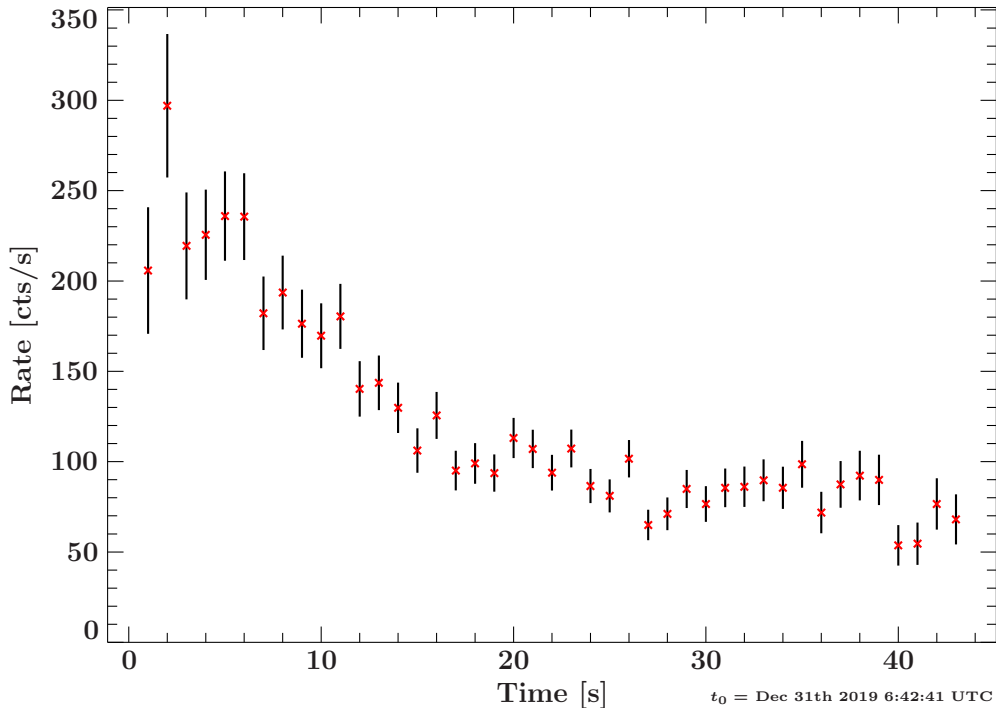


Figure 5.22: Lightcurve in the 0.1 to 10.0 keV band in 1 s bins of the slew by *eROSITA* over the position of the transient during its outburst. During the slew itself the count-rate drops during the first half of the observation to a level between 50 cts/s and 100 cts/s.

emission of an accretion disk. Although the count-rate is already causing pileup the short exposure time of  $\sim 40$  s yields in a low SNR, thus Cash (1979) statistic was used to fit the models to the data. The equivalent hydrogen column density for the foreground absorption was taken as  $N_{\text{H}} = 7.87 \times 10^{20} \text{ cm}^{-2}$  from `HEASoFT`'s `nH tool`<sup>10</sup> which in turn calculated it for the source's position using maps from the HI4PI survey (HI4PI Collaboration et al., 2016) and was fixed during the fitting procedure. All best-fit parameters for each model combination are listed in Tab. 5.3 and the respective residuals are shown in Fig. 5.23. `TBnew1` describes the galactic foreground absorption. All models only taking that into account are not able to describe the data accurately. The best fit with `stat/dof` = 3.45 of these models is achieved by the combination of `powerlaw` + `blackbody`. As can be seen in the panels of Fig. 5.23, showing the residuals, the largest deviations from the models are present in the low energy range where the models are overestimating the flux. Therefore, I added another absorption component depicted `TBnew2` which could, if the spectrum was to describe the emission of the source accurately, represent source-intrinsic absorption caused by for example the ISM of a galaxy hosting the compact object. It is, however, also possible that this suppression of flux in the low energy regime is caused by strong effects related to the pileup. Allowing for this additional component yields significantly better fits. The best was achieved by the combination of a `powerlaw` and a `blackbody` with `stat/dof` = 1.65. These individual components, affected by both absorption components, are additionally shown in the top panel of Fig. 5.23. Under the assumption that this model is indeed describing the data correctly a lower limit of the flux in the 0.5 to 7.0 keV energy range can be given as  $(2.1 \pm 0.30) \times 10^{-10} \text{ erg cm}^{-2} \text{ s}^{-1}$ .

The source matching process performed by the NRTA did not identify any possible counterparts to the source and no previously known X-ray source at the same position. Also, the SIMBAD database<sup>11</sup> does not list any known sources at this position. The positions of three stars with optical magnitudes of  $\sim 21$  mag, listed in the VISTA Hemisphere Survey (McMahon et al., 2013) and Pan-STARRS data release 2 (Chambers et al., 2016), are compatible with the position determined by *eROSITA*. One of these stars was

<sup>10</sup><https://heasarc.gsfc.nasa.gov/cgi-bin/Tools/w3nh/w3nh.pl>

<sup>11</sup>[simbad.u-strasbg.fr](http://simbad.u-strasbg.fr)

Table 5.3: Best-fit parameters, statistics and fluxes for all empirical models used to describe the spectrum during the outburst of the X-ray transient. Errors are given in terms of the 90% confidence interval. The residuals of all models are shown in Fig. 5.23. Fluxes are calculated in the 0.5 to 7.0 keV energy band. For galactic foreground absorption the hydrogen column is fixed at  $N_{\text{H}} = 7.87 \times 10^{20} \text{ cm}^{-2}$ . Only the models with source intrinsic absorption, a **powerlaw** and either a **blackbody** or **diskbb** component achieve an acceptable fit.

Model	$N_{\text{H}2} [10^{22} \text{ cm}^{-2}]$	$\Gamma$	normpowerlaw	$kT$ [keV]	normblackbody	$T_{\text{in}}$ [keV]	normdiskbb	stat/dof	Flux [ $10^{-10} \text{ erg cm}^{-2} \text{ s}^{-1}$ ]
TBnew1 $\times$ blackbody	-	-	-	$0.466^{+0.011}_{-0.014}$	$(1.91 \pm 0.08) \times 10^{-3}$	-	-	6.86	$1.4 \pm 0.03$
TBnew1 $\times$ diskbb	-	-	-	-	-	$0.98^{+0.07}_{-0.06}$	$10.8^{+2.4}_{-2.1}$	4.29	$1.8 \pm 0.28$
TBnew1 $\times$ powerlaw	-	$1.45^{+0.07}_{-0.06}$	$0.0398^{+0.0015}_{-0.0012}$	-	-	-	-	5.47	$2.5 \pm 0.08$
TBnew1 $\times$ (powerlaw+blackbody)	-	$0.65^{+0.29}_{-0.22}$	$(8.8^{+4.6}_{-2.4}) \times 10^{-3}$	$0.336^{+0.016}_{-0.021}$	$(1.12^{+0.08}_{-0.18}) \times 10^{-3}$	-	-	3.45	$2.2 \pm 0.35$
TBnew1 $\times$ (powerlaw+diskbb)	-	$0.2^{+0.8}_{-1.3}$	$(1.9^{+6.3}_{-1.9}) \times 10^{-3}$	-	-	$0.79^{+0.12}_{-0.11}$	$21^{+10}_{-7}$	4.12	$2.7 \pm 1.73$
TBnew1 $\times$ TBnew2 $\times$ blackbody	$(s^{+278489}) \times 10^{-8}$	-	-	$0.466^{+0.011}_{-0.014}$	$(1.91 \pm 0.08) \times 10^{-3}$	-	-	6.96	$1.4 \pm 0.03$
TBnew1 $\times$ TBnew2 $\times$ diskbb	$0.049^{+0.025}_{-0.026}$	-	-	-	-	$0.89^{+0.08}_{-0.06}$	$16^{+6}_{-5}$	4.20	$1.7 \pm 0.35$
TBnew1 $\times$ TBnew2 $\times$ powerlaw	$0.34 \pm 0.05$	$2.47 \pm 0.15$	$0.086^{+0.008}_{-0.009}$	-	-	-	-	2.75	$1.7 \pm 0.12$
TBnew1 $\times$ TBnew2 (powerlaw+diskbb)	$0.68^{+0.04}_{-0.05}$	$1.92^{+0.24}_{-0.14}$	$0.059^{+0.013}_{-0.007}$	-	-	$0.145^{+0.004}_{-0.005}$	$(2.3^{+11.3}_{-1.2}) \times 10^5$	1.68	$2.3 \pm 0.55$
TBnew1 $\times$ TBnew2 (powerlaw+blackbody)	$0.60^{+0.15}_{-0.10}$	$1.94^{+0.26}_{-0.18}$	$0.059^{+0.015}_{-0.010}$	$0.127^{+0.015}_{-0.014}$	$(s^{+10}) \times 10^{-3}$	-	-	1.65	$2.1 \pm 0.30$

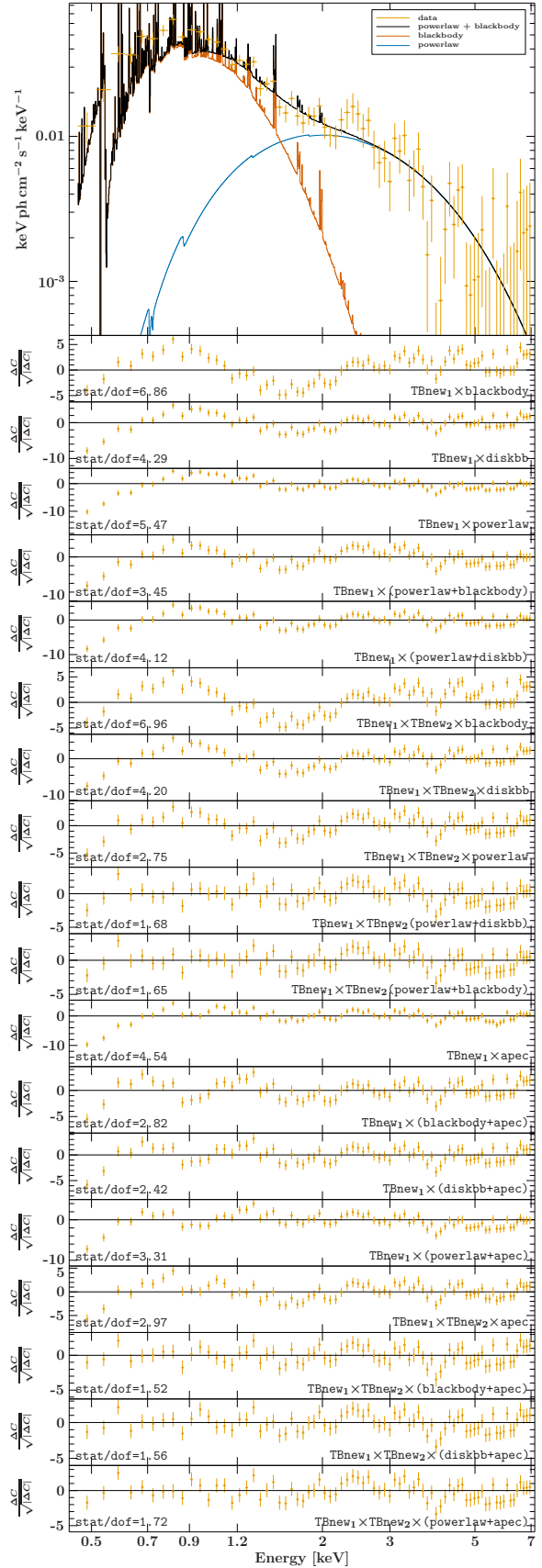


Figure 5.23: Spectrum of the transient during its outburst in the 0.5 to 7 keV range with residuals for all empirical models fitted to the data. The **powerlaw** and **blackbody** components shown in the top panel are the ones achieving the best fit and are shown including the effect of both absorption components. Note the strong residuals in the low energy range for all models except those using a **powerlaw** and either a **blackbody** or a **diskbb** component with source intrinsic absorption. All model parameters are listed in Tab. 5.3. The spectral shape is most likely affected by pileup.

also found during the infrared survey performed by NEOWISE (Mainzer et al., 2011).

As described in Section 5.8.1, short-lived X-ray emission can originate from compact sources such as stars, neutron stars and black holes. Also, the afterglow of GRBs could potentially create an X-ray source only being present for a couple of hours. As described in the ATel by Wilms et al. (2020), a stellar flare is unlikely to have caused the presented X-ray burst because the optical counterpart would most likely be known if it existed. For the three stars which were found to be possibly consistent with the position determined by *eROSITA* the optical and infrared magnitudes would place them at distances too far away to cause the observed high X-ray flux. Also, the outburst of a neutron star appears unlikely because of the lack of an optical counterpart. *ART-XC*, *eROSITA*'s complementary instrument onboard *SRG*, also detected the transient, as reported in ATel #13415<sup>12</sup> by Semena et al. (2020), with a count-rate of 4 cts/s in the 4 to 20 keV band, corresponding to a flux of  $7 \times 10^{-11}$  erg cm<sup>-2</sup> s<sup>-1</sup> from 4 to 10 keV and  $6 \times 10^{-11}$  erg cm<sup>-2</sup> s<sup>-1</sup> from 10 to 16 keV. After the publication of both mentioned ATels Ho (2020) initiated a 20 min long radio observation of the reported position by the Very Large Array (Thompson et al., 1980) which was reported as ATel #13485<sup>13</sup>. Two sources were found in the stated 10'' region, one of which was consistent with the position of one of the stars listed by Pan-STARRS, the other one had no counterpart. With this current state of knowledge the actual nature of the source remains a mystery.

---

<sup>12</sup><https://www.astronomerstelegam.org/?read=13415>

<sup>13</sup><https://www.astronomerstelegam.org/?read=13485>



## 6 The X-ray Observatory *XMM-Newton*

The *X-ray Multi-Mirror Mission (XMM-Newton)* observatory was launched on December 10, 1999, with the Ariane V launch V 504 from Kourou, French Guiana. The high throughput observatory provides spectroscopic imaging in the energy range from 0.1 to 10 keV. It is equipped with three mirror modules similar to those of *eROSITA*, two types of CCD sensors, European Photon Imaging Camera (EPIC)-pn and EPIC-MOS, and gratings for spectroscopy. Additionally, next to the apertures of the X-ray telescopes, an optical/UV telescope for simultaneous monitoring is located. A detailed description of the spacecraft and its operation can be found in Jansen et al. (2001). It has a mass of roughly four tons and is ten meters long. *XMM-Newton* has a highly eccentric orbit with a perigee of 7000 km, an apogee of 114000 km and the inclination is  $-40^\circ$ . Because of Earth's radiation belts science operations are only possible for altitudes of 60000 km or more.

### 6.1 Optical Tube Assembly

As described by Jansen et al. (2001), *XMM-Newton* uses three modules of Wolter type I grazing incidence mirrors with 58 shells each to focus X-ray photons onto their focal plane. The outer aperture of each module is 700 mm in diameter while the innermost shell has a diameter of 306 mm. With 1.07 mm thickness of the outermost mirror and 0.47 mm of the innermost mirror the smallest distance between two shells is 1 mm. Made of nickel and coated with gold on the reflective side, each module is 600 mm in length and provides a focal length of 7.5 m. Spiders with 16 spokes hold the shells in place and an X-ray baffle consisting of two sieve plates provides protection from stray light by acting as collimators with 58 annular apertures. Behind the mirror modules deflectors for low energetic electrons are located which use circumferential magnetic fields. Each individual mirror module provides an effective area of roughly  $1500 \text{ cm}^2$  at 1 keV and roughly  $500 \text{ cm}^2$  at 8 keV. The image quality has been confirmed by in-orbit calibration measurements to be identical to the ground-based calibration at the PANTER facility and is roughly  $4.4''$  FWHM at 1.5 keV. Sensors

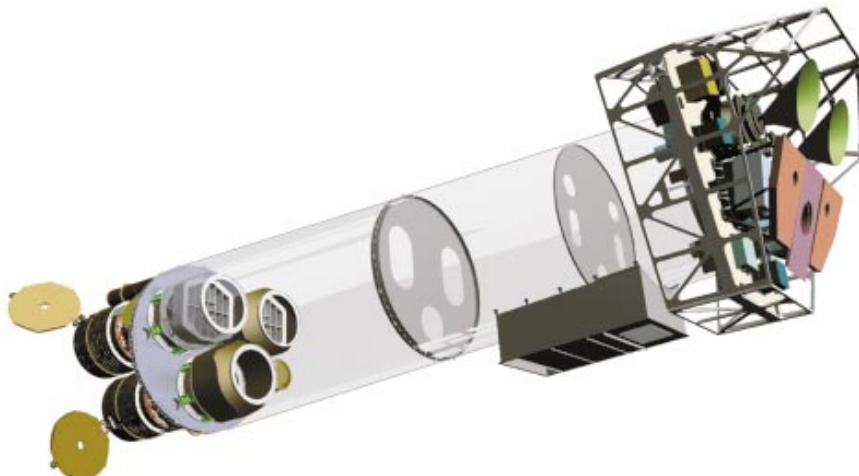


Figure 6.1: Schematic view of *XMM-Newton*'s OTA. Photons enter the telescope on the left and are focused by the three mirror assemblies onto the focal plane on the right. Behind both upper mirror modules the gratings are mounted. The structures at the back end of the satellite are radiators for the cooling systems. Taken from Jansen et al. (2001).

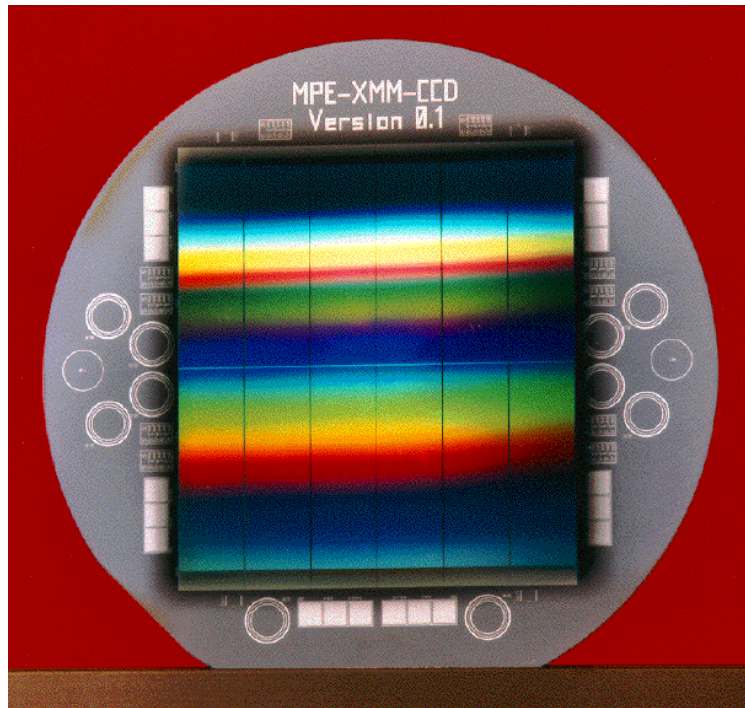


Figure 6.2: Illuminated back side of the EPIC-pn wafer with its twelve individual CCDs. Taken from the HEASARC website<sup>1</sup>; Image credit: XMM-Newton SOC, VILSPA.

in the form of CCDs are located at the end of a carbon fiber tube, connecting the optical bench with the mirror assemblies and the instrument platform. Roughly 50% of the photons are diffracted by gratings after passing through two of the mirror modules while the remaining photons are focused onto the two imaging MOS CCDs (Gondoin et al., 1998a,b, 2000)

## 6.2 EPIC-pn

The EPIC-pn CCDs are one of the two CCD models in operation onboard *XMM-Newton*. They can be considered as predecessors to *eROSITA*'s CCDs but do not offer a frame store are. As described by Strüder et al. (2001), the total imaging area of EPIC-pn consists of 12 individual CCDs with  $200 \times 64$  square shaped pixels with an edge length of  $150 \mu\text{m}$ . The sensors are organized in four quadrants with three sensors each next to each other along their long edges at a distance of  $194 \mu\text{m}$ . The distance between the quadrants in the direction perpendicular to the long edges is  $214 \mu\text{m}$  and  $41 \mu\text{m}$  along the short edges. An exception to the square shaped pixels are the ones along the short edges at the center of the entire assembly. They are  $150 \times 200 \mu\text{m}$  in size and elongated along the long edge of the individual CCDs. In each quadrant the CCDs are enumerated from CCD0 to CCD2, starting from the center of the assembly. The center of the FOV is located at CCD0, in quadrant 1. With the focal length of the mirror modules the pixel pitch corresponds to  $4.13''$ , but the positional accuracy of the sensors is  $120 \mu\text{m}$ , increasing the spatial resolution to  $3.3''$ , limited by the mirror assembly. The total size of all sensors is  $6 \times 6 \text{ cm}$ , where 97% of the telescope's FOV of  $27.2 \times 26.2'$  is covered and where the uncovered area was accepted to provide redundancy. Roughly  $6 \text{ cm}^2$  are not covered by the FOV and are used for background studies. Due to the thickness of  $300 \mu\text{m}$  of the silicon substrate the quantum efficiency at 10 keV is higher than 90%. The sensors are cooled to  $-90 \text{ }^\circ\text{C}$  for best energy response.

Six different modes of operation can be chosen for the EPIC-pn, each providing a different readout region with different timing resolution. In full frame mode all four quadrants are exposing in parallel for 68.7 ms,

<sup>1</sup><https://heasarc.gsfc.nasa.gov/Images/xmm/pn-front.gif>

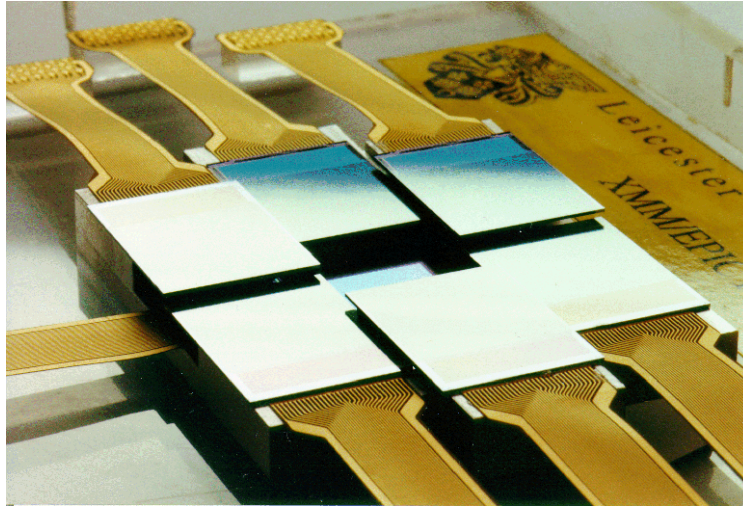


Figure 6.3: Assembly of seven MOS CCDs. The outer sensors are elevated to better approximate the shape of the focal plane. Image taken from the HEASARC website<sup>2</sup>; Image credit: XMM-Newton SOC, VILSPA

followed by a readout cycle which takes 4.6 ms. This ratio of the total cycle time of 73.3 ms leads to 6.2% out of time events. This value can be reduced to 2.3% by using the extended full frame mode, for which a single exposure lasts for 199.2 ms. In the large and small window modes a defined inner region is used to collect data during the exposure. After that the charge clouds are rapidly transferred to the outer region of the sensors which act as a frame store area. In the large window mode the inner half of the sensors is operating to collect data with a time resolution of 47.7 ms and 0.2% amount of out of time events while for the small window mode the imaging area is reduced to only  $63 \times 64$  pixels on CCD0 in quadrant 1 providing a time resolution of 5.7 ms and 1.1% out of time events. In timing mode only this CCD operates and combines 10 pixels in the direction of the columns to provide a time resolution of  $30 \mu\text{s}$ . The perpendicular spatial resolution is retained. As a last option the burst mode is designed for very bright sources. When it is used 179 rows are discarded every cycle and the remaining pixels are read out normally providing a time resolution of only  $7 \mu\text{s}$  but only a detector lifetime of 3%. A FW located in front of the sensors provides an open and a closed position and filters of four different thicknesses.

The total effective area of the EPIC-pn instrument is  $1227 \text{ cm}^2$  at 1 keV with an energy resolution in the range from 20 to 50, depending on the location on the sensor and the energy.

## 6.3 EPIC-MOS

In the focal planes of the two other mirror modules and behind the attached reflection grating assemblies seven EPIC-MOS CCDs are located. A description of these cameras is given by Turner et al. (2001). The outer six sensors are arranged in a hexagonal pattern and are elevated towards the mirrors compared to the central sensor which provides better image quality due to the curved focal plane. The effective dead space between the imaging areas of adjacent CCDs is  $300 \mu\text{m}$ . Each sensor is square shaped with an edge length of 2.5 cm and  $600 \times 600$  also squared shaped,  $40 \mu\text{m}$  pixels. In this arrangement the total area covered in the FOV is  $28.4'$  and one pixel corresponds to  $1.1''$  angular extent.

The MOS sensors also offer different readout modes similar to EPIC-pn's modes. In full frame mode an exposure takes 2.6 s while in large window mode a  $300 \times 300$  pixel area can be arbitrarily positioned on the sensors and exposed for 0.9 s. Using small window mode this area shrinks to  $100 \times 100$  pixels and the time resolution increases to 0.3 s. In full frame mode an electric chopper can be enabled which discards most of the collected data and only exposes for 0.2 s decreasing the detector lifetime to 6.9%. MOS also offers a timing mode which works similarly to the timing mode of the pn sensors but combines 100 pixels in one

<sup>2</sup><https://heasarc.gsfc.nasa.gov/Images/xmm/mos-array.gif>

dimension providing a time resolution of 1.75 ms.

Sensitivity of the MOS cameras also ranges from 0.1 to 15 keV and they provide an effective area of  $922 \text{ cm}^2$  at 1 keV and a similar spectral resolution as EPIC-pn. The sensors are cooled to 170 K using cone-shaped radiators (compare Fig. 6.1) and are also equipped with FWs which have two thin filters, a medium filter and a thick filter mounted and can also be set to closed and completely open.

## 6.4 Reflection Grating Spectrometer

The Reflection Grating Spectrometer (RGS), as described by den Herder et al. (2001), consists of two arrays of 182 and 181 gratings behind the two mirror modules focusing onto the MOS imaging cameras. They deflect roughly 50% of the photons passing through the mirrors by diffraction onto a row of nine CCDs. The gratings and the CCDs are located on the so called *Rowland circle* to prevent aberrations of the deflected light without a variable slit geometry (Paerels, 2010). On this circle also the prime focus of the mirrors is located. The CCDs integrating the spectrum are cooled to  $-80 \text{ }^\circ\text{C}$ , which can be lowered to  $-120 \text{ }^\circ\text{C}$ , and have  $384 \times 1024$  square pixels with an edge length of  $27 \mu\text{m}$  and an equally sized frame store area. In total the nine CCDs cover a range of 253 mm with a gap of 0.5 mm between two adjacent sensors. Aluminum on-chip filters block optical light. The spectral orders overlap on the sensor assembly but can be separated by the energy resolution of 160 eV FWHM of the CCDs at 2 keV.

In this configuration the RGS offers an energy resolution of 100 to 500 over an energy range from 0.3 to 2.1 keV with an effective area of  $140 \text{ cm}^2$  at 0.83 keV. The elongation of the FOV along the gratings is  $5''$ . These parameters were targeted to enable the investigation of the L transition edge of iron and the K transition edge of carbon, nitrogen, oxygen, neon, magnesium, and silicon in astrophysical sources.

## 6.5 Optical Monitor

The three X-ray telescopes onboard XMM-Newton with their sensors are accompanied by a Ritchey Chrétien reflector telescope operating in the optical and UV regime, called Optical Monitor (OM). Its details are described in Mason et al. (2001). The optics consists of an  $f/2$  primary mirror with a diameter of 30 cm and a hyperbolic secondary mirror which increases the focal length to 3.81 m, resulting in a focal ratio of 12.7. Two redundant sets of imaging sensors in the focal plane can be selected by an additional mirror angled at  $45^\circ$  in the optical path. In front of each detector a FW with 11 positions is located. Six filters can be selected for color discrimination from 180 nm to 580 nm, one filter has a bandpass over this entire range and another position is used as a shutter. The three remaining positions contain two grisms (a combination of a prism and a grating) to enable low resolution spectroscopy and a four times magnifier for wavelengths from 380 nm to 650 nm.

As detectors microchannelplate-intensified CCDs are used. The incoming photons first create photoelectrons through a photocathode, which hit a microchannel plate stack amplifying the signal after which the electrons are converted back to photons through a phosphor screen. After passing through fiber tapers, correcting for different pixel sizes, the photons are registered by a CCD which has  $256 \times 256$  physical pixels which yields  $2048 \times 2048$  pixels on the sky by employing the centering of the tapers. Each pixel corresponds to  $0.69''$  when projected onto the sky. In full frame mode the CCD is read out every 11 ms. The full FOV covered in this way is  $17 \times 17'$  in size.

# 7 *eROSITA*'s view of the Active Galactic Nucleus 1H 0707–495

1H 0707–495, initially cataloged as 1H 0659–494 in the *HEAO-1* catalog (Wood et al., 1984), is a NLS1 galaxy located in the constellation of Puppis. In the first *ROSAT* catalog it was detected as 1RXS J070840.9–493305 at  $\alpha = 07^{\text{h}} 08^{\text{m}} 40.9008^{\text{s}}$  and  $\delta = -49^{\circ} 33' 05.508''$  (Voges et al., 1999). As identified by the Two Micron All Sky Survey (2MASS) (Skrutskie et al., 2006) the AGN is hosted in a galaxy which has a semi-major axis of  $12.42''$  in the near infrared. The 6dF Galaxy Survey determined the cosmological redshift of the object to  $z = 0.04057$  (Jones et al., 2009) and Véron-Cetty & Véron (2010) found its V-band magnitude to be 15.7.

*eROSITA* carried out an observation of 1H 0707–495 in the CalPV phase (see Section 5.3) accompanied by a simultaneous observation by *XMM-Newton*. The results of this observation were already published in Boller et al. (2021) with major contributions of the author of this thesis. Therefore, the structure and content of the following section will closely resemble that of said publication, focusing on these contributions.

## 7.1 Past Developments around the Source

The analysis of an observation of 1H 0707–495 by *XMM-Newton* in October 2000 by Boller et al. (2002) showed that the X-ray spectrum of this source has a very prominent drop in flux at  $\sim 7$  keV. Explicitly pointed out in this publication is the lack of a narrow Fe  $K\alpha$  emission line. During the observation the flux of the source varied strongly on timescales of hours by a factor of  $\sim 4$ . Boller et al. (2002) interpreted the behavior as either partial-covering absorption by neutral clouds or relativistically blurred reflection off the accretion disk by material with varying degree of ionization. For the partial covering model three absorbers with different  $N_{\text{H}}$  were used. Both models describe the data accurately when allowing for a high abundance of iron in the absorbing and reflecting material and a steep powerlaw with  $\Gamma = 3.5$ . An alternative explanation for the observed spectrum was given by Fabian et al. (2002a) who used a threefold ionized reflection model to describe the data.

Tanaka et al. (2004) employed a multi-color disk blackbody to account for the soft excess in the spectrum, presumably caused by an optically-thick disk. Adding an exponential rolloff to the underlying powerlaw enabled them to significantly lower the iron abundance to achieve a good fit, while only relying on two covering components.

Another observation using *XMM-Newton* was carried out by Gallo et al. (2004) roughly two years later and showed that the energy of the prominent edge has shifted to  $\sim 7.5$  keV and its depth has halved, while the underlying continuum emission is steeper at high energies and the temperature of the disk blackbody increased. The total bolometric luminosity doubled compared to the previous observation and an additional emission feature at 0.9 keV was found, similar to another one found earlier by *ASCA* (Leighly et al., 1997; Leighly, 1999). Gallo et al. (2004) interpreted the observed changes as evidence of a warm absorber moving outward with  $\sim 0.01 c$ . Fabian et al. (2004) applied a model for relativistically blurred ionized reflection to the same data and found that a change in the ionization stage and emissivity profile can also explain the energy shift of the edge. In this picture the variability is explained by an interplay between the ionization state of the disk and the powerlaw continuum.

A comparison between models describing complex absorption, relativistic reflections and an additional continuum component was done by Sobolewska & Done (2007). They concluded that all three versions can describe the observed data but propose that the model of intrinsic absorption should be preferred because the parameters are less extreme. Done et al. (2007) demonstrated that the shape of the Fe  $K\alpha$  line can also be produced by a P Cygni line profile caused by a combination of absorption, scattering and emission in strong winds.

With an additional 330 ks deep observation using *XMM-Newton* Fabian et al. (2009) and Zoghbi et al. (2010) could show that the edge at  $\sim 7$  keV and the soft excess can be explained with a relativistically blurred iron  $K\alpha$  and  $L\alpha$  line, respectively, using the `laor` model (see Section 3.5.2). For the  $L\alpha$  line this was the first time it has been observed. This argument is especially convincing because the ratio between the flux of both emission lines corresponds well with theoretical predictions for ionized iron. With the Fe  $L\alpha$  line Fabian et al. (2009) and Zoghbi et al. (2010) also found a reverberation lag of  $\sim 30$  s between the continuum and the flux of the emission lines, which is interpreted as the delay between the X-ray continuum and the reflection off matter close to the black hole. Zoghbi et al. (2010) also state that the complex spectral shape caused by the Fe  $L\alpha$  line cannot be explained with an alternative model employing partial covering. Wilkins & Fabian (2011) use the same data to determine the emissivity profile of the accretion disk by assuming separate reflection components at different radii. In this way they could show that, as expected for reflection, the profile is much steeper closer to the black hole where it follows  $I \propto r^{-5.6}$  and  $I \propto r^{-3.3}$  further out which is close to the profile expected from the standard  $\alpha$ -disk model (compare Section 3.5.1).

The hypothesis of Fabian et al. (2009) and Zoghbi et al. (2010) that the reverberation is caused by the lag between radiation from matter falling into the black hole and its reflection off the inner accretion disk was shown to be inconsistent by Miller et al. (2010). Instead, they provided an explanation of reverberation using only scattering or reflection over the entire X-ray band and partial obscuration of this radiation. Zoghbi et al. (2011) point out that the explanation by Miller et al. (2010) did not account for the soft component contributed by blackbody emission, which only works under special geometric circumstances and predicts sharp spectral features which are not observed.

Blustin & Fabian (2009) found several broad emission lines in RGS data from *XMM-Newton* which have blue- and redshifted components originating from the accretion disk at a distance of  $\sim 1600 r_g$ .

End of 2010, a monitoring campaign with the *Swift* observatory found that the X-ray luminosity of 1H0707–495 dropped which caused Fabian et al. (2012) to trigger a 100 ks target of opportunity (ToO) observation with *XMM-Newton*. Analysis of the obtained spectrum showed that the flux has decreased by a factor of  $\sim 10$ . With the same model of relativistically blurred reflections Fabian et al. (2012) find an even steeper emissivity profile from which they inferred that the primary source must be located within only one gravitational radius of the source.

The X-ray variability was interpreted by Chainakun & Young (2012) as a lamp-post source changing its height above the black hole. They concluded that the observed reverberation effects and variability in the 1–4 keV band cannot be explained by the moving but non-variable primary source. A source which varies on shorter timescales at lower heights would be necessary and the innermost region of the disk must not be highly ionized. Still, some aspects of the time lags are not covered by this model.

An analysis of an even deeper *XMM-Newton* observation with 500 ks, accompanied by a 120 ks long observation with *Chandra*, was performed by Dauser et al. (2012) who used the `relconv` model (see Section 3.5.2) to test for relativistically blurred ionized reflection from the accretion disk. Comparison to previous observations showed that the parameters of the system concerning the black hole and reflection was unchanged, but a slight variation in the spectral shape was found and explained by a highly ionized outflow in the system which increased its velocity from  $0.11 c$  to  $0.18 c$  over roughly two and a half years. According to Dauser et al. (2012), the observed spectrum can also be modelled with an absorption scenario, but the obtained parameters are unphysical, ruling out this option.

Wilkins et al. (2014) used a relativistic reflection model to fit the emissivity profile with a twice-broken powerlaw model. In combination with the previous reverberation measurements, and under the assumption of a classical corona on the surface of the accretion disk, they could infer that this corona must expand with  $\sim 0.25 c$  to  $\sim 0.30 c$  when the luminosity of the source increases.

Taking a different approach, Mizumoto et al. (2014) used two partial absorbers with the same covering fraction but different ionization stages to explain the features attributed to the Fe  $L\alpha$  and  $K\alpha$  lines before, including the variation observed in the spectra obtained over the previous years.

Kara et al. (2015a) performed an observation of 1H0707–495 using *NuSTAR* which covered a higher energy band up to  $\sim 30$  keV. The source was found to show very low flux but the edge at  $\sim 7$  keV was again detected. Kara et al. (2015a) found that the energy of the edge positively correlates with the X-ray brightness which could be explained by a change in the height of the primary source in the lamp-post model.

By correlating X-ray and UV lightcurves, Robertson et al. (2015) found no significant correlation between

both, suggesting that the lamp-post model could deliver a more accurate description of the source geometry.

Pan et al. (2016) reported on a possible quasi-periodic oscillation (QPO) in the X-rays observed from 1H 0707–495. They state a period of 3800 s was found in the energy range from 0.2 to 10 keV with very high confidence.

Not using a model of relativistic reflections, Hagino et al. (2016) were able to fit all spectra available with a model describing the outflow of wind from the central area of the system. In this picture the sharp drop at  $\sim 7$  keV is produced by material having different velocities and directions along the line of sight.

Pawar et al. (2016) ruled out that the soft excess and sharp drop in the spectrum are caused by the superposition of different time-dependent spectral shape, adding further evidence that both features are indeed caused by relativistic effects. Additionally, Pawar et al. (2017) determined that no significant positive correlation between the variability of the UV and X-ray fluxes exists. This indicates that the UV photons do not serve as seed photons for the Comptonization process. Instead, a correlation between the continuum emission and the soft excess was found, adding further evidence that this excess is caused by radiation reprocessing in the inner area of the disk and the corona changes in size and or height.

Adding to the finding by Pan et al. (2016), Zhang et al. (2018) discovered an additional QPO with roughly half the frequency which lines 1H 0707–495 up in a variety of other black holes, from stellar mass to SMBHs, showing the same ratio between QPOs and their masses.

In an analysis of flux resolved *XMM-Newton* spectra, Kosec et al. (2018) found absorption features of an ultrafast outflow (UFO) at  $\sim 0.13$  c, consisting of ionized material with  $\log \xi = 4.3$ . Additionally, they found blueshifted photoionized emission of ionized material with  $\log \xi = 2.4$ , moving with  $\sim 8000$  km s $^{-1}$  towards the observer.

Caballero-García et al. (2018) used their reverberation model to calculate time-dependent spectra generated by reflection from a burst of powerlaw shaped radiation from a central source in the lamp-post geometry. By fitting this model to observations of, among other sources, 1H 0707–495, it was found that the primary source must be located at  $\sim 4r_g$ , although the remaining residuals could indicate that the lamp-post geometry is insufficient to fully explain the observed behavior.

Deviating from the reflection model, Mizumoto et al. (2019) show that all observed effects in spectra and lightcurves, including reverberation observed from the Fe K $\alpha$  line, can alternatively be caused by scattering in highly ionized wind which has velocities of  $\sim 0.2$  c and moves outward in a spiral shape.

After developing a physical model for a spherical corona which encloses the central black hole to explain the described time lags, Chainakun et al. (2019) applied it to observations of, among other AGN, 1H 0707–495. In this model the seed photons for the Comptonization process are supplied in form of UV radiation from the accretion disk, an initial assumption contrary to the findings of Robertson et al. (2015) and Pawar et al. (2017). The time lag arises from the photons being subject to multiple scatterings in the corona. Their model can explain the observed reverberation profiles and for 1H 0707–495 gives an extent of the corona of  $\sim 10r_g$ .

A model which takes the extent and rotation of the primary source in the lamp-post model into account was developed by Szanecki et al. (2020) and applied to *XMM-Newton* observations of 1H 0707–495. They found that this source must be very compact with a size of maximal one gravitational radius and close to the black hole. The authors explicitly state that an extended corona cannot explain the observed spectra. Additional wind in the system can influence the reflection parameters drastically.

The main components of the two competing models most often used in these past works are partial covering and relativistic reflection. In the following sections, which focus in the observation and the analysis of the obtained data, I show that combining both approaches yields the possibility to not only describe the spectral shape but also explain source intrinsic variability of 1H 0707–495.

## 7.2 Observational Details

### 7.2.1 Time Coverage and Operating Modes

During the extended commissioning phase of *eROSITA* on October 11th, 2019, the *SRG* spacecraft oriented its instruments towards the position of 1H 0707–495. As outlined in Section 5.3, this phase was extended to investigate the susceptibility of the CE to SEUs. As part of this investigation not all CCDs of the seven

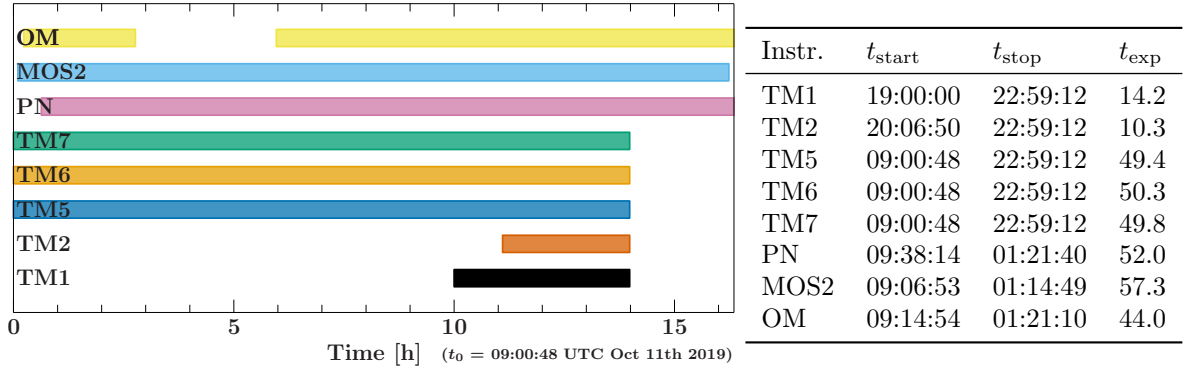


Figure 7.1: Time coverage of the instruments in use onboard *eROSITA* and *XMM-Newton* during the observation of 1H0707–495. All times are given in UTC, except for the exposure time,  $t_{\text{exp}}$ , which are ks. The observation started on October 11th, ended for *eROSITA* on the same day and for *XMM-Newton* one day later. Note that from 11:46:42 to 14:58:42 the OM was not operating, causing a gap in the top bar. EPIC-pn started the observation slightly delayed and TMs 1 and 2 were switched on very late into to observation.

TMs were taking science data. TMs 5, 6 and 7 were already active when the observation began at 09:00:48 UTC. The time coverage of all instruments in use is shown in Fig. 7.1. As can be seen, additionally TMs 1 and 2 were activated after roughly three quarters of the allocated observation time. TMs 3 and 4 did not operate during the entire observation. All FWs of the TMs in use were set to the FILTER position. *eROSITA*'s CCDs do not offer different operating modes, the frame times were nominal at 50 ms and the entire frames were read out. The observation ID (ObsID) of this *eROSITA* observation is 300003.

*XMM-Newton* initiated the observation with ObsID 0853000101 almost at the same time as *eROSITA*, only  $\sim 6$  min later. MOS2 immediately started taking science data followed by a slight delay of  $\sim 8$  min for the OM. EPIC-PN started operating  $\sim 37$  min after *eROSITA*. The first instrument of *XMM-Newton* stopping taking data was MOS2 2.25 h after *eROSITA* concluded its observation, followed by EPIC-pn and the OM  $\sim 6$  min later. Examining Fig. 7.1, one finds that the OM did not operate for 3 h and 12 min. MOS1 was in the CALCLOSED setup because in a previous observation a SEU occurred, thus did not take any science data. Both RGSs were also taking data during the entire observation but, as will be explained in the next sections, the low brightness of the source did not yield any usable signal after the dispersion through the gratings. EPIC-pn and MOS2 were operating in large window mode (see Sections 6.2 and 6.3 respectively) with the MEDIUM filters selected in the FW. The OM did take 11 exposures in total with the UVW1 filter, which has a bandpass in the UV range from 245 to 320 nm (Mason et al., 2001).

## 7.2.2 Data Extraction

For the extraction of the products needed for the analysis, such as lightcurves and spectra, for each of the instruments the regions from which the source and background events were taken have to be defined and certain criteria to filter the data for bad events must be applied. These are, in combination with the software in use, described in the next two sections.

### *eROSITA*

The raw data taken by *eROSITA* has been automatically prepared by the pipeline processing of the eSASS running at MPE. Version C945 of this data was retrieved to extract the science products. `srctool` version 1.49, which is part of the eSASS, was used to extract light curves and spectra for source and background, including the accompanying auxiliary files, the effective area and response matrix. All events have a 32 bit long mask assigned in which the individual fields correspond to certain conditions the event is subject to. For this analysis the flag `0xc00f7f30` (in hexadecimal representation) was used to filter events which were considered bad. This includes all events which were identified as a or next to a dead, bright or

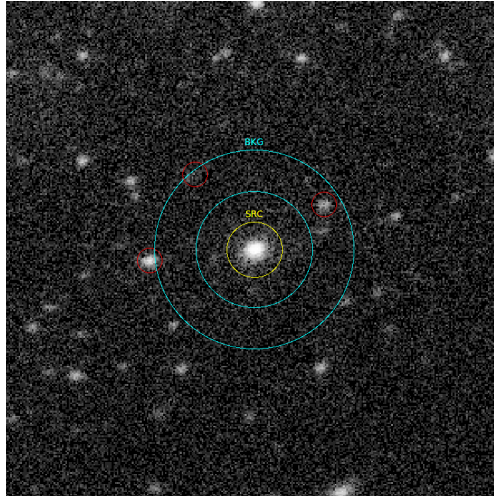


Figure 7.2: Image of 1H0707–495 and its surroundings from all available TMs with the filtering criteria described in Section 7.2.2 applied. The source (cyan) and background (yellow) extraction regions are labeled and centered around the source of interest. Red circles around contaminating background sources are excluded from the background region.

flickering pixel, originating from a corrupt frame (see Section 5.6.6) or associated with the impact of a MIP. Additionally, only events with valid patterns up to quadruples (see Section 4.1.3) were accepted. For the temporal analysis events with energies down to 0.2 keV were considered while for the spectral analysis all events below 0.5 keV were rejected. This was done because most of the available data was taken by TMs 5 and 7 which are subject to the optical light leak described in Section 5.6.4. At the time of performing this analysis the exact influence of this effect on the spectra was not clear, but it was known that it has mostly effect on energies below 0.5 keV. Extraction of source events was done from a circular region with 60'' radius around the source of interest and background events were taken from an annular region around it with an inner radius of 140'' and an outer radius of 240''. Contaminating sources in the background region have been explicitly excluded. An image of the source and the extraction region can be seen in Fig. 7.2. The lightcurves and spectra created by `srctool` are normalized to the values which would be obtained if all seven telescopes were operational. This makes it possible to create continues light curves, although the time coverage is not the same for all TMs.

### ***XMM-Newton***

Extraction of the data obtained by *XMM-Newton* was performed by the colleagues at MPE using XMM Science Analysis Software (XMM SAS) version 18.0.0. The source region on EPIC-pn was chosen as a circular region 35'' in radius around the source and the background region as another circle with a 106'' radius next to the source on the same CCD in an area with no other point sources and without any defect columns. The same was done for MOS2, but the regions were 17'' and 55'' in radius respectively. For the OM the `omichain` and `omfchain` tasks were used to extract a light curve of the point source.

## **7.3 Timing Analysis**

For all instruments lightcurves with 400 s bins in the energy range from 0.2 to 7.0 keV were created. Additionally, in the energy bands from 0.2 to 0.8 keV, considered the soft band, and from 0.8 to 7.0 keV, considered the hard band, lightcurves with 600 s bins were extracted. From these bands the time-dependent

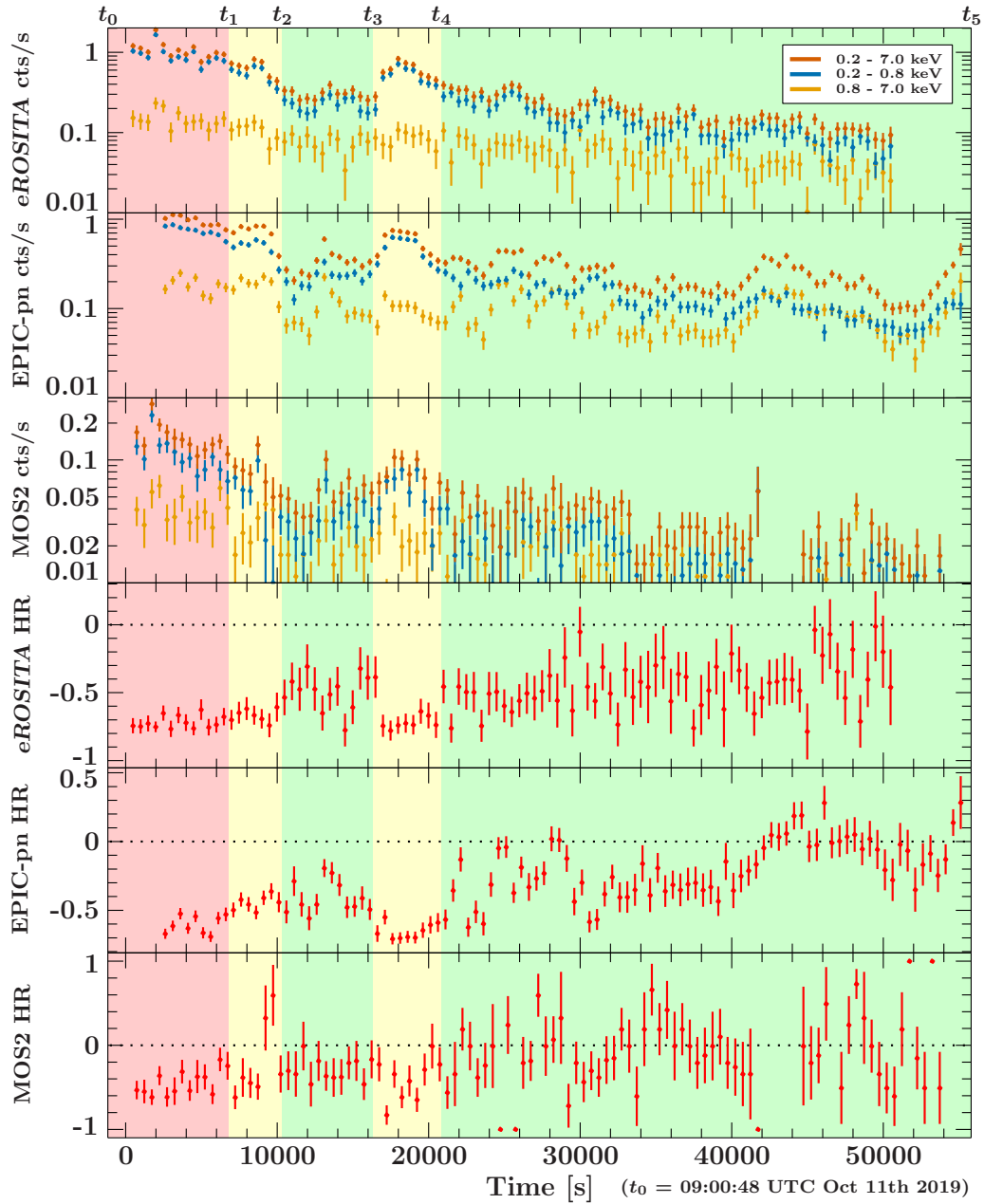


Figure 7.3: Top three panels: Light curves in the soft (0.2-0.8 keV), hard (0.8-7.0 keV) and full (0.2-7.0 keV) band as taken by *eROSITA*, EPIC-pn and MOS2 in that order. The bins are 400 s wide for the lightcurves in the full energy band and 600 s wide in the hard and soft bands. Over the entire observation the source dims by a factor of more than 50 and strong fluctuations can be observed in the soft band. Bottom three panels: HRs calculated from each of the lightcurves above as given in equation 7.1, in the same order. Note that for all instruments the HR appears to anti-correlate with the soft lightcurves, which is to be expected due to the less variable hard band. The colored areas indicate the intervals in which the source is considered to be in the soft (red), medium (yellow) and hard (green) state (see Section 7.5).

hardness ratio (HR) was calculated, defined as

$$\text{HR} = \frac{H - S}{H + S} \quad (7.1)$$

with  $H$  and  $S$  being the count-rate of the hard and soft band. It is unit-less, normalized to the range from -1 to 1 and gives a measure for the spectral hardness of the emission. -1 means the spectrum is dominated by soft emission and 1 dominated by hard emission (as constraint by the chosen energy bands).

At the beginning of the observation *eROSITA* measured a count-rate of  $\sim 1$  cts/s from the source in the full energy band apart from one bin  $\sim 4$  ks into the observation. Over the following  $\sim 10$  ks the count-rate declined until it stabilized around  $\sim 0.2$  cts/s for about 6 ks. At this point it rose again, peaked at  $\sim 0.6$  cts/s 2 ks later and from this point on continuously declined for the remaining observation. The minimal measured count-rate was  $0.063 \pm 0.017$  cts/s. The lightcurve of the soft band essentially followed the same pattern but is  $\sim 10\%$  to  $\sim 30\%$  lower than the lightcurve of the full band. Interestingly, the lightcurve of the hard band does not show this high amplitude variability which can explain that the lightcurve of the full band behaves the same way as the soft band.

A method quantifying the variability is the normalized excess variance (NEV). It can be used to estimate how much the variability exceeds the value expected from the intrinsic Poisson noise in the stochastic process (Nandra et al., 1997a; Boller et al., 2016; Buchner et al., 2021). Following Boller et al. (2016), the NEV of a lightcurve with a count-rate,  $r_i$ , and the corresponding error,  $\sigma_i$ , in the  $i$ th bin can be calculated as

$$\text{NEV}^2 = \frac{1}{N\bar{r}^2} \sum_i^N \left( (r_i - \bar{r})^2 - \sigma_i^2 \right) \quad (7.2)$$

where  $\bar{r}$  denotes the mean of all bins and  $N$  is the total number of bins. Using Monte Carlo simulations Vaughan et al. (2003) found that the error,  $\Delta\text{NEV}$ , on NEV can be approximated as

$$(\Delta\text{NEV})^2 = \sqrt{\left( \sqrt{\frac{2}{N}} \cdot \frac{\overline{\sigma_i^2}}{\bar{r}^2} \right)^2 + \left( \sqrt{\frac{\overline{\sigma_i^2}}{N}} \cdot \frac{2\text{NEV}}{\bar{r}^2} \right)^2} \quad (7.3)$$

where  $\overline{\sigma_i^2} = \left( \sum_i^N \sigma_i^2 \right) / N$  denotes the mean square error of the errors on all bins. The NEV can be expressed in units of the confidence interval,  $\sigma$ , by giving the ratio of NEV and its error,

$$\frac{\text{NEV}}{\Delta\text{NEV}} \quad (7.4)$$

From the *eROSITA* lightcurve the NEV was determined to  $34.8\sigma$  in the full band and  $44.6\sigma$  in the soft band while in the hard band it was only  $2.1\sigma$ , showing that the variability on the total count-rate was mostly caused by soft radiation. The reason exactly these energy ranges were chosen for the bands is evident in Fig. 7.4 where energy resolved values for NEV are shown. Because the overall count-rate given by MOS2 was substantially smaller than that of *eROSITA* and EPIC-pn (see Fig. 7.3) the energy bins for this detector are much larger and the bin size of the lightcurve was increased to 600 s for this calculation. For all detectors the photon flux is concentrated below  $\sim 1$  keV, therefore the bins are smaller at these energies. The effective area of *eROSITA* is significantly smaller at high energies than that of *XMM-Newton* (see Fig. 5.6), thus the photon flux was not sufficient to calculate values for NEV above 2 keV for this instrument. A sharp drop in the NEV spectrum can be observed at  $\sim 0.8$  keV, thus the variability in the count-rate is mainly present below this energy, corresponding to the given values for NEV of the entire soft and full band, while at higher energies it is much smaller. From the NEV given by EPIC-pn and MOS2 it is indicated that the variability is slightly increased around 3 keV. The UV lightcurve of the OM only gave a NEV of  $1.7\sigma$  and is therefore much less variable than the X-ray lightcurves.

This situation also manifests itself in the time-resolved hardness ratio shown in Fig. 7.3. Because the hard band is much more stable the hardness ratio shows an anti-correlation to the total count-rate in all detectors. During intervals of high count-rate the measured radiation is softer compared to intervals of low

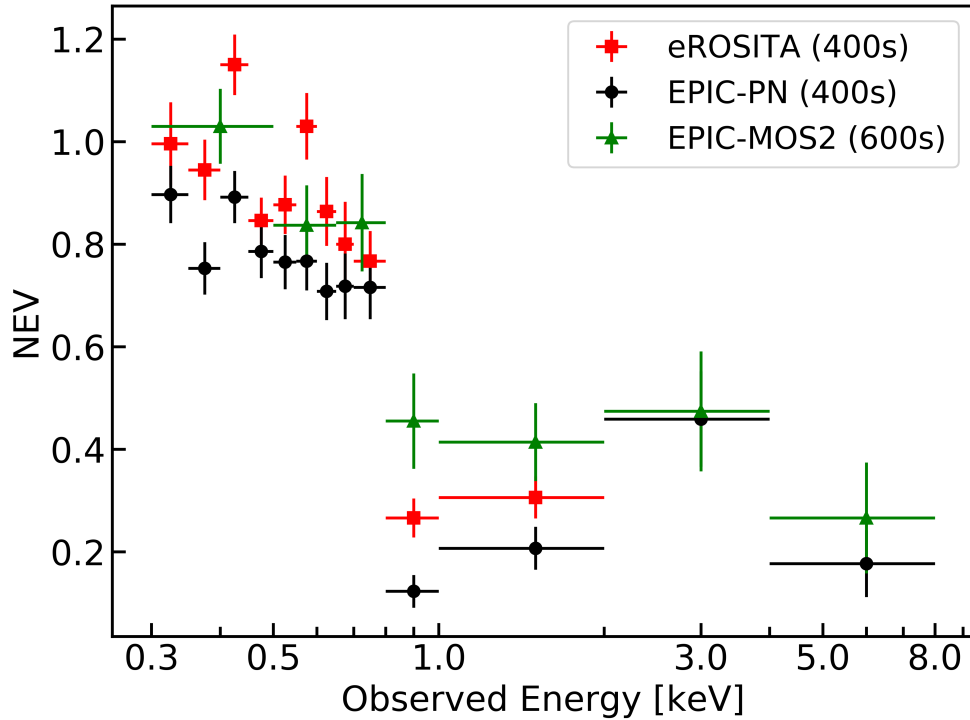


Figure 7.4: Energy resolved values for the NEV as determined from the data of all three instruments. For MOS2 the energy and time bins were chosen larger due to the weaker signal. Because of the higher flux in the regime below  $\sim 1$  keV the bins are smaller. For *eROSITA* the NEV could not be calculated above 2 keV due to the low statistics given by the lower effective area compared to *XMM-Newton* above 2 keV (see Fig. 5.6). Note that the NEV has a sharp drop at  $\sim 0.8$  keV, therefore the border between the soft and hard band was set at this energy. Taken from Boller et al. (2021).

count-rate. However, because the signal is very low during periods of increased hardness also the errors are larger which is especially evident in the second half of the observation.

All these findings are confirmed by the data from *XMM-Newton* apart from the fact that EPIC-pn shows a slightly increased level in the hard band at the beginning of the observation and another period of elevated count-rate in the soft band four quarters into the observation. Intriguingly, EPIC-pn, which was the instrument observing 1H0707–495 for the longest period of time, witnessed a significant increase in flux right at the very end of the observation during which also the hard band increased in intensity.

## 7.4 Spectral Analysis

The X-ray spectra obtained by *eROSITA*, EPIC-pn and MOS2 are shown in Fig. 7.5. They reveal the familiar shape of a strong soft component and an almost flat part at intermediate energies which is interrupted by the sharp drop at  $\sim 7$  keV, first found by Boller et al. (2002). As described in Section 7.1, 1H0707–495 has been observed several times in the last two decades and multiple different models have been proposed and employed to explain this characteristic shape. These include ionized reflection from the accretion disk under the influence of the relativistic environment (see for example Boller et al., 2002; Fabian et al., 2002a, 2004; Blustin & Fabian, 2009; Fabian et al., 2009; Zoghbi et al., 2010; Wilkins & Fabian, 2011; Zoghbi et al., 2011; Chainakun & Young, 2012; Dauser et al., 2012; Fabian et al., 2012; Wilkins et al., 2014; Kara et al., 2015a; Caballero-García et al., 2018; Chainakun et al., 2019; Szanecki et al., 2020) partial absorption (see for example Boller et al., 2002; Gallo et al., 2004; Tanaka et al., 2004; Miller et al., 2010; Mizumoto et al., 2014), a windy absorber (see for example Dauser et al., 2012; Hagino et al., 2016; Mizumoto et al., 2019)

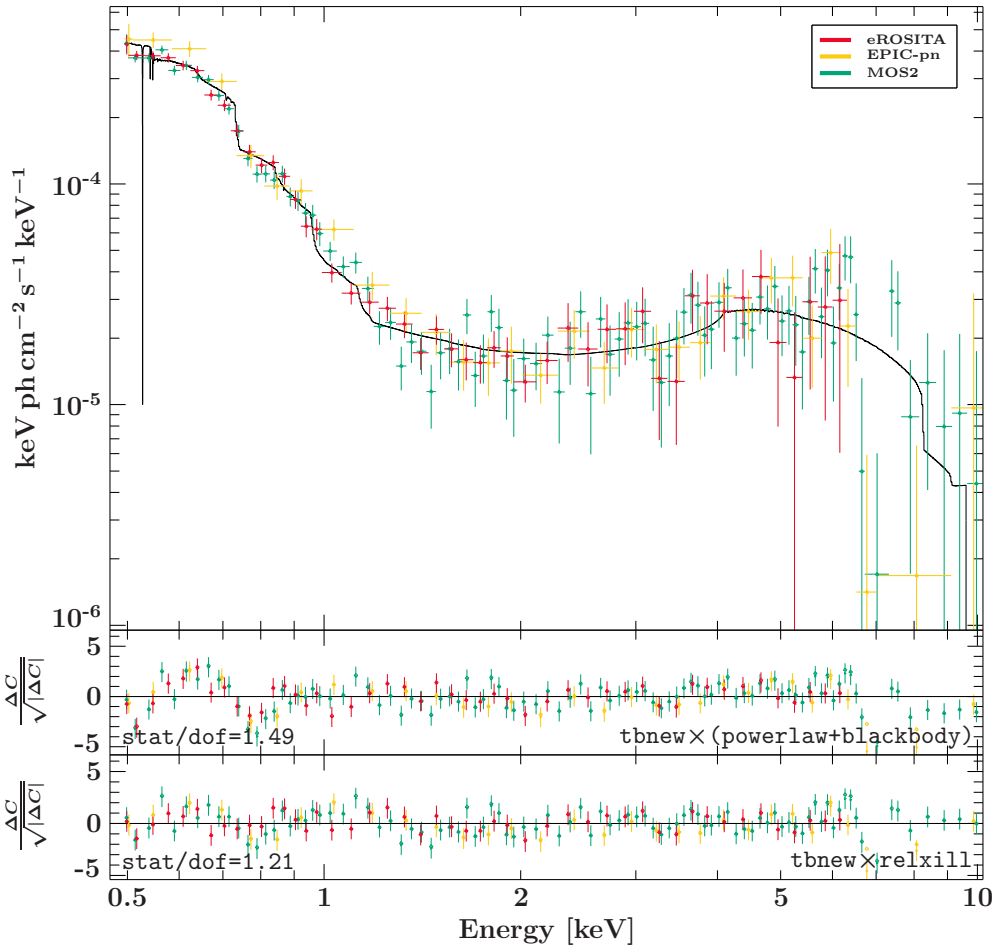


Figure 7.5: Upper panel: Spectra obtained by *eROSITA*, EPIC-pn and MOS2 over the entire observation. All spectra have been rebinned for visual purposes only and the spectra of *eROSITA* and MOS2 were scaled according to the detector constants  $C_{\text{eROSITA}}$  and  $C_{\text{MOS2}}$ . Middle panel: Residuals of the fit of an empirical model consisting of a `blackbody` to describe the soft excess and a `powerlaw`. Lower panel: Residuals of the relativistic reflection model using `relxill`.

or a combination of them. Our goal is to develop a model for the observed spectra by incorporating these previous results and explain the spectral variability.

Galactic foreground absorption is accounted for in all following models using the `tbnew` model (see Section 3.3.4) in its simple form where the elemental abundances are fixed at the default values (Wilms et al., 2000). `HEASoft`'s `nH tool`<sup>1</sup>, which employs the HI4PI survey (HI4PI Collaboration et al., 2016) of the galactic column density, provided the value of  $N_{\text{H}} = 4.02 \times 10^{22} \text{ cm}^{-2}$  at the position of 1H 0707–495 which is fixed during spectral fitting.

The cosmological redshift of the source was taken as  $z = 0.04057$  (Jones et al., 2009). Possible differences in the calibration of the instruments are considered by including detector-depending multiplicative constants  $C_{\text{eROSITA}}$  and  $C_{\text{MOS2}}$  in each fit which scale with respect to the data obtained by EPIC-pn.

Fitting of the spectra was performed using the Interactive Spectral Interpretation System (ISIS) in combination with `HEASoft` version 6.27.2. The low SNR of the spectra caused the low observed flux was insufficient for  $\chi^2$  statistics, so Cash (1979) statistics (C-stat) was used to judge the quality of the fits by dividing by the number of degrees of freedom (dof). All spectra were binned optimally during fitting as described by Kaastra & Bleeker (2016).

<sup>1</sup><https://heasarc.gsfc.nasa.gov/cgi-bin/Tools/w3nh/w3nh.pl>

Table 7.1: Best-fit parameters for the empirical consisting of a soft blackbody and a hard powerlaw component. Galactic foreground absorption was taken into account by the `tbnew` model with a fixed  $N_{\text{H}} = 4.02 \times 10^{20} \text{ cm}^{-2}$ . Note that the powerlaw component has a very flat slope with  $\Gamma = 0.80^{+0.06}_{-0.12}$ . Uncertainties are given in terms of the 90% confidence interval. The residuals of the model are shown the middle panel of Fig. 7.5.

Parameter	Value & confidence
$kT$ [keV]	$0.1062^{+0.0020}_{-0.0016}$
<code>norm<sub>blackbody</sub></code>	$(8.4 \pm 0.4) \times 10^{-6}$
$\Gamma$	$0.80^{+0.06}_{-0.12}$
<code>norm<sub>powerlaw</sub></code>	$(1.57^{+0.12}_{-0.19}) \times 10^{-5}$
$C_{\text{eROSITA}}$	$0.977^{+0.032}_{-0.029}$
$C_{\text{MOS2}}$	$1.13^{+0.07}_{-0.06}$
C-statistic/dof	391.5/262

### 7.4.1 A Simple Empirical Model

In a variety of previous studies the soft component of the observed spectrum was phenomenologically explained by a blackbody component accounting for the thermal emission of the accretion disk (see Section 3.3.1) (Gallo et al., 2004; Tanaka et al., 2004; Blustin & Fabian, 2009; Fabian et al., 2009; Zoghbi et al., 2010, 2011; Dauser et al., 2012; Fabian et al., 2012; Mizumoto et al., 2014; Wilkins et al., 2014; Kara et al., 2015a; Pawar et al., 2017) although it has been shown that this soft excess is more likely arising from the relativistically blurred Fe L emission line (Fabian et al., 2009; Zoghbi et al., 2010; Kara et al., 2015a; Pawar et al., 2017). Following this approach, we first applied a simple empirical model with a `blackbody` for the soft excess and a `powerlaw` for the hard tail in the spectrum to the data. The residuals of this fit are shown in the middle panel of Fig. 7.5, while the best-fit parameters are listed in Tab. 7.1. With C-stat/dof of 1.49 this model fits the data reasonable well, however, strong residuals remain in the soft energy regime and above  $\sim 7$  keV. We interpret these as this empirical model inaccurately describing the relativistically broadened Fe L $\alpha$  and Fe K $\alpha$  lines. The slope of the powerlaw is with  $\Gamma = 0.80^{+0.06}_{-0.12}$  very flat, even more than reported by Boller et al. (2002) who found  $\Gamma = 1.07 \pm 0.09$  and also all other studies listed in Section 7.1. Gallo et al. (2004) reported the inner temperature of a fitted multi-temperature disk-blackbody to be 103 eV for the *XMM-Newton* observation from the year 2000 (see Fig. 7.6) which is consistent with our result.

### 7.4.2 Comparison to Previous *XMM-Newton* Observations

To further compare the recent observation of 1H 0707–495 by *eROSITA* and *XMM-Newton* to the past, all available spectra taken by *XMM-Newton* over the last two decades (6 in total) are shown in Fig. 7.6. The data were taken from the *XMM-Newton* Science Archive<sup>2</sup> and extracted by following the same procedure as outlined in Section 7.2.2. For each observation the spectra of all available instruments were combined to aid visualization. Additionally, to determine the absolute flux for each observation, the same phenomenological `blackbody + powerlaw` model described in Section 7.3 was fitted and the flux in the soft, hard and full band, as defined above, was calculated. The resulting values are listed in Tab. 7.2 and shown, depending on the observation date, in Fig. 7.7. The spectrum closest to the one of the recent observation is from 2011 (Fabian et al., 2012) and shows a slightly more pronounced soft excess. While the 2019 observation was with a flux of  $(0.56 \pm 0.035) \times 10^{-12} \text{ erg s}^{-1} \text{ cm}^{-2}$  as determined by *eROSITA* and  $(0.63 \pm 0.022) \times 10^{-12} \text{ erg s}^{-1} \text{ cm}^{-2}$  by EPIC-pn in a historically low state, the flux from 2011 is with  $(0.072 \pm 0.007) \times 10^{-12} \text{ erg s}^{-1} \text{ cm}^{-2}$  only slightly higher. The highest flux was measured during the observation from 2010 with  $(8.99 \pm 0.009) \times 10^{-12} \text{ erg s}^{-1} \text{ cm}^{-2}$ , but the flux from 2008 is with  $(8.24 \pm 0.007) \times 10^{-12} \text{ erg s}^{-1} \text{ cm}^{-2}$  only slightly lower followed by the measurement from 2002 with  $(8.12 \pm 0.028) \times 10^{-12} \text{ erg s}^{-1} \text{ cm}^{-2}$ . This similarity in flux can also be seen in the spectra in Fig. 7.6. The first spectrum ever taken by *XMM-Newton* in the year 2000 lies

<sup>2</sup><https://www.cosmos.esa.int/web/xmm-newton/xsa>

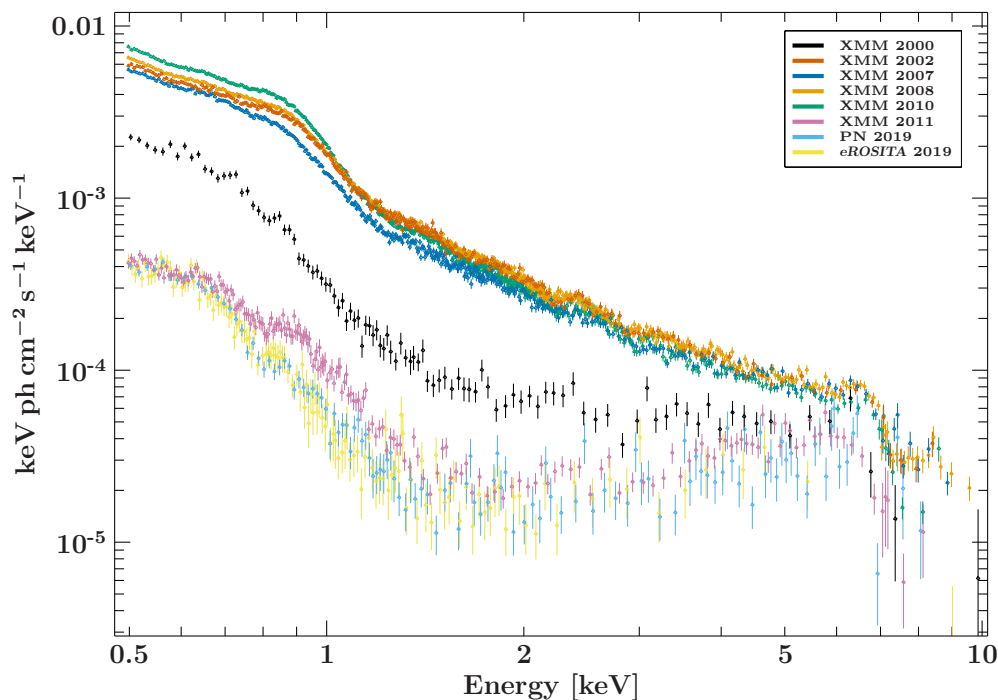


Figure 7.6: Comparison of all available spectra of 1H0707–495 taken by *XMM-Newton* over the last two decades including the 2019 observation by *eROSITA*. For *XMM-Newton* spectra of all available instruments of the respective observations were combined.

Table 7.2: Fluxes in units of  $10^{-12} \text{ erg s}^{-1} \text{ cm}^{-2}$  in the soft band from 0.2 to 0.8 keV, the hard band from 0.8 to 7.0 keV and the full band, which is the combination of both, as determined from previous *XMM-Newton* observations and the 2019 observation by *eROSITA* and EPIC-pn. The values for the fluxes have been derived by fitting an empirical `blackbody + powerlaw` model including galactic foreground absorption.

Year	$F_{\text{soft}}$	$F_{\text{hard}}$	$F_{\text{full}}$
XMM 2000	$2.10 \pm 0.017$	$0.78 \pm 0.017$	$2.87 \pm 0.024$
XMM 2002	$5.21 \pm 0.020$	$2.94 \pm 0.011$	$8.12 \pm 0.028$
XMM 2007	$3.95 \pm 0.006$	$2.01 \pm 0.007$	$5.97 \pm 0.009$
XMM 2008	$5.28 \pm 0.005$	$2.95 \pm 0.005$	$8.24 \pm 0.007$
XMM 2010	$6.10 \pm 0.006$	$2.89 \pm 0.006$	$8.99 \pm 0.009$
XMM 2011	$0.35 \pm 0.003$	$0.37 \pm 0.007$	$0.72 \pm 0.007$
PN 2019	$0.37 \pm 0.013$	$0.26 \pm 0.010$	$0.63 \pm 0.022$
<i>eROSITA</i> 2019	$0.33 \pm 0.004$	$0.23 \pm 0.035$	$0.56 \pm 0.035$

with  $(2.87 \pm 0.024) \times 10^{-12} \text{ erg s}^{-1} \text{ cm}^{-2}$  in between both of these groups. Note that the determination of the source flux strongly depends on the assumed model, the binning of the data, the quality of the resulting fit and the energy bands in which the flux is calculated. Because of this inconsistencies with the literature can arise.

### 7.4.3 Relativistic Modelling

As described in the previous section, the spectrum taken in 2011 is very similar to the one obtained in 2019 by *eROSITA* and *XMM-Newton*. Fabian et al. (2012) interpreted the data as a result of reflections off the accretion disk concentrated very close to the central black hole. This model can describe the data

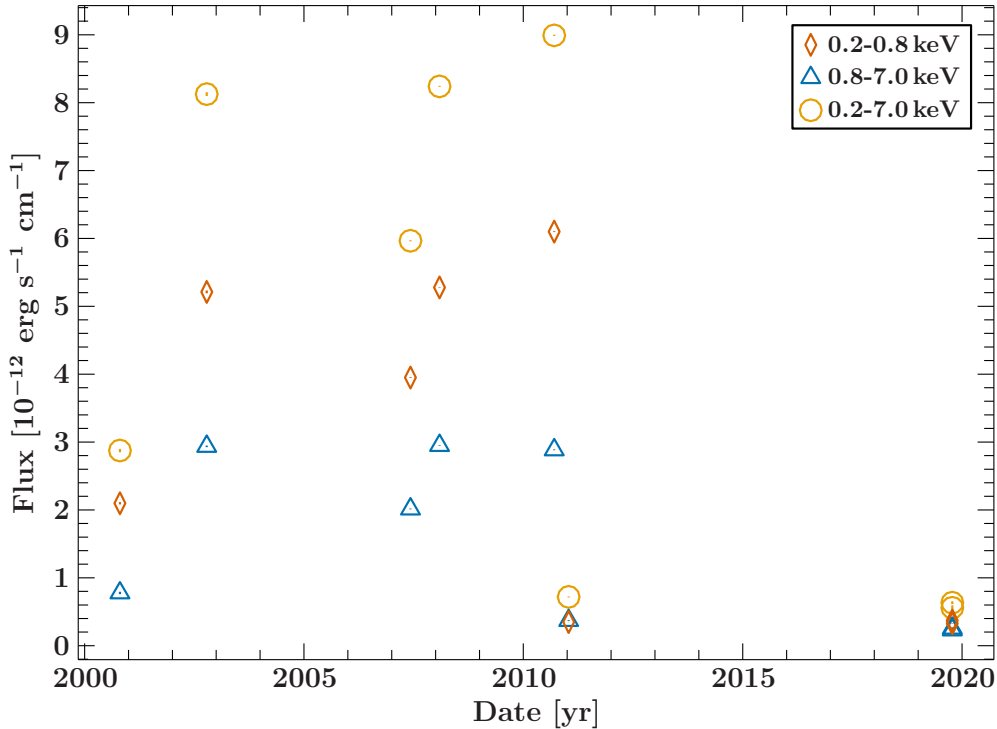


Figure 7.7: Measured fluxes of all available observations from *XMM-Newton* and the 2019 CalPV observation by *eROSITA* versus the date of the observation. Error bars are also shown but very small. The fluxes were determined for the soft, hard and full energy bands by fitting an empirical model consisting of a blackbody in the low energy regime and a powerlaw to the spectra while considering the foreground absorption with a fixed  $N_{\text{H}}$  of  $4.02 \times 10^{20} \text{ cm}^{-2}$ . It is clearly evident that *eROSITA* and *XMM-Newton* caught 1H 0707–495 at a historically low flux even though the 2011 observation with 80 ks (Fabian et al., 2012) almost reaches down to the same low flux. See Tab. 7.2 for a tabularized form of the data.

obtained over the last two decades, also in the higher flux states (Fabian et al., 2009; Zoghbi et al., 2010; Dauser et al., 2012). Motivated by this approach, and the result presented by Fabian et al. (2009), we aim to also describe the new data under this scenario. To this end, we use the `relxill` model in its lamp-post flavor, `relxilllp` (see Section 3.5.2), with galactic foreground absorption provided by `tbnew`, as outlined in Section 7.4. The exponential rolloff of the powerlaw was fixed at the default energy of  $E_{\text{cut}} = 300 \text{ keV}$ .

Fitting this model to the spectra yields the result shown in Fig. 7.5 with the residuals shown in the lower panel of this figure and the best-fit parameters listed in Tab. 7.3. The ratio between the C-stat and the dof is  $353.3/291 = 1.21$ , which indicates that the model gives an accurate description of the observed data. Adding another blackbody component with  $kT \sim 0.1 \text{ keV}$  in the soft part of the spectrum does not improve the statistics of the fit. We interpret this as the relativistic reflection model fully explaining the soft excess with Fe L line emission. The fit yields an iron abundance,  $A_{\text{Fe}}$ , of  $10^{+0.0}_{-1.5}$ , which is identical to the upper limit provided by the model. This overabundance agrees with previous studies (Fabian et al., 2004, 2009, 2012; Kara et al., 2015a). For the underlying powerlaw of the incident radiation a photon index of  $\Gamma = 2.64^{+0.04}_{-0.08}$  was obtained which is much steeper than the one given by the empirical model in Section 7.4.1 and also agrees with mentioned previous works. The spin of the black hole was found to be  $a = 0.9960^{+0.0013}_{-0.0030}$ , which is very close to the maximal possible value of  $a = 0.998$ . Note, however, that this value and its stated statistical error have been derived using a spectral model which in turn is based on particular assumptions like the lamp-post structure. The real difference between the value for  $a$  derived from the fit and the real spin of the black hole is most likely much larger. For the height of the lamp-post source above the black hole  $h = 1.385^{+0.023}_{-0.142} r_g$  was found which is closer than what Dauser et al. (2012) found and consistent with the result obtained by Kara et al. (2015a) while Fabian et al. (2012) finds it to be even closer but not in the

Table 7.3: Best-fit parameters for the relativistic reflection model using `relxill` including 90% confidence limits. The model itself and the residuals are shown in Fig. 7.5. `relxill` defines the spin parameter as  $cJ/GM^2$  where  $M$  is the mass of the black hole and  $J$  the angular momentum and the value obtained here is close to the theoretical maximum if 0.998. Dauser et al. (2016b) gives a detailed explanation of the normalization in this model. The iron abundance defined as  $A_{\text{Fe}}$  in solar values (Grevesse et al., 1996) reached the upper limit of the model. Note that especially the value of the spin has a very low statistical error but it is only well constraint within the limitations imposed by the underlying model.

Parameter	Value & Confidence
spin	$0.9960^{+0.0013}_{-0.0030}$
$\theta$ [°]	$73.1^{+1.8}_{-1.6}$
$\Gamma$	$2.64^{+0.04}_{-0.08}$
$h$ [ $r_g$ ]	$1.385^{+0.023}_{-0.142}$
$\text{norm}_{\text{relxillp}}$	$(3.9^{+26.0}_{-2.4}) \times 10^{-4}$
$f_{\text{refl}}$	$46^{+13}_{-10}$
$A_{\text{Fe}}$	$10.0^{+0.0}_{-1.5}$
$\log \xi$	$0.73^{+0.12}_{-0.15}$
$C_{\text{MOS2}}$	$1.14 \pm 0.07$
$C_{\text{eROSITA}}$	$0.985^{+0.031}_{-0.030}$
$C$ -statistic/dof	353.3/291

lamp-post scenario. Szanecki et al. (2020) confirmed, using their newly developed `monaco` code for extended sources in the lamp-post geometry, that the primary source is very compact and close to the black hole. The inclination of the accretion disk was determined to  $\theta = 73.1^{+1.8}_{-1.5}$ °. In the past a wide range of possible values for this parameter was found for 1H 0707–495, the most extreme being 23° by Fabian et al. (2002a) and 78° by Dauser et al. (2012). The result of this analysis is at the upper end of this range. As outlined by Dauser (2014), a degeneracy between the inclination and the lamp-post height exists which might be a possible explanation for this large spread. Compared to previous analyses by Fabian et al. (2002a), Fabian et al. (2004), Fabian et al. (2012), Hagino et al. (2016), and Kosec et al. (2018) the ionization parameter from our analysis is with  $\log \xi = 0.73^{+0.12}_{-0.15}$  comparatively low, only Kara et al. (2015a) obtained a lower value when also applying the `relxillp` model to data taken by *NuSTAR* in 2014. Only a small amount of radiation from the primary source can be observed directly, as is indicated by the high value for the reflection fraction of  $f_{\text{refl}} = 46^{+13}_{-10}$ . A much higher portion is focussed onto the accretion disk. Already Fabian et al. (2002a) but, especially Kara et al. (2015a), using the same model, found that this source is extremely dominated by reflection. As outlined by Dauser et al. (2014), the expected reflection fraction can be calculated for a point-like source at a certain height above a rotating black hole, which yields 12...20 which is substantially lower than the value obtained for  $f_{\text{refl}}$  from the spectral fit.

Investigating the residuals for the relativistic reflection model in Fig. 7.5, one can see that the sharp drop at  $\sim 7$  keV is not completely reproduced by `relxillp` and also at lower energies some deviations from the data can be observed. A possible explanation for this behavior might be absorption by a fast and ionized outflow (Done et al., 2007; Dauser et al., 2012) which could cause absorption features at soft energies and an over-prediction of the flux at  $\sim 7$  keV. Hagino et al. (2016) used a model of an absorbing ionized wind intercepting the line of sight at different angles to explain the shape of the edge, however, in their model residual effects of a possible reflection component remain. This alternative wind based explanation is also supported by the findings of Kosec et al. (2018) that an ionized outflow of material with velocities of  $\sim 0.13$  c and  $\log \xi = 4.3$  could play a role.

Table 7.4: Start and stop times in MJD of the time intervals in which the source is considered to be in the soft, medium and hard state respectively.  $t_0$  marks the beginning of the observation and  $t_5$  the end. See Fig. 7.3 for the lightcurve.

$t_0$	58767.361111
$t_1$	58767.453704
$t_2$	58767.494213
$t_3$	58767.563657
$t_4$	58767.615741
$t_5$	58768.020833

## 7.5 Time Selected Spectra: Partial Covering

As outlined in Section 7.3, 1H0707–495 showed strong fluctuations in its flux during the roughly 14 h long observation which are mostly concentrated in the soft energy band below 1 keV. To investigate the origin of these fluctuations we divide the data obtained during the observation into three flux resolved states and created a spectrum for each of them. At the start of the observation the count-rate measured by all three instruments was highest (see the lightcurve in Fig 7.3), therefore in this first 8 ks long section the source is considered to be in the high count-rate state. In it's continuing decline for the next 3.5 ks it is considered in the medium state and in the following minimum of the count-rate, which lasted for 6 ks, the source reached the defined low count-rate state. After that the flux shows an additional increase for 4.5 ks which brings it back to the medium state and for the remaining 35 ks of the observation the flux stays low, and the source is therefore considered to be in the low count-rate state. These defined intervals are shown as red, yellow and green background in Fig. 7.3 for the high, medium and low state respectively. The corresponding beginnings of all sections in MJD are listed in Tab. 7.4 and enumerated  $t_i$ , where  $t_0$  marks the beginning and  $t_5$  the end of the observation.

In Fig. 7.8 the spectra obtained by *eROSITA* and EPIC-pn for each state are shown. MOS2 was omitted to aid visual clarity but is included for all analytical steps. As was found from the analysis of the lightcurves in Fig. 7.3, the largest portion of variability is present in the soft energy band. This also manifests itself in the shape of the count-rate-selected spectra. While the hard parts of the spectra above 5 keV mostly coincide for the different states large deviations can be found in the soft part, especially below 1 keV. In this regime the flux of the spectra in the high state is almost ten times higher than in the low state with that of the medium state roughly in the middle.

As explained in Section 7.1, another widely used method to explain the observed spectral shape of 1H0707–495 is partial covering by an absorber located in the line of sight towards the emission region. Because this process mainly has an effect on soft X-rays (see Fig. 3.8) we add a partial absorption component to the model developed in the previous section. The additional component is provided by the `TBpcf` model (Wilms et al., 2000) which has, next to the equivalent hydrogen column density,  $N_{\text{H}}$ , of the absorbing material, the partial covering fraction,  $f_{\text{pc}}$ , as an additional parameter. This fraction is unitless, ranges from zero to one and gives the amount of initial radiation which is affected by the absorber. If  $f_{\text{pc}} = 0$  the absorber does not have any effect on the original spectrum and if  $f_{\text{pc}} = 1$  all radiation is affected, which means `TBpcf` acts like `tbabs` itself. To implement this model for spectral fitting, a separate partially absorbed reflection model was assigned to each individual state but most of the parameters of `relxilllp` and `TBpcf` were tied together between these states to represent the physical scenario. These are the equivalent hydrogen column density,  $N_{\text{H}}$ , of the partially absorbing material, the lamp-post height,  $h$ , and powerlaw index,  $\Gamma$ , of the primary source of radiation, the spin,  $a$ , of the black hole, the inclination,  $\theta$ , towards the accretion disk and its iron abundance,  $A_{\text{Fe}}$ , as well as the reflection fraction,  $f_{\text{ref}}$ . The covering fraction,  $f_{\text{pc}}$ , and the ionization state,  $\log \xi$ , were allowed to vary between the spectra of different states. Galactic foreground absorption and the detector constants for *eROSITA* and MOS2 were also still included as illustrated before.

Applying this model to the spectra of different states yields a best fit with C-stat/dof = 1209.3/806 = 1.50, indicating that it can accurately describe the observed behavior. The set of best-fit parameters is listed in Tab. 7.5 and the corresponding model and its residuals to the data for each state is shown in Fig. 7.8. A

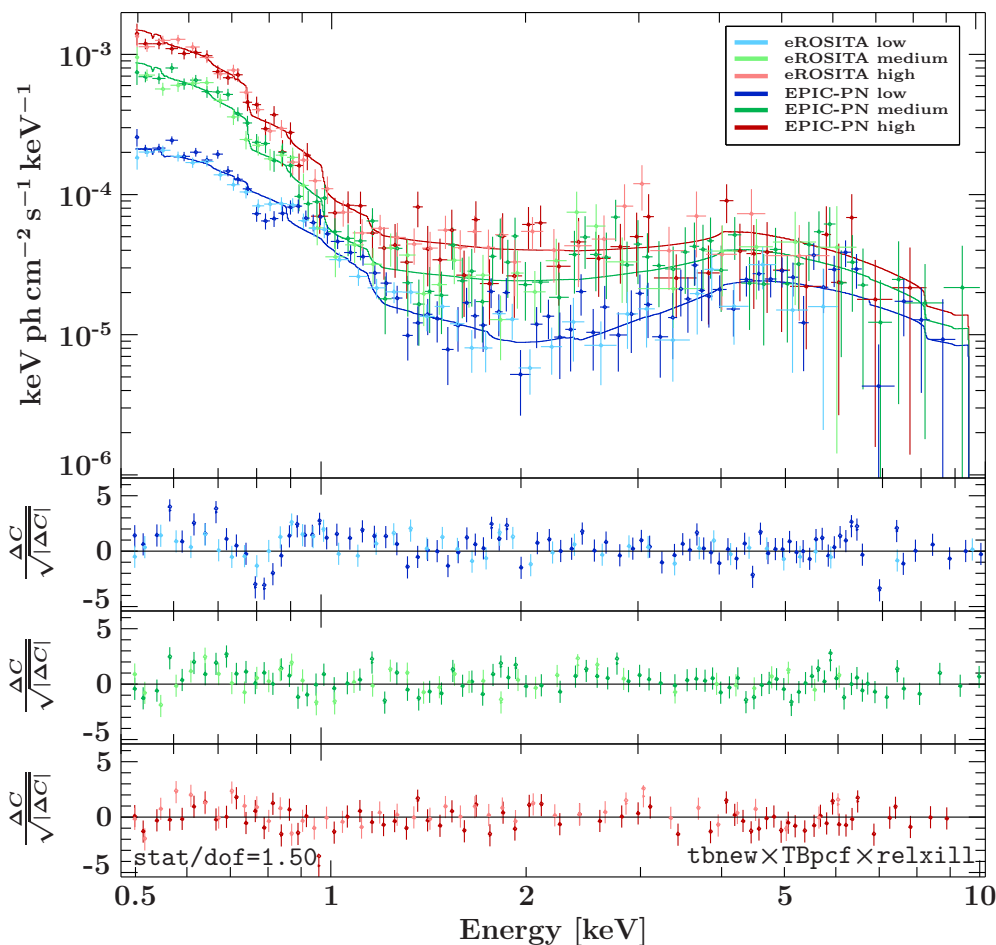


Figure 7.8: *eROSITA* and EPIC-pn spectra (MOS2 was omitted for clarity) from the three count-rate-selected intervals (see Fig. 7.3 and Tab. 7.4) including the best-fitting partially absorbed relativistic reflection models with a varying covering fraction (see Tab. 7.5 for the best-fitting parameters). For clarity the data were rebinned. Note that in the high energies the spectra from all states coincide while in the lower part large differences in flux can be found. The residuals belonging to the fit of each interval are shown in the lower three panels. An observable edge at  $\sim 0.8$  keV in the interval with the lowest flux might indicate a windy absorber (Dauser et al., 2012).

decomposition for the model of each state is shown in Fig. 7.9. Most importantly, the covering fraction for the highest flux state is with  $f_{\text{pc}} < 0.05$  very low, indicating that during this interval an almost unobscured view towards the central region of the source is possible.  $f_{\text{pc}}$  then increases drastically to  $0.28^{+0.16}_{-0.22}$  in the medium state and  $0.75 \pm 0.06$  in the low state. Except of the iron abundance all other parameters of the relativistic reflection model are consistent with the results obtained for the spectra taken over the entire observation.  $A_{\text{Fe}}$  dropped from the maximal possible value given by the model to  $4.8^{+3.8}_{-1.2}$  of the solar abundance which could be considered more reasonable.

When fixing the ionization parameter between the states, strong residuals around 1 keV remained, possibly due to emission from the Fe L band. The fit statistics indicated that the model is not able to describe the data accurately. However, the only parameter we would expect to change on such a short timescale is the lamp-post height which was found to vary by Kara et al. (2015a). In the case at hand no change of the lamp-post height could be found. The ionization state in the applied model was similar in the high and medium state with  $0.68^{+0.10}_{-0.21}$  and  $0.64^{+0.17}_{-0.24}$  respectively and increased to  $1.74^{+0.05}_{-0.04}$  in the low state. This behavior might indicate that the covering material is ionized but because this aspect was not included in

Table 7.5: Best-fit parameters for the partially absorbed relativistic reflection model with three different covering fractions and ionization states as shown in Fig. 7.8. Again, although the stated statistical error of the spin is very low, it is only valid under the assumptions of the underlying model.

Parameter	Low (1)	Medium (2)	High (3)
Time-dependent parameters			
$\text{norm}_{\text{relxillp}} (\times 10^{-3})$	$3.5^{+1.6}_{-1.2}$	$4.7^{+2.9}_{-2.1}$	$5.6^{+2.9}_{-2.8}$
$f_{\text{pc}}$	$0.75 \pm 0.06$	$0.28^{+0.16}_{-0.22}$	$< 0.05$
$\log \xi$	$1.74^{+0.05}_{-0.04}$	$0.64^{+0.17}_{-0.24}$	$0.68^{+0.10}_{-0.21}$
Time-independent parameters			
$N_{\text{H}} [10^{22}/\text{cm}^2]$		$12^{+6}_{-4}$	
$A_{\text{Fe}}$		$4.8^{+3.8}_{-1.2}$	
$\theta [^\circ]$		$74.4^{+1.4}_{-1.9}$	
spin		$0.9968 \pm 0.0013$	
$\Gamma$		$2.73^{+0.10}_{-0.09}$	
$h [r_{\text{g}}]$		$1.25^{+0.11}_{-0.04}$	
$f_{\text{refl}}$		$46^{+18}_{-16}$	
$C_{\text{MOS2}}$		$1.04 \pm 0.06$	
$C_{\text{eROSITA}}$		$0.954^{+0.030}_{-0.029}$	
$C$ -statistic/dof		$1209.3/806$	

the model the ionization parameter of the relativistic reflection model might be mimicking this effect. To investigate this possibility we replaced `TBpcf` with the `zxipcf` model which can account for ionization in the covering material (Reeves et al., 2008). The ionization state of this model was then free to vary in between the three states and the ionization state of the reflection model was tied together. Because of the low count statistics it was, however, not possible to constrain these values for the ionized partial covering model.

## 7.6 Cross-Calibration

Fitting the spectra obtained by *eROSITA* and *XMM-Newton* simultaneously enables us to test the cross-calibration between the two instruments. Especially when investing the residuals in Fig. 7.5 and Fig. 7.8 we find that the spectra of *eROSITA* and EPIC-pn are indeed in good agreement. The multiplicative detector constants, which were free parameters in the fits to the entire dataset and to the spectra of the individual selected intervals, agree with  $C_{\text{eROSITA}} = 0.985^{+0.031}_{-0.030}$  and  $C_{\text{eROSITA}} = 0.954^{+0.030}_{-0.029}$  with each other and indicate that the flux retrieved from *eROSITA* is slightly lower than that determined by EPIC-pn. Interestingly, the situation is different for MOS2. In the combined case the constant for this instrument is  $C_{\text{MOS2}} = 1.14 \pm 0.07$  which would indicate that the flux determined by MOS2 is significantly higher than that of EPIC-pn. From the fit of the individual intervals, however, the constant is  $C_{\text{MOS2}} = 1.04 \pm 0.06$ , so within the 90% confidence limit the flux measured by MOS2 is identical to that of EPIC-pn. The lower SNR resulting from the division of the data in three segments might play a role in this case, as well as a possible over-estimation of the background.

## 7.7 Conclusion

From the analysis presented above multiple conclusions can be drawn about the physical nature of the source. The soft X-ray flux is strongly variable and dropped by a factor of  $\sim 50$  during the observation while the

UV flux stayed mainly constant. Buisson et al. (2017) used observations of 21 AGN performed by *Swift* to investigate the variability properties from the optical over the UV to the X-ray band. They found that, while 9 out of these sources show a lag of the UV emission behind the X-ray emission, 1H 0707–495 in particular does not exhibit any significant correlation of these two regimes which is consistent with our analysis of the recent observation from 2019. Additionally, during a period of the *Swift* monitoring, 1H 0707–495 was also in a very low flux state in which Buisson et al. (2017) found the source of primary radiation to be very compact and also very close to the black hole, causing a concentration of the illumination of the accretion disk at its center. These findings are also agree with the results of our analysis in Tab. 7.3 and Tab. 7.5. According to Buisson et al. (2017), most of the UV emission is generated in a region up to  $500 r_g$  from the black hole while at the determined low lamp-post heights the illuminated part of the accretion disk is mainly smaller than  $10 r_g$ , which makes it very difficult to find correlations between the UV and X-ray variability. In the scenario developed throughout our analysis the variability in the X-rays is attributed to a change of the covering fraction of a partial absorber. Because no such variability was observed in the UV lightcurve, meaning it was unaffected by the absorber, the X-ray and UV radiation must be generated by different source intrinsic mechanisms. Compared to most other AGN of the NLS1 type, 1H 0707–495 shows a very low brightness in X-rays, especially during the 2019 observation (Gallo, 2006; Liu et al., 2016) while in the 2008 observation it was more in line with the rest of the population (Fabian et al., 2009). Because this change in flux occurs on very short timescales and the source has been observed at much higher flux levels, comparable to that of other AGN of the same type, the suppression by variable absorption could deliver an accurate explanation for the observed variability.

By fitting the spectra with a relativistic reflection model, being subject to a partial absorber changing its covering fraction multiple times during the observation, we were able to explain the rapid variability found in soft X-rays. The covering fraction increases significantly with decreasing flux and the obtained column density is  $N_H = 12_{-4}^{+6} \times 10^{22} \text{ cm}^{-2}$ . Markowitz et al. (2014) used the entire data obtained by *RXTE* over its mission lifetime to search systematically for similar absorption events in AGN. They found twelve such events distributed among eight sources for which the column densities were measured to be in the range from  $4 \times 10^{22} \text{ cm}^{-2}$  to  $26 \times 10^{22} \text{ cm}^{-2}$ . This agrees well with our result. In a more recent study, Laha et al. (2020) used data obtained by *XMM-Newton*, *Chandra* and *Suzaku* to systematically search for variability in the hydrogen column density of the intrinsic absorption of 20 Compton-thin type II AGN. For eleven of these sources a partial covering component is necessary to explain the observed spectra. The values for  $N_H$  found in their analysis covers a wide range from less than  $1 \times 10^{22} \text{ cm}^{-2}$  to more than  $50 \times 10^{22} \text{ cm}^{-2}$ , which is also well in agreement found by our model for the partial coverer in the observation of 1H 0707–495.

In other previous works the nature of the edge at  $\sim 7 \text{ keV}$  was explained by a partial covering model (Boller et al., 2002; Tanaka et al., 2004; Miller et al., 2010; Mizumoto et al., 2014). According to our analysis the drop in flux is caused by the extreme distortion of the Fe  $K\alpha$  line due to the effects of relativistic reflection occurring very close, less than a few gravitational radii, to the central black hole. The partial coverer located at much larger distances of a few hundred gravitational radii mainly affects the spectra at soft energies. In analyses of previous, much longer observations with higher SNR residual effects were present when fitting a similar model for relativistic reflections. These were interpreted as fast outflowing wind, either ionized (Dauser et al., 2012; Kosec et al., 2018; Hagino et al., 2016; Mizumoto et al., 2019) or neutral (Gallo et al., 2004). An absorption feature around  $0.8 \text{ keV}$  can be seen in the residuals in Fig. 7.5 for the combined spectra and especially the low flux state shown in Fig. 7.8. The origin of this absorption feature could lie in the reported outflow. According to Parker et al. (2017) and Reeves et al. (2018), the manifestation of the wind in the spectra strongly depends on the flux of the source, which could explain why the absorption feature is much less pronounced in the residuals of the medium and high flux state in Fig. 7.8. PDS 456 is another NLS1 galaxy (Patrick et al., 2012) for which a connection between the partial covering component and the outflow was found by Reeves et al. (2018). Therefore, the partial covering found by our analysis might be an effect caused by such an outflow previously found for 1H 0707–495 by Kosec et al. (2018). If this is true, the shape of the Fe K line should also be affected but because of the low SNR of the spectra of the 2019 observation it was not possible to further test this hypothesis.

In Fig. 7.9 a decomposition of the partially absorbed relativistic reflection model for each count-rate state is shown. The powerlaw emission of the primary source of radiation, which directly reaches the observer, is shown as dotted lines and the component reflected off the disk towards the observer is dashed.

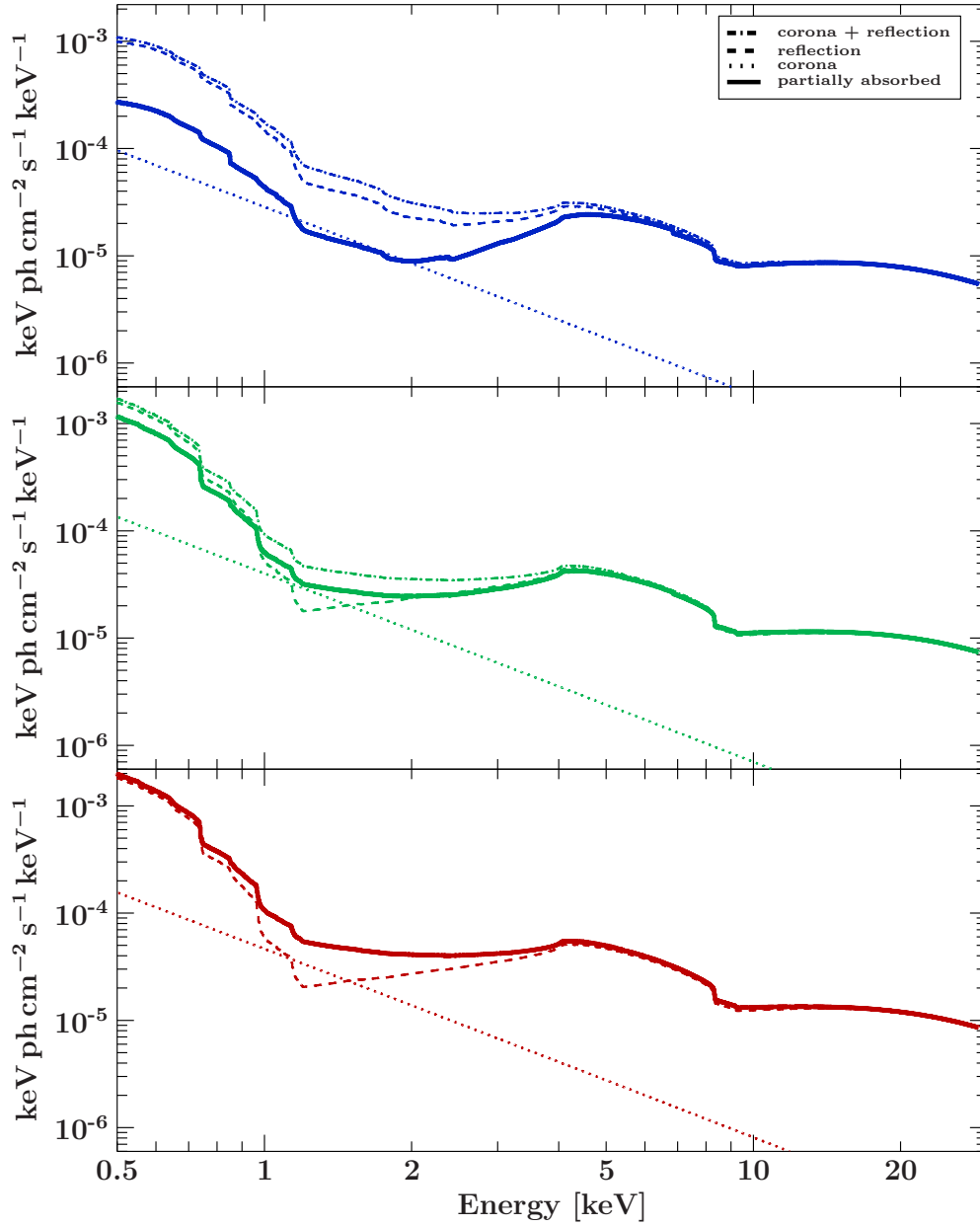


Figure 7.9: Decomposition of the best-fitting model for each count-rate state. The component of the radiation from the corona, which leaves directly towards the observer, is dotted, the portion directed towards the observer after being reflected off the disk is dashed and the combination of both dashed-dotted. This radiation passes through the partial coverer with different covering fractions which creates the solid spectra for the low count-rate state at the top, the medium one at the center and the high one at the bottom. Note that in the high state the corona + reflection component coincides with the partially absorbed spectrum because the covering fraction is zero. The foreground absorption due to the ISM in the Milky Way is not considered in this depiction.

A combination of both, shown as dashed-dotted lines, leaves the central emission region and is along the line of sight subject to the partial coverer which results in the spectra shown as solid lines. Because the covering fraction was found to be with  $f_{pc} < 0.05$  very low in the high state the absorber has almost no influence on the resulting spectrum, hence the solid and dashed-dotted spectra are almost identical in the bottom panel.

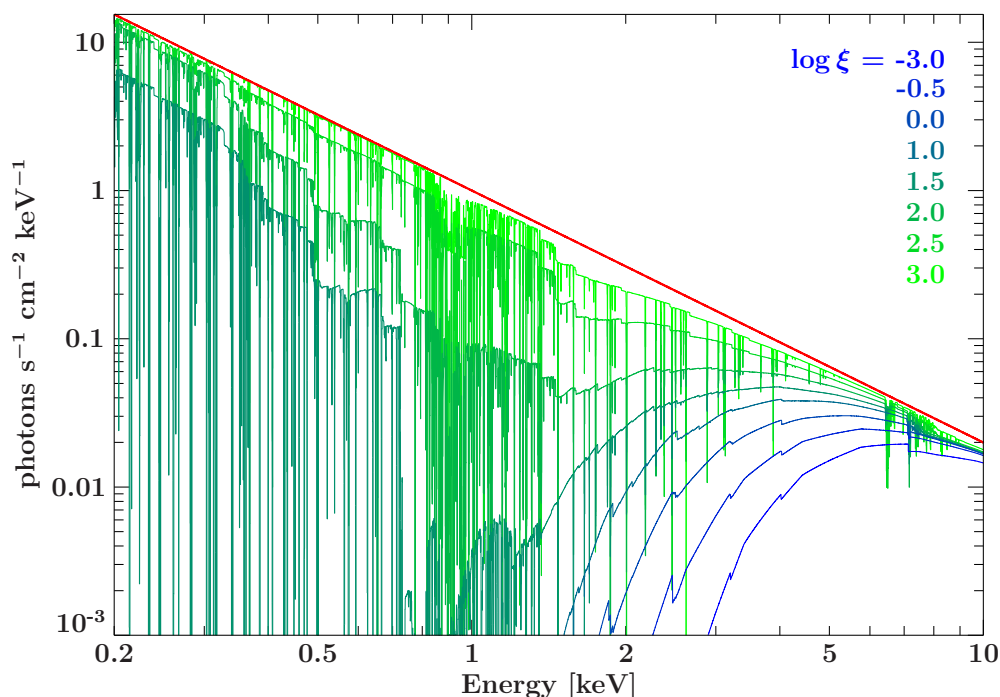


Figure 7.10: Influence of an ionized absorber on a powerlaw with photon index  $\Gamma = 1.7$  (red) at different ionization states. The lower the ionization state, the less affected is the spectrum at soft energies. The spectra were calculated using the `zxipcf` model (Reeves et al., 2008).

In the other two panels it can be seen that the partial covering mostly affects the spectral shape at energies below  $\sim 4$  keV, which explains the increased NEV values found in this regime (see Fig. 7.4). These variations could be thought of as being caused by material passing through the line of sight. We showed that, in the framework of the partially absorbed relativistic reflection model developed in Section 7.5, not only a change of the covering fraction but also of the ionization state of the accretion disk is necessary to accurately describe the observed spectra.  $\log \xi$  is consistent in the medium and high state but significantly increased in the low state. We expect that this change of the ionization of the accretion disk is most likely not real but indicates an improper treatment of a possible ionized absorber which can also change its ionization state. Unfortunately, as outlined above, the low SNR of the obtained data did not enable us to include an ionized absorber in the model. The changes in the covering fraction occur over a timespan of a few 10 ks which places the absorbing material at a close distance to the central black hole and the main emission region, so it is most likely also at least partly ionized and not neutral. In Fig. 7.10 the effect of an ionized absorber at different ionization states is shown. It is clearly evident that with increasing  $\log \xi$  the spectrum at soft energies is less affected, meaning that the material is more transparent and more incident radiation can leak through it towards the observer. As can be seen in Fig. 3.9, the situation is similar for an ionized reflector. This supports our presumption that the change of the ionization state of the reflector is mimicking that of an ionized absorber.

Fig. 7.11 illustrates the physical scenario underlying the model used in this analysis to explain the observed spectra and their variability. At the center of the system is a black hole, spinning with an angular momentum close to the maximal possible value. Above it, on its rotational axis at a close distance less than  $1.5 r_g$ , is the compact X-ray corona emitting the primary powerlaw component. Because of the extreme curvature of spacetime in this environment only a minority of the photons can leave the system directly. Most photons either pass the event horizon of the black hole or hit the ionized accretion disk. After being reflected by the accretion disk, a portion of the reprocessed photons leaves the system towards the observer. Their trajectories are intercepted by clouds of material obscuring the central emission region for the distant observer. The amount of obscuration changes such that in the high flux state most photons are unaffected,

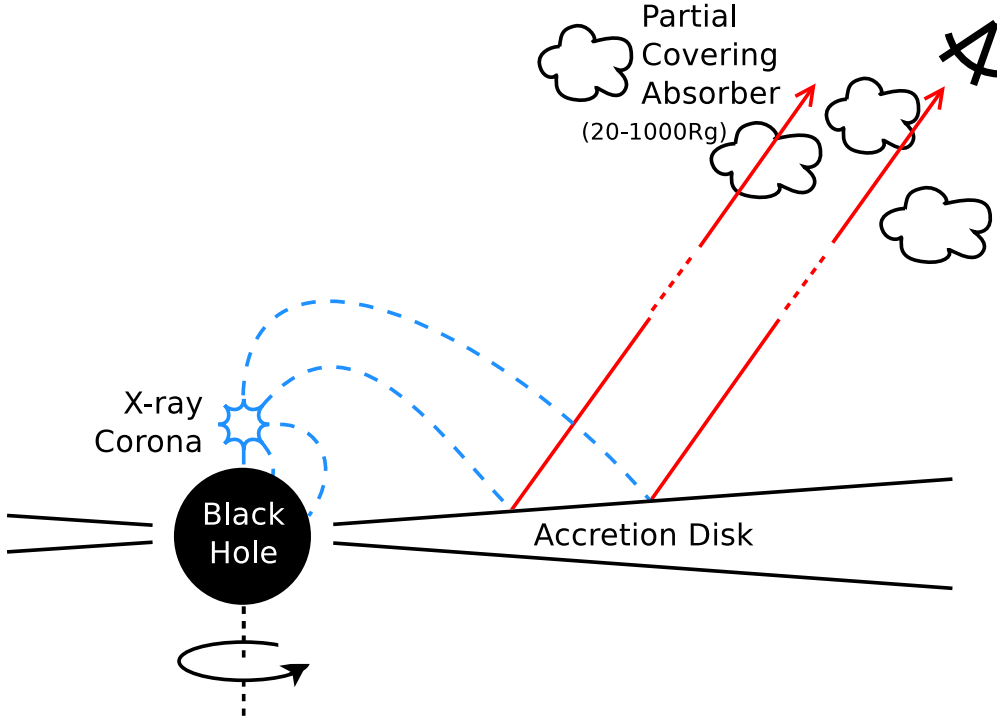


Figure 7.11: Sketch of the physical layout behind the model used to explain the observed data. The primary source of emission is a compact X-ray corona located at a close distance above the black hole which is spinning close to the maximal possible angular momentum. Because of this proximity most of the photons originating from the corona are deflected by the curved spacetime onto the accretion disk or into the black hole itself while a small portion is directly emitted towards the observer. Most of the observed radiation is reflected by the accretion disk. Clouds of material moving at larger distances between the central emission region and the observer cause a varying amount of absorption which is evident as strong variability in the soft X-ray lightcurves and spectra. Taken from Boller et al. (2021).

and the covering fraction is low, but it increases as the obscuration by the absorbing material increases causing a strong suppression of the soft X-ray flux. Fig. 7.11 also demonstrates aspects of the spectral decomposition in Fig. 7.9. Most of the observed radiation does not come from the X-ray corona but from reflection off the accretion disk caused by bending of the photon trajectories due to the curved spacetime. This results in reflection fractions much larger than one and the low powerlaw distributions in Fig. 7.9.

Beuchert et al. (2017) applied a more sophisticated model of partially absorbed relativistic reflections to a set of *XMM-Newton*, *NuSTAR* and *Suzaku* observations of the Seyfert I type AGN NGC 4151. They state that, when assuming Keplerian orbits, the distance,  $R$ , of an absorber to the central black hole can be calculated from the column density,  $N_{\text{H}}$ , and cloud number density,  $n_{\text{H}}$ , as

$$R = 3.6 \times 10^{17} \frac{M}{10^7 M_{\odot}} \left( \frac{n_{\text{H}}}{10^9 \text{ cm}^{-3}} \right)^2 \left( \frac{\Delta t}{2 d} \right)^2 \left( \frac{N_{\text{H}}}{10^{22} \text{ cm}^{-2}} \right)^2 \text{ cm} \quad (7.5)$$

where  $M$  is the mass of the central black hole and  $\Delta t$  the timescale of variability. As suggested by Beuchert et al. (2017), who followed Netzer (1990), Kaspi & Netzer (1999), and Netzer (2008), the cloud number density of  $10^9 \dots 10^{10} \text{ cm}^{-3}$  in the BLR could be used for the calculation. The lightcurve in Fig. 7.3 suggests that at the beginning of the observation from  $t_0$  to  $t_3$  an obscuration event with a length of roughly 20 ks occurred. Carrying out the calculation for these values gives a distance of the absorber to the central emission region of  $11 r_g$  to  $1100 r_g$  and an orbital velocity of  $0.2c$  to  $0.02c$ . The projected length of the absorbing material complex is then  $1.2 \times 10^{13 \dots 14} \text{ cm}$  which corresponds to 0.03 to 0.3 light days. This calculation assumes a very simple geometry of the absorber and relies on the given cloud number density

of the BLR and is therefore highly speculative.



## 8 Summary and Outlook

Throughout the course of this work a variety of different facets of X-ray astronomy addressed by *eROSITA* and other observing facilities have been highlighted. *eROSITA*, as an X-ray survey instrument, is another step forward in the evolution of space born observatories dedicated to the investigation of the most energetic phenomena in the universe.

### 8.1 Discovering Transient Events with the *eROSITA* NRTA

Apart from providing a new extensive catalog of X-ray sources, which will serve as a cosmic inventory of AGN and galaxy clusters, the survey operation of *eROSITA* provides a unique opportunity to discover and study transient events in the X-ray sky. Its FOV, covering an area roughly  $1^\circ$  in diameter, visits each location in the sky in intervals of 4 h for at least six consecutive scans. At most half a year later the same location is covered again. To harvest the potential of recognizing significant changes or even the sudden appearance of previously completely unknown X-ray sources we created a software pipeline which automatically analyzes the data of selected regions in the sky as soon as they arrive on ground. This Near Real-Time analysis can be provided with a list of target regions for source detection or already known point sources externally, while it also recognizes very bright sources passing through the FOV autonomously. This is achieved by creating an optimal segmentation of the time-dependent total rate of events registered by each CCD of the individual TMs with the Bayesian Block algorithm developed by Scargle et al. (2013b) and detecting a significant increase in this rate originating from a bright source. The other target regions and monitoring sources can be ingested into the pipeline at any point in time, making it very easy to dynamically define new targets based on time critical results from other observatories.

After source detection is performed on the regions identified by the Bayesian Block algorithm and externally ingested into the pipeline, basic source products such as lightcurves and spectra are extracted for each detected source and all monitoring sources. Counterparts in other catalogs covering all wavelengths are identified for each source and additional parameters such as hardness ratios and effective exposure times are calculated. By defining a set of flexible trigger criteria, this information is evaluated for each source and if all specified criteria for a trigger are fulfilled an alert is generated and the relevant scientists are informed via e-mail. A manual assessment of the source triggering the alert can be done in a browser based user interface. When all data for a ground-contact session have been processed individual sources are identified across multiple scans and trigger based on changes of source properties are evaluated.

At the time of writing this thesis, the NRTA has analyzed 21.4 million occurrences of sources, of which roughly one million were found by source detection in regions ingested into the pipeline or identified as containing a bright source. About 150 thousand alerts were generated based on trigger criteria defined by members of the German *eROSITA* consortium to target a variety of different science cases.

One of these is the identification of previously completely unknown X-ray sources. On New Year's Eve, 2019, the Bayesian block algorithm identified a very bright source passing through the FOV. After performing source detection and cross-matching with other catalogs an alert was generated based on a trigger which aims to identify new sources in the X-ray sky. Indeed, after manual verification by humans, the alert was found to be valid and caused by a very bright transient source with a count-rate of more than 100 cts/s, as seen by *eROSITA*. The event was also independently discovered and therefore verified by *ART-XC*, the other instrument onboard *SRG*. No other X-ray source was ever seen by any other mission at this position and no possible counterpart could be identified causing the true nature of the source to remain a mystery because only two scans later it has vanished completely. This event provides a nice demonstration of the capabilities provided by the NRTA to discover new X-ray transients.

During the first two years of *eROSITA*'s all-sky survey, the NRTA identified a variety of other interesting events like stellar flares, GRBs and classical novae. *SRG* will continue survey operations for another two

years, so it can be expected that during this time even more interesting events will be found by the NRTA in the data obtained by *eROSITA*.

## 8.2 The Variable Nature of 1H 0707–495

Before *eROSITA* started its all-sky survey, a variety of observations to calibrate the instrument and verify its performance were carried out in 2019. One of these observations targeted the Seyfert I galaxy 1H 0707–495 and was accompanied by the X-ray observatory *XMM-Newton*. As described by Boller et al. (2021) and this thesis, the lightcurve of the source showed large amplitude variability. Another characteristic property of this source is a steep drop in flux at  $\sim 7$  keV detected in its spectrum. In the past this feature was mainly explained as an effect of either relativistically blurred reflection from the inner region of the accretion disk (see for example Boller et al., 2002; Fabian et al., 2002a, 2004; Blustin & Fabian, 2009; Fabian et al., 2009; Zoghbi et al., 2010; Wilkins & Fabian, 2011; Zoghbi et al., 2011; Chainakun & Young, 2012; Dauser et al., 2012; Fabian et al., 2012; Wilkins et al., 2014; Kara et al., 2015a; Caballero-García et al., 2018; Chainakun et al., 2019; Szanecki et al., 2020) or partial absorption along the line of sight from the observer to the emission region (see for example Boller et al., 2002; Gallo et al., 2004; Tanaka et al., 2004; Miller et al., 2010; Mizumoto et al., 2014).

By first performing an analysis of the lightcurve and time-dependent hardness ratio we were able to show that the variability is strongly concentrated in the soft energy band below 0.8 keV. The count-rate measured from the source by *eROSITA* was with  $\sim 1$  cts/s highest at the beginning of the observation and dropped over the course of 14 h to below 0.1 cts/s. In the soft band the normalized excess variance in units of sigma is  $44.6\sigma$  while from 0.8 to 7.0 keV it is only  $2.1\sigma$ . The UV lightcurve measured by the OM onboard *XMM-Newton* only showed a variability of  $1.7\sigma$ .

To describe the spectrum we first employed an empirical model consisting of a soft blackbody component originating from the accretion disk and a hard powerlaw component generated by inverse Compton scattering, as was already done in previous works by for example Gallo et al. (2004), Tanaka et al. (2004), Blustin & Fabian (2009), Fabian et al. (2009), Zoghbi et al. (2010), Zoghbi et al. (2011), Dauser et al. (2012), Fabian et al. (2012), Mizumoto et al. (2014), Wilkins et al. (2014), Kara et al. (2015a), and Pawar et al. (2017). A good fit could be achieved by this simple approach. To compare the present to previous observations of the source performed by *XMM-Newton* all available data have been downloaded, the spectra were extracted, and the same model was fitted to these spectra. Calculating the flux from the resulting fits showed that during the observation by *eROSITA* and *XMM-Newton* in 2019 the source was in a historically low flux state.

It has been shown that the soft excess is more likely to arise from relativistically blurred Fe L line emission (Fabian et al., 2009; Zoghbi et al., 2010; Kara et al., 2015a; Pawar et al., 2017) which is in line with the same explanation for the sharp drop at  $\sim 7$  keV, caused by blurred Fe K line emission. Motivated by this we used the relativistic reflection model `relxill` in its self-consistent lamp-post geometry flavor to describe the entire spectrum without any additional components apart from galactic foreground absorption. This yields a good fit to the data and indicates that the primary source of emission, assumed to be located on the rotational axis above the black hole, is very close to the event horizon. Because the source is located so close to the black hole most of radiation reaching the observer has been reflected off the accretion disk which is also indicated by the high value found for the reflection fraction. This effect agrees with previous studies which found the emissivity profile on the accretion disk to be very steep (Dauser et al., 2012; Fabian et al., 2012; Kara et al., 2015a). In the past also ionized outflows have been reported for the source (Done et al., 2007; Dauser et al., 2012) but the low SNR of the new observation did not enable us to test this hypothesis.

To further explore the origin of the strong soft variability we extracted three spectra from time periods when the source was considered to show low, intermediate and high flux. The other popular approach taken to describe the spectrum of 1H 0707–495 is a partial covering model. Motivated by these efforts, and with the relativistic reflection model as a baseline, we added a partial covering component for which the covering fraction was allowed to vary between the three different flux selected spectra. The resulting best fits describe the data very well and allow an interesting interpretation: For the spectra with the highest flux the covering fraction was found to be almost zero, but it increases over the spectrum with intermediate flux

to around three quarters for the spectrum with the lowest flux. This means that the observed variability can be interpreted as clouds of material passing through the line of sight towards the central emission region and causing a varying degree of absorption concentrated on the soft part of the spectrum. To achieve an acceptable fit to the data the ionization state of the accretion disk in the lamp-post model had to be allowed to vary and was found to be elevated in the low flux state compared to the others. We argued that this change in ionization of the accretion disk is not real but possibly mimics a change of the ionization state of the absorbing material itself. Because of the low SNR of the data we were not able to test this hypothesis.

The fact that *eROSITA* and *XMM-Newton* observed 1H 0707–495 exactly during this period of extremely variable flux can only properly be described as a lucky coincidence. But this lucky coincidence is what enabled us to gain further insight into the inner workings of the source and move a step closer to understanding the true nature of 1H 0707–495. However, one could argue that the lamp-post model with its primary source being assumed to be point-like and the simple ionization structure of the accretion disk cannot be expected to represent the physical reality. Other models with extended coronae are already being developed and tested (Wilkins & Fabian, 2012; Lickleder, 2019; Szanecki et al., 2020) but with the X-ray data obtained by current observatories, such as *eROSITA* and *XMM-Newton*, no clear distinction between these more generalized models and the simpler and proven “toy models” used in this work to describe the data has been found. Upcoming X-ray observatories such as *XRISM* (XRISM Science Team, 2020) and *Athena* (Barret et al., 2016; Rau et al., 2016) will utilize micro calorimeters as X-ray detectors which will provide greatly improved spectral resolution. Specifically for the *Athena* X-ray Integral Field Unit (X-IFU), Barret & Cappi (2019) showed by simulating observations of AGN with typical fluxes and assuming the `relxill` model that the main parameters in the lamp-post scenario, such as the black hole spin and lamp-post height, can be constraint within uncertainties of 0.05 and  $0.2 r_g$  respectively. Parameters regarding neutral, ionized, or moving absorbers, such as the column density, ionization state, covering fraction, and velocity, will be able to be measured with an error of  $\sim 5\%$ . In case of a superimposed UFO the velocity is expected to be constraint within  $< 1\%$ . Given of these capabilities the launches of these missions are highly anticipated by the scientific community.



# References

- Agrawal P.C., Koyama K., Matsuoka M., Tanaka Y., 1986, PASJ38, 723
- Aird J., Nandra K., Laird E.S., et al., 2010, MNRAS401, 2531 \_eprint: 0910.1141
- Aiton E.J., 1969, Isis 60, 75
- Ajello M., Romani R.W., Gasparrini D., et al., 2014, ApJ780, 73 \_eprint: 1310.0006
- Alexandrov Y.A., Andreyanov V.V., Babakin N.G., et al., 2012a, Solar System Research 46, 458
- Alexandrov Y.A., Andreyanov V.V., Babakin N.G., et al., 2012b, Solar System Research 46, 466
- Altamirano D., van der Klis M., Méndez M., et al., 2008, ApJ687, 488 \_eprint: 0806.4149
- Anders E., Ebihara M., 1982, Geochim. Cosmochim. Acta46, 2363
- Anders E., Grevesse N., 1989, Geochim. Cosmochim. Acta53, 197
- Anderson A., 1983, Nature301, 647
- Antonelli L.A., Piro L., Vietri M., et al., 2000, ApJ545, L39 \_eprint: astro-ph/0010221
- Antonucci R., 1993, ARA&A31, 473
- Armitage P.J., 1998, ApJ501, L189 \_eprint: astro-ph/9805133
- Arnaud K., Smith R., Siemiginowska A., 2011, Handbook of X-ray Astronomy, Cambridge University Press
- Arnaud K.A., 1996, In: Jacoby G.H., Barnes J. (eds.) Astronomical Data Analysis Software and Systems V, Vol. 101. Astronomical Society of the Pacific Conference Series, p. 17
- Arp H., 1959, Leaflet of the Astronomical Society of the Pacific 8, 73
- Arzoumanian Z., Gendreau K.C., Baker C.L., et al., 2014, In: Takahashi T., den Herder J.W.A., Bautz M. (eds.) Space Telescopes and Instrumentation 2014: Ultraviolet to Gamma Ray, Vol. 9144. Society of Photo-Optical Instrumentation Engineers (SPIE) Conference Series, p. 914420
- Aschenbach B., Bräuninger H., Kettenring G., 1982, Advances in Space Research 2, 251
- Audley M.D., Kelley R.L., Boldt E.A., et al., 1996, ApJ457, 397
- B. T.A.A., Dreyer J.L.E., Heath T., 1955, The Mathematical Gazette 39, 88
- Ballo L., Giustini M., Schartel N., et al., 2008, åp 483, 137 \_eprint: 0802.2936
- Balucinska-Church M., McCammon D., 1992, ApJ400, 699
- Bambynek W., Crasemann B., Fink R.W., et al., 1972, Reviews of Modern Physics 44, 716
- Barker G.F., 1887, Proceedings of the American Philosophical Society 24, 166 Publisher: American Philosophical Society
- Barret D., Cappi M., 2019, åp 628, A5 \_eprint: 1906.02734
- Barret D., Lam Trong T., den Herder J.W., et al., 2016, In: den Herder J.W.A., Takahashi T., Bautz M. (eds.) Space Telescopes and Instrumentation 2016: Ultraviolet to Gamma Ray, Vol. 9905. Society of Photo-Optical Instrumentation Engineers (SPIE) Conference Series, p. 99052F \_eprint: 1608.08105
- Barthelmy S.D., Barbier L.M., Cummings J.R., et al., 2005, Space Sci. Rev. 120, 143 \_eprint: astro-ph/0507410
- Basinska E.M., Lewin W.H.G., Cominsky L., et al., 1980, ApJ241, 787
- Bautista M.A., Kallman T.R., 2001, ApJS134, 139
- Beckmann V., Shrader C.R., 2012, Active Galactic Nuclei, Wiley-VCH
- Belmont R., Malzac J., Marcowith A., 2008, A&A491, 617 \_eprint: 0808.1258
- Ben-Menahem A., 1992, QJRAS33, 175
- Bennett C.L., Bay M., Halpern M., et al., 2003, ApJ583, 1 \_eprint: astro-ph/0301158
- Berger M., van der Klis M., van Paradijs J., et al., 1996, arXiv e-prints astro-ph/9607110 \_eprint: astro-ph/9607110
- Berthelsdorf R.F., Culhane J.L., 1979, MNRAS187, 17P
- Bessel F.W., 1838, Astronomische Nachrichten 16, 65
- Beuchert T., Markowitz A.G., Dauser T., et al., 2017, åp 603, A50 \_eprint: 1703.10856
- Bhalerao V., Bhattacharya D., Vibhute A., et al., 2017, Journal of Astrophysics and Astronomy 38, 31 \_eprint: 1608.03408
- Bhattacharyya S., 2010, Advances in Space Research 45, 949 \_eprint: 1001.1642
- Bian W.H., Zhao Y.H., 2003, PASJ55, 599 \_eprint: astro-ph/0305095
- Bianchi S., Guainazzi M., Matt G., et al., 2005, åp 442, 185 \_eprint: astro-ph/0507323
- Binette L., Magris C.G., Stasińska G., Bruzual A.G., 1994, A&A292, 13
- Birt W.R., 1863, Astronomical register 1, 101
- Bissinger M., 2016, PhD Thesis, Dr. Karl Remeis-Sternwarte, Astronomical Institute of the FAU
- Bizony P., 2011, Engineering & Technology 6, 34
- Blandford R., Meier D., Readhead A., 2019, ARA&A57, 467 \_eprint: 1812.06025
- Blissett R.J., Mason K.O., Culhane J.L., 1981, MNRAS194, 77
- Blustin A.J., Fabian A.C., 2009, MNRAS399, L169

## References

- \_eprint: 0908.3457
- Boch T., Fernique P., 2017, In: Lorente N.P.F., Shortridge K., Wayth R. (eds.) *Astronomical Data Analysis Software and Systems XXV*, Vol. 512. Astronomical Society of the Pacific Conference Series, p. 105
- Boella G., Butler R.C., Perola G.C., et al., 1997a, *A&AS*122, 299
- Boella G., Chiappetti L., Conti G., et al., 1997b, *A&AS*122, 327
- Boller T., Fabian A.C., Sunyaev R., et al., 2002, *MNRAS*329, L1 \_eprint: astro-ph/0110367
- Boller T., Freyberg M.J., Trümper J., et al., 2016, *A&A*588, A103 \_eprint: 1609.09244
- Boller T., Liu T., Weber P., et al., 2021, *A&A*647, A6 \_eprint: 2011.03307
- Bouchet L., Mandrou P., Roques J.P., et al., 1991, *ApJ*383, L45
- Bowen I.S., 1927, *Nature*120, 473
- Brack-Bernsen L., 2005, *Centaurus* 47, 1
- Brandt S., Lund N., Rao A.R., 1990, *Advances in Space Research* 10, 239
- Brenneman L.W., Reynolds C.S., 2006, *ApJ*652, 1028 \_eprint: astro-ph/0608502
- Brenneman L.W., Reynolds C.S., Nowak M.A., et al., 2011, *ApJ*736, 103 \_eprint: 1104.1172
- Briel U.G., Pfeiffermann E., 1986, *Nuclear Instruments and Methods in Physics Research A* 242, 376
- Briel U.G., Pfeiffermann E., Hartner G., Hasinger G., 1988, In: Golub L. (ed.) *X-ray instrumentation in astronomy II*, Vol. 982. Society of Photo-Optical Instrumentation Engineers (SPIE) Conference Series, p.401
- Brinkman A.C., Heise J., de Jager C., 1974, *Philips Technical Review* 34, 43
- Britto R.J., Bottacini E., Böttcher M., et al., 2016, In: Reylé C., Richard J., Cambrésy L., Deleuil M., Pécontal E., Tresse L., Vauglin I. (eds.) *SF2A-2016: Proceedings of the Annual meeting of the French Society of Astronomy and Astrophysics.*, p.93
- Britton J.P., 2010, *Archive for History of Exact Sciences* 64, 617
- Brunner H., Boller T., Coutinho D., et al., 2018, In: den Herder J.W.A., Nikzad S., Nakazawa K. (eds.) *Space Telescopes and Instrumentation 2018: Ultraviolet to Gamma Ray*, Vol. 10699. Society of Photo-Optical Instrumentation Engineers (SPIE) Conference Series, p. 106995G
- Buchner J., Boller T., Bogensberger D., et al., 2021, *arXiv e-prints arXiv:2106.14529* \_eprint: 2106.14529
- Buisson D.J.K., Lohfink A.M., Alston W.N., Fabian A.C., 2017, *MNRAS*464, 3194 \_eprint: 1609.08638
- Bult P., Jaisawal G.K., Güver T., et al., 2019, *ApJ*885, L1 \_eprint: 1909.03595
- Burbidge E.M., 1967, *ARA&A*5, 399
- Burke B.E., Mountain R.W., Daniels P.J., et al., 1993, In: Siegmund O.H. (ed.) *EUV, X-Ray, and Gamma-Ray Instrumentation for Astronomy IV*, Vol. 2006. Society of Photo-Optical Instrumentation Engineers (SPIE) Conference Series, p.272
- Burke B.E., Mountain R.W., Daniels P.J., et al., 1994, *IEEE Transactions on Nuclear Science* 41, 375
- Burnell S.J.B., Culhane J.L., 1979, *MNRAS*188, 1P
- Burrows D.N., Hill J.E., Nousek J.A., et al., 2005, *Space Sci. Rev.* 120, 165 \_eprint: astro-ph/0508071
- Butler C.P., 1924, *Nature*113, 703
- Byram E.T., Chubb T.A., Friedman H., 1966a, *AJ*71, 379
- Byram E.T., Chubb T.A., Friedman H., 1966b, *Science* 152, 66
- Caballero-García M.D., Papadakis I.E., Dovčiak M., et al., 2018, *MNRAS*480, 2650 \_eprint: 1804.03503
- Cannon A.J., 1915, *JRASC*9, 203
- Cannon A.J., Pickering E.C., 1918a, *Annals of Harvard College Observatory* 92, 1
- Cannon A.J., Pickering E.C., 1918b, *Annals of Harvard College Observatory* 91, 1
- Cannon A.J., Pickering E.C., 1919a, *Annals of Harvard College Observatory* 93, 1
- Cannon A.J., Pickering E.C., 1919b, *Annals of Harvard College Observatory* 94, 1
- Cannon A.J., Pickering E.C., 1920, *Annals of Harvard College Observatory* 95, 1
- Cannon A.J., Pickering E.C., 1921, *Annals of Harvard College Observatory* 96, 1
- Cannon A.J., Pickering E.C., 1922, *Annals of Harvard College Observatory* 97, 1
- Cannon A.J., Pickering E.C., 1923, *Annals of Harvard College Observatory* 98, 1
- Cannon A.J., Pickering E.C., 1924, *Annals of Harvard College Observatory* 99, 1
- Cardelli J.A., Meyer D.M., Jura M., Savage B.D., 1996, *ApJ*467, 334
- Cash W., 1979, *ApJ*228, 939
- Cavaliere A.G., Gursky H., Tucker W.H., 1971, *Nature*231, 437
- Chainakun P., Watcharangkool A., Young A.J., Hancock S., 2019, *MNRAS*487, 667 \_eprint: 1905.03683
- Chainakun P., Young A.J., 2012, *MNRAS*420, 1145
- Chambers K.C., Magnier E.A., Metcalfe N., et al., 2016, *arXiv e-prints arXiv:1612.05560* \_eprint: 1612.05560
- Chandrasekhar S., 1931, *ApJ*74, 81
- Chandrasekhar S., 1935, *MNRAS*95, 207
- Chomiuk L., Metzger B.D., Shen K.J., 2020, *arXiv e-prints arXiv:2011.08751* \_eprint: 2011.08751
- Clark G.W., Jernigan J.G., Bradt H., et al., 1976, *ApJ*207, L105
- Clark G.W., Woo J.W., Nagase F., et al., 1990, *ApJ*353, 274
- Clayton D.D., 1983, *Principles of stellar evolution and nucleosynthesis*, University of Chicago Press
- Coe M.J., Engel A.R., Quenby J.J., 1976, *Nature*262, 563
- Coldwell G.V., Alonso S., Duplancic F., Mesa V., 2018, *MNRAS*476, 2457 \_eprint: 1803.00946
- Compton A.H., 1923, *Physical Review* 21, 483
- Cooke B.A., 1976, *Nature*261, 564
- Cooke B.A., Elvis M., Maccacaro T., et al., 1976, *MNRAS*177, 121P
- Cotterell B., Dickson F., Kamminga J., 1986, *Journal of*

- Archaeological Science 13, 31
- Cotton W.D., Tody D., Pence W.D., 1995, *aps* 113, 159
- Cui W., Shrader C.R., Haswell C.A., Hynes R.I., 2000, arXiv e-prints astro-ph/0004236 \_eprint: astro-ph/0004236
- Cunningham C.J., (ed.) 2018, *The Scientific Legacy of William Herschel, Historical & Cultural Astronomy*, Springer International Publishing, Cham
- Curtis H.D., 1918, *Publications of Lick Observatory* 13, 9
- Daphne C., 2010 31
- Dauser T., 2010, Diploma Thesis, FAU Erlangen Nuernberg
- Dauser T., 2014, PhD Thesis, Dr. Karl Remeis-Sternwarte, Astronomical Institute of the FAU
- Dauser T., Garcia J., Parker M.L., et al., 2014, *MNRAS*444, L100 \_eprint: 1408.2347
- Dauser T., Garcia J., Wilms J., et al., 2013, *MNRAS*430, 1694 \_eprint: 1301.4922
- Dauser T., García J., Walton D.J., et al., 2016a, *A&A*590, A76 \_eprint: 1601.03771
- Dauser T., García J., Wilms J., 2016b, *Astronomische Nachrichten* 337, 362 \_eprint: 1810.09149
- Dauser T., Svoboda J., Schartel N., et al., 2012, *MNRAS*422, 1914 \_eprint: 1112.1796
- Dauser T., Wilms J., Reynolds C.S., Brenneman L.W., 2010, *MNRAS*409, 1534 \_eprint: 1007.4937
- Davison P.J.N., Culhane J.L., Mitchell R.J., Fabian A.C., 1975, *ApJ*196, L23
- de Jong T., 2007, *Wiener Zeitschrift für die Kunde des Morgenlandes* 97, 107
- de Korte P.A.J., Bleeker J.A.M., den Boggende A.J.F., et al., 1981, *Br* 30, 495
- Delvecchio I., Lutz D., Berta S., et al., 2015, *MNRAS*449, 373 \_eprint: 1501.07602
- Demtröder W., 2008, *Experimentalphysik 1*, Springer
- Demtröder W., 2009a, *Experimentalphysik 2*, Springer
- Demtröder W., 2009b, *Experimentalphysik 3*, Springer
- den Boggende A.J.F., Lafleur H.T.J.A., 1975, *IEEE Transactions on Nuclear Science* 22, 555
- den Herder J.W., Brinkman A.C., Kahn S.M., et al., 2001, *A&A*365, L7
- Denney K.D., De Rosa G., Croxall K., et al., 2014, *ApJ*796, 134 \_eprint: 1404.4879
- DiPompeo M.A., Myers A.D., Brotherton M.S., et al., 2014, *ApJ*787, 73 \_eprint: 1404.3151
- Domingo V., Fleck B., Poland A.I., 1995, *Sol. Phys.*162, 1
- Done C., Sobolewska M.A., Gierliński M., Schurch N.J., 2007, *MNRAS*374, L15 \_eprint: astro-ph/0610078
- Dopita M.A., Sutherland R.S., 1995, *ApJ*455, 468
- Dopita M.A., Sutherland R.S., 1996, *ApJS*102, 161
- Dotti M., Merloni A., Montuori C., 2015, *MNRAS*448, 3603 \_eprint: 1502.03101
- Dove J.B., Wilms J., Begelman M.C., 1997, *ApJ*487, 747 \_eprint: astro-ph/9705108
- Dovčiak M., Karas V., Yaqoob T., 2004, *ApJS*153, 205 \_eprint: astro-ph/0403541
- Dunlop J.S., Peacock J.A., 1990, *MNRAS*247, 19
- Ebrero J., Carrera F.J., Page M.J., et al., 2009, *A&A*493, 55 \_eprint: 0811.1450
- Eddington A.S., 1916a, *MNRAS*77, 16
- Eddington A.S., 1916b, *MNRAS*77, 16
- Eddington A.S., 1919a, *Nature*104, 372
- Eddington A.S., 1919b, *The Observatory* 42, 119
- Eder J., Predehl P., Scheuerle H., 2018, In: den Herder J.W.A., Nikzad S., Nakazawa K. (eds.) *Space Telescopes and Instrumentation 2018: Ultraviolet to Gamma Ray*, Vol. 10699. Society of Photo-Optical Instrumentation Engineers (SPIE) Conference Series, p. 106991Z
- Einstein A., 1912, *Annalen der Physik* 343, 355
- Einstein A., 1915a, *Ständiger Beobachter der Preussischen Akademie der Wissenschaften, Part 2 ??*, 844
- Einstein A., 1915b, *Ständiger Beobachter der Preussischen Akademie der Wissenschaften, Part 2 ??*, 831
- Einstein A., 1915c, *Ständiger Beobachter der Preussischen Akademie der Wissenschaften, Part 2 ??*, 831
- Einstein A., 1915d, *Ständiger Beobachter der Preussischen Akademie der Wissenschaften, Part 1 ??*, 315
- Einstein A., 1915e, *Ständiger Beobachter der Preussischen Akademie der Wissenschaften, Part 2 ??*, 778
- Einstein A., 1915f, *Ständiger Beobachter der Preussischen Akademie der Wissenschaften, Part 2 ??*, 778
- Einstein A., 1916, *Annalen der Physik (1900) (series 4)* 354, 769
- Eisenhauer F., Genzel R., Alexander T., et al., 2005, *ApJ*628, 246 \_eprint: astro-ph/0502129
- Elvis M., 1976, *MNRAS*177, 7P
- Elvis M., Page C.G., Pounds K.A., et al., 1975, *Nature*257, 656
- Emlyn-Jones C., Preddy W., 2017, *Plato: Euthyphro, Apology, Crito, Phaedo*, Harvard Univ. Press
- Engels D., 1985, *The American Journal of Philology* 106, 298
- Enoki M., Ishiyama T., Kobayashi M.A.R., Nagashima M., 2014, *ApJ*794, 69 \_eprint: 1408.3726
- Eyles C.J., Skinner G.K., Willmore A.P., Rosenberg F.D., 1975a, *MNRAS*173, 63P
- Eyles C.J., Skinner G.K., Willmore A.P., Rosenberg F.D., 1975b, *Nature*257, 291
- Fabian A.C., Ballantyne D.R., Merloni A., et al., 2002a, *MNRAS*331, L35 \_eprint: astro-ph/0202297
- Fabian A.C., Miniutti G., Gallo L., et al., 2004, *MNRAS*353, 1071 \_eprint: astro-ph/0405160
- Fabian A.C., Rees M.J., Stella L., White N.E., 1989, *MNRAS*238, 729
- Fabian A.C., Ross R.R., 1981, *MNRAS*194, 29P
- Fabian A.C., Vaughan S., Nandra K., et al., 2002b, *MNRAS*335, L1 \_eprint: astro-ph/0206095
- Fabian A.C., Willingale R., Pye J.P., et al., 1980, *MNRAS*193, 175
- Fabian A.C., Zoghbi A., Ross R.R., et al., 2009, *Nature*459, 540
- Fabian A.C., Zoghbi A., Wilkins D., et al., 2012, *MNRAS*419, 116 \_eprint: 1108.5988

## References

- Fanaroff B.L., Riley J.M., 1974, MNRAS167, 31P
- Fath E.A., 1909, Lick Observatory Bulletin 149, 71
- Favata F., Maggio A., Peres G., Sciortino S., 1997, A&A326, 1013 \_eprint: astro-ph/9707058
- Favata F., Micela G., 2003, *br* 108, 577 \_eprint: astro-ph/0302565
- Filippenko A.V., Terlevich R., 1992, ApJ397, L79
- Finocchiaro M.A., 2010, Journal for the History of Astronomy 41, 525
- Finoguenov A., Chernyakova M., 1998, Advances in Space Research 21, 109
- Flanagan K.A., Canizares C.R., Dewey D., et al., 2003, In: Truemper J.E., Tananbaum H.D. (eds.) X-Ray and Gamma-Ray Telescopes and Instruments for Astronomy., Vol. 4851. Society of Photo-Optical Instrumentation Engineers (SPIE) Conference Series, p.45
- Fomenko A.T., Kalashnikov V.V., Nosovsky G.V., 1989, Acta Applicandae Mathematicae 17, 203
- Forman W., Jones C., Cominsky L., et al., 1978, ApJS38, 357
- Forman W., Kellogg E., Gursky H., et al., 1972, ApJ178, 309
- Fotopoulou S., Buchner J., Georgantopoulos I., et al., 2016, A&A587, A142 \_eprint: 1601.06002
- Fragile P.C., Blaes O.M., Anninos P., Salmonson J.D., 2007, ApJ668, 417 \_eprint: 0706.4303
- Fraunhofer J., 1817, Annalen der Physik 56, 264
- Friedman H., Lichtman S.W., Byram E.T., 1951, Physical Review 83, 1025
- Friedrich P., Bräuninger H., Budau B., et al., 2008, In: Turner M.J.L., Flanagan K.A. (eds.) Space Telescopes and Instrumentation 2008: Ultraviolet to Gamma Ray, Vol. 7011. Society of Photo-Optical Instrumentation Engineers (SPIE) Conference Series, p. 70112T
- Friedrich P., Rohé C., Gaida R., et al., 2014, In: Takahashi T., den Herder J.W.A., Bautz M. (eds.) Space Telescopes and Instrumentation 2014: Ultraviolet to Gamma Ray, Vol. 9144. Society of Photo-Optical Instrumentation Engineers (SPIE) Conference Series, p. 91444R
- Fritz G., Davidsen A., Meekins J.F., Friedman H., 1971, ApJ164, L81
- Frontera F., Antonelli L.A., Amati L., et al., 2000, ApJ540, 697 \_eprint: astro-ph/0002527
- Frontera F., Costa E., dal Fiume D., et al., 1997, A&AS122, 357
- Fukazawa Y., Makishima K., Tamura T., et al., 1998, PASJ50, 187 \_eprint: astro-ph/9802126
- Fürmetz M., Pfeiffermann E., Predehl P., et al., 2008, In: Turner M.J.L., Flanagan K.A. (eds.) Space Telescopes and Instrumentation 2008: Ultraviolet to Gamma Ray, Vol. 7011. Society of Photo-Optical Instrumentation Engineers (SPIE) Conference Series, p. 70113Y
- Gagandeep Kaur 2017 4, 627
- Gaia CollaborationPrusti T., de Bruijne J.H.J., et al., 2016, A&A595, A1 \_eprint: 1609.04153
- Gaillardetz R., Bjorkholm P., Mastronardi R., et al., 1978, IEEE Transactions on Nuclear Science 25, 437
- Galle J.G., 1846, MNRAS7, 153
- Gallo L.C., 2006, MNRAS368, 479 \_eprint: astro-ph/0602145
- Gallo L.C., Miniutti G., Miller J.M., et al., 2011, MNRAS411, 607 \_eprint: 1009.2987
- Gallo L.C., Tanaka Y., Boller T., et al., 2004, MNRAS353, 1064 \_eprint: astro-ph/0405159
- Galloway D.K., Goodwin A.J., Keek L., 2017, PASA34, e019 \_eprint: 1703.07485
- Gangui A., Casazza R., Paez C., 2014, The Physics Teacher 52, 403
- García J., Dauser T., Lohfink A., et al., 2014, ApJ782, 76 \_eprint: 1312.3231
- García J., Dauser T., Reynolds C.S., et al., 2013, ApJ768, 146 \_eprint: 1303.2112
- García J., Kallman T.R., 2010, ApJ718, 695 \_eprint: 1006.0485
- García J.A., Dauser T., Steiner J.F., et al., 2015, ApJ808, L37 \_eprint: 1505.03616
- Gariel J., MacCallum M.A.H., Marcilhacy G., Santos N.O., 2010, A&A515, A15
- Garmire G.P., Bautz M.W., Ford P.G., et al., 2003, In: Truemper J.E., Tananbaum H.D. (eds.) X-Ray and Gamma-Ray Telescopes and Instruments for Astronomy., Vol. 4851. Society of Photo-Optical Instrumentation Engineers (SPIE) Conference Series, p.28
- Gatuzz E., García J., Kallman T.R., et al., 2015, ApJ800, 29 \_eprint: 1412.3813
- Gebhard R., Krause R., 2010, In: Bernstorf. Archäologisch- naturwissenschaftliche Analysen der Gold- und Bernsteinfunde vom Bernstorfer Berg bei Kranzberg, Oberbayern., Landesamt für Denkmalpflege und Archäologie Sachsen-Anhalt
- Gehrels N., Chincarini G., Giommi P., et al., 2004, ApJ611, 1005 \_eprint: astro-ph/0405233
- Geisler J.G., 1807, Technische Geschichte des reflektierenden oder Spiegel-Teleskops nebst vollständiger Beschreibung desselben sowohl als aller derjenigen Instrumente, welche sich auf Reflexion gründen, und der Art ihrer Aufstellung, Walther, Dresden
- Gendreau K., Arzoumanian Z., 2017, Nature Astronomy 1, 895
- Gendreau K.C., Arzoumanian Z., Adkins P.W., et al., 2016, In: den Herder J.W.A., Takahashi T., Bautz M. (eds.) Space Telescopes and Instrumentation 2016: Ultraviolet to Gamma Ray, Vol. 9905. Society of Photo-Optical Instrumentation Engineers (SPIE) Conference Series, p. 99051H
- General Notes 1906, Popular Astronomy 14, 638
- Genty D., Konik S., Valladas H., et al., 2011, Radiocarbon 53, 479 Publisher: Cambridge University Press
- George I.M., Fabian A.C., 1991, MNRAS249, 352
- Gertoux G., 2013, arXiv e-prints arXiv:1309.2758 \_eprint: 1309.2758
- Gezari S., 2021, arXiv e-prints arXiv:2104.14580 \_eprint: 2104.14580
- Gezari S., Hung T., Cenko S.B., et al., 2017, ApJ835, 144 \_eprint: 1612.04830

- Giacconi R., Branduardi G., Briel U., et al., 1979, ApJ230, 540
- Giacconi R., Gursky H., Kellogg E., et al., 1971, ApJ167, L67
- Giacconi R., Gursky H., Paolini F.R., Rossi B.B., 1962, Phys. Rev. Lett.9, 439
- Giacconi R., Murray S., Gursky H., et al., 1974, ApJS27, 37
- Giacconi R., Murray S., Gursky H., et al., 1972, ApJ178, 281
- Gibson B.K., Loewenstein M., Mushotzky R.F., 1997, MNRAS290, 623 [\\_eprint: astro-ph/9706138](#)
- Gil S., 2018, Public Understanding of Science 27, 745
- Gilfanov M., Syunyaev R., Churazov E., et al., 1991, Soviet Astronomy Letters 17, 437
- Gingerich O., 2011, In: Valls-Gabaud D., Boksenberg A. (eds.) The Role of Astronomy in Society and Culture, Vol. 260., p.172
- Ginzburg V.L., 1987, Soviet Physics Uspekhi 30, 46
- Gokus A., Rau A., Wilms J., et al., 2020, The Astronomer's Telegram 13657, 1
- Gondoin P., Aschenbach B., Erd C., et al., 2000, In: Flanagan K.A., Siegmund O.H. (eds.) X-Ray and Gamma-Ray Instrumentation for Astronomy XI, Vol. 4140. Society of Photo-Optical Instrumentation Engineers (SPIE) Conference Series, p.1
- Gondoin P., Aschenbach B.R., Beijersbergen M.W., et al., 1998a, In: Hoover R.B., Walker A.B. (eds.) X-Ray Optics, Instruments, and Missions, Vol. 3444. Society of Photo-Optical Instrumentation Engineers (SPIE) Conference Series, p.278
- Gondoin P., Aschenbach B.R., Beijersbergen M.W., et al., 1998b, In: Hoover R.B., Walker A.B. (eds.) X-Ray Optics, Instruments, and Missions, Vol. 3444. Society of Photo-Optical Instrumentation Engineers (SPIE) Conference Series, p.290
- Grevesse N., Anders E., 1989, In: Waddington C.J. (ed.) Cosmic Abundances of Matter, Vol. 183. American Institute of Physics Conference Series, p.1
- Grevesse N., Noels A., Sauval A.J., 1996, In: Holt S.S., Sonneborn G. (eds.) Cosmic Abundances, Vol. 99. Astronomical Society of the Pacific Conference Series, p. 117
- Grindlay J., Gursky H., Schnopper H., et al., 1976, ApJ205, L127
- Grindlay J.E., Gursky H., 1977, ApJ218, L117
- Grotova I., Rau A., Knies J., et al., 2020, The Astronomer's Telegram 14046, 1
- Groves B.A., Dopita M.A., Sutherland R.S., 2004a, ApJS153, 9 [\\_eprint: astro-ph/0404175](#)
- Groves B.A., Dopita M.A., Sutherland R.S., 2004b, ApJS153, 75 [\\_eprint: astro-ph/0404176](#)
- Gruber D.E., Blanco P.R., Heindl W.A., et al., 1996, A&AS120, 641
- Guainazzi M., Mihara T., Otani C., Matsuoka M., 1996, PASJ48, 781 [\\_eprint: astro-ph/9610180](#)
- Gursky H., Bradt H., Doxsey R., et al., 1978, ApJ223, 973
- Gursky H., Kellogg E.M., Leong C., et al., 1971a, ApJ165, L43
- Gursky H., Kellogg E.M., Leong C., et al., 1971b, In: Bulletin of the American Astronomical Society, Vol. 3., p. 236
- Gursky H., Schnopper H., Parsignault D., 1975, ApJ201, L127
- Grzadyan V.G., 2000, S&T100, 40 [\\_eprint: physics/0311114](#)
- Grzadyan V.G., 2003, arXiv:physics/0311036 [arXiv: physics/0311036](#)
- Güdel M., 2004, A&A Rev.12, 71 [\\_eprint: astro-ph/0406661](#)
- Güdel M., Nazé Y., 2009, A&A Rev.17, 309 [\\_eprint: 0904.3078](#)
- Haardt F., 1993, ApJ413, 680
- Haberl F., Motch C., Buckley D.A.H., et al., 1997, A&A326, 662
- Haberl F., Motch C., Pietsch W., 1998, Astronomische Nachrichten 319, 97
- Haberl F., Pietsch W., Motch C., 1999, A&A351, L53 [\\_eprint: astro-ph/9911159](#)
- Haberl F., Wilms J., Gokus A., et al., 2020, The Astronomer's Telegram 13828, 1
- Hagino K., Odaka H., Done C., et al., 2016, MNRAS461, 3954 [\\_eprint: 1509.05645](#)
- Hahn J., 1982 12
- Haiman Z., Menou K., 2000, ApJ531, 42 [\\_eprint: astro-ph/9810426](#)
- Hain T., 2017, *Master's thesis*, FAU Erlangen Nuernberg
- Haisch B., Strong K.T., Rodono M., 1991, ARA&A29, 275
- Hakucho TeamInoue H., Koyama K., et al., 1979a, In: International Cosmic Ray Conference, Vol. 1. International Cosmic Ray Conference, p. 52
- Hakucho TeamInoue H., Koyama K., et al., 1979b, In: International Cosmic Ray Conference, Vol. 1. International Cosmic Ray Conference, p. 55
- Hakucho TeamInoue H., Koyama K., et al., 1979c, In: International Cosmic Ray Conference, Vol. 1. International Cosmic Ray Conference, p. 57
- Hakucho TeamInoue H., Koyama K., et al., 1979d, In: International Cosmic Ray Conference, Vol. 1. International Cosmic Ray Conference, p. 60
- Halley, Edmond 1705, A synopsis of the astronomy of comets, Printed for John Senex
- Hardy R., 1991, Journal of the British Astronomical Association 101, 261
- Harrison F.A., Craig W.W., Christensen F.E., et al., 2013, ApJ770, 103 [\\_eprint: 1301.7307](#)
- Harvey P., Sanders J., Cabral R., et al., 1976, IEEE Transactions on Nuclear Science 23, 487
- Harwit M., 2004, Advances in Space Research 34, 568
- Hawley J.F., Gammie C.F., Balbus S.A., 1996, ApJ464, 690
- Hayes M.J.C., Culhane J.L., Blissett R.J., et al., 1980a, MNRAS193, 15P
- Hayes M.J.C., Culhane J.L., Burnell S.J.B., 1980b,

## References

- MNRAS192, 1P
- Hearn D.R., Richardson J.A., 1977, ApJ213, L115
- Hearn D.R., Richardson J.A., Bradt H.V.D., et al., 1976a, ApJ203, L21
- Hearn D.R., Richardson J.A., Clark G.W., 1976b, ApJ210, L23
- Heath T., 2013, *Aristarchus of Samos, the Ancient Copernicus: A History of Greek Astronomy to Aristarchus, Together with Aristarchus's Treatise on the Sizes and Distances of the Sun and Moon*, Cambridge University Press, Cambridge
- Heckman T.M., 1980, A&A500, 187
- Heise J., Brinkman A.C., den Boggende A.J.F., et al., 1976, Nature261, 562
- Heise J., Brinkman A.C., Schrijver J., et al., 1975, ApJ202, L73
- Henke B.L., Lee P., Tanaka T.J., et al., 1982, Atomic Data and Nuclear Data Tables 27, 1
- Herschel W., Watson D., 1781, Philosophical Transactions of the Royal Society of London Series I 71, 492
- Herten F., Waldmann G., 2018, In: Siegmund F., Scherzler D., Schön W. (eds.) *Archäologische Informationen*, Vol. 41., Deutsche Gesellschaft für Ur- und Frühgeschichte, Mainz, p.275
- Hetherington N.S., Ronan C.A., 1984, Journal of the British Astronomical Association 94, 256
- HI4PI Collaboration Ben Bekhti N., Flöer L., et al., 2016, A&A594, A116 \_eprint: 1610.06175
- Higbie P.R., Chupp E.L., Forrest D.J., Gleske I.U., 1972, IEEE Transactions on Nuclear Science 19, 606
- Hirano T., Hayakawa S., Nagase F., Tawara Y., 1986, Ap&SS119, 77
- Hirschmann M., Dolag K., Saro A., et al., 2014, MNRAS442, 2304 \_eprint: 1308.0333
- Hirschmann M., Naab T., Somerville R.S., et al., 2012a, MNRAS419, 3200 \_eprint: 1104.1626
- Hirschmann M., Somerville R.S., Naab T., Burkert A., 2012b, MNRAS426, 237 \_eprint: 1206.6112
- Ho A.Y.Q., 2020, The Astronomer's Telegram 13485, 1
- Hockey T., Trimble V., Williams T.R., et al., (eds.) 2014, *Biographical Encyclopedia of Astronomers*, Springer New York, New York, NY
- Hoffleit E.D., 2002, Physics in Perspective (PIP) 4, 370
- Hoffman J.A., Lewin W.H.G., Doty J., et al., 1976, ApJ210, L13
- Holmes C.N., 1916, Popular Astronomy 24, 218
- Holt S.S., 1976, Ap&SS42, 123
- Holt S.S., Boldt E.A., Schwartz D.A., et al., 1971, ApJ166, L65
- Holt S.S., Boldt E.A., Serlemitsos P.J., Kaluzienski L.J., 1976a, ApJ205, L143
- Holt S.S., Kaluzienski L.J., Boldt E.A., Serlemitsos P.J., 1976b, Nature261, 213
- Hopkins P.F., Hernquist L., Cox T.J., et al., 2005a, ApJ630, 716 \_eprint: astro-ph/0504252
- Hopkins P.F., Hernquist L., Cox T.J., et al., 2005b, ApJ632, 81 \_eprint: astro-ph/0504253
- Hopkins P.F., Richards G.T., Hernquist L., 2007, ApJ654, 731 \_eprint: astro-ph/0605678
- Houck J.C., Denicola L.A., 2000, In: Manset N., Veillet C., Crabtree D. (eds.) *Astronomical Data Analysis Software and Systems IX*, Vol. 216. Astronomical Society of the Pacific Conference Series, p. 591
- Hubble E., 1929, Proceedings of the National Academy of Science 15, 168
- Hubble E.P., 1925a, The Observatory 48, 139
- Hubble E.P., 1925b, ApJ62, 409
- Hubble E.P., 1926, ApJ64, 321
- Huffman C., 2020, Philolaus. In: Zalta E.N. (ed.) *The Stanford Encyclopedia of Philosophy*. Metaphysics Research Lab, Stanford University, fall 2020 edition
- Hughes D. W. 1987, Philosophical Transactions of the Royal Society of London 349-367
- Hurley K., Atteia J.L., Barraud C., et al., 2009, arXiv e-prints arXiv:0907.2709 \_eprint: 0907.2709
- Hutchings J.B., 2014, Ap&SS354, 143
- Imhausen A., 2010, Ancient Egyptian star tables: A reinterpretation of their fundamental structure. In: Pommerening T. (ed.) *Beiträge zur Altertumskunde*. DE GRUYTER, Berlin, New York
- in 't Zand J.J.M., Amati L., Antonelli L.A., et al., 1998, ApJ505, L119 \_eprint: astro-ph/9807314
- in 't Zand J.J.M., Heise J., van Paradijs J., Fenimore E.E., 1999, ApJ516, L57
- Inoue H., 1991, Advances in Space Research 11, 259
- Inoue H., 1993, Experimental Astronomy 4, 1
- Inoue H., Koyama K., Makishima K., et al., 1979, In: *International Cosmic Ray Conference*, Vol. 1. International Cosmic Ray Conference, p. 5
- Ishibashi W., Courvoisier T.J.L., 2009, åp 504, 61 \_eprint: 0905.4842
- Ives J.C., Sanford P.W., Bell Burnell S.J., 1975, Nature254, 578
- Iwasawa K., Fabian A.C., Matt G., 1997, MNRAS289, 443 \_eprint: astro-ph/9703159
- Iwasawa K., Fabian A.C., Mushotzky R.F., et al., 1996a, MNRAS279, 837
- Iwasawa K., Fabian A.C., Reynolds C.S., et al., 1996b, MNRAS282, 1038 \_eprint: astro-ph/9606103
- Jackson J.D., 2014, *Classical Electrodynamics*, 5. ed., De Gruyter
- Jager R., Mels W.A., Brinkman A.C., et al., 1997, A&AS125, 557
- Jagoda N., Austin G., Mickiewicz S., Goddard R., 1972, IEEE Transactions on Nuclear Science 19, 579
- Jahoda K., Markwardt C.B., Radeva Y., et al., 2006, ApJS163, 401 \_eprint: astro-ph/0511531
- Jahoda K., Swank J.H., Giles A.B., et al., 1996, In: Siegmund O.H.W., Gummin M.A. (eds.) *PROCEEDINGS OF SPIE.*, Denver, CO, p.59
- Jansen F., Lumb D., Altieri B., et al., 2001, A&A365, L1
- Jansky K.G., 1933a, Popular Astronomy 41, 548
- Jansky K.G., 1933b, Nature132, 66
- Jeffery G.B., 1921, Proceedings of the Royal Society of London Series A 99, 123
- Jernigan J.G., Apparao K.M.V., Bradt H.V., et al., 1977,

- Nature270, 321
- Jernigan J.G., Klein R.I., Arons J., 1999, In: AAS/High Energy Astrophysics Division #4, Vol. 4. AAS/High Energy Astrophysics Division, p. 10.03
- Jones D.H., Read M.A., Saunders W., et al., 2009, MNRAS399, 683 \_eprint: 0903.5451
- Jones F.C., 1968, Physical Review 167, 1159
- Joyce R.M., Becker R.H., Birsa F.B., et al., 1978, IEEE Transactions on Nuclear Science 25, 453
- Kaaret P., Feng H., Roberts T.P., 2017, ARA&A55, 303 \_eprint: 1703.10728
- Kaastra J.S., Bleeker J.A.M., 2016, A&A587, A151 \_eprint: 1601.05309
- Kaluziński L.J., Holt S.S., Boldt E.A., Serlemitsos P.J., 1977, Nature265, 606
- Kara E., Fabian A.C., Lohfink A.M., et al., 2015a, MNRAS449, 234 \_eprint: 1501.06849
- Kara E., Zoghbi A., Marinucci A., et al., 2015b, MNRAS446, 737 \_eprint: 1410.3357
- Kaspi S., Netzer H., 1999, ApJ524, 71 \_eprint: astro-ph/9905241
- Kawai N., Yoshida A., Tamagawa T., et al., 2001, In: Paczynski B., Chen W.P., Lemme C. (eds.) IAU Colloq. 183: Small Telescope Astronomy on Global Scales, Vol. 246. Astronomical Society of the Pacific Conference Series, p. 149
- Kelley R.L., Mitsuda K., Allen C.A., et al., 2007, PASJ59, 77
- Kellogg E., Gursky H., Murray S., et al., 1971a, ApJ169, L99
- Kellogg E., Gursky H., Tananbaum H., et al., 1972a, ApJ174, L65
- Kellogg E., Schreier E., Tananbaum H., et al., 1972b, In: Bulletin of the American Astronomical Society, Vol. 4., p. 336
- Kellogg E., Tananbaum H., Gursky H., et al., 1972c, In: Bulletin of the American Astronomical Society, Vol. 4., p. 260
- Kellogg E.M., Gursky H., Leong C., et al., 1971b, In: Bulletin of the American Astronomical Society, Vol. 3., p. 236
- Kemp J.C., Herman L.C., Barbour M.S., 1978, AJ83, 962
- Kenter A.T., Chappell J.H., Kraft R.P., et al., 2000, In: Truemper J.E., Aschenbach B. (eds.) X-Ray Optics, Instruments, and Missions III, Vol. 4012. Society of Photo-Optical Instrumentation Engineers (SPIE) Conference Series, p.467
- Kerr R.P., 1963, Phys. Rev. Lett.11, 237
- Kestenbaum H.L., Cohen G.G., Long K.S., et al., 1976, ApJ210, 805
- Khabibullin I., Sazonov S., Sunyaev R., 2012, MNRAS426, 1819 \_eprint: 1206.6801
- Kirk T.H., 2000, The Observatory 120, 308
- Kitamoto S., Tsunemi H., Miyamoto S., et al., 1989, Nature342, 518
- Klebesadel R.W., Strong I.B., Olson R.A., 1973, ApJ182, L85
- Klein O., Nishina T., 1929, Zeitschrift fur Physik 52, 853
- Knies J., 2021, PhD Thesis, Dr. Karl Remeis-Sternwarte, Astronomical Institute of the FAU
- Knoll G.F., 2000, Radiation detection and measurement, John Wiley & Sons, Inc.
- Koenig O., Rau A., Haberl F., et al., 2020a, The Astronomer's Telegram 14057, 1
- Koenig O., Wilms J., Kreykenbohm I., et al., 2020b, The Astronomer's Telegram 13765, 1
- Koester D., Chanmugam G., 1990, Reports on Progress in Physics 53, 837
- Kohmura Y., Fukazawa Y., Ikebe Y., et al., 1993, In: Siegmund O.H. (ed.) EUV, X-Ray, and Gamma-Ray Instrumentation for Astronomy IV, Vol. 2006. Society of Photo-Optical Instrumentation Engineers (SPIE) Conference Series, p.78
- Komossa S., Bade N., 1999, åp 343, 775 \_eprint: astro-ph/9901141
- Komossa S., Greiner J., 1999, åp 349, L45 \_eprint: astro-ph/9908216
- Komossa S., Halpern J., Schartel N., et al., 2004, ApJ603, L17 \_eprint: astro-ph/0402468
- Kompaneets A.S., 1957, Soviet Journal of Experimental and Theoretical Physics 4, 730
- Konar S., 2017, Journal of Astrophysics and Astronomy 38, 47 \_eprint: 1709.07106
- Kormendy J., Gebhardt K., 2001, In: Wheeler J.C., Martel H. (eds.) 20th Texas Symposium on relativistic astrophysics, Vol. 586. American Institute of Physics Conference Series, p.363 \_eprint: astro-ph/0105230
- Kosec P., Buisson D.J.K., Parker M.L., et al., 2018, MNRAS481, 947 \_eprint: 1808.08204
- Koyama K., Hyodo Y., Inui T., et al., 2007a, PASJ59, 245 \_eprint: astro-ph/0609215
- Koyama K., Inoue H., Makishima K., et al., 1981, ApJ247, L27
- Koyama K., Petre R., Gotthelf E.V., et al., 1995, Nature378, 255
- Koyama K., Tsunemi H., Dotani T., et al., 2007b, PASJ59, 23
- Kraft R.P., Chappell J.H., Kenter A.T., et al., 2000, In: Truemper J.E., Aschenbach B. (eds.) X-Ray Optics, Instruments, and Missions III, Vol. 4012. Society of Photo-Optical Instrumentation Engineers (SPIE) Conference Series, p.493
- Kretschmar P., Fürst F., Sidoli L., et al., 2019, New A Rev.86, 101546 \_eprint: 2009.03244
- Kubota A., Tanaka Y., Makishima K., et al., 1998, PASJ50, 667
- Kuijt I., Goring-Morris N., 2002, Journal of World Prehistory 16, 361
- Kuiper G.P., Johnson J.R., 1956, ApJ123, 90
- Kulkarni G., Worseck G., Hennawi J.F., 2019, MNRAS488, 1035 \_eprint: 1807.09774
- Kumar P., Zhang B., 2015, Phys. Rep.561, 1 \_eprint: 1410.0679
- Kumitzsch 1987 42–43
- Kuulkers E., Antonelli L.A., Kuiper L., et al., 2000, ApJ538, 638 \_eprint: astro-ph/0003258

## References

- Laha S., Markowitz A.G., Krumpke M., et al., 2020, ApJ897, 66 \_eprint: 2005.06079
- LaMassa S.M., Cales S., Moran E.C., et al., 2015, ApJ800, 144 \_eprint: 1412.2136
- Lamers H.J.G.L.M., Cassinelli J.P., 1999, Introduction to Stellar Winds, Cambridge University Press
- Langley D., Coutu, Ronald A. J., Starman L.A., Rogers S., 2009, In: Rogers S., Casasent D.P., Dolne J.J., Karr T.J., Gamiz V.L. (eds.) Adaptive Coded Aperture Imaging, Non-Imaging, and Unconventional Imaging Sensor Systems, Vol. 7468. Society of Photo-Optical Instrumentation Engineers (SPIE) Conference Series, p. 74680H
- Laor A., 1991, ApJ376, 90
- Laplace P.S., 1796, Exposition du système du monde, l'Imprimerie du CERCLE-SOCIAL
- Laplace P.S., 1799, Allgemeine Geographische Ephemeriden 4, 1
- Lasker B.M., Sturch C.R., McLean B.J., et al., 1990, AJ99, 2019
- Leavitt H.S., Pickering E.C., 1912, Harvard College Observatory Circular 173, 1
- Leighly K.M., 1999, ApJS125, 317 \_eprint: astro-ph/9907295
- Leighly K.M., Mushotzky R.F., Nandra K., Forster K., 1997, ApJ489, L25 \_eprint: astro-ph/9708112
- Lense J., Thirring H., 1918, Physikalische Zeitschrift 19, 156
- Levine A.M., Bradt H., Cui W., et al., 1996, ApJ469, L33 \_eprint: astro-ph/9608109
- Levine A.M., Lang F.L., Lewin W.H.G., et al., 1984, ApJS54, 581
- Lewin W.H.G., Doty J., Clark G.W., et al., 1976a, ApJ207, L95
- Lewin W.H.G., Hoffman J.A., Doty J., et al., 1976b, MNRAS177, 83P
- Li F.K., Lewin W.H.G., Clark G.W., et al., 1977, MNRAS179, 21P
- Li X., Song L., Li X., et al., 2019, arXiv e-prints arXiv:1910.04390 \_eprint: 1910.04390
- Lickleder S., 2019, *Master's thesis*, FAU Erlangen Nuernberg
- Lightman A.P., White T.R., 1988, ApJ335, 57
- Lincke E.S., 2011, Die Prinzipien der Klassifizierung im Altägyptischen, Göttinger Orientforschungen. IV. Reihe, Ägypten 38, Harrassowitz Verlag, Wiesbaden OCLC: ocn422767621
- Liran, Roy 2011, Antiquity 85
- Liu Z., Merloni A., Georgakakis A., et al., 2016, MNRAS459, 1602 \_eprint: 1605.00207
- Loewenstein M., Mushotzky R.F., 1996, ApJ466, 695
- Long K.S., Helfand D.J., 1979, ApJ234, L77
- Longair M.S., 1994, High energy astrophysics, Vol. 2, Cambridge University Press
- Loznikov V.M., Iamburenko N.S., 1982, Soviet Astronomy Letters 8, 255
- Lu P., 2015, history of science in south asia 22
- Lum K.S.K., Canizares C.R., Clark G.W., et al., 1992, ApJS78, 423
- Lund N., Budtz-Jørgensen C., Westergaard N.J., et al., 2003, åp 411, L231
- Lynden-Bell D., 1969, Nature223, 690
- Lynn W.T., 1891, The Observatory 14, 285
- Léna P., Lebrun F., Mignard F., 1998, Observational astrophysics., Springer
- MacLeod C.L., Ross N.P., Lawrence A., et al., 2016, MNRAS457, 389 \_eprint: 1509.08393
- MacPherson H., 1916, Popular Astronomy 24, 358
- Mahmood A., Devriendt J.E.G., Silk J., 2005, MNRAS359, 1363 \_eprint: astro-ph/0401003
- Mahoney W.A., Ling J.C., Jacobson A.S., Tapphorn R.M., 1980, Nuclear Instruments and Methods 178, 363
- Mainzer A., Grav T., Bauer J., et al., 2011, ApJ743, 156 \_eprint: 1109.6400
- Makishima K., Maejima Y., Mitsuda K., et al., 1986, ApJ308, 635
- Makishima K., Mihara T., Ishida M., et al., 1990, ApJ365, L59
- Makishima K., Mitsuda K., Inoue H., et al., 1983, ApJ267, 310
- Manzo G., Giarrusso S., Santangelo A., et al., 1997, A&AS122, 341
- Maraschi L., Maccagni D., 1988, Mem. Soc. Astron. Italiana59, 277
- Marinucci A., Matt G., Kara E., et al., 2014, MNRAS440, 2347 \_eprint: 1402.7245
- Markert T.H., Winkler P.F., Laird F.N., et al., 1979, ApJS39, 573
- Markowitz A.G., Krumpke M., Nikutta R., 2014, MNRAS439, 1403 \_eprint: 1402.2779
- Markwardt C.B., 2004, Nuclear Physics B Proceedings Supplements 132, 689
- Marshall F.J., Clark G.W., 1984, ApJ287, 633
- Marshall H.L., Ulmer M.P., Hoffman J.A., et al., 1979, ApJ227, 555
- Martocchia A., Matt G., 1996, MNRAS282, L53
- Mas-Hesse J.M., Giménez A., Culhane J.L., et al., 2003, åp 411, L261
- Mason K.O., Breeveld A., Much R., et al., 2001, A&A365, L36 \_eprint: astro-ph/0011216
- Massaro E., Giommi P., Leto C., et al., 2009, A&A495, 691 \_eprint: 0810.2206
- Matilsky T.A., Giacconi R., Gursky H., et al., 1972, ApJ174, L53
- Matsuoka M., Ikegami T., Inoue H., Koyama K., 1986a, PASJ38, 285
- Matsuoka M., Inoue H., Koyama K., et al., 1980, ApJ240, L137
- Matsuoka M., Kawasaki K., Ueno S., et al., 2009, PASJ61, 999 \_eprint: 0906.0631
- Matsuoka M., Takano S., Makishima K., 1986b, MNRAS222, 605
- Matt G., Guainazzi M., Maiolino R., 2003, MNRAS342, 422 \_eprint: astro-ph/0302328
- Matteson, J. L. 1978, In: Aerospace Sciences Meeting.,

- Huntsville, p. 9 Publication Title: AIAA, Aerospace Sciences Meeting
- Maughan B.J., Reiprich T.H., 2019, *The Open Journal of Astrophysics* 2, 9 \_eprint: 1811.05786
- Mayall N.U., 1939, *Leaflet of the Astronomical Society of the Pacific* 3, 145
- Mayer W.F., 1975, *Johns Hopkins APL Technical Digest* 14, 14
- Mazengo D.T., Pović M., Jiwaji N.T., Sunzu J.M., 2021, *IAU Symposium* 356, 323
- McClintock J.E., 1975, In: *X-Rays in Space - Cosmic, Solar, and Auroral X-Rays, Volume 1, Vol. 1.*, p.172
- McElroy R.E., Husemann B., Croom S.M., et al., 2016, *ApJ* 819, L8 \_eprint: 1609.04423
- McHardy I., 1988, *Mem. Soc. Astron. Italiana* 59, 239
- McHardy I.M., Koerding E., Knigge C., et al., 2006, *Nature* 444, 730 \_eprint: astro-ph/0612273
- McHardy I.M., Lawrence A., Pye J.P., Pounds K.A., 1981, *MNRAS* 197, 893
- McMahon R.G., Banerji M., Gonzalez E., et al., 2013, *The Messenger* 154, 35
- Meegan C., Lichti G., Bhat P.N., et al., 2009, *ApJ* 702, 791 \_eprint: 0908.0450
- Meekins J.F., Fritz G., Chubb T.A., Friedman H., 1971, *Nature* 231, 107
- Meekins J.F., Wood K.S., Hedler R.L., et al., 1984, *ApJ* 278, 288
- Meidinger N., Andritschke R., Aschauer F., et al., 2012, In: *Holland A.D., Beletic J.W. (eds.) High Energy, Optical, and Infrared Detectors for Astronomy V, Vol. 8453. Society of Photo-Optical Instrumentation Engineers (SPIE) Conference Series*, p. 84530P
- Meidinger N., Andritschke R., Bornemann W., et al., 2014, In: *Takahashi T., den Herder J.W.A., Bautz M. (eds.) Space Telescopes and Instrumentation 2014: Ultraviolet to Gamma Ray, Vol. 9144. Society of Photo-Optical Instrumentation Engineers (SPIE) Conference Series*, p. 91441W
- Meidinger N., Andritschke R., Ebermayer S., et al., 2010, *Nuclear Instruments and Methods in Physics Research A* 624, 321
- Meidinger N., Andritschke R., Elbs J., et al., 2011, In: *Society of Photo-Optical Instrumentation Engineers (SPIE) Conference Series, Vol. 8145. Society of Photo-Optical Instrumentation Engineers (SPIE) Conference Series*, p. 814502
- Meier D.L., 2012, *Black Hole Astrophysics: The Engine Paradigm*, Springer
- Mendez M., 2003, In: *Truemper J.E., Tananbaum H.D. (eds.) X-Ray and Gamma-Ray Telescopes and Instruments for Astronomy, Vol. 4851. Society of Photo-Optical Instrumentation Engineers (SPIE) Conference Series*, p.57
- Menghin W., 2000, *Acta praehistorica et archaeologica* 32, 31
- Merloni A., Predehl P., Becker W., et al., 2012, arXiv e-prints arXiv:1209.3114 \_eprint: 1209.3114
- Messier, Charles 1771, *Académie royale des sciences* 435–461
- Messier, Charles 1783, *Bureau des Longitudes* 225–251
- Messier, Charles 1784, *Bureau des Longitudes* 227–267
- Mewe R., Heise J., Gronenschild E.H.B.M., et al., 1975a, *ApJ* 202, L67
- Mewe R., Heise J., Gronenschild E.H.B.M., et al., 1975b, *Nature* 256, 711
- Mewe R., Heise J., Gronenschild E.H.B.M., et al., 1976, *Ap&SS* 42, 217
- Mewe R., Kaastra J.S., White S.M., Pallavicini R., 1996, *A&A* 315, 170
- Meyer D.M., Cardelli J.A., Sofia U.J., 1997, *ApJ* 490, L103 \_eprint: astro-ph/9710162
- Meyer D.M., Jura M., Cardelli J.A., 1998, *ApJ* 493, 222 \_eprint: astro-ph/9710163
- Micallef C., 2001 9
- Michell J., 1784, *Philosophical Transactions of the Royal Society of London Series I* 74, 35
- Michelson A.A., 1879, *American Journal of Science* 18, 390
- Mihara T., Makishima K., Kamijo S., et al., 1991, *ApJ* 379, L61
- Mihara T., Nakajima M., Sugizaki M., et al., 2011, *PASJ* 63, S623 \_eprint: 1103.4224
- Miller J.M., 2007, *ARA&A* 45, 441 \_eprint: 0705.0540
- Miller L., Turner T.J., Reeves J.N., Braitto V., 2010, *MNRAS* 408, 1928 \_eprint: 1006.5035
- Miniutti G., Fabian A.C., Anabuki N., et al., 2007, *PASJ* 59, 315 \_eprint: astro-ph/0609521
- Mitchell R.J., Culhane J.L., 1977, *MNRAS* 178, 75P
- Mitsuda K., Bautz M., Inoue H., et al., 2007, *PASJ* 59, S1
- Mitsuda K., Inoue H., Koyama K., et al., 1984, *PASJ* 36, 741
- Mizumoto M., Ebisawa K., Sameshima H., 2014, *PASJ* 66, 122 \_eprint: 1409.3019
- Mizumoto M., Ebisawa K., Tsujimoto M., et al., 2019, *MNRAS* 482, 5316 \_eprint: 1808.06625
- Molteni D., Rapisarda M., Robba N.R., Scarsi L., 1980, *A&A* 87, 88
- Morrison R., McCammon D., 1983, *ApJ* 270, 119
- Mortlock D.J., Warren S.J., Venemans B.P., et al., 2011, *Nature* 474, 616 \_eprint: 1106.6088
- Morton D.C., 1964, *ApJ* 140, 460
- Mossoux E., Finocciety B., Beckers J.M., Vincent F.H., 2020, *ApJ* 900, 636, A25 \_eprint: 2003.06191
- Motch C., Haberl F., Zickgraf F.J., et al., 1999, *A&A* 351, 177 \_eprint: astro-ph/9907306
- Mukai K., 2017, *PASP* 129, 062001 \_eprint: 1703.06171
- Murakami T., Fujii M., Hayashida K., et al., 1989, *PASJ* 41, 405
- Murdin P., 2000, *Lipperhey [Lippershey], Hans [Jan] (1570?-1619)*. In: *Encyclopedia of Astronomy and Astrophysics*. Nature Publishing Group, p. 3816
- Murray S.S., Fabbiano G., Fabian A.C., et al., 1979, *ApJ* 234, L69
- Mushotzky R., Loewenstein M., Arnaud K.A., et al., 1996, *ApJ* 466, 686

## References

- Mushotzky R.F., 1984, *Advances in Space Research* 3, 157
- Nakagawa Y.E., Hete-2 Collaboration 2009, In: Giovannelli F., Mannocchi G. (eds.) *Frontier Objects in Astrophysics and Particle Physics.*, p. 315
- Nandra K., George I.M., Mushotzky R.F., et al., 1997a, *ApJ*476, 70
- Nandra K., George I.M., Mushotzky R.F., et al., 1997b, *ApJ*477, 602 \_eprint: astro-ph/9606169
- Nandra K., George I.M., Mushotzky R.F., et al., 1997c, *ApJ*488, L91 \_eprint: astro-ph/9708030
- Nandra K., George I.M., Turner T.J., Fukazawa Y., 1996, *ApJ*464, 165
- Nandra K., Mushotzky R.F., Yaqoob T., et al., 1997d, *MNRAS*284, L7 \_eprint: astro-ph/9608171
- Nash D.J., Ciborowski T.J.R., Ulyott J.S., et al., 2020, *Science Advances* 6, eabc0133
- Netzer H., 1990, *Active Galactic Nuclei*. In: R. D. Blandford, H. Netzer, L. Woltjer, T. J.-L. Courvoisier, M. Mayor (eds.) *AGN Emission Lines*. Springer-Verlag Berlin Heidelberg, 1 edition, p.57 Section: 2
- Netzer H., 2008, *New A Rev.*52, 257
- Netzer H., 2015, *ARA&A*53, 365 \_eprint: 1505.00811
- Newman E.T., Couch E., Chinnapared K., et al., 1965, *Journal of Mathematical Physics* 6, 918
- Newman E.T., Janis A.I., 1965, *Journal of Mathematical Physics* 6, 915
- Nicastro L., Amati L., Antonelli L.A., et al., 1999, *A&AS*138, 437 \_eprint: astro-ph/9904169
- Nordström G., 1918, *Koninklijke Nederlandse Akademie van Wetenschappen Proceedings Series B Physical Sciences* 20, 1238
- Novikov I.D., Thorne K.S., 1973, In: *Black Holes (Les Astres Occlus)*, p.343
- Nugent J.J., Jensen K.A., Nousek J.A., et al., 1983, *ApJS*51, 1
- Oda M., Gorenstein P., Gursky H., et al., 1971, *ApJ*166, L1
- of Rosse E., 1968, *Hermathena* 5–13
- Ohashi T., Inoue H., Koyama K., et al., 1984, *PASJ*36, 699
- Ohashi T., Makishima K., Ishida M., et al., 1991, In: Siegmund O.H., Rothschild R.E. (eds.) *EUV, X-Ray, and Gamma-Ray Instrumentation for Astronomy II*, Vol. 1549. Society of Photo-Optical Instrumentation Engineers (SPIE) Conference Series, p.9
- Oppenheimer J.R., Volkoff G.M., 1939, *Physical Review* 55, 374
- Osterbrock D.E., 1977, *ApJ*215, 733
- Osterbrock D.E., 1981, *ApJ*249, 462
- Osterbrock D.E., Pogge R.W., 1985, *ApJ*297, 166
- Owens A.J., 1977, *Nature*266, 749
- Padovani P., Alexander D.M., Assef R.J., et al., 2017, *A&A Rev.*25, 2 \_eprint: 1707.07134
- Paerels F., 2010, *fr* 157, 15
- Pan H.W., Yuan W., Yao S., et al., 2016, *ApJ*819, L19 \_eprint: 1601.07639
- Park S., Burrows D.N., Garmire G.P., et al., 2007, In: Immler S., Weiler K., McCray R. (eds.) *Supernova 1987A: 20 Years After: Supernovae and Gamma-Ray Bursters*, Vol. 937. American Institute of Physics Conference Series, p.43 \_eprint: 0704.0209
- Parker M.L., Pinto C., Fabian A.C., et al., 2017, *Nature*543, 83 \_eprint: 1703.00071
- Parker M.L., Wilkins D.R., Fabian A.C., et al., 2014, *MNRAS*443, 1723 \_eprint: 1407.8223
- Parmar A.N., Martin D.D.E., Bavdaz M., et al., 1997, *A&AS*122, 309
- Particle Data GroupZyla P.A., Barnett R.M., et al., 2020, *Progress of Theoretical and Experimental Physics* 2020, 083C01
- Patrick A.R., Reeves J.N., Porquet D., et al., 2012, *MNRAS*426, 2522 \_eprint: 1208.1150
- Pavlinsky M., Tkachenko A., Levin V., et al., 2021, *A&A*650, A42 \_eprint: 2103.12479
- Pawar P.K., Dewangan G.C., Papadakis I.E., et al., 2017, *MNRAS*472, 2823 \_eprint: 1708.08664
- Pawar P.K., Dewangan G.C., Patil M.K., et al., 2016, *Research in Astronomy and Astrophysics* 16, 169 \_eprint: 1607.02635
- Peacock A., Andresen R.D., Manzo G., et al., 1981, *fr* 30, 525
- Pence W.D., Chiappetti L., Page C.G., et al., 2010, *ap* 524, A42
- Penrose R., 1969, *Nuovo Cimento Rivista Serie* 1, 252
- Pernicka E., Adam J., Borg G., et al., 2020, *Archaeologia Austriaca Band* 104/2020, 89
- Pfeffermann E., Briel U., 1982, *Advances in Space Research* 2, 255
- Pfeffermann E., Briel U.G., Hippmann H., et al., 1986, In: *Society of Photo-Optical Instrumentation Engineers (SPIE) Conference Series*, Vol. 733. Society of Photo-Optical Instrumentation Engineers (SPIE) Conference Series, p.519
- Pickering E.C., 1890, *Annals of Harvard College Observatory* 27, 1
- Piconcelli E., Fiore F., Nicastro F., et al., 2007, *ap* 473, 85 \_eprint: 0707.2465
- Pomraning G.C., 1972, *J. Quant. Spec. Radiat. Transf.*12, 1047
- Ponti G., Gallo L.C., Fabian A.C., et al., 2010, *MNRAS*406, 2591 \_eprint: 0911.1003
- Pounds K.A., 1986, *QJRAS*27, 435
- Pounds K.A., Nandra K., Stewart G.C., Leighly K., 1989, *MNRAS*240, 769
- Pounds K.A., Turner T.J., 1988, *Mem. Soc. Astron. Italiana*59, 261
- Pozdnyakov L.A., Sobol I.M., Syunyaev R.A., 1983, *Astrophys. Space Phys. Res.*2, 189
- Predehl P., Andritschke R., Arefiev V., et al., 2021, *A&A*647, A1 \_eprint: 2010.03477
- Predehl P., Sunyaev R.A., Becker W., et al., 2020, *Nature*588, 227 \_eprint: 2012.05840
- Priedhorsky W.C., Terrell J., Holt S.S., 1983, *ApJ*270, 233
- Pringle J.E., 1981, *ARA&A*19, 137

- Pringle J.E., 1989, *Monthly Notices of the Royal Astronomical Society* 239, 361
- Pringle J.E., Rees M.J., Pacholczyk A.G., 1973, *A&A* 29, 179
- Pye J., 1984, In: Brinkmann W., Truemper J. (eds.) *X-ray and UV Emission from Active Galactic Nuclei.*, p.261
- Pye J.P., Rosen S., Fyfe D., Schröder A.C., 2015, *ap* 581, A28 [\\_eprint: 1506.05289](#)
- Ramadevi M.C., Seetha S., Bhattacharya D., et al., 2017, *Experimental Astronomy* 44, 11
- Ramaty R., Leiter D., Lingenfelter R.E., 1981, *Annals of the New York Academy of Sciences* 375, 338
- Rappenglück M., 1997, In: *Astronomy and Culture.*, p.217
- Rappenglück M., 2003, *Uppsala Astronomical Observatory Reports* 59, 51
- Rappenglück M.A., 2001, *Earth Moon and Planets* 85, 391
- Rau A., Maitra C., Ducci L., et al., 2020, *The Astronomer's Telegram* 13844, 1
- Rau A., Nandra K., Aird J., et al., 2016, In: den Herder J.W.A., Takahashi T., Bautz M. (eds.) *Space Telescopes and Instrumentation 2016: Ultraviolet to Gamma Ray*, Vol. 9905. Society of Photo-Optical Instrumentation Engineers (SPIE) Conference Series, p. 99052B [\\_eprint: 1607.00878](#)
- Rector T.A., Stocke J.T., Perlman E.S., et al., 2000, *AJ* 120, 1626 [\\_eprint: astro-ph/0006215](#)
- Reeves J., Done C., Pounds K., et al., 2008, *MNRAS* 385, L108 [\\_eprint: 0801.1587](#)
- Reeves J.N., Braito V., Nardini E., et al., 2018, *ApJ* 867, 38 [\\_eprint: 1809.07164](#)
- Reeves J.N., Fabian A.C., Kataoka J., et al., 2006, *Astronomische Nachrichten* 327, 1079 [\\_eprint: astro-ph/0610436](#)
- Reid P.B., Becker R.H., Long K.S., 1982, *ApJ* 261, 485
- Reig P., 2011, *Astrophysics and Space Science* 332, 1
- Reissner H., 1916, *Annalen der Physik* 355, 106
- Reynolds S.P., 1996, *ApJ* 459, L13
- Rezzolla L., Most E.R., Weih L.R., 2018, *ApJ* 852, L25 [\\_eprint: 1711.00314](#)
- Ricci C., Bauer F.E., Arevalo P., et al., 2016, *ApJ* 820, 5 [\\_eprint: 1602.00702](#)
- Richter P.H., 1997, *Sterne und Weltraum* 640–644
- Ricker G.R., Clarke G.W., Doxsey R.E., et al., 1978, *Nature* 271, 35
- Ridderstad M., 2009, *arXiv e-prints* [arXiv:0910.0560](#) [\\_eprint: 0910.0560](#)
- Risaliti G., Miniutti G., Elvis M., et al., 2009, *ApJ* 696, 160 [\\_eprint: 0901.4809](#)
- Robberto M., Sivaramakrishnan A., Bacinski J.J., et al., 2000, In: Breckinridge J.B., Jakobsen P. (eds.) *UV, Optical, and IR Space Telescopes and Instruments*, Vol. 4013. Society of Photo-Optical Instrumentation Engineers (SPIE) Conference Series, p.386
- Robertson D.R.S., Gallo L.C., Zoghbi A., Fabian A.C., 2015, *MNRAS* 453, 3455 [\\_eprint: 1507.05201](#)
- Romero G.E., Boettcher M., Markoff S., Tavecchio F., 2017, *fr* 207, 5 [\\_eprint: 1611.09507](#)
- Roming P.W.A., Kennedy T.E., Mason K.O., et al., 2005, *Space Sci. Rev.* 120, 95 [\\_eprint: astro-ph/0507413](#)
- Roques J.P., Paul J., Mandrou P., Lebrun F., 1990, *Advances in Space Research* 10, 223
- Rosas-Guevara Y., Bower R.G., Schaye J., et al., 2016, *MNRAS* 462, 190 [\\_eprint: 1604.00020](#)
- Rosenberg F.D., Eyles C.J., Skinner G.K., Willmore A.P., 1975, *Nature* 256, 628
- Ross N.P., McGreer I.D., White M., et al., 2013, *ApJ* 773, 14 [\\_eprint: 1210.6389](#)
- Ross R.R., Fabian A.C., 1993, *MNRAS* 261, 74
- Ross R.R., Fabian A.C., 2005, *MNRAS* 358, 211 [\\_eprint: astro-ph/0501116](#)
- Ross R.R., Fabian A.C., Young A.J., 1999, *MNRAS* 306, 461 [\\_eprint: astro-ph/9902325](#)
- Rothschild R., Boldt E., Holt S., et al., 1979, *Space Science Instrumentation* 4, 269
- Rothschild R.E., Blanco P.R., Gruber D.E., et al., 1998, *ApJ* 496, 538 [\\_eprint: astro-ph/9710328](#)
- Rothschild R.E., Mushotzky F.R., Baity W.A., et al., 1983, *ApJ* 269, 423
- Ruan J.J., Anderson S.F., Cales S.L., et al., 2016, *ApJ* 826, 188 [\\_eprint: 1509.03634](#)
- Runnoe J.C., Cales S., Ruan J.J., et al., 2016, *MNRAS* 455, 1691 [\\_eprint: 1509.03640](#)
- Rupert Hall A., Simpson A.D.C., 1996, *Notes and Records: the Royal Society Journal of the History of Science* 11
- Russell H.N., 1914a, *Popular Astronomy* 22, 331
- Russell H.N., 1914b, *Popular Astronomy* 22, 275
- Rutledge R.E., 1998, *PASP* 110, 754 [\\_eprint: astro-ph/9802256](#)
- Salpeter E.E., 1964, *ApJ* 140, 796
- Salvato M., Buchner J., Budavári T., et al., 2018, *MNRAS* 473, 4937 [\\_eprint: 1705.10711](#)
- Sanford P.W., 1974, *Proceedings of the Royal Society of London Series A* 340, 411
- Sanford P.W., Ives J.C., Bell Burnell S.J., et al., 1975, *Nature* 256, 109
- Sarazin C.L., 1986, *Reviews of Modern Physics* 58, 1
- Savage B.D., Sembach K.R., 1996, *ARA&A* 34, 279
- Sawyer H.B., 1948, *AJ* 53, 117
- Scargle J.D., 1998, *ApJ* 504, 405 [\\_eprint: astro-ph/9711233](#)
- Scargle J.D., Norris J.P., Jackson B., Chiang J., 2013a, *arXiv e-prints* [arXiv:1304.2818](#) [\\_eprint: 1304.2818](#)
- Scargle J.D., Norris J.P., Jackson B., Chiang J., 2013b, *ApJ* 764, 167 [\\_eprint: 1207.5578](#)
- Schaubach J.K., 1802, *Geschichte der griechischen Astronomie bis auf Eratosthenes : von J.K. Schaubach, Römer Medium: XXVIII, 507 S. : Ill. ; 20 cm*
- Schilling G.F., Sterne T.E., 1957, *SAO Special Report* 1
- Schmid C., 2012, *PhD Thesis, Dr. Karl Remeis-Sternwarte, Astronomical Institute of the FAU*
- Schnopper H.W., Delvaile J.P., Epstein A., et al., 1976, *ApJ* 210, L75

## References

- Schreier E.J., Feigelson E., Delvaille J., et al., 1979, *ApJ*234, L39
- Schreier E.J., Gorenstein P., Feigelson E.D., 1982, *ApJ*261, 42
- Schwabe S.H., 1844, *Astronomische Nachrichten* 20, 234
- Schwabe, Samuel Heinrich 1843, *Astronomische Nachrichten* 20, 283
- Schwarzschild K., 1916, *Sitzungsberichte der Königlich Preußischen Akademie der Wissenschaften (Berlin)* 189–196
- Schwope A.D., Hasinger G., Schwarz R., et al., 1999, *A&A*341, L51 [\\_eprint: astro-ph/9811326](#)
- Semena A., Mereminskiy I., Lutovinov A., et al., 2020, *The Astronomer’s Telegram* 13415, 1
- Serlemitsos P.J., Kaluzienski L.J., Pravdo S.H., et al., 1976, *Nature*260, 592
- Serlemitsos P.J., Petre R., Glasser C., Birsa F., 1984, *IEEE Transactions on Nuclear Science* 31, 786
- Serlemitsos P.J., Smith B.W., Boldt E.A., et al., 1977, *ApJ*211, L63
- Serlemitsos P.J., Soong Y., Chan K.W., et al., 2007, *PASJ*59, S9
- Seyfert C.K., 1943, *ApJ*97, 28
- Shakura N.I., Sunyaev R.A., 1973a, In: Bradt H., Giacconi R. (eds.) *X- and Gamma-Ray Astronomy*, Vol. 55., p. 155
- Shakura N.I., Sunyaev R.A., 1973b, *A&A*500, 33
- Shapiro S.L., 1973a, *ApJ*180, 531
- Shapiro S.L., 1973b, *ApJ*185, 69
- Shapley H., Davis H., 1917, *PASP*29, 177
- Shirasaki Y., Kawai N., Sakamoto T., et al., 2003, In: *International Cosmic Ray Conference*, Vol. 5. *International Cosmic Ray Conference*, p. 2745
- Shklovskii I.S., 1976a, *Pisma v Astronomicheskii Zhurnal* 2, 482
- Shklovskii I.S., 1976b, *Soviet Astronomy Letters* 2, 188
- Shklovsky I.S., 1967, *ApJ*148, L1
- Shull J.M., 1993, *Physica Scripta Volume T* 47, 165
- Shvartsman V.F., 1971, *Soviet Ast.*15, 377
- Sijacki D., Vogelsberger M., Genel S., et al., 2015, *MNRAS*452, 575 [\\_eprint: 1408.6842](#)
- Silverman J.D., Green P.J., Barkhouse W.A., et al., 2008, *ApJ*679, 118 [\\_eprint: 0710.2461](#)
- Singh K.P., Stewart G.C., Chandra S., et al., 2016, In: den Herder J.W.A., Takahashi T., Bautz M. (eds.) *Space Telescopes and Instrumentation 2016: Ultraviolet to Gamma Ray*, Vol. 9905. *Society of Photo-Optical Instrumentation Engineers (SPIE) Conference Series*, p. 99051E
- Singh K.P., Tandon S.N., Agrawal P.C., et al., 2014, In: Takahashi T., den Herder J.W.A., Bautz M. (eds.) *Space Telescopes and Instrumentation 2014: Ultraviolet to Gamma Ray*, Vol. 9144. *Society of Photo-Optical Instrumentation Engineers (SPIE) Conference Series*, p. 91441S
- Singh K.P., White N.E., Drake S.A., 1996, *ApJ*456, 766
- Singh R., van de Ven G., Jahnke K., et al., 2013, *A&A*558, A43 [\\_eprint: 1308.4271](#)
- Siuniaev R.A., Babichenko S.I., Goganov D.A., et al., 1990, *Advances in Space Research* 10, 233
- Skrutskie M.F., Cutri R.M., Stiening R., et al., 2006, *AJ*131, 1163
- Smale A.P., Done C., Mushotzky R.F., et al., 1993, *ApJ*410, 796
- Smale A.P., Zhang W., White N.E., 1996, In: *American Astronomical Society Meeting Abstracts*, Vol. 189. *American Astronomical Society Meeting Abstracts*, p. 44.12
- Smith J.F., Courtier G.M., 1976, *Proceedings of the Royal Society of London Series A* 350, 421
- Snow T.P., Witt A.N., 1996, *ApJ*468, L65
- Sobolewska M.A., Done C., 2007, *MNRAS*374, 150 [\\_eprint: astro-ph/0609223](#)
- Sofia S., 1973, *ApJ*179, L25
- Sofia U.J., Cardelli J.A., Savage B.D., 1994, *ApJ*430, 650
- Soltan A., 1982, *MNRAS*200, 115
- Speller R.D., Royle G.J., Triantis F.A., et al., 2001, *Nuclear Instruments and Methods in Physics Research A* 457, 653
- Stasińska G., Vale Asari N., Cid Fernandes R., et al., 2008, *MNRAS*391, L29 [\\_eprint: 0809.1341](#)
- Steel D., 1998, In: Peiser B.J., Palmer T., Bailey M.E. (eds.) *Natural Catastrophes During Bronze Age Civilisations: Archaeological, Geological, Astronomical and Cultural Perspectives.*, p. 33
- Steele J., 2012a, *Journal for the History of Astronomy* 43, 247
- Steele J.M., 2012b, *Ancient Astronomical Observations and the Study of the Moon’s Motion (1691-1757)*, Springer US, Boston, MA
- Stella L., 1988, *Mem. Soc. Astron. Italiana*59, 185
- Stephan K.H., Englhauser J., 1986, In: *X-ray calibration: Techniques, sources, and detectors*, Vol. 689. *Society of Photo-Optical Instrumentation Engineers (SPIE) Conference Series*, p.128
- Strohmayer T.E., 2001, *arXiv e-prints astro-ph/0104487* [\\_eprint: astro-ph/0104487](#)
- Strohmayer T.E., Arzoumanian Z., Bogdanov S., et al., 2018, *ApJ*858, L13 [\\_eprint: 1808.04392](#)
- Strüder L., Briel U., Dennerl K., et al., 2001, *A&A*365, L18
- Sunyaev R., Arefiev V., Babyshkin V., et al., 2021, *arXiv e-prints arXiv:2104.13267* [\\_eprint: 2104.13267](#)
- Sunyaev R.A., Churazov E.M., Gilfanov M.R., et al., 1991, *Advances in Space Research* 11, 177
- Sunyaev R.A., Titarchuk L.G., 1980, *A&A*500, 167
- Suzuki K., Matsuoka M., Inoue H., et al., 1984, *PASJ*36, 761
- Swank J.H., Becker R.H., Boldt E.A., et al., 1977, *ApJ*212, L73
- Szanecki M., Niedźwiecki A., Done C., et al., 2020, *A&A*641, A89 [\\_eprint: 2006.15016](#)
- Takahashi T., Abe K., Endo M., et al., 2007, *PASJ*59, 35 [\\_eprint: astro-ph/0611232](#)
- Tamura T., Day C.S., Fukazawa Y., et al., 1996, *PASJ*48, 671

- Tamura T., Maeda Y., Mitsuda K., et al., 2009, *ApJ*705, L62 [\\_eprint: 0909.5003](#)
- Tanaka Y., Boller T., Gallo L., et al., 2004, *PASJ*56, L9 [\\_eprint: astro-ph/0405158](#)
- Tanaka Y., Fujii M., Inoue H., et al., 1984, *PASJ*36, 641
- Tananbaum H., Gursky H., Kellogg E.M., et al., 1972, *ApJ*174, L143
- Tarter C.B., Tucker W.H., Salpeter E.E., 1969, *ApJ*156, 943
- Tauber J.A., Mandolesi N., Puget J.L., et al., 2010a, *A&A*520, A1
- Tauber J.A., Norgaard-Nielsen H.U., Ade P.A.R., et al., 2010b, *A&A*520, A2
- Tawara Y., Hayakawa S., Kunieda H., et al., 1982, *Nature*299, 38
- Terada Y., Hayashi T., Ishida M., et al., 2008, *PASJ*60, 387 [\\_eprint: 0711.2716](#)
- Terashima Y., Ptak A., Fujimoto R., et al., 1998, *ApJ*496, 210
- Terekhov O.V., Siuniaev R.A., Kuznetsov A.V., et al., 1991, *Advances in Space Research* 11, 129
- Thirring H., 1918, *Physikalische Zeitschrift* 19, 33
- Thirring H., 1921, *Physikalische Zeitschrift* 22, 29
- Thompson A.R., Clark B.G., Wade C.M., Napier P.J., 1980, *ApJS*44, 151
- Thorne K.S., 1974, *ApJ*191, 507
- Titarchuk L., 1994, *ApJ*434, 570
- Tolman R.C., 1939, *Physical Review* 55, 364
- Tomida H., Tsunemi H., Kimura M., et al., 2011, *PASJ*63, 397 [\\_eprint: 1101.3651](#)
- Truemper J., 1982, *Advances in Space Research* 2, 241
- Truffa G., 2018, In: *Proceedings of 2018 IEEE International Workshop on Metrology for Archaeology and Cultural Heritage (MetroArchaeo 2018) in Cassino (Italy)*., Cassino (Italy), p.544
- Tsu W.S., 1934, *Popular Astronomy* 42, 136
- Tsunemi H., Kitamoto S., Manabe M., et al., 1989a, *PASJ*41, 391
- Tsunemi H., Kitamoto S., Okamura S., Roussel-Dupre D., 1989b, *ApJ*337, L81
- Tuohy I.R., 1980, *Proceedings of the Astronomical Society of Australia* 4, 4
- Tuohy I.R., Burton W.M., Clark D.H., 1982, *ApJ*260, L65
- Turner M.J.L., Abbey A., Arnaud M., et al., 2001, *A&A*365, L27 [\\_eprint: astro-ph/0011498](#)
- Turner M.J.L., Smith A., Zimmermann H.U., 1981, *br* 30, 513
- Turner M.J.L., Thomas H.D., Patchett B.E., et al., 1989, *PASJ*41, 345
- Turner M.L., Rutledge R.E., Letcavage R., et al., 2010, *ApJ*714, 1424 [\\_eprint: 1003.3955](#)
- Turner T.J., Pounds K.A., 1989, *MNRAS*240, 833
- Ubertini P., 1983, *Advances in Space Research* 3, 123
- Ubertini P., Lebrun F., Di Cocco G., et al., 2003, *ap* 411, L131
- Ulmer M.P., Baity W.A., Wheaton W.A., Peterson L.E., 1972, *ApJ*178, L121
- Ulmer M.P., Baity W.A., Wheaton W.A., Peterson L.E., 1974, *ApJ*192, 691
- Ulmer M.P., Lewin W.H.G., Hoffman J.A., et al., 1977, *ApJ*214, L11
- Urry C.M., Padovani P., 1995, *PASP*107, 803 [\\_eprint: astro-ph/9506063](#)
- van Paradijs J., Cominsky L., Lewin W.H.G., 1979, *MNRAS*189, 387
- Vaughan S., Edelson R., Warwick R.S., Uttley P., 2003, *MNRAS*345, 1271 [\\_eprint: astro-ph/0307420](#)
- Vedrenne G., Roques J.P., Schönfelder V., et al., 2003, *ap* 411, L63
- Verbunt F., van Gent R.H., 2010, *Astronomy and Astrophysics* 516, A28
- Verdenius W., 1958, *Mnemosyne* 11, 193
- Vidaña I., 2018, *European Physical Journal Plus* 133, 445 [\\_eprint: 1805.00837](#)
- Villa G., Page C.G., Turner M.J.L., et al., 1976, *MNRAS*176, 609
- Voges W., Aschenbach B., Boller T., et al., 2000, *iaucirc* 7432, 3
- Voges W., Aschenbach B., Boller T., et al., 1999, *A&A*349, 389 [\\_eprint: astro-ph/9909315](#)
- Vondrovský V., Beneš J., Rauerová M., et al., 2015, *Anthropologie (1962-)* 53, 457 Publisher: Moravian Museum
- Véron-Cetty M.P., Véron P., 2010, *A&A*518, A10
- Waki I., Inoue H., Koyama K., et al., 1984, *PASJ*36, 819
- Walter F.M., Wolk S.J., Neuhäuser R., 1996, *Nature*379, 233
- Walton D.J., Risaliti G., Harrison F.A., et al., 2014, *ApJ*788, 76
- Wang P.K., Siscoe G.L., 1980, *Solar Physics* 66, 187
- Warwick R.S., Marshall N., Fraser G.W., et al., 1981, *MNRAS*197, 865
- Watson M.G., Schröder A.C., Fyfe D., et al., 2009, *ap* 493, 339 [\\_eprint: 0807.1067](#)
- Watson P.S., 1949, *Popular Astronomy* 57, 14
- Weaver K.A., Mushotzky R.F., Arnaud K.A., et al., 1992, *ApJ*401, L11
- Weaver K.A., Yaqoob T., Mushotzky R.F., et al., 1997, *ApJ*474, 675
- Weir J.D., 1982, *Journal for the History of Astronomy* 13, 23
- Weisskopf M.C., Brinkman B., Canizares C., et al., 2002, *PASP*114, 1 [\\_eprint: astro-ph/0110308](#)
- Wells D.C., Greisen E.W., Harten R.H., 1981, *aps* 44, 363
- Wenger M., Ochsenbein F., Egret D., et al., 2000, *A&AS*143, 9 [\\_eprint: astro-ph/0002110](#)
- Werner N., Urban O., Simionescu A., Allen S.W., 2013, *Nature*502, 656 [\\_eprint: 1310.7948](#)
- Werner W.S.M., Glantschnig K., Ambrosch-Draxl C., 2009, *Journal of Physical and Chemical Reference Data* 38, 1013 [\\_eprint: https://doi.org/10.1063/1.3243762](#)
- Weyl H., 1917, *Annalen der Physik* 359, 117
- White N.E., Mason K.O., Sanford P.W., Murdin P., 1976, *MNRAS*176, 201

## References

- White N.E., Peacock A., 1988, *Mem. Soc. Astron. Italiana*59, 7
- Wilkins D.R., Fabian A.C., 2011, *MNRAS*414, 1269 \_eprint: 1102.0433
- Wilkins D.R., Fabian A.C., 2012, *MNRAS*424, 1284 \_eprint: 1205.3179
- Wilkins D.R., Kara E., Fabian A.C., Gallo L.C., 2014, *MNRAS*443, 2746 \_eprint: 1406.6658
- Wilms J., 2017, *Lecture on X-ray astronomy*
- Wilms J., Allen A., McCray R., 2000, *ApJ*542, 914 \_eprint: astro-ph/0008425
- Wilms J., Kreykenbohm I., Weber P., et al., 2020, *The Astronomer's Telegram* 13416, 1
- Wilms J., Reynolds C.S., Begelman M.C., et al., 2001, *MNRAS*328, L27 \_eprint: astro-ph/0110520
- Wilson A.S., Colbert E.J.M., 1995, *ApJ*438, 62 \_eprint: astro-ph/9408005
- Winkler C., Courvoisier T.J.L., Di Cocco G., et al., 2003, *ap* 411, L1
- Winkler C., Diehl R., Ubertini P., Wilms J., 2011, *br* 161, 149 \_eprint: 1110.6279
- Wolter H., 1952a, *Annalen der Physik* 445, 94
- Wolter H., 1952b, *Annalen der Physik* 445, 286
- Woo J.H., Urry C.M., 2002, *ApJ*579, 530 \_eprint: astro-ph/0207249
- Wood K.S., Meekins J.F., Yentis D.J., et al., 1984, *ApJS*56, 507
- Wächtler M., 1957, *Deutsche Hydrographische Zeitschrift* 10, 169
- XRISM Science Team 2020, *arXiv e-prints* arXiv:2003.04962 \_eprint: 2003.04962
- Yadav J.S., Agrawal P.C., Antia H.M., et al., 2016, In: *den Herder J.W.A., Takahashi T., Bautz M. (eds.) Space Telescopes and Instrumentation 2016: Ultraviolet to Gamma Ray*, Vol. 9905. Society of Photo-Optical Instrumentation Engineers (SPIE) Conference Series, p. 99051D
- Yamashita A., Matsumoto C., Ishida M., et al., 1997, *ApJ*486, 763
- Yamauchi S., Kawada M., Koyama K., et al., 1990, *ApJ*365, 532
- Yang Q., Wu X.B., Fan X., et al., 2018, *ApJ*862, 109 \_eprint: 1711.08122
- Yaqoob T., Edelson R., Weaver K.A., et al., 1995, *ApJ*453, L81
- Yu Q., Lu Y., 2004, *ApJ*602, 603 \_eprint: astro-ph/0311404
- Yuan Z., Wang J., Worrall D.M., et al., 2018, *ApJS*239, 33 \_eprint: 1810.12713
- Zampieri L., Campana S., Turolla R., et al., 2001, *A&A*378, L5 \_eprint: astro-ph/0108456
- Zdziarski A.A., Poutanen J., Johnson W.N., 2000, *ApJ*542, 703 \_eprint: astro-ph/0006151
- Zhang P.f., Zhang P., Liao N.h., et al., 2018, *ApJ*853, 193 \_eprint: 1703.07186
- Zhang W., Giles A.B., Jahoda K., et al., 1993, In: *Siegmund O.H. (ed.) EUV, X-Ray, and Gamma-Ray Instrumentation for Astronomy IV*, Vol. 2006. Society of Photo-Optical Instrumentation Engineers (SPIE) Conference Series, p.324
- Zimmerman E.R., Narayan R., McClintock J.E., Miller J.M., 2005, *ApJ*618, 832 \_eprint: astro-ph/0408209
- Zoghbi A., Cackett E.M., Reynolds C., et al., 2014, *ApJ*789, 56 \_eprint: 1405.3674
- Zoghbi A., Fabian A.C., Uttley P., et al., 2010, *MNRAS*401, 2419 \_eprint: 0910.0367
- Zoghbi A., Uttley P., Fabian A.C., 2011, *MNRAS*412, 59 \_eprint: 1010.3744
- Zombeck M.V., Chappell J.H., Kenter A.T., et al., 1995a, In: *Siegmund O.H., Vallerga J.V. (eds.) EUV, X-Ray, and Gamma-Ray Instrumentation for Astronomy VI*, Vol. 2518. Society of Photo-Optical Instrumentation Engineers (SPIE) Conference Series, p.96
- Zombeck M.V., Conroy M., Harnden F.R., et al., 1990, In: *Hudson H.S., Siegmund O.H. (eds.) EUV, X-ray, and Gamma-ray instrumentation for astronomy*, Vol. 1344. Society of Photo-Optical Instrumentation Engineers (SPIE) Conference Series, p.267
- Zombeck M.V., David L.P., Harnden F.R., Kearns K., 1995b, In: *Siegmund O.H., Vallerga J.V. (eds.) EUV, X-Ray, and Gamma-Ray Instrumentation for Astronomy VI*, Vol. 2518. Society of Photo-Optical Instrumentation Engineers (SPIE) Conference Series, p.304
- Zycki P.T., Krolik J.H., Zdziarski A.A., Kallman T.R., 1994, *ApJ*437, 597
- Özel F., Psaltis D., Narayan R., Santos Villarreal A., 2012, *ApJ*757, 55 \_eprint: 1201.1006

# Acknowledgments

This work is based on data from eROSITA, the soft X-ray instrument aboard SRG, a joint Russian-German science mission supported by the Russian Space Agency (Roskosmos), in the interests of the Russian Academy of Sciences represented by its Space Research Institute (IKI), and the Deutsches Zentrum für Luft- und Raumfahrt (DLR). The SRG spacecraft was built by Lavochkin Association (NPOL) and its subcontractors, and is operated by NPOL with support from the Max Planck Institute for Extraterrestrial Physics (MPE).

The development and construction of the eROSITA X-ray instrument was led by MPE, with contributions from the Dr. Karl Remeis Observatory Bamberg & ECAP (FAU Erlangen-Nuernberg), the University of Hamburg Observatory, the Leibniz Institute for Astrophysics Potsdam (AIP), and the Institute for Astronomy and Astrophysics of the University of Tübingen, with the support of DLR and the Max Planck Society. The Argelander Institute for Astronomy of the University of Bonn and the Ludwig Maximilians Universität Munich also participated in the science preparation for eROSITA.

The eROSITA data shown here were processed using the eSASS/NRTA software system developed by the German eROSITA consortium.

This research has made use of ISIS functions (ISISscripts) provided by ECAP/Remeis observatory and MIT (<http://www.sternwarte.uni-erlangen.de/isis/>).



# Eigenständigkeitserklärung

Hiermit bestätige ich, dass ich diese Arbeit selbstständig und nur unter Verwendung der angegebenen Hilfsmittel angefertigt habe.

---

(Ort, Datum)

---

Philipp Weber